

UC Irvine

UC Irvine Electronic Theses and Dissertations

Title

Principles of Molecular Design in the Development of Ligand Frameworks that Control the Primary and Secondary Coordination Spheres of Metal Ions

Permalink

<https://escholarship.org/uc/item/9bv209vn>

Author

Cook, Sarah

Publication Date

2015

Peer reviewed|Thesis/dissertation

UNIVERSITY OF CALIFORNIA,
IRVINE

Principles of Molecular Design in the Development of Ligand Frameworks that Control
the Primary and Secondary Coordination Spheres of Metal Ions

DISSERTATION

submitted in partial satisfaction of the requirements
for the degree of

DOCTOR OF PHILOSOPHY

in Chemistry

by

Sarah A. Cook

Dissertation Committee:
Professor Andrew S. Borovik, Chair
Professor Alan F. Heyduk
Professor William J. Evans

2015

Portion of Chapter 1 © American Chemical Society
Portion of Chapter 2 © Royal Society of Chemistry
Portions of Chapters 3 and 4 © American Chemical Society
All other materials © Sarah A. Cook

DEDICATION

To my dad, who was taken from us too early.
To my family, who has joined together in love and support.
And most of all to my mom, who is so much stronger than she knows.

TABLE OF CONTENTS

	Page
LIST OF FIGURES	iv
LIST OF TABLES	xi
LIST OF SCHEMES	xiii
LIST OF CHARTS	xiv
ACKNOWLEDGMENTS	xv
CURRICULUM VITAE	xvii
ABSTRACT OF THE DISSERTATION	xix
CHAPTER 1: Introduction	1
CHAPTER 2: Influences of Group 2 Metal Ions on the Properties of Fe and Mn Heterobimetallic Complexes	23
CHAPTER 3: Intramolecular Hydroxylation of Tripodal Sulfonamido Ligands by Putative High-Valent Fe and Mn Complexes	48
CHAPTER 4: Evidence for Formation of an Fe(IV)–oxo Intermediate in a Tripodal Sulfonamido Fe Complex	78
CHAPTER 5: Coordination Properties of a Tridentate, Redox Active, Sulfonamido Ligand	96
CHAPTER 6: Mononuclear Fe(II) and Co(II) Complexes of a Tridentate, Redox Active Ligand Derivative Containing Sulfonamido Groups	124
APPENDIX A: Supplementary Information	151

LIST OF FIGURES

	Page
1.1. Catalytic cycle of substrate hydroxylation by cytochrome P450 and a depiction of the competent oxidant (Compound I).....	2
1.2. Depiction of the H-bonding interactions within the active site of cytochrome P450 that serve to orient the substrate (camphor) and assist in O–O bond cleavage.....	3
1.3. A) Cu(III) complexes stabilized by the strong donation of the amide groups in the tetraglycine fragment. B) High valent Mn(V)– and Fe(V)–oxo complexes developed by Collins that utilized the same concepts of strong amide donors and methylation of the methylene linkers that was described for the Cu(III) tetrapeptide complexes.	4
1.4. Complexes supported by redox noninnocent ligands that provide access to formally A) -2 and B) +4 oxidation states. Select bond lengths are shown that were used to determine that the ligand had been reduced or oxidized.	6
1.5. Picket fence porphyrin complex that was used to structurally characterize the first example of an Fe–O ₂ adduct.	7
1.6. Modified picket fence porphyrin complex containing a urea group that is capable of forming a H-bond to the superoxide ligand.....	8
1.7. Examples of tripodal ligand frameworks that establish secondary sphere interactions: A) Cu(II)–hydroperoxide and Co(II)–azide complexes reported by Masuda; B) select complexes of Mareque-Rivas that were used to study the influence of H-bonds on the acidity of the coordinated water molecule. Shown are the two symmetric ligand frameworks, but unsymmetric derivatives containing 1 and 2 unfunctionalized pyridyl donors were also developed; C) one of the intermediate species from the reduction of N ₂ that was isolated by Schrock.	9
1.8. Examples of complexes that establish non-covalent interactions within the secondary coordination sphere.	11
1.9. Complexes supported by ligands containing varying numbers of H-bond donors that were used to examine the influence of H-bonds on O ₂ activation.	12
1.10. Depiction of the H-bonding interactions that stabilize the oxido ligand in [Fe ^{III} H ₃ buea(O)] ⁻	12
1.11. A) [MST] ³⁻ ligand framework; B) Fe(III)–NH ₃ complex showing the H-bonding interactions to the sulfonamido oxygen atoms; C) an example of a heterobimetallic complex that was prepared from reduction of O ₂	14

1.12. Three of the heterobimetallic complexes studied in Chapter 2.....	15
1.13. Product that resulted from intramolecular oxidation of the [MST] ³⁻ ligand system.....	16
1.14. Example of the reactivity studies described in Chapter 4.....	16
1.15. Depiction of the dinuclear complexes that are examined in Chapter 5.	17
1.16. An example of the mononuclear complexes described in Chapter 6.....	18
2.1. Structure of the oxygen-evolving complex in Photosystem II. Red = O, purple = Mn, light blue = Ca. Dotted lines represent H-bonding interactions.....	24
2.2. Abbreviated depiction of the multinuclear clusters developed by Agapie.....	25
2.3. The multifunctional MST ³⁻ ligand system.....	26
2.4. Electronic absorbance spectra for the addition of dioxygen to a solution of NMe ₄ [Fe ^{II} MST] and Sr ^{II} (OTf) ₂ /15-crown-5. Spectra were recorded every 30 sec on a 0.3 mM DCM solution at 20 °C. The inset shows the spectrum of the isolated product in DCM.....	27
2.5. Molecular structure of [(15-crown-5)⊃Ca ^{II} -(μ-OH)-Fe ^{III} MST] ⁺ determined by XRD methods. Thermal ellipsoids are drawn at the 50% probability level, and only the hydroxo proton is shown for clarity.	28
2.6. Core molecular structures of A) [(15-crown-5)⊃Ca ^{II} -(μ-OH)-Fe ^{III} MST] ⁺ , B) [(15- crown-5)⊃Sr ^{II} -(μ-OH)-Fe ^{III} MST] ⁺ , and C) [(OTf)(18-crown-6)⊃Ba ^{II} -(μ-OH)- Fe ^{III} MST].....	30
2.7. Molecular structures of the products from the reaction of NMe ₄ [Fe ^{II} MST], Ba(OTf) ₂ /15-crown-5, and O ₂ that were crystallized from (A) DCM/pentane at room temperature and (B) MeCN/ether at -30 °C. Ellipsoids are drawn at the 50% probability and only H1 is shown for clarity. In (A), only the primary coordination spheres of the four [Fe ^{III} MST] ⁻ complexes and the oxygen atoms involved in coordination of the Ba ^{II} ion are shown. Red atoms correspond to oxygen, yellow to sulfur, blue to nitrogen, and black to carbon.	32
2.8. FTIR spectra in Nujol of the OH vibration in [Ca ^{II} (OH)Fe ^{III}] ⁺ (grey), [Sr ^{II} (OH)Fe ^{III}] ⁺ (black), [(OTf)Ba ^{II} (OH)Fe ^{III}] (dashed black).....	34
2.9. Initial rate data for (A) the reaction of [Fe ^{II} MST] ⁻ with dioxygen in the presence of NMe ₄ ⁺ , 3 equivalents of Ca(OTf) ₂ /15-crown-5, 3 equivalents of Sr(OTf) ₂ /15-crown-5, and 3 equivalents of Ba(OTf) ₂ /18-crown-6. (B) The reaction of [Mn ^{II} MST] ⁻ with dioxygen in the presence of NMe ₄ ⁺ , 1 equivalent Ca(OTf) ₂ /15-crown-5, 1 equivalent Sr(OTf) ₂ /15-crown-5, and 1 equivalent Ba(OTf) ₂ /18-crown-6.....	35

2.10. Cyclic voltammograms of (A) $[M^{II}(OH)Fe^{III}]^+$ and (B) $[M^{II}(OH)Mn^{III}]^+$ where M^{II} = Ca (grey), Sr (black), and Ba (dashed black) showing a quasi-reversible Fe^{II}/Fe^{III} or Mn^{II}/Mn^{III} redox couple in DCM (0.1 M TBAP, 100 mV/s, with ferrocene as an internal standard).	37
3.1. Spectra collected of the reaction mixture of $NMe_4[Fe^{II}MST]$ and O_2 five hours after the addition of O_2 : A) ESI-MS showing the molecular ion peak assigned to $[Fe^{III}MST(OH)]^-$; B) perpendicular mode EPR spectrum collected at 77 K; C) solution IR spectrum of a 24 mM DCM solution.....	51
3.2. ESI mass spectrum of $NMe_4[Fe^{III}MST(OH)]$ after the addition of 1 equivalent of $H_2^{18}O$ in DCM (bottom) and the calculated isotope distribution patterns for the $[Fe^{III}MST^{16}OH]^-$ ion (black) and the $[Fe^{III}MST^{18}OH]^-$ ion (red).	52
3.3. Molecular structure of the $NMe_4[Fe^{II}MST(OH_2)]$ product that was crystallized from the reaction of $NMe_4[Fe^{II}MST]$ with excess O_2 . Ellipsoids are drawn at the 50% probability level. The counter cation and all hydrogen atoms except those of the aquo ligand are omitted for clarity.	53
3.4. A) FTIR spectra showing the conversion of $[Fe^{III}MST(OH)]^-$ to $[Fe^{II}MST(OH_2)]^-$ after the removal of excess O_2 from the reaction of $NMe_4[Fe^{II}MST]$ with O_2 . The spectra were collected on a 24 mM DCM solution over the course of 7 days (dashed black), with the first spectrum collected after 5 hours (solid black). B) FTIR spectrum of independently prepared $NMe_4[Fe^{II}MST(OH_2)]$ in 24 mM DCM solution.....	54
3.5. Spectra obtained of the reaction mixture of $NMe_4[Fe^{II}MST]$ and 2 equivalents of NMO: A) FTIR spectra of a 24 mM DCM solution showing the conversion of the initial product to $[Fe^{II}MST(OH_2)]^-$ over the course of 9 days (dashed black), with the first spectrum collected after 5 hours (solid black); B) ESI-MS showing the molecular ion peak assigned to $[Fe^{III}-O-MST]^-$	56
3.6. Thermal ellipsoid diagram depicting $[Fe^{III}-O-MST]^-$. Ellipsoids are drawn at the 50% probability level, and all hydrogen atoms and the counter cation are omitted for clarity....	57
3.7. ESI mass spectra from reaction of $[Fe^{II}NST]$ with NMO in (A) MeCN and (B) THF where 786 = hydroxide product and 784 = phenoxide product. (C) Calculated isotope pattern of $[Fe^{III}NST(OH)]^-$ ($C_{36}H_{34}FeN_4O_7S_3$). (D) Reaction of $[Mn^{II}NST]$ in THF and (E) MeCN where 785 = hydroxide product and 783 = phenoxide product. (F) Calculated isotope pattern of $[Mn^{III}NST(OH)]^-$ ($C_{36}H_{34}MnN_4O_7S_3$).....	63
4.1. Thermal ellipsoid diagram depicting $[Fe^{III}TST(OH)]^-$. Ellipsoids are drawn at the 50% probability level, and only the hydroxo hydrogen atom is shown. The NMe_4^+ counter ion is omitted for clarity.	81

4.2. Spectra collected of isolated $\text{NMe}_4[\text{Fe}^{\text{III}}\text{TST}(\text{OH})]$: A) ESI-MS showing the molecular ion peak assigned to $[\text{Fe}^{\text{III}}\text{TST}(\text{OH})]^-$; B) perpendicular mode EPR spectrum collected at 77 K on a 5 mM 1:1 DCM:THF solution, inset showing an expansion of the $g = 9.6$ signal; C) IR spectrum of the crystalline solid as a KBr disk.	83
4.3. Electronic absorption spectra for the oxidation of a 0.2 mM DCM solution of $\text{NMe}_4[\text{Fe}^{\text{II}}\text{TST}(\text{H}_2\text{O})]$ with NMO at 25 °C showing (A) conversion of the Fe(II) complex (dashed black) to the intermediate species (solid black) and (B) further reaction of the intermediate to the final $\text{NMe}_4[\text{Fe}^{\text{III}}\text{TST}(\text{OH})]$ product (dotted black). The inset of (B) shows the decay of the low energy band in a 5 mM DCM solution.	84
4.4. Electronic absorption spectra of 0.2 mM MeCN solutions for (A) oxidation of $[\text{Fe}^{\text{II}}\text{TST}(\text{OH}_2)]^-$ with NMO in the presence of $\text{Ca}(\text{OTf})_2/15\text{-crown-5}$ at 20 °C showing the direct conversion to a single species that was assigned to $[15\text{-crown-5}\supset\text{Ca}^{\text{II}}-(\mu\text{-OH})\text{-Fe}^{\text{III}}\text{TST}]\text{OTf}$ and (B) addition of $\text{Ca}(\text{OTf})_2/15\text{-crown-5}$ to the proposed $[\text{Fe}^{\text{IV}}\text{TST}(\text{O})]^-$ intermediate stabilized at -40 °C (dotted black) showing immediate conversion to $[15\text{-crown-5}\supset\text{Ca}^{\text{II}}-(\mu\text{-OH})\text{-Fe}^{\text{III}}\text{TST}]\text{OTf}$	86
4.5. Electronic absorption spectra for the reaction of 0.2 mM $[\text{Fe}^{\text{IV}}\text{TST}(\text{O})]^-$ intermediate stabilized at -40 °C with (A) 0.5 DPH in THF and (B) 20 DHA in MeCN.	87
5.1. Depictions of the molecular structures of the $[\text{M}^{\text{II}}_2(\text{tbaps})_2]^{2-}$ complexes determined by XRD methods: A) complexes with NR_4^+ counter ions; B) complexes with K^+ counter ions. The tolyl groups adopt the same arrangement in all five complexes but are shown only for the $[\text{Cu}_2(\text{tbaps})_2]^-$ complex in A. The three complexes in A and the Co complex in B contain a two-fold rotation axis that is orthogonal to the plane of the diamond core. Thermal ellipsoids are drawn at the 50% probability level.	103
5.2. Depiction of the interactions of the K^+ ions with the pockets of sulfonamido oxygen atoms that give rise to a polymeric structure. The tolyl groups are excluded for clarity. Thermal ellipsoids are drawn at the 50% probability level.	106
5.3. Electronic absorbance spectra for the $[\text{M}^{\text{II}}_2(\text{tbaps})_2]^{2-}$ complexes in MeCN at room temperature.	107
5.4. EPR spectra of the $\text{K}_2[\text{Cu}_2(\text{tbaps})_2]$ complex at 77K A) as a 5 mM solution (relative to Cu) in 1:1 DMF:THF with an inset showing the 13-line hyperfine pattern on the $g = 2.04$ signal, and B) as a solid sample.	108
5.5. Parallel mode EPR spectrum of a 5 mM (based on Fe) solution of $\text{K}_2[\text{Fe}_2(\text{tbaps})_2]$ in 1:1 DMF:THF at 10 K.	109
5.6. Cyclic voltammograms of the six $[\text{M}_2(\text{tbaps})_2]^{2-}$ salts in MeCN referenced to $\text{Fc}^{0/+}$ (1mM, 0.1 M TBAP, 100 mV/s, with cobaltocenium hexafluorophosphate as an internal standard).	110

5.7. A) UV-vis spectral changes for the addition of Ca(OTf) ₂ /15-crown-5 to a 0.24 mM (with respect to Cu) solution of (NMe ₄) ₂ [Cu ₂ (tbaps) ₂] in acetonitrile, and B) Comparison of the spectra obtained from the addition of group 2 metal ions as crown ether adducts.....	112
5.8. Molecular structure of the complex obtained from crystallization of [Cu ₂ (tbaps) ₂] ²⁻ in the presence of Ca(OTf) ₂ /15-crown-5.....	113
6.1. Molecular structure of [Co ^{II} (ibaps)DMAP] ⁻ determined by XRD methods. The NEt ₄ ⁺ counter ion is omitted for clarity. Thermal ellipsoids are drawn at the 50% probability level.	128
6.2. Molecular structures of the [M ^{II} (ibaps)bpy] ⁻ complexes determined by XRD methods; A) [Fe ^{II} (ibaps)bpy] ⁻ , B) Space filling model of [Fe ^{II} (ibaps)bpy] ⁻ illustrating the open coordination site that is framed by the sulfonamido oxygen atoms; C) [Co ^{II} (ibaps)bpy] ⁻ . All of the NEt ₄ ⁺ counter ions are excluded for clarity. Thermal ellipsoids of C are drawn at the 50% probability level.	130
6.3. EPR spectra of the monomeric M(II) complexes at 10 K: A) 10 mM NEt ₄ [Co ^{II} (ibaps)DMAP] in THF; B) parallel mode spectrum of 1 mM NEt ₄ [Fe ^{II} (ibaps)bpy] in 1:1 THF:Et ₂ O; C) 10 mM NEt ₄ [Co ^{II} (ibaps)bpy] in THF.....	132
6.4. Cyclic voltammogram of NEt ₄ [Co ^{II} (ibaps)DMAP] in MeCN referenced to Fc ^{0/+} (1mM, 0.1 M TBAP, 100 mV/s, with cobaltocenium hexafluorophosphate as an internal standard).....	133
6.5. Spectral changes upon addition of 1 equivalent of FcBF ₄ (black) to NEt ₄ [Co ^{II} (ibaps)DMAP] (grey) in THF at -80 °C: A) UV-vis spectra of a 0.12 mM solution, and B) EPR spectra of 10 mM solutions collected at 10 K. The g = 4.4 signal in the oxidized sample is thought to arise from an error in stoichiometry.....	134
6.6. Cyclic voltammograms of A) NEt ₄ [Co ^{II} (ibaps)bpy] in THF, B) NEt ₄ [Fe ^{II} (ibaps)bpy] in MeCN, and C) NEt ₄ [Fe ^{II} (ibaps)bpy] in THF showing the irreversible behavior observed when the potential is scanned to the edges of the solvent window (grey). Conditions for all experiments are 1 mM complex, 0.1 M TBAP, 100 mV/s, with cobaltocenium hexafluorophosphate as an internal standard. Potentials are referenced to Fc ^{0/+}	135
6.7. Spectral changes upon addition of 1 equivalent (grey) and 2 equivalents (dashed black) of FcBF ₄ to THF solutions of the NEt ₄ [M ^{II} (ibaps)bpy] salts (black) at -80 °C: A) 0.1 mM Fe and B) 0.24 mM Co. C) Overlay of the singly oxidized spectra of Fe (black) and Co (grey).....	137
6.8. Spectral changes upon addition of 1 equivalent (grey) and 2 equivalents (black) of FcBF ₄ to THF solutions of the NEt ₄ [M ^{II} (ibaps)bpy] complexes at -80 °C: A) 5 mM Fe collected at 77K and B) 10 mM Co collected at 10K.	138

6.9. Spectral changes (solid black) upon addition of excess O ₂ to NEt ₄ [Co ^{II} (ibaps)DMAP] (dashed black) in THF at -100 °C: A) UV-vis spectra of a 0.12 mM solution and B) EPR spectra of 10 mM solutions at 10 K with an expansion of the g=2 signal. The spectrum of the Co(II) starting complex is shown for reference.....	139
6.10. Spectral changes (solid black) upon addition of excess O ₂ to the NEt ₄ [M ^{II} (ibaps)bpy] complexes (dashed black) in THF at -100 °C: A) EPR spectrum of 10 mM Co at 10 K with an expansion of the g=2 signal; B) UV-vis spectra of a 0.12 mM Co solution; C) EPR spectrum of 6 mM Fe at 10 K with an expansion of the g=2 signal; D) UV-vis spectra of a 0.15 mM Fe solution; E) Comparison of the optical spectra from the reactions of NEt ₄ [Fe ^{II} (ibaps)bpy] with 1 equivalent of FcBF ₄ at -80 °C (black) and excess O ₂ at -100 °C (grey).....	140
6.11. Molecular structure of [Co ^{II} (Hibaps)bpy] determined by XRD methods. Thermal ellipsoids are drawn at the 50% probability level.....	142
A.1. ¹ H NMR spectrum of ligand product 1 that was isolated from crystalline NMe ₄ [Fe ^{II} -O-MST].....	153
A.2. ¹³ C NMR spectrum of ligand product 1 that was isolated from crystalline NMe ₄ [Fe ^{II} -O-MST].....	154
A.3. ¹ H NMR spectrum of a mixture of ligand products 1 and 2 that was separated from the remainder of the products via column chromatography.	155
A.4. ¹³ C NMR spectrum of a mixture of ligand products 1 and 2 that was separated from the remainder of the products via column chromatography.	156
A.5. ¹ H NMR spectrum of a ligand product 3 with a small impurity of H ₃ MST that was separated from the remainder of the products via column chromatography.	157
A.6. ¹³ C NMR spectrum of a ligand product 3 with a small impurity of H ₃ MST that was separated from the remainder of the products via column chromatography.	158
A.7. ¹ H NMR spectrum of a mixture of H ₃ MST and ligand products 3 and 4 that was separated from the remainder of the products via column chromatography.	159
A.8. ¹³ C NMR spectrum of a mixture of H ₃ MST and ligand products 3 and 4 that was separated from the remainder of the products via column chromatography.	160
A.9. ¹ H NMR spectrum of the mixture of ligand products isolated after the reaction of NMe ₄ [Fe ^{II} MST] and 2 equivalents of NMO.	161

A.10. ^1H NMR spectrum of a mixture of ligand products 1 and the unidentified ligand product 5 that was produced from the reaction of $\text{NMe}_4[\text{Mn}^{\text{II}}\text{MST}]$ and PhIO in the presence of $\text{Ca}(\text{OTf})_2/15\text{-crown-5}$. Products 1 and 5 were separated from H_3MST via column chromatography.....	162
A.11. ^{13}C NMR spectrum of a mixture of ligand products 1 and the unidentified ligand product 5 that was produced from the reaction of $\text{NMe}_4[\text{Mn}^{\text{II}}\text{MST}]$ and PhIO in the presence of $\text{Ca}(\text{OTf})_2/15\text{-crown-5}$. Products 1 and 5 were separated from H_3MST via column chromatography.....	163
A.12. Molecular structure of $[15\text{-crown-5}\supset\text{Ca}^{\text{II}}-(\mu\text{-OH})\text{-Fe}^{\text{III}}\text{TST}]\text{OTf}$ determined by XRD methods. Thermal ellipsoids are drawn at the 50% probability level.	164
A.13. ^1H NMR spectrum of the DHA products isolated from the reaction of $\text{NMe}_4[\text{Fe}^{\text{II}}\text{TST}(\text{OH}_2)]$ with 2 equivalents of NMO in MeCN.	165
A.14. Numbering scheme that corresponds to the metrical parameters shown in Table A.7....	167
A.15. Numbering scheme that corresponds to the metrical parameters shown in Table A.8....	169

LIST OF TABLES

	Page
2.1. Select bond lengths (Å) for the $[M^{II}(OH)Fe^{III}]^+$ complexes.	31
2.2. Select bond lengths (Å) for the $[M^{II}(OH)Mn^{III}]^+$ complexes.	31
2.3. Select metrical parameters for $[(OTf)(15\text{-crown-}5)\supset Ba^{II}-(\mu\text{-OH})\text{-}Fe^{III}MST]$	33
3.1. Select metrical parameters for $[Fe^{III}\text{-O}\text{-}MST]^-$	57
3.2. Distribution of the isolated ligand products.....	59
4.1. Select metrical parameters for $[Fe^{III}TST(OH)]^-$	82
5.1. Metrical parameters for the primary coordination spheres of the $[M^{II}_2(tbaps)_2]^{2-}$ complexes.....	104
5.2. Metrical parameters for the primary coordination spheres of the two distinct Cu(II) centers in $(NMe_4)_2[Cu_2(tbaps)_2]$	105
5.3. Metrical parameters for the primary coordination spheres of the two distinct Cu(II) centers in the $[Cu_2(tbaps)_2]^-$ containing Ca(II) ions.....	113
6.1. Key metrical parameters for $NEt_4[Co^{II}(ibaps)DMAP]$	129
6.2. Key metrical parameters for $NEt_4[Co^{II}(ibaps)bpy]$	131
6.3. Electrochemical potentials (V vs. $Fc^{0/+}$) of the $[M^{II}(ibaps)bpy]^-$ complexes in THF and MeCN.....	135
6.4. Key metrical parameters for the $[Co^{II}(Hibaps)bpy]$ complex.....	143
A.1. Crystallographic data and structure refinement parameters for the molecular structures presented in Chapter 2.....	151
A.2. Crystallographic data and structure refinement parameters for the molecular structures presented in Chapter 3.....	151
A.3. Select metrical parameters for $NMe_4[Fe^{II}MST(OH_2)]$	152
A.4. Crystallographic data and structure refinement parameters for the molecular structures presented in Chapter 4.....	164
A.5. Select metrical parameters for $[15\text{-crown-}5\supset Ca^{II}-(\mu\text{-OH})\text{-}Fe^{III}TST]OTf$	165

A.6. Crystallographic data and structure refinement parameters for the molecular structures presented in Chapter 5.	166
A.7. Crystallographic data and structure refinement parameters for molecular structures presented in Chapter 5.	166
A.8. Bond distances (Å) within the backbone of one [tbaps] ³⁻ ligand for each of the [M ₂ (tbaps) ₂] ²⁻ structures. The numbering scheme of the backbone is shown in Figure A.14.....	167
A.9. Crystallographic data and structure refinement parameters for molecular structures presented in Chapter 6.	168
A.10. Bond distances (Å) within the [ibaps] ³⁻ ligand backbone of the monomeric complexes and within the bpy ligand of the five-coordinate complexes. The numbering scheme used to describe the bond lengths is shown in Figure A.15.	169

LIST OF SCHEMES

	Page
2.1. Preparative route to heterobimetallic complexes.....	27
3.1. Preparation of heterobimetallic complexes from O-atom transfer reagents.....	55
3.2. Major products observed in the oxidation of $\text{NMe}_4[\text{Fe}^{\text{II}}\text{NST}]$ with NMO.....	63
3.3. Two possible mechanistic routes leading to the observed mixture of Fe(III)–hydroxide and Fe(III)–alkoxide products from the oxidation of $[\text{Fe}^{\text{II}}\text{MST}]^-$ with an O-atom transfer reagent: A) intramolecular (or radical rebound) mechanism; B) intermolecular reaction of the ligand-based radical with solvent, substrate, or oxidant.	67
3.4. Possible mechanism leading to the observed mixture of Fe(III)–hydroxide and Fe(III)–phenoxide products from the oxidation of $[\text{Fe}^{\text{II}}\text{NST}]^-$ with an O-atom transfer reagent. A) Electrophilic attack of the Fe(IV)–oxo unit on the aromatic ring followed by oxidation to give the Fe(III)–phenoxide product. B) Intermolecular H-atom abstraction to give the Fe(III)–hydroxide product.	68
4.1. Reactivity of $\text{NMe}_4[\text{Fe}^{\text{II}}\text{MST}(\text{OH}_2)]$ with O_2 and NMO.	80
4.2. Oxidation products of dihydroanthracene: (A) anthracene, (B) 9,9',10,10'-tetrahydro-9,9'-bianthracene, and (C) anthraquinone and percent conversion obtained from reaction in DCM and MeCN.	87
4.3. Reaction conditions that give catalytic conversion of DHA.....	88
5.1. Synthetic route to H_3tbaps	101
5.2. Synthetic route to $[\text{M}^{\text{II}}_2(\text{tbaps})_2]^{2-}$ complexes. The third step is omitted in the isolation of the dipotassium salts.	102
6.1. Synthetic route to monomeric complexes containing bipyridine. DMAP was also added in the place of 2,2'-bipyridine to give a $[\text{Co}(\text{II})\text{DMAP}]^-$ complex.	127

LIST OF CHARTS

	Page
3.1. A) Bimetallic and B) monometallic Fe(III)–hydroxide complexes.....	50
3.2. Ligand products isolated from oxidation of $[\text{Mn}^{\text{II}}\text{MST}]^-$ and $[\text{Fe}^{\text{II}}\text{MST}]^-$ with O-atom transfer reagents.	58
3.3. Ligand derivatives studied in an attempt to prevent ligand oxidation.	62
3.4. Alkoxide and phenoxide products of A) Chang and B) Que that were generated from reaction of the corresponding Fe(II) salts with O-atom transfer reagents.....	65
5.1. Complexes whose redox active ligand frameworks have facilitated A) oxidative addition of Cl_2 gas at a d^0 Zr(IV) center , B) activation of aryl azide at a d^0 Ta(V) center, C) C–C bond formation with organo zinc reagents, and D) cycloaddition of dienes, enynes, and diyne.	98
5.2. The Co(II) complexes of MacBeth that are supported by the amidate derivate of the $[\text{NNN}]^{3-}$ ligand framework (A), and the sulfonamido ligand derivative examined in this chapter (B).	99
6.1. Complexes of the β -diketiminato ligand system that illustrate the influence of steric bulk on the coordination properties: A) An example of an early homoleptic complex prepared with a non-bulky derivative; B) The first example of a three coordinate Cu(II) complex made possible by the introduction of 2,6-diisopropylbenzene; C) Cu–superoxide complex isolated from the reaction of the starting Cu(I) complex with O_2 ; D) A three coordinate Fe(II) complex whose isolation required additional steric bulk in the ligand backbone; E) Unusual dinitrogen compound isolated from a three coordinate Fe(I) complex.	125

ACKNOWLEDGMENTS

There are a number of key people who have had a profound positive impact on my career at UCI. First and foremost, I would like to thank my advisor Andy, who has provided me with a safe and encouraging environment in which to develop as a scientist. Your constant confidence in me has directly caused me to have more confidence in myself, and your willingness to praise has helped me to pinpoint my strengths and formulate my career goals. I greatly appreciate all of the opportunities you have given me to develop my writing and editing skills, and for pushing me to be proactive in pursuing my goals. But most of all, I want to thank you for your clear understanding of the priorities in life. I will never forget you giving me the chance to spend as much time with my family as I needed without any guilt or questions asked. The memories from those frequent and sometimes long trips home are part of what gets me through the hard times of missing my dad. I am so incredibly grateful to have had you as my advisor.

I would like to give special thanks to my box-mate Dr. Young Jun Park, who showed great patience and trust in me as I was first getting started in lab. Those were scary times for me, and your calm demeanor was instrumental in helping me to relax and gain confidence. I greatly value the knowledge that I gained from you in the short period that our careers overlapped and consider myself very lucky to have had the opportunity to learn from you. To the other labmates that came before me and taught me the ways of the Borovik lab, specifically Taketo, Sonja, David, Nate, Dave, and Jon—thank you for establishing such a friendly and collaborative environment in which to do science and for integrating me into the group so smoothly. To the labmates who have joined the lab after me, including Yohei, Ethan, Nate, Jason, Sam, Victoria, Noam, and Kelsey—thank you for maintaining the cozy environment and for brightening my days with your crazy antics. The people that have surrounded me every day have played a huge part in creating my positive experience at UCI and I will always look back fondly on the experiences we have shared. And I assure you, I *WILL* miss you!

To my labmate and friend, Ethan: your drive and passion for everything that you choose to do impresses me and reminds me to be fully present and focused in my hobbies and career. Your continued motivation even in the face of little reward is truly inspiring. I know that a lot of people say this, but I truly mean it when I say that I have no doubt that you will be successful in everything that you choose to do. I have greatly enjoyed our many conversations about chemistry, and I know that I am smarter and have made more progress because of them. I have many specific memories that I will look back on and miss, including our late night Sonic runs during helium operation, the many times we chatted over a glass of scotch at the end of the day, and our occasional walks home together. I hope that we can maintain our close friendship in the future, because I value it more than you know.

The love and encouragement of my family were invaluable in helping me to maintain a positive attitude. Your visits have meant so much to me, especially the last two for the commencement ceremony and my defense. Having everyone here made those events truly special. Mom, I appreciate you listening to my problems, asking questions, and trying to help come up with solutions. No matter my stage of life and the problems I face, talking to you always makes me feel better. I hope you know how big of a role you played in getting me to where I am today.

And finally, I don't know where I would be without my future wife Kristen, who provided unending support throughout this process. I appreciate how you always try to convince me that you are not biased when you tell me that my work is outstanding, and I promise you, I really do believe you more and more every day! You have provided a constant source of motivation for always doing my best, and your support has helped me to be proud of what I have accomplished in these five years. I cannot wait to have you by my side every single day as we face new challenges and share great experiences together!

CURRICULUM VITAE

Sarah A. Cook

EDUCATION

Ph.D., Chemistry, August 2015
University of California, Irvine
Research Advisor: Andrew S. Borovik

B.A., ACS Chemistry, *summa cum laude*, May 2010
Ohio Wesleyan University, Delaware, OH

PUBLICATIONS

S. A. Cook, D. C. Lacy, A. S. Borovik. Terminal Metal-Oxo Species with Unusual Spin States. In *Spin States in Biochemistry and Inorganic Chemistry*; M. Costas and M. Swart, Eds.; Wiley, 2015, *In Press*.

S. A. Cook, A. S. Borovik. Molecular Designs for Controlling the Local Environments around Metal Ions. *Acc. Chem. Res.* **2015**, *48*, 2407-2414.

S. A. Cook, E. A. Hill, A. S. Borovik. Lessons from Nature: A Bio-inspired Approach to Molecular Design. *Biochemistry.* **2015**, *54*, 4167-4180.

S. A. Cook, J. W. Ziller, A. S. Borovik. Iron(II) Complexes Supported by Sulfonamido Tripodal Ligands: Endogenous versus Exogenous Substrate Oxidation. *Inorg. Chem.* **2014**, *53*, 11029-11035.

J. M. Blacquiere, M. L. Pegis, S. Raugei, W. Kaminsky, A. Forget, **S. A. Cook**, T. Taguchi, J. M. Mayer. Synthesis and Reactivity of Tripodal Complexes Containing Appended Bases. *Inorg. Chem.* **2014**, *53*, 9242-9253.

S. A. Cook, A. S. Borovik. Deconstructing Water Oxidation. *Nature Chem.* **2013**, *5*, 259-260.

Y. J. Park, **S. A. Cook**, N. S. Sickerman, Y. Sano, J. W. Ziller, A. S. Borovik. Heterobimetallic complexes with $M^{III}-(\mu-OH)-M^{II}$ cores ($M^{III} = Fe, Mn, Ga$; $M^{II} = Ca, Sr$, and Ba): structural, kinetic, and redox properties. *Chem. Sci.* **2013**, *4*, 717-726.

PRESENTATIONS

S. A. Cook, J. W. Ziller, A. S. Borovik. Intra- and intermolecular C–H bond activation by a putative Fe(IV)–oxo complex. Bioinorganic Gordon Research Seminar, Ventura, CA, January 29-February 1, 2015.

S. A. Cook, J. W. Ziller, A. S. Borovik. Intra- and intermolecular C–H bond activation by a putative Fe(IV)–oxo complex. Abstracts of Papers, 248th ACS National Meeting, San Francisco, CA, August 10-14, 2014.

S. A. Cook, J. W. Ziller, A. S. Borovik. Intra- and intermolecular C–H bond activation by a putative Fe(IV)–oxo complex. UCI Student Inorganic Seminar Series, Irvine, CA, April 24, 2014.

S. A. Cook, J. W. Ziller, A. S. Borovik. Intra- and intermolecular C–H bond activation by a putative Fe(IV)–oxo complex. Frontiers in C–H Functionalization Symposium, Atlanta, GA, August 15-18, 2013.

S. A. Cook, Y. J. Park, A. S. Borovik. Group II metal ions enhance the rate of dioxygen reduction by an Fe(II) complex. 2nd Penn State Bioinorganic Workshop, State College, PA, May 31-June 9, 2012.

S. A. Cook, A. Thibon, V. C. Pierre. Progress toward the synthesis of a selective luminescent sensor for the time-resolved detection of potassium. Abstracts of Papers, 237th ACS National Meeting, Salt Lake City, UT, March 22-26, 2009.

AWARDS

Dissertation Fellowship Award, University of California, Irvine	Fall 2014
NSF Graduate Research Fellowship Honorable Mention	2011
Chancellor's Fellow, University of California, Irvine	2010
Academic All-America 3 rd Team, ESPN The Magazine	2010
Julian Higley Prize for Chemistry Recipient, Ohio Wesleyan University	2010
• Awarded to two graduating seniors for meritorious scholarship in chemistry and promise of professional attainment	
Top 50 Scholar Athlete, Dale J. Bruce	2008, 2009, 2010
All-America Scholar-Athlete, National Fastpitch Coaches Association	2008, 2009, 2010
Academic All-District IV 2 nd Team, ESPN The Magazine	2009
Best Poster Runner-Up, MRSEC-SURE/Younger Chemists Committee Summer Research Symposium, University of Minnesota	2008
Charles H. and Magdalen Schafer Chemistry Scholarship recipient	2008
• Annual scholarship given to one or more outstanding chemistry majors entering their third year	

AFFILIATIONS

American Chemical Society	2008 – Present
Center for Selective C-H Functionalization	2012 – 2013
Chi Gamma Nu Chemistry Honor Society	2010
Phi Beta Kappa	2010
Sigma Xi Scientific Research Society	2009
Phi Society	2008
The National Scholars Honor Society	2008

ABSTRACT OF THE DISSERTATION

Principles of Molecular Design in the Development of Ligand Frameworks that Control the Primary and Secondary Coordination Spheres of Metal Ions

By

Sarah A. Cook

Doctor of Philosophy in Chemistry

University of California, Irvine, 2015

Professor Andrew S. Borovik, Chair

Metalloproteins have evolved to contain specific combinations of primary and secondary coordination spheres within their active sites that contribute to the high activity and selectivity of their chemical transformations. One approach to developing small molecule analogs with comparable reactivity is to design molecular constructs that exhibit similar control over aspects of the primary and secondary coordination spheres. This dissertation describes the design and reactivity of multifunctional ligands that position hydrogen-bond acceptors within the secondary coordination spheres of transition metal complexes. Two classes of ligands were studied: the first is a tetradentate, tripodal ligand ($[\text{MST}]^{3-}$) that was previously demonstrated to support formation of heterobimetallic complexes containing a Mn center and a redox inactive metal ion. The extension to the Fe analog is described here, as well as the continued examination of the influence of group 2 metal ions on the properties and reactivity of both the Mn and Fe complexes. The most important finding of these studies is that Ca(II) and Sr(II) ions impart nearly identical influences on the Mn and Fe centers—a result with relevance to biological water oxidation. Reaction of $[\text{MnMST}]^-$ and $[\text{FeMST}]^-$ with oxygen-atom transfer reagents in the absence of secondary metal ions uncovered a limitation of the $[\text{MST}]^{3-}$ ligand system in which

weak C–H bonds are susceptible to intramolecular oxidation. In order to address this limitation, ligand derivatives were designed that removed weak C–H bonds, which led to the observation of a putative Fe(IV)–oxo intermediate.

The last two chapters of this dissertation describe the development of a new type of ligand that utilizes a tridentate, redox-active framework that has been shown to provide access to multi-electron transformations at first row transition metal centers. The first derivative of this ligand was shown to form dinuclear complexes of Fe, Co, and Cu with a pre-organized binding pocket for secondary metal ions. Modification of the steric bulk of the ligand prevented formation of these dinuclear complexes and instead supported mononuclear Fe and Co centers. The structural, electronic, and electrochemical properties of both of these series of complexes are described.

CHAPTER 1

Introduction

Metalloproteins facilitate life's essential chemical reactions with an impressive activity and selectivity that provides a source of motivation for synthetic chemists. The high reactivity of these natural systems is made possible through a combination of structural and electronic features within and around the active site that contribute to the reactions occurring at the metal center. These features extend beyond the primary coordination sphere formed by the ligands that are directly bound to the metal center—also included are non-covalent interactions such as hydrogen bonding (H-bonding) networks, steric influences, electron transfer relays, and water channels that make up the secondary coordination sphere.

A metalloprotein that exemplifies the important contributions of both the primary and secondary coordination sphere influences to its function is the cytochrome P450 monooxygenase enzyme. This enzyme utilizes dioxygen to perform the stereo- and regiospecific functionalization of C–H bonds in a variety of metabolic processes (Figure 1.1).^{1,2} The activation of dioxygen occurs at a heme iron(II) center and produces an Fe(IV)–oxo intermediate with a ligand-delocalized radical that is understood to be the competent oxidant in the hydroxylation reactions (known as Compound I).^{3,4} A number of design features within the active site have been pinpointed as essential contributors to the efficiency and selectivity of this transformation. First, the strong electron donation from the axially coordinated cysteine residue facilitates the cleavage of the O–O bond after dioxygen binds to the metal center.⁵ The importance of this factor is evident in the comparison to the oxygen transport proteins hemoglobin (Hb) and myoglobin (Mb),

which are coordinated by a histidine residue instead of cysteine and are not capable of activating O_2 . The strong electron-donating ability of the cysteine residue is also credited with increasing the basicity of the oxido ligand in Compound I, which contributes to the high reactivity of this potent intermediate while allowing the oxidation potential to remain low.⁶ This property is important for preventing deleterious intramolecular reactivity of Compound I with the protein scaffold.

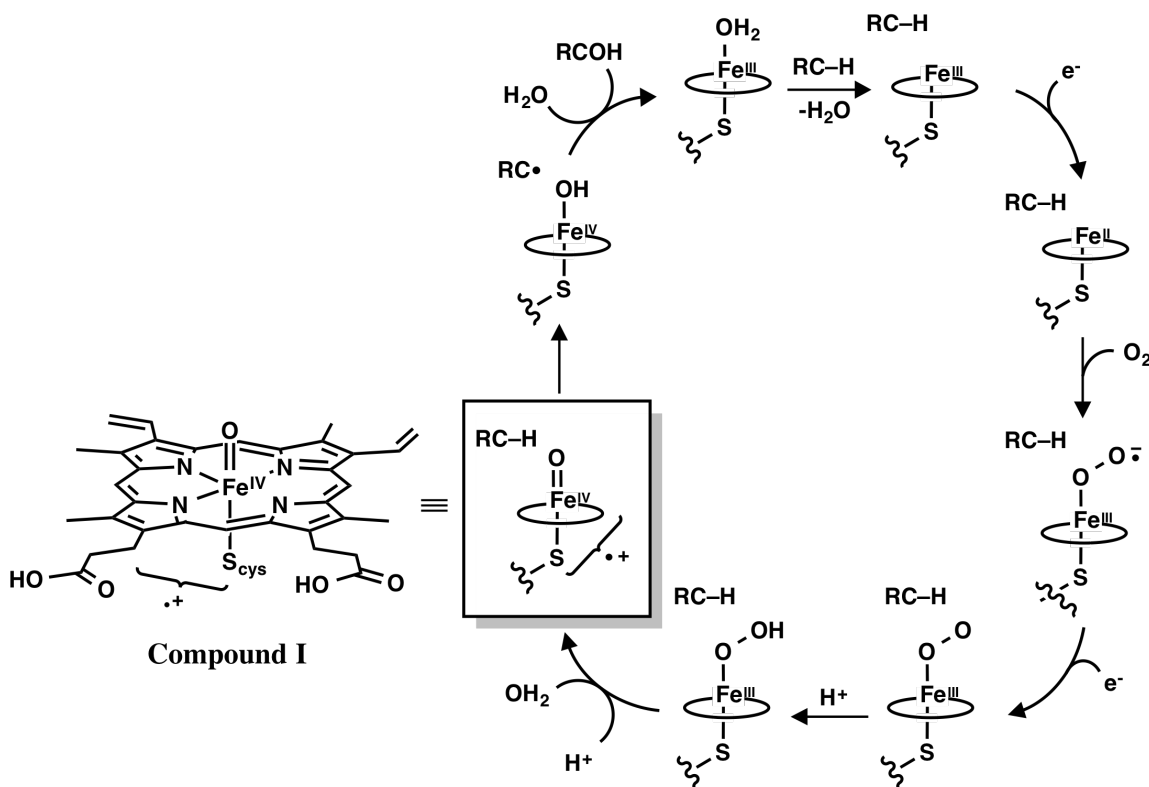


Figure 1.1. Catalytic cycle of substrate hydroxylation by cytochrome P450 and a depiction of the competent oxidant (Compound I).

A secondary sphere feature that is essential for the cleavage of the O–O bond by cytochrome P450 is the presence of a H-bonding network between the coordinated dioxygen ligand, nearby water molecules, and neighboring amino acid residues (Figure 1.2). This network facilitates proton transfer to the hydroperoxido ligand and directs reactivity to O–O bond cleavage; disruption of the network via mutation of the threonine

residue with alanine shuts down hydroxylation and instead generates peroxide.^{2,7} Other non-covalent interactions within the secondary coordination sphere establish the regioselectivity of the oxidation reaction. For example, in the cytochrome P450 derivative that oxidizes the substrate camphor, a H-bonding interaction between a tyrosine residue and the carbonyl oxygen of the camphor molecule as well as a number of hydrophobic interactions with aliphatic and aromatic residues further position the substrate such that only the C5 position is hydroxylated.⁸

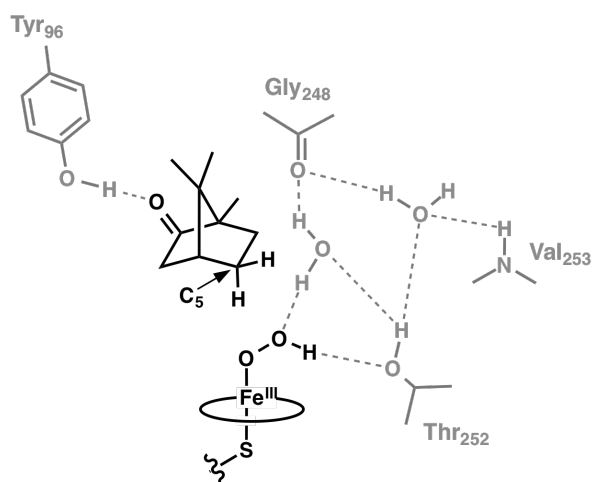


Figure 1.2. Depiction of the H-bonding interactions within the active site of cytochrome P450 that serve to orient the substrate (camphor) and assist in O–O bond cleavage.

Molecular Design in Synthetic Systems

Primary Coordination Sphere Considerations

The highly active and selective catalytic systems that are born out of the complex combination of secondary sphere interactions within metalloproteins illustrate how rational molecular design of synthetic constructs containing similar combinations of interactions can be used to control reactivity in synthetic systems. Manipulation of the primary coordination sphere of metal complexes is a well-established concept in

coordination chemistry that has long been used to influence the electronic properties of the metal center. For instance, varying the donor strength of the ligands that are directly coordinated to the metal center is known to influence the range of accessible and stable oxidation states. This concept was illustrated by early studies on the coordination of deprotonated amide groups in peptides to metal ions, which found that the donor strength of the amide groups better stabilize the unusual +3 oxidation state of Cu than the more weakly donating carboxylate moieties (Figure 1.3A).⁹⁻¹² The stabilities of these complexes were further improved by the rational modification of the ligand to prevent oxidation of the methylene groups in the backbone via replacement of the H atoms with methyl groups (Figure 1.3A, right).^{13,14} These same design principles were applied by Collins and coworkers in the development of a robust macrocyclic ligand framework for the stabilization of extremely high oxidation states, which lead to the notable isolation of Mn(V)-oxo and Fe(V)-oxo complexes (Figure 1.3B).¹⁵⁻¹⁸ In the opposite direction,

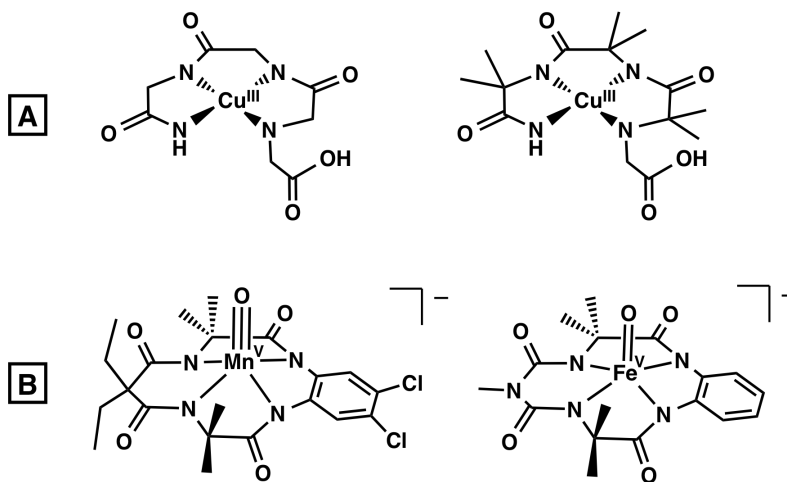


Figure 1.3. A) Cu(III) complexes stabilized by the strong donation of the amide groups in the tetraglycine fragment. B) High valent Mn(V)- and Fe(V)-oxo complexes developed by Collins that utilized the same concepts of strong amide donors and methylation of the methylene linkers that was described for the Cu(III) tetrapeptide complexes.

electron-accepting donors such as CO and phosphines are known to provide access to transition metal ions in low oxidation states.¹⁹ For example, the first characterization of a complex containing a transition metal ion in a negative oxidation state was reported for $[\text{Fe}(\text{CO})_4]^{2-}$ in 1931,²⁰ and the first complex that utilized a ligand other than CO to stabilize a negative oxidation state was $[\text{Co}(\text{PF}_3)_4]^-$.²¹

The donor ability of ligands can be further tuned by modifying the electron donating or withdrawing nature of the functional groups contained in the ligand framework. This principle was clearly established over 50 years ago with complexes of tertiary phosphine ligands in which the stretching frequency of the CO ligands in $[\text{Ni}(\text{CO})_3\text{PR}_3]^{2+}$ was found to span over 50 cm^{-1} from $\text{R} = \text{tBu}$ to $\text{R} = \text{CF}_3$.²² The effect of this change in the electron donating properties was visible in the rate of hydrogenation with *para*-substituted $\text{RhCl}(\text{P}(p\text{-C}_6\text{H}_4\text{R})_3)_3$ complexes, in which a nearly 20-fold rate enhancement was observed for $\text{R} = \text{F}$ compared to $\text{R} = \text{OMe}$.²³

Another design concept that has been used to access both high and low formal oxidation states is the incorporation of a redox active component within the ligand framework that can accept or donate electrons. Ligands that can accept electrons have been used to stabilize low formal oxidation states, such as 2,2'-bipyridine and its phosphine derivative, 2,2'-biphosphinine (Figure 1.4A). Shortening of the C–C bridge within homoleptic, dianionic complexes of these ligands indicated that a significant amount of electron density resided on the ligands instead of the metal ions.^{24,25} Similarly, in the first report of a square planar complex containing a Co(IV) center, distortion of the aromatic ring suggested contribution of electron density from the ligand, which led to reformulation of the oxidation state as Co(III) with a ligand radical (Figure 1.4B).^{26,27}

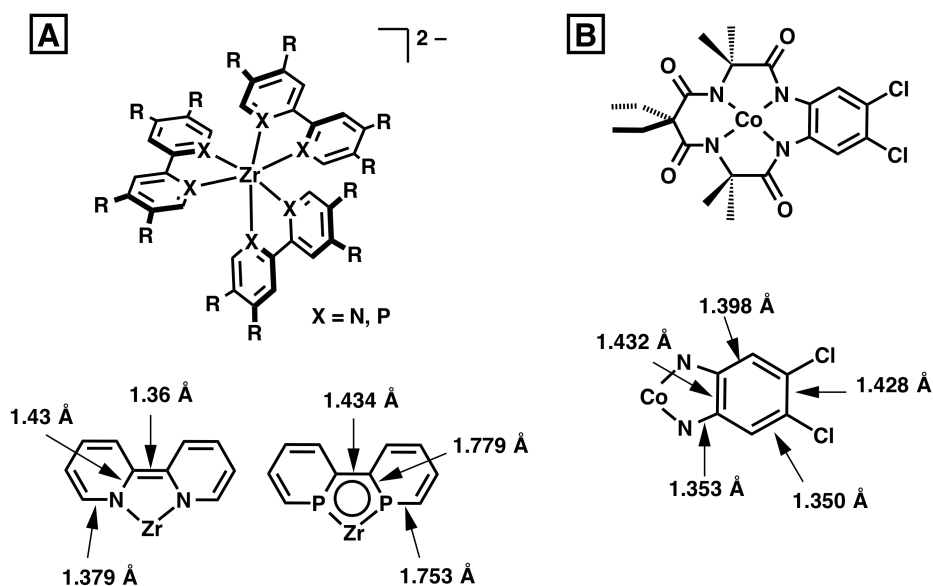


Figure 1.4. Complexes supported by redox noninnocent ligands that provide access to formally A) -2 and B) +4 oxidation states. Select bond lengths are shown that were used to determine that the ligand had been reduced or oxidized.

Secondary Sphere Considerations

The rational design of ligand frameworks that contain a combination of specific primary and secondary coordination sphere properties have been much less explored due to synthetic difficulties in reproducibly positioning functional groups in high impact locations. However, the efficacy of this approach as demonstrated by the cytochrome P450 enzyme described above warrants the pursuit of such systems. The impact of secondary sphere interactions in synthetic constructs is illustrated by the early work of Collman on the development of synthetic mimics of Hb and Mb. These metalloproteins reversibly bind dioxygen at a heme iron center that is buried within a cleft of the protein, which serves to protect the resulting Fe–superoxo unit from deleterious reactions.²⁸⁻³⁰ The protein scaffold is also responsible for supporting the formation of a five coordinate iron center, which is known to be essential for O₂ binding.³¹ In his seminal work, Collman designed a synthetic mimic that fulfilled the role of the protein matrix by constructing a

protective fence around one face of the corresponding iron-porphyrin complex (Figure 1.5).³² When combined with a sterically encumbered imidazole, this fence limited coordination of an axial ligand to the unhindered side of the iron center while still allowing small molecules such as dioxygen to bind within the cavity of the hindered face. In addition, the fence protected the coordinated O₂ unit from further reaction with a second iron center. These properties led to the first crystallographic characterization of an iron-dioxygen adduct in either a protein or a synthetic complex.^{33,34}

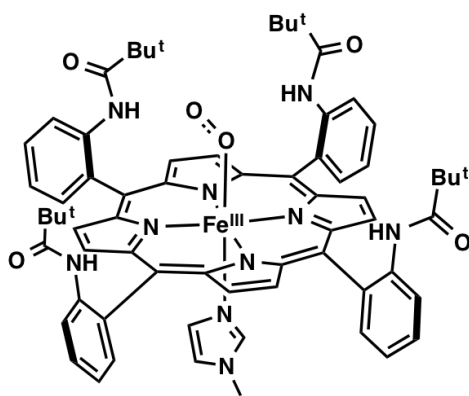


Figure 1.5. Picket fence porphyrin complex that was used to structurally characterize the first example of an Fe–O₂ adduct.

The successful imitation of the hydrophobic pocket and face differentiation of Hb and Mb within a synthetic construct marked a significant advancement in molecular design and provided a foundation to which further rational modification could be applied. For example, a variety of picket fence porphyrin derivatives were subsequently developed that appended H-bond donors adjacent to the open coordination site on the metal center,³⁵⁻⁴¹ in Hb and Mb, a H-bonding interaction between the superoxide ligand and the distal histidine residue is thought to contribute to the affinity for O₂ binding and to the stabilization of the coordinated superoxide ligand. Although the amide linkages that form the fence in the original picket fence porphyrin complex could potentially act as H-bond donors to the Fe(III)–superoxo unit in a similar manner as the histidine residue,

these groups are too far removed from the Fe(III)–superoxo unit at a distance of over 5 Å to form intramolecular H-bonds. New derivatives were therefore developed that positioned H-bond donors in closer proximity to the metal center. In one example, a series of derivatives in which one of the pivalamide pickets was functionalized with H-bond donating groups were prepared and the O₂ binding affinity of their corresponding Fe complexes was examined.⁴⁰ A derivative containing an appended phenyl urea moiety was found to enhance the affinity by a factor of nine—a result that was attributed to interaction of the urea N–H group with the superoxide ligand (Figure 1.6).

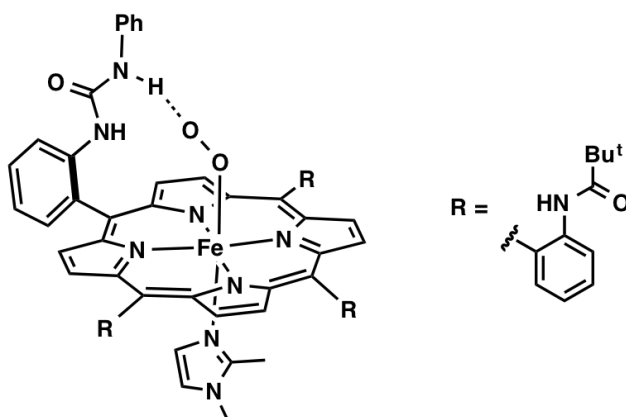


Figure 1.6. Modified picket fence porphyrin complex containing a urea group that is capable of forming a H-bond to the superoxide ligand.

The utilization of a rigid organic framework to position key functional groups around an open coordination site in the picket fence porphyrin system illustrated a universal design principle that can be used to establish controlled secondary sphere interactions in any rigid ligand framework. One ligand system in which this concept has been applied with great success is tripodal, tetradentate frameworks. For example, Masuda and coworkers designed a set of tripodal pyridylamine frameworks with appended amide groups that led to the stabilization and characterized a number of hydroxo, hydroperoxo, superoxo, and azide-coordinated complexes (Figure 1.7A).⁴²⁻⁴⁹

Intramolecular H-bonding interactions to the exogenous ligand and steric protection of the open coordination site to prevent dimerization were key factors in the development of these complexes. Mareques-Rivas and coworkers have also used similar functionalized tripodal pyridylamine ligands coordinated to zinc and copper ions to examine the effects of secondary sphere H-bonding interactions on a variety of structural and functional properties of the complexes (Figure 1.7B).⁵⁰⁻⁶⁰ For instance, the researchers found that changing the number of H-bonding groups has at least an equal influence on the pK_a

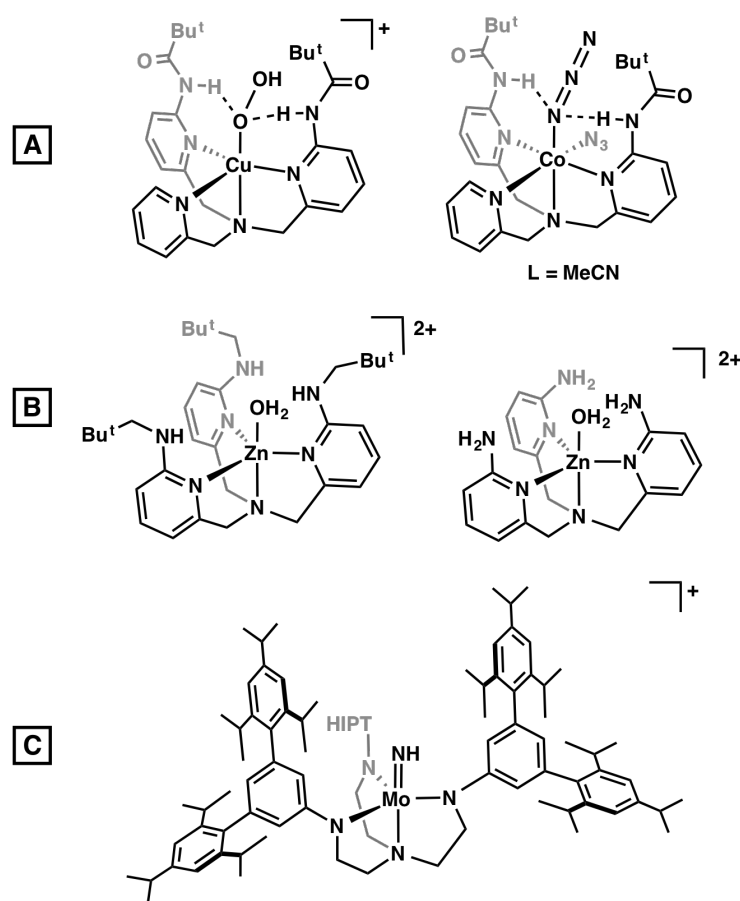


Figure 1.7. Examples of tripodal ligand frameworks that establish secondary sphere interactions: A) Cu(II)–hydroperoxide and Co(II)–azide complexes reported by Masuda; B) select complexes of Mareque-Rivas that were used to study the influence of H-bonds on the acidity of the coordinated water molecule. Shown are the two symmetric ligand frameworks, but unsymmetric derivatives containing 1 and 2 unfunctionalized pyridyl donors were also developed; C) one of the intermediate species from the reduction of N_2 that was isolated by Schrock.

values of a coordinated water molecule as changes to the primary coordination sphere.^{54,55} Schrock and coworkers utilized a triamidoamine tripod derivative functionalized with tremendously bulky 3,5-(2,4,6-*i*-Pr₃C₆H₂)₂C₆H₃ (hexaisopropylterphenyl (HIPT)) substituents to characterize an impressive series of eight intermediates along the pathway of N₂ reduction to ammonia (Figure 1.7C).⁶¹⁻⁶³ The extreme steric encumbrance of the substituents established a deep cavity of ~7 Å around the open coordination site of the metal center that protected the axial ligand from intermolecular reactions but that also maintained a pathway in the equatorial plane by which reactants could approach. This fine-tuned steric balance supported the stepwise protonation and reduction of a coordinated N₂ molecule to NH₃ via stoichiometric reactions with an organic acid and a chemical reductant.

A variety of other rigid ligand frameworks besides tetradentate tripods have also been used to establish secondary sphere interactions within transition metal complexes. For example, installation of another bulky terphenyl substituent in a bidentate, α -diimine ligand allowed for the isolation of an unusual Pd(II) complex with two terminal hydroxide ligands (Figure 1.8A).⁶⁴ Similarly, incorporation of *t*-butyl groups into a tris-(pyrazolyl)borate ligand framework permitted the isolation of the first examples of both a four-coordinate Zn(II) complex with a terminal hydroxide ligand and a four-coordinate Cu-nitrosyl complex (Figure 1.8B).^{65,66} DuBois and coworkers have developed a bidentate, macrocyclic phosphine ligand that positions basic amine groups within the secondary coordination sphere of a Ni(II) electrocatalyst used for H₂ production (Figure 1.8C). Remarkably high turnover frequencies for this catalyst are attributed to the contribution of the pendant amine groups to the relay of protons to the metal center.⁶⁷

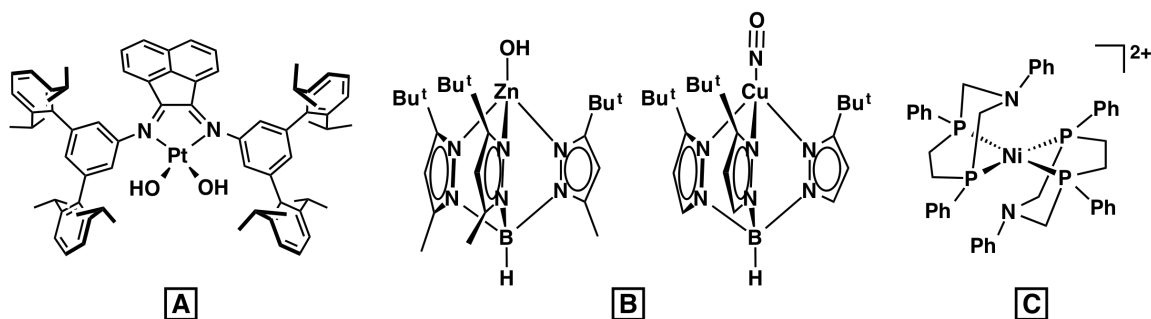


Figure 1.8. Examples of complexes that establish non-covalent interactions within the secondary coordination sphere.

Previous Work in the Borovik Lab

The Borovik lab has utilized a combination of the molecular design principles described above to develop a variety of multifunctional ligand frameworks for the stabilization of unusual first row transition metal complexes.⁶⁸⁻⁷¹ These ligands employ a rigid tripodal framework to incorporate secondary sphere interactions around an open coordination site of a transition metal center. Until recently, the focus of these research efforts was on complexes that contain H-bond *donating* interactions. These interactions have been shown to significantly influence the properties and reactivities of the corresponding transition metal complexes, such as the ability to activate dioxygen at Co(II) centers and to stabilize complexes containing oxido and hydroxido ligands. For example, a series of ligands containing 0, 1, 2, and 3 H-bond donors were used to study the influence of H-bonds on dioxygen activation by Co(II) (Figure 1.9).⁷² While the complex supported by the ligand with no H-bond donors showed no reaction with excess O₂, the ligand with one H-bond donor did react to form an unstable Co(III)–OH species. In contrast, both of the complexes containing 2 and 3 H-bond donors reacted with half an equivalent of dioxygen to form Co(III)–OH complexes whose stabilities differed according to the number of H-bonding interactions; the complex supported by the ligand

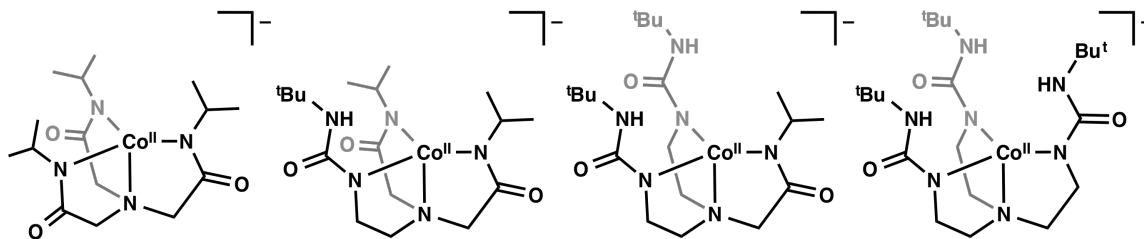


Figure 1.9. Complexes supported by ligands containing varying numbers of H-bond donors that were used to examine the influence of H-bonds on O₂ activation.

with 3 H-bond donors (denoted [H₃buea]³⁻) was stable for weeks in solution, while the complexes with 2 and 1 H-donors decayed with initial rate constants of 5.9×10^{-8} and $2.5 \times 10^{-7} \text{ M min}^{-1}$, respectively. The stabilizing influence of the three H-bond donors in [H₃buea]³⁻ also provided access to an unprecedented Fe(III)–oxo complex from the reaction of the Fe(II) species with dioxygen (Figure 1.10).⁷³ In this complex, the H-bonding interactions are thought to take the place of the M–oxo π -bond that is typically required to stabilize an oxido ligand. Also essential to the isolation of this unique species was the steric bulk of the *tert*-butyl groups within the secondary coordination sphere, which prevented intermolecular interactions that form μ -oxo bridged dimers. These same design features, in addition to the strong donor ability of the deprotonated amide moieties, supported the isolation of an impressive series of high spin Fe and Mn complexes with hydroxo and oxido ligands in oxidation states ranging from +2 to +5.⁷³⁻⁸¹

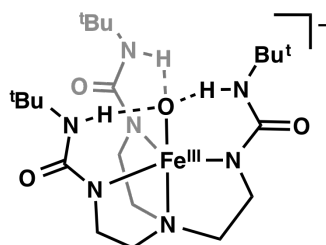


Figure 1.10. Depiction of the H-bonding interactions that stabilize the oxido ligand in [Fe^{III}H₃buea(O)]⁻.

The successes of the $[\text{H}_3\text{buea}]^{3-}$ ligand system in stabilizing M–oxo and M–hydroxo complexes led to the question of how altering the type of intramolecular H-bonding interactions would change the types of complexes that could be prepared and stabilized. To probe this question, a tripodal ligand with the same primary coordination environment and symmetry of the $[\text{H}_3\text{buea}]^{3-}$ ligand but that contained H-bond *accepting* sulfonamido groups instead of H-bond *donating* ureas was designed (Figure 1.11A, $[\text{MST}]^{3-}$).⁸² The switch to sulfonamido groups changed the polarity of the cavity from partially positive to partially negative, which altered the types of ligands that could be stabilized within the cavity—while the urea ligand was best suited to oxido and hydroxido ligands, the sulfonamido tripod supports ligands with multiple protons that were not stable in $[\text{H}_3\text{buea}]^{3-}$, such as water and ammonia (Figure 1.11B).^{83,84} An unexpected consequence of redesigning the cavity in $[\text{MST}]^{3-}$ was that the sulfonamido oxygen atoms create an auxiliary binding site for a second metal ion that allows for systematic preparation of discreet heterobimetallic complexes. These complexes are prepared from oxidation of $[\text{M}^{\text{II}}\text{MST}]^-$ complexes with dioxygen in the presence of a secondary metal ion. For example, reaction of $[\text{Mn}^{\text{II}}\text{MST}]^-$ and $\text{Ca}^{\text{II}}(\text{OTf})_2/15\text{-crown-5}$ or $\text{Ba}^{\text{II}}(\text{OTf})_2/18\text{-crown-6}$ with excess dioxygen led to the isolation of Mn(III)–hydroxide complexes containing a Ca(II) or Ba(II) ion in the secondary coordination sphere (Figure 1.11C).⁸² Similarly, when $\text{Mn}^{\text{II}}(\text{OTf})_2 \cdot 2\text{MeCN}$ or $\text{Fe}^{\text{II}}(\text{OTf})_2 \cdot 2\text{MeCN}$ and 1,4,7-trimethyl-1,4,7-triazacyclonane were added as the secondary metal ion, bimetallic complexes containing two transition metal centers were generated.⁸⁵

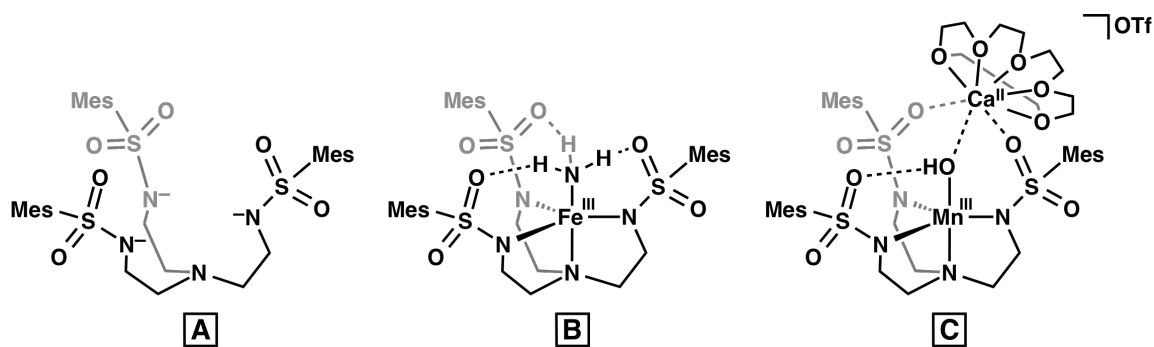


Figure 1.11. A) [MST]³⁻ ligand framework; B) Fe(III)-NH₃ complex showing the H-bonding interactions to the sulfonamido oxygen atoms; C) an example of a heterobimetallic complex that was prepared from reduction of O₂.

Overview of the Remaining Chapters

The research described in this dissertation continues to build on the studies of the tripodal ligand systems that contain sulfonamido groups. In particular, the reactions of these complexes with oxidants in the presence and absence of group 2 metal ions were examined. Furthermore, a new ligand system was developed that incorporates sulfonamido groups within the secondary coordination sphere of a tridentate redox active framework.

Chapter 2

The preliminary report on the [MST]³⁻ ligand system described the preparation and characterization of Mn(III)-hydroxide complexes containing a Ca(II) or Ba(II) ion within the secondary coordination sphere.⁸² This chapter extends the study to include the Sr(II) analog, as well as the related Fe(III) heterobimetallic complexes of the same three group 2 ions (Figure 1.12). The primary focus of this work was on the investigation of the influence of the group 2 metal ions on the preparation and properties of these heterobimetallic complexes. In particular, the influence of the secondary ions on the rate of O₂ activation and on the redox properties of the isolated complexes was examined.

Studies were also performed to elucidate the source of the oxygen atom and the proton in the hydroxido ligand of the isolated products. Finally, the influence of the crown size in the Fe complex containing a Ba(II) ion was studied.

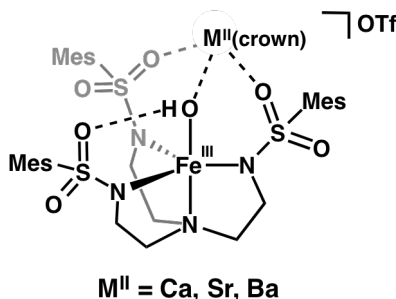


Figure 1.12. Three of the heterobimetallic complexes studied in Chapter 2.

Chapter 3

In order to fully understand the influences of secondary metal ions on the properties of the heterobimetallic complexes, the properties of the analogous monometallic $[\text{Mn}^{\text{III}}\text{MST}(\text{OH})]^-$ and $[\text{Fe}^{\text{III}}\text{MST}(\text{OH})]^-$ complexes needed to be determined for comparison. Towards this goal, the generation of $[\text{Fe}^{\text{III}}\text{MST}(\text{OH})]^-$ from dioxygen and oxygen-atom transfer reagents in the absence of secondary metal ions was explored. These studies uncovered a limitation of the $[\text{MST}]^{3-}$ ligand framework: the *ortho* methyl groups in the mesityl units are susceptible to intramolecular oxidation in the reaction of $[\text{Fe}^{\text{II}}\text{MST}]^-$ with oxygen-atom transfer reagents (Figure 1.13). In an attempt to prevent this intramolecular reactivity, two derivatives that replaced the mesityl units with more robust groups were designed and the reactivities of their corresponding Fe(II) and Mn(II) complexes were explored. Although a derivative containing naphthyl groups ($[\text{NST}]^{3-}$) still suffered from intramolecular oxidation, incorporation of tolyl groups

([TST]³⁻) successfully prevented this undesirable reactivity and permitted further study of the oxidation of its Fe(II) complex, which is described in Chapter 4.

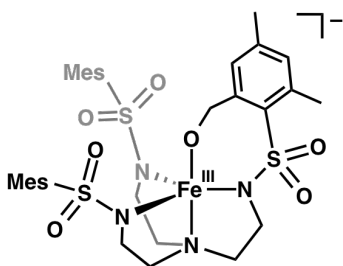


Figure 1.13. Product that resulted from intramolecular oxidation of the [MST]³⁻ ligand system.

Chapter 4

In this chapter, the oxidation of the Fe(II) complex of [TST]³⁻ with dioxygen and oxygen-atom transfer reagents is described. Both of these reagents lead to the isolation of an Fe(III)–hydroxide complex as the final product. However, these two reactions appeared to proceed through different mechanisms, as the oxygen-atom transfer reagent generated an observable intermediate that was not produced in the reaction with dioxygen (Figure 1.14). This intermediate species contained a low energy, low intensity band in its optical spectrum, which is suggestive of an Fe(IV)–oxo intermediate. Reactivity studies of this proposed Fe(IV)–oxo species with a substrate containing weak C–H bonds are described. In addition, the ability to bind a secondary metal ion to the oxido ligand was explored.

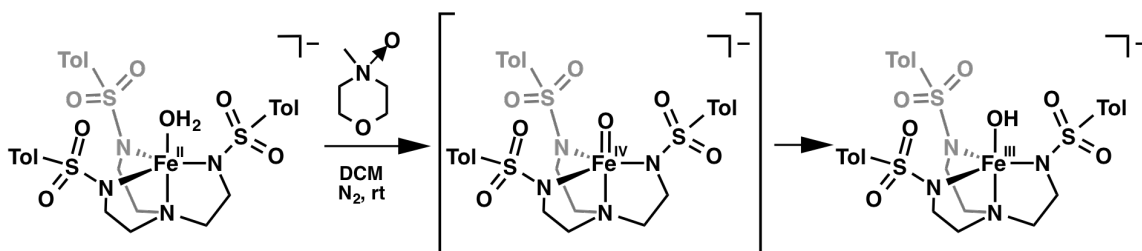


Figure 1.14. Example of the reactivity studies described in Chapter 4.

Chapter 5

The development of a new ligand system for the purpose of accessing multi-electron transformations with late first row transition metal centers is described in this chapter. This ligand system incorporates sulfonamido groups within the secondary coordination sphere of a tridentate, trianionic, redox active ligand framework. Metalation with Fe(II), Co(II), and Cu(II) salts resulted in the formation of dinuclear complexes containing two metal ions supported by two ligand frameworks to form a diamond core structure. The structural, electronic, and electrochemical properties of these complexes and the coordination of secondary metal ions to the sulfonamido groups are described. The formation of the dinuclear cores with this ligand system and the propensity for secondary metal ions to bridge between complexes prompted the development of a modified ligand derivative that is the topic of Chapter 6.

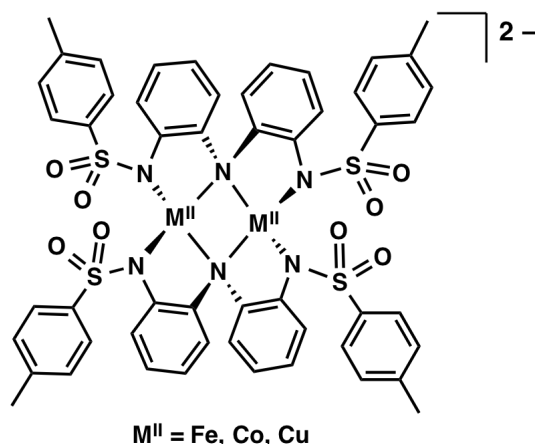


Figure 1.15. Depiction of the dinuclear complexes that are examined in Chapter 5.

Chapter 6

In an extension of the work described in Chapter 5 on the redox active ligand framework, the preparation of a second derivative that contains sterically encumbering triisopropylbenzene units is described. This modification of the ligand led to the

formation of mononuclear complexes of Fe(II) and Co(II) whose coordination spheres were completed by mono- or bidentate neutral pyridine donors (Figure 1.16). The structural, electronic, and electrochemical properties of these four- and five-coordinate complexes were examined by X-ray diffraction methods, UV-vis and EPR spectroscopies, and cyclic voltammetry. The five-coordinate complexes exhibited rich and reversible electrochemical properties, which supports the hypothesis that the redox active ligand framework can provide access to multi-electron processes. Preliminary reactivity studies with dioxygen and the chemical oxidant FcBF₄ illustrate the high reactivity of these complexes and the accessibility of multi-electron processes. Furthermore, the isolation of a complex in which one of the amine donors had been protonated, in addition to the ability to isolate discreet four- and five-coordinate complexes, provides a number of variables that can be used to modify the properties and reactivities of the complexes in future work.

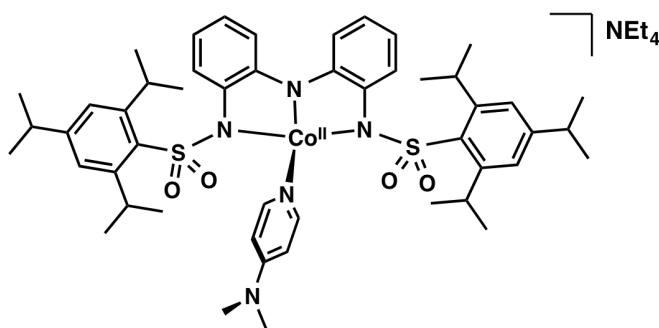


Figure 1.16. An example of the mononuclear complexes described in Chapter 6.

References

- (1) Ortiz de Montellano, P. R. *Chem. Rev.* **2010**, *110*, 932–948.
- (2) Schlichting, I.; Berendzen, J.; Chu, K.; Stock, A. M.; Maves, S. A.; Benson, D. E.; Sweet, R. M.; Ringe, D.; Petsko, G. A.; Sligar, S. G. *Science* **2000**, *287*, 1615–1622.
- (3) Rittle, J.; Green, M. T. *Science* **2010**, *330*, 933–937.
- (4) Rittle, J.; Younker, J. M.; Green, M. T. *Inorg. Chem.* **2010**, *49*, 3610–3617.
- (5) Green, M. T. *Curr. Opin. Chem. Biol.* **2009**, *13*, 84–88.
- (6) Yosca, T. H.; Rittle, J.; Krest, C. M.; Onderko, E. L.; Silakov, A.; Calixto, J. C.;

- Behan, R. K.; Green, M. T. *Science* **2013**, *342*, 825–829.
- (7) Nagano, S.; Poulos, T. L. *J. Biol. Chem.* **2005**, *280*, 31659–31663.
- (8) Poulos, T. L.; Finzel, B. C.; Gunsalus, I. C.; Wagner, G. C.; Kraut, J. *J. Biol. Chem.* **1985**, *260*, 16122–16130.
- (9) Bour, J. J.; Steggerda, J. J. *Chem. Commun.* **1967**, 85b–86.
- (10) Margerum, D. W.; Chellappa, K. L.; Bossu, F. P.; Burce, G. L. *J. Am. Chem. Soc.* **1975**, *97*, 6894–6896.
- (11) Bossu, F. P.; Chellappa, K. L.; Margerum, D. W. *J. Am. Chem. Soc.* **1977**, *99*, 2195–2203.
- (12) Sigel, H.; Martin, R. B. *Chem. Rev.* **1982**, *82*, 385–426.
- (13) Kirksey, S. T.; Neubecker, T. A.; Margerum, D. W. *J. Am. Chem. Soc.* **1979**, *101*, 1631–1633.
- (14) Diaddario, L. L.; Robinson, W. R.; Margerum, D. W. *Inorg. Chem.* **1983**, *22*, 1021–1025.
- (15) Collins, T. J. *Acc. Chem. Res.* **1994**, *27*, 279–285.
- (16) Collins, T. J.; Powell, R. D.; Slebodnick, C.; Uffelman, E. S. *J. Am. Chem. Soc.* **1990**, *112*, 899–901.
- (17) de Oliveira, F. T.; Chanda, A.; Banerjee, D.; Shan, X.; Mondal, S.; Que, L.; Bominaar, E. L.; Münck, E.; Collins, T. J. *Science* **2007**, *315*, 835–838.
- (18) Ghosh, M.; Singh, K. K.; Panda, C.; Weitz, A.; Hendrich, M. P.; Collins, T. J.; Dhar, B. B.; Gupta, Sen, S. *J. Am. Chem. Soc.* **2014**, *136*, 9524–9527.
- (19) Ellis, J. E. *Inorg. Chem.* **2006**, *45*, 3167–3186.
- (20) Ellis, J. E. *Organometallics* **2003**, *22*, 3322–3338.
- (21) Kruck, T.; Lang, W.; Engelmann, A. *Angew. Chem. Int. Ed. Engl.* **1965**, *4*, 148–149.
- (22) Tolman, C. A. *J. Am. Chem. Soc.* **1970**, *92*, 2953–2956.
- (23) Montelatici, S.; van der Ent, A.; Osborn, J. A.; Wilkinson, G. *J. Chem. Soc. A* **1968**, 1054–1058.
- (24) Rosa, P.; Mézailles, N.; Ricard, L.; Mathey, F.; Le Floch, P. *Angew. Chem. Int. Ed.* **2000**, *39*, 1823–1826.
- (25) Mézailles, N.; Rosa, P.; Ricard, L.; Mathey, F.; Le Floch, P. *Organometallics* **2000**, *19*, 2941–2943.
- (26) Collins, T. J.; Powell, R. D.; Slebodnick, C.; Uffelman, E. S. *J. Am. Chem. Soc.* **1991**, *113*, 8419–8425.
- (27) Popescu, D.-L.; Chanda, A.; Stadler, M.; de Oliveira, F. T.; Ryabov, A. D.; Münck, E.; Bominaar, E. L.; Collins, T. J. *Coord. Chem. Rev.* **2008**, *252*, 2050–2071.
- (28) Kendrew, J. C.; Bodo, G.; Dintzis, H. M.; Parrish, R. G.; Wyckoff, H.; Phillips, D. C. *Nature* **1958**, *181*, 662–666.
- (29) Kendrew, J. C.; Dickerson, R. E.; Strandberg, B. E.; Hart, R. G.; Davies, D. R.; Phillips, D. C.; Shore, V. C. *Nature* **1960**, *185*, 422–427.
- (30) Perutz, M. F.; Rossmann, M. G.; Cullis, A. F.; Muirhead, H.; Will, G.; North, A. C. T. *Nature* **1960**, *185*, 416–422.
- (31) Collman, J. P.; Reed, C. A. *J. Am. Chem. Soc.* **1973**, *95*, 2048–2049.
- (32) Collman, J. P.; Gagne, R. R.; Halbert, T. R.; Marchon, J. C.; Reed, C. A. *J. Am. Chem. Soc.* **1973**, *95*, 7868–7870.

- (33) Collman, J. P.; Gagne, R. T.; Reed, C. A. *J. Am. Chem. Soc.* **1974**, *96*, 2629–2631.
- (34) Collman, J. P.; Gagne, R. R.; Reed, C. A.; Robinson, W. T.; Rodley, G. A. *Proc. Natl. Acad. Sci. U.S.A.* **1974**, *71*, 1326–1329.
- (35) Momenteau, M.; Reed, C. A. *Chem. Rev.* **1994**, *94*, 659–698.
- (36) Collman, J. P.; Boulatov, R.; Sunderland, C. J.; Fu, L. *Chem. Rev.* **2004**, *104*, 561–588.
- (37) Momenteau, M.; Lavalette, D. *J. Chem. Soc., Chem. Commun.* **1982**, 341–343.
- (38) Mispelter, J.; Momenteau, M.; Lavalette, D.; Lhoste, J. M. *J. Am. Chem. Soc.* **1983**, *105*, 5165–5166.
- (39) Gerotheranassis, I. P.; Momenteau, M.; Looock, B. *J. Am. Chem. Soc.* **1989**, *111*, 7006–7012.
- (40) Wuenschell, G. E.; Tetreau, C.; Lavalette, D.; Reed, C. A. *J. Am. Chem. Soc.* **1992**, *114*, 3346–3355.
- (41) Collman, J. P.; Zhang, X.; Wong, K.; Brauman, J. I. *J. Am. Chem. Soc.* **1994**, *116*, 6245–6251.
- (42) Harata, M.; Jitsukawa, K.; Masuda, H.; Einaga, H. *J. Am. Chem. Soc.* **1994**, *116*, 10817–10818.
- (43) Ogo, S.; Wada, S.; Watanabe, Y.; Iwase, M.; Wada, A.; Harata, M.; Jitsukawa, K.; Masuda, H.; Einaga, H. *Angew. Chem. Int. Ed. Engl.* **1998**, *37*, 2102–2104.
- (44) Wada, A.; Harata, M.; Hasegawa, K.; Jitsukawa, K.; Masuda, H.; Mukai, M.; Kitagawa, T.; Einaga, H. *Angew. Chem. Int. Ed. Engl.* **1998**, *37*, 798–799.
- (45) Wada, A.; Ogo, S.; Watanabe, Y.; Mukai, M.; Kitagawa, T.; Jitsukawa, K.; Masuda, H.; Einaga, H. *Inorg. Chem.* **1999**, *38*, 3592–3593.
- (46) Wada, A.; Ogo, S.; Nagatomo, S.; Kitagawa, T.; Watanabe, Y.; Jitsukawa, K.; Masuda, H. *Inorg. Chem.* **2002**, *41*, 616–618.
- (47) Ogo, S.; Yamahara, R.; Roach, M.; Suenobu, T.; Aki, M.; Ogura, T.; Kitagawa, T.; Masuda, H.; Fukuzumi, S.; Watanabe, Y. *Inorg. Chem.* **2002**, *41*, 5513–5520.
- (48) Yamaguchi, S.; Wada, A.; Funahashi, Y.; Nagatomo, S.; Kitagawa, T.; Jitsukawa, K.; Masuda, H. *Eur. J. Inorg. Chem.* **2003**, *2003*, 4378–4386.
- (49) Matsumoto, J.; Suzuki, T.; Kajita, Y.; Masuda, H. *Dalton Trans.* **2012**, *41*, 4107–4117.
- (50) Mareque-Rivas, J. C.; Torres Mart n de Rosales, R.; Parsons, S. *Dalton Trans.* **2003**, 2156–2163.
- (51) Rivas, J. C. M.; Salvagni, E.; de Rosales, R. T. M. N.; Parsons, S. *Dalton Trans.* **2003**, 3339.
- (52) Rivas, J. C. M.; Salvagni, E.; Parsons, S. *Dalton Trans.* **2004**, 4185–4192.
- (53) Rivas, J. C. M.; Prabakaran, R.; de Rosales, R. T. M.; Metteau, L.; Parsons, S. *Dalton Trans.* **2004**, 2800–2807.
- (54) Mareque-Rivas, J. C.; Prabakaran, R.; Parsons, S. *Dalton Trans.* **2004**, 1648.
- (55) Mareque-Rivas, J. C.; Prabakaran, R.; Mart n de Rosales, R. T. *Chem. Commun.* **2004**, 76.
- (56) Rivas, J. C. M.; Salvagni, E.; Parsons, S. *Chem. Commun.* **2004**, 460–461.
- (57) Mareque-Rivas, J. C.; Torres Mart n de Rosales, R.; Parsons, S. *Chem. Commun.* **2004**, 610.
- (58) Guoqiang Feng; Juan C Mareque-Rivas; R Torres Mart n de Rosales, A.;

- Nicholas H Williams. *J. Am. Chem. Soc.* **2005**, *127*, 13470–13471.
- (59) Rivas, J. C. M.; Hinchley, S. L.; Metteau, L.; Parsons, S. *Dalton Trans.* **2006**, 2316–2322.
- (60) Metteau, L.; Parsons, S.; Mareque-Rivas, J. C. *Inorg. Chem.* **2006**, *45*, 6601–6603.
- (61) Yandulov, D. V.; Schrock, R. R. *J. Am. Chem. Soc.* **2002**, *124*, 6252–6253.
- (62) Yandulov, D. V.; Schrock, R. R.; Rheingold, A. L.; Ceccarelli, C.; Davis, W. M. *Inorg. Chem.* **2003**, *42*, 796–813.
- (63) Schrock, R. R. *Phil. Trans. R. Soc. A* **2005**, *363*, 959–969.
- (64) Lohr, T. L.; Piers, W. E.; Parvez, M. *Inorg. Chem.* **2012**, *51*, 4900–4902.
- (65) Alsfasser, R.; Trofimenko, S.; Looney, A.; Parkin, G.; Vahrenkamp, H. *Inorg. Chem.* **1991**, *30*, 4098–4100.
- (66) Carrier, S. M.; Ruggiero, C. E.; Tolman, W. B.; Jameson, G. B. *J. Am. Chem. Soc.* **1992**, *114*, 4407–4408.
- (67) Helm, M. L.; Stewart, M. P.; Bullock, R. M.; DuBois, M. R.; DuBois, D. L. *Science* **2011**, *333*, 863–866.
- (68) Borovik, A. S. *Acc. Chem. Res.* **2005**, *38*, 54–61.
- (69) Shook, R. L.; Borovik, A. S. *Chem. Commun.* **2008**, 6095–6107.
- (70) Shook, R. L.; Borovik, A. S. *Inorg. Chem.* **2010**, *49*, 3646–3660.
- (71) Cook, S. A.; Borovik, A. S. *Acc. Chem. Res.* **2015**, ASAP.
- (72) Lucas, R. L.; Zart, M. K.; Mukherjee, J.; Murkerjee, J.; Sorrell, T. N.; Powell, D. R.; Borovik, A. S. *J. Am. Chem. Soc.* **2006**, *128*, 15476–15489.
- (73) MacBeth, C. E.; Golombek, A. P.; Young, V. G.; Yang, C.; Kuczera, K.; Hendrich, M. P.; Borovik, A. S. *Science* **2000**, *289*, 938–941.
- (74) Shirin, Z.; Hammes, B. S.; Young, V. G.; Borovik, A. S. *J. Am. Chem. Soc.* **2000**, *122*, 1836–1837.
- (75) MacBeth, C. E.; Hammes, B. S.; Young, V. G., Jr; Borovik, A. *Inorg. Chem.* **2001**, *40*, 4733–4741.
- (76) Gupta, R.; MacBeth, C. E.; Young, V. G.; Borovik, A. S. *J. Am. Chem. Soc.* **2002**, *124*, 1136–1137.
- (77) MacBeth, C. E.; Gupta, R.; Mitchell-Koch, K. R.; Young, V. G.; Lushington, G. H.; Thompson, W. H.; Hendrich, M. P.; Borovik, A. S. *J. Am. Chem. Soc.* **2004**, *126*, 2556–2567.
- (78) Parsell, T. H.; Behan, R. K.; Green, M. T.; Hendrich, M. P.; Borovik, A. S. *J. Am. Chem. Soc.* **2006**, *128*, 8728–8729.
- (79) Lacy, D. C.; Gupta, R.; Stone, K. L.; Greaves, J.; Ziller, J. W.; Hendrich, M. P.; Borovik, A. S. *J. Am. Chem. Soc.* **2010**, *132*, 12188–12190.
- (80) Taguchi, T.; Gupta, R.; Lassalle-Kaiser, B.; Boyce, D. W.; Yachandra, V. K.; Tolman, W. B.; Yano, J.; Hendrich, M. P.; Borovik, A. S. *J. Am. Chem. Soc.* **2012**, *134*, 1996–1999.
- (81) Taguchi, T.; Stone, K. L.; Gupta, R.; Kaiser-Lassalle, B.; Yano, J.; Hendrich, M. P.; Borovik, A. S. *Chem. Sci.* **2014**, *5*, 3064–3071.
- (82) Park, Y. J.; Ziller, J. W.; Borovik, A. S. *J. Am. Chem. Soc.* **2011**, *133*, 9258–9261.
- (83) Sickerman, N. S.; Peterson, S. M.; Ziller, J. W.; Borovik, A. S. *Chem. Commun.* **2014**, *50*, 2515–2517.

- (84) Lau, N.; Ziller, J. W.; Borovik, A. S. *Polyhedron* **2015**, *85*, 777–782.
- (85) Sano, Y.; Weitz, A. C.; Ziller, J. W.; Hendrich, M. P.; Borovik, A. S. *Inorg. Chem.* **2013**, *52*, 10229–10231.

CHAPTER 2

Influences of Group 2 Metal Ions on the Properties of Fe and Mn Heterobimetallic Complexes

Introduction

Redox-inactive Lewis acidic metal ions are known to play a pivotal role in a broad range of chemical transformations. Although some of these metal ions are independently capable of catalyzing reactions such as the bond-forming reactions performed by alkaline earth metal ions,¹⁻⁴ redox-inactive metal ions are most often seen assisting in redox processes occurring at transition metal centers. For example, Collins observed that the presence of a secondary metal cation such as Na^I, Li^I, Mg^{II}, Ba^{II}, Sc^{III}, or Zn^{II} was required for oxygen-atom transfer from a Mn^V-oxo complex to PPh₃.⁵ Similarly, Fukuzumi observed that a metal ion from group 1, 2, or 3 was required for the reaction of a Co^{II}-tetraphenylporphyrin (Co^{II}TPP) complex with either dioxygen or *p*-benzylquinone.⁶ Furthermore, these ions promoted the transfer of an electron from Co^{II}TPP to the substrate with rates that were directly correlated to the strength of the Lewis acid. In another study by Fukuzumi and Nam, a two-electron transfer from a square pyramidal Fe^{IV}-oxo species to ferrocene was observed in the presence of Sc^{III} and Ca^{II} ions; in the absence of these metal ions, a single electron was transferred.⁷ Many other examples in which redox-inactive metal ions were required for the binding or activation of small molecules in synthetic systems have also been observed.⁸⁻²⁵

Several metalloproteins have demonstrated similar cooperation between a transition metal center and a redox-inactive metal ion in promoting function.²⁶ The enzyme most relevant to the work described in this report is the oxygen-evolving complex (OEC) within Photosystem II. This complex contains a Ca^{II} ion within a Mn₄O₇

cluster and is responsible for the oxidation of water to dioxygen (Figure 2.1).²⁷⁻³¹ Although the exact function of the Ca^{II} ion in the cluster is still unknown, it is now widely accepted that the ion directly participates in the oxidation of water to dioxygen.³²⁻³⁷ Furthermore, the reactivity of this enzyme critically depends on the presence of the Ca^{II} ion within the cluster.³⁷⁻⁴¹ The removal or replacement of this ion renders the enzyme completely inactive, with only one exception; substitution with a Sr^{II} ion results in an active but less efficient enzyme.^{38,39,42-44} No other metal ions have shown comparable reactivity, even those with a similar ionic radius (Cd^{II}) or stronger Lewis acidity (Mg^{II} , La^{III}). In fact, these metal ions actually *inhibit* reactivity.^{37,45,46} One proposed explanation for this specificity to Ca^{II} and Sr^{II} ions is based on a specific combination of size and Lewis acidity; the correct size is required for structural stabilization of the cluster, while the Lewis acidity determines the pKa of a coordinated aquo ligand.^{34,36}

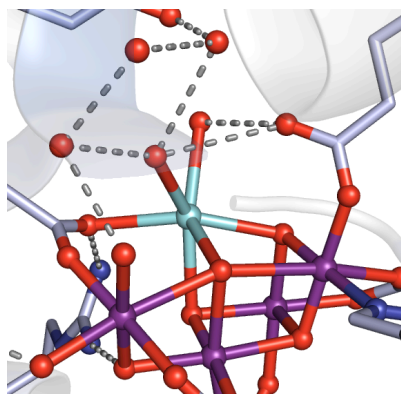


Figure 2.1. Structure of the oxygen-evolving complex in Photosystem II (PDB 3ARC). Red = O, purple = Mn, light blue = Ca.²⁷ Dotted lines represent H-bonding interactions.

A number of structural and functional models of the OEC have been developed that contain a Ca^{II} or Sr^{II} ion within a Mn cluster.⁴⁷⁻⁵⁵ However, there is still a need for the development of systems in which the effects of a group 2 metal ion on the redox properties of a single transition metal center can be examined. These efforts are made

difficult by the challenges of preparing complexes containing two different metal centers. Although several examples of such heterometallic complexes have been reported, they either lack the ability to vary the group 2 metal ion without drastically changing the structure,⁴⁷⁻⁵¹ or the complex examined does not participate in redox processes.^{22,56} A notable exception comes from the lab of Agapie, whose Mn₃ cluster scaffold supported two types of tetranuclear clusters that contained several different redox-inactive metal ions in the fourth position while maintaining the same core structure (Figure 2.2).^{54,55} These clusters exhibited clean electrochemical processes that allowed the influence of the redox-inactive metal ion on the reduction potential of the cluster to be examined.

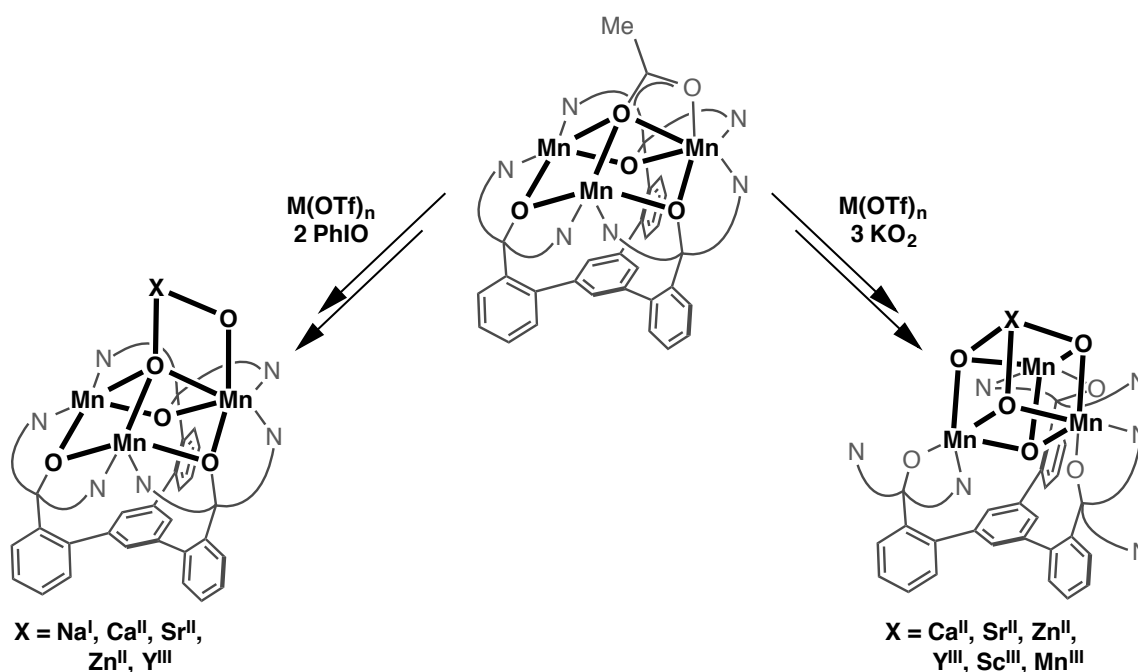


Figure 2.2. Abbreviated depiction of the multinuclear clusters developed by Agapie.

Our development of the multifunctional *N,N,N'*-[2,2',2''-nitriлотris(ethane-2,1-diyl)]tris-(2,4,6-trimethylbenzene-sulfonamido, ([MST]³⁻) ligand containing two distinct metal ion binding sites has given us the opportunity to directly probe the effects of group 2 metal ions on the electron transfer processes occurring at a transition metal center

(Figure 2.3).¹⁶ This ligand contains anionic nitrogen donors for the binding of a transition metal ion and sulfonamido groups that are capable of both hydrogen bonding (H-bonding) with exogenous ligands and of binding a second redox-inactive metal ion. The isolation of heterobimetallic complexes of this ligand with $M^{II}-(\mu-OH)-Mn^{III}$ cores ($M^{II} = Ca, Ba$, denoted $[M^{II}(OH)Mn^{III}]^+$) were first described in the seminal publication on this system.¹⁶ The work described in this chapter was performed in collaboration with Dr. Young Jun Park and expanded the study to include the Fe^{III} analogs in which the effects of Ca^{II} , Sr^{II} , and Ba^{II} ions were examined.⁵⁷ In addition, the $[Sr^{II}(OH)Mn^{III}]^+$ complex was prepared and its properties compared to the previously described $[Ca^{II}(OH)Mn^{III}]^+$ and $[Ba^{II}(OH)Mn^{III}]^+$ complexes.

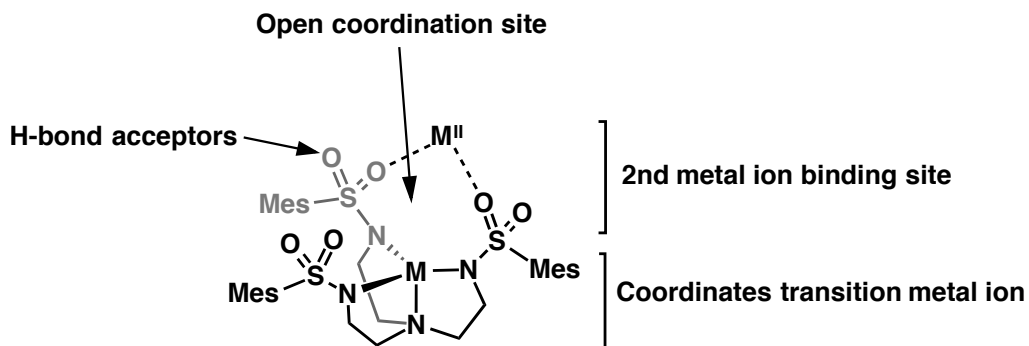
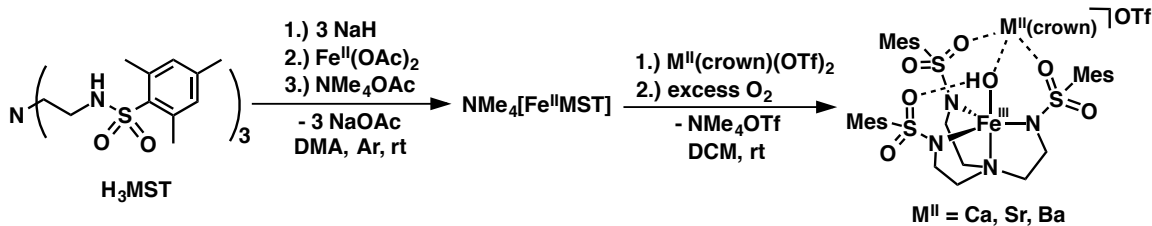


Figure 2.3. The multifunctional MST^{3-} ligand system.

Results and Discussion

Preparation of Heterobimetallic Complexes. The ligand H_3MST was prepared according to literature procedure from tris-(2-aminoethyl)amine and 2-mesitylene sulfonyl chloride in one step.¹⁶ $NMe_4[Fe^{II}MST]$ was obtained via deprotonation of the H_3MST ligand with three equivalents of NaH followed by metalation with $Fe^{II}(OAc)_2$. Treatment with NMe_4OAc gave the metathesis product, $NMe_4[Fe^{II}MST]$, that was precipitated from dimethylacetamide (DMA) in 70 – 80% yield (Scheme 2.1). From this product, a series of heterobimetallic complexes of the form $[(crown)\supset M^{II}-(\mu-OH)-$



Scheme 2.1. Preparative route to heterobimetallic complexes.

$[\text{Fe}^{\text{III}}\text{MST}]^+$ ($\text{M}^{\text{II}} = \text{Ca, Sr, Ba}$) were prepared by treating a dichloromethane (DCM) solution of $\text{NMe}_4[\text{Fe}^{\text{II}}\text{MST}]$ with excess O_2 in the presence of a group 2 metal ion crown ether adduct ($\text{Ca}(\text{OTf})_2/15\text{-crown-5}$, $\text{Sr}(\text{OTf})_2/15\text{-crown-5}$, $\text{Ba}(\text{OTf})_2/18\text{-crown-6}$). Monitoring of the UV-visible spectral changes upon addition of O_2 indicated completion of the reaction within ten minutes (Figure 2.4), which is significantly faster than the ten hours required for complete reaction of the Mn^{II} analog in the presence of a group 2 metal ion.¹⁶ The features of the final spectrum match those of the isolated crystalline material redissolved in DCM ($\lambda_{\text{max}} (\epsilon_{\text{M}}) = 383 \text{ nm} (4800)$, Figure 2.4 inset).

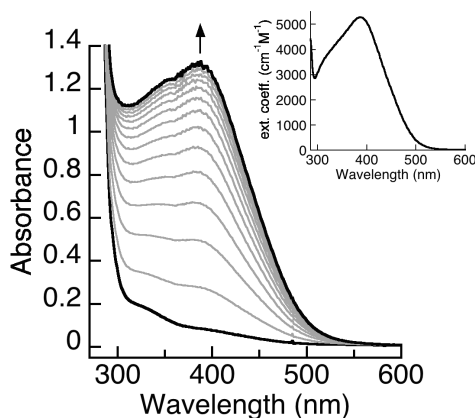


Figure 2.4. Electronic absorbance spectra for the addition of dioxygen to a solution of $\text{NMe}_4[\text{Fe}^{\text{II}}\text{MST}]$ and $\text{Sr}^{\text{II}}(\text{OTf})_2/15\text{-crown-5}$. Spectra were recorded every 30 sec on a 0.3 mM DCM solution at 20 °C. The inset shows the spectrum of the isolated product in DCM.

The Fe-containing complexes, originally isolated and crystallographically characterized by Dr. Young Jun Park, contained the heterobimetallic core $[\text{M}^{\text{II}}(\mu\text{-OH})\text{Fe}^{\text{III}}\text{MST}]^+$, abbreviated as $[\text{M}^{\text{II}}(\text{OH})\text{Fe}^{\text{III}}]^+$, in which the hydroxide ligand is derived from

oxygen. As depicted in Figure 2.5, the Fe^{III} center resides within the N₄ binding pocket that is established by the three anionic sulfonamide nitrogen atoms and the neutral apical nitrogen atom. The hydroxide ligand occupies the fifth coordination site opposite of the apical nitrogen and bridges to the group 2 metal ion, which is also coordinated to two sulfonamido oxygen atoms of the supporting ligand. The third ligand arm participates in a H-bonding interaction with the hydroxo ligand. The crown ether molecule completes the coordination sphere of the group 2 metal ion.

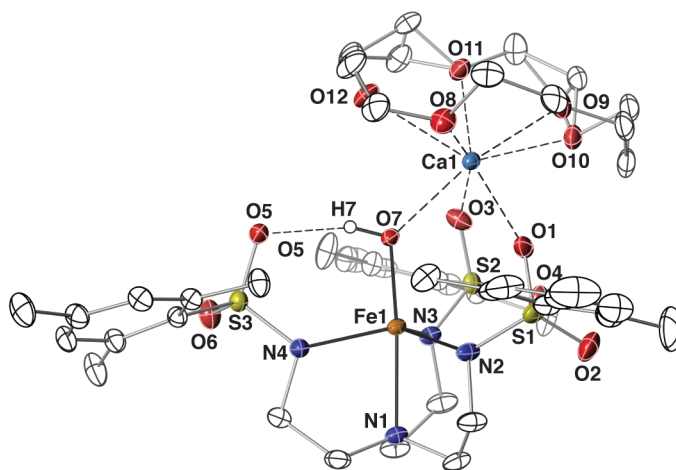


Figure 2.5. Molecular structure of $[(15\text{-crown-}5)\text{Ca}^{\text{II}}-(\mu\text{-OH})\text{-Fe}^{\text{III}}\text{MST}]^+$ determined by XRD methods. Thermal ellipsoids are drawn at the 50% probability level, and only the hydroxo proton is shown for clarity.

The source of the oxygen atom in the hydroxide ligand of the above complexes was shown to come from dioxygen via reaction of $\text{NMe}_4[\text{Fe}^{\text{II}}\text{MST}]$ and $\text{Sr}(\text{OTf})_2/15\text{-crown-}5$ with $^{18}\text{O}_2$. The Sr^{II} complex was chosen over the Ca^{II} and Ba^{II} analogs because it exhibits a sharper band for the OH vibration than Ca^{II} (full width at half maximum (FWHM) = 70 cm^{-1}), which allows for a shift in $\nu(\text{OH})$ to be more easily measured. The $\nu(\text{OH})$ band of the ^{18}O isotopomer shifted 10 cm^{-1} relative to $[\text{Sr}^{\text{II}}(^{16}\text{OH})\text{Fe}^{\text{III}}]^+$ ($\nu(^{18}\text{OH}) = 3379\text{ cm}^{-1}$, $\nu(^{16}\text{OH}) = 3389\text{ cm}^{-1}$), which is consistent with the prediction based on the harmonic oscillator model.

The source of the H-atom in the hydroxide ligand is unknown, although we have proposed that it is derived from H-atom abstraction from the solvent (DCM). To test this hypothesis, the reaction of $[\text{Fe}^{\text{II}}\text{MST}]^-$ with O_2 in the presence of $\text{Sr}(\text{OTf})_2/15\text{-crown-5}$ was conducted in deuterated DCM, and the product was analyzed by IR spectroscopy and ESI-MS. Replacement of the OH^- ligand for OD^- was predicted to shift the OH vibration from 3389 cm^{-1} to 2465 cm^{-1} based on the harmonic oscillator model, and the molecular ion peak of the complex was expected to shift by one mass unit. However, this experiment proved difficult, presumably due to the facile exchangeability of the deuteron with adventitious protons, as the coordination of the redox-inactive metal ion to the hydroxide unit makes it more acidic. Therefore, a second experiment was conducted in which an excess of a substrate containing weak C–H bonds (dihydroanthracene (DHA), 15 equivalents, 30 equivalents of H-atoms) was added to the reaction of $[\text{Fe}^{\text{II}}\text{MST}]^-$ and $\text{Ca}(\text{OTf})_2/15\text{-crown-5}$ with O_2 . After the reaction, the organic product was extracted into diethyl ether and analyzed by NMR spectroscopy. However, no conversion to anthracene from the abstraction of two H atoms was observed. This result might be explained by the large excess of DCM over DHA and the smaller size of the DCM molecule, which may be able to approach the active oxidizing species more closely than the larger DHA molecule. Therefore, the source of the H-atom is still unknown, although the solvent remains the most likely source.

Effects of Group 2 Metal Ions

Structural Properties. The molecular structures of the series of Mn^{III} and Fe^{III} heterobimetallic complexes with group 2 metal ions were characterized by Dr. Young Jun Park via X-ray diffraction (XRD) methods (Figure 2.6), and a short discussion of the

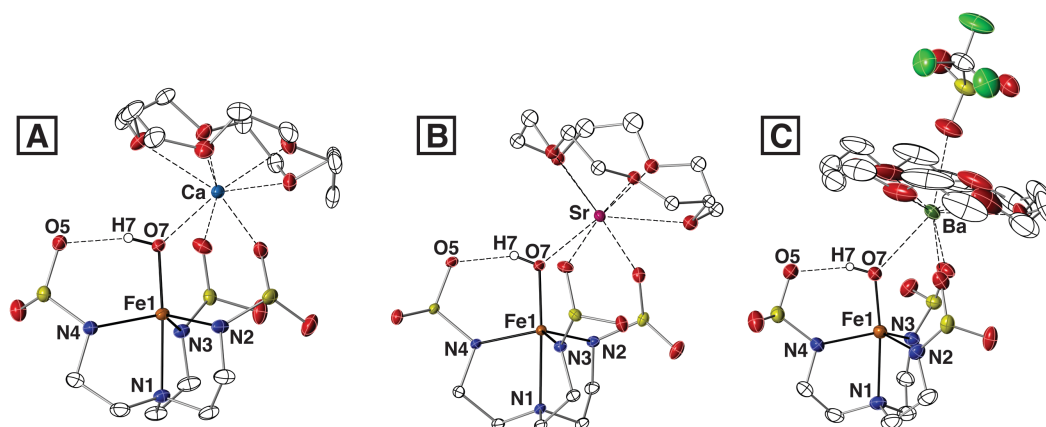


Figure 2.6. Core molecular structures of A) [(15-crown-5)⊃Ca^{II}-(μ-OH)-Fe^{III}MST]⁺, B) [(15-crown-5)⊃Sr^{II}-(μ-OH)-Fe^{III}MST]⁺, and C) [(OTf)(18-crown-6)⊃Ba^{II}-(μ-OH)-Fe^{III}MST].

metrical parameters that are relevant to this chapter are provided here. The similar ionic radii of Ca^{II} and Sr^{II} ions (1.12 Å and 1.26 Å, respectively, for the 8-coordinate ions) allowed 15-crown-5 to be used as the ancillary ligand for both species, giving rise to nearly identical structures for the Ca^{II} and Sr^{II} complexes within both the Mn^{III} and Fe^{III} series (Figures 2.6A and 2.6B). In contrast, the significantly larger ionic radius of Ba^{II} (1.42 Å for the 8-coordinate ion) required the use of a larger ancillary ligand, 18-crown-6. In addition, a triflate ion occupies a coordination site on the Ba^{II} ion, giving rise to a 10-coordinate ion in the solid state, whereas the triflate anions act as outer sphere counter ions in the Ca^{II} and Sr^{II} complexes (Figure 2.6C). Despite these differences, the metrical parameters of the primary coordination environment of the transition metal centers were nearly unaffected by the identity of the secondary metal ion (Tables 2.1 and 2.2). For example, the average M^{III}-N_{eq} distances differ by less than 0.02 Å within the Mn^{III} and Fe^{III} series, and the M^{III}-O7 distances are identical within experimental error. In contrast, the M^{II}-O bond lengths and the distances between the transition metal center and group 2 metal ion followed a trend that was consistent with the ionic radius of the redox inactive metal ion. For instance, the average distance between the crown ether oxygen atoms and

the M^{II} ion increased with increasing ionic radius, from 2.486 Å for [Ca^{II}(OH)Mn^{III}]⁺ to 2.640 Å for [Sr^{II}(OH)Mn^{III}]⁺, and finally to 2.877 Å for [(OTf)Ba^{II}(OH)Mn^{III}].

Table 2.1. Select bond lengths (Å) for the [M^{II}(OH)Fe^{III}]⁺ complexes.

[M ^{II} (OH)Fe ^{III}] ⁺	M ^{II}		
	Ca	Sr	Ba
Fe1—O7	1.865(2)	1.872(2)	1.859(2)
Fe1—N1	2.230(2)	2.280(3)	2.284(2)
Avg Fe1—N _{eq}	2.029(2)	2.013(5)	2.028(2)
M1—O7	2.316(2)	2.464(2)	2.695(2)
M1···O1	2.344(2)	2.538(3)	2.773(2)
M1···O3	2.370(2)	2.547(2)	2.756(2)
Fe1···M1	3.719(2)	3.839(2)	4.174(2)
O7···O5	2.700(6)	2.685(6)	2.692(6)
Avg M1—O _{crown}	2.508(2)	2.619(5)	2.866(3)
d[Fe—N _{eq}]	0.392	0.399	0.431
d[M1—O _{crown}]	1.156	1.334	0.776

Table 2.2. Select bond lengths (Å) for the [M^{II}(OH)Mn^{III}]⁺ complexes.

[M ^{II} (OH)Mn ^{III}] ⁺	M ^{II}		
	Ca	Sr	Ba
Mn1—O7	1.829(2)	1.836(2)	1.824(2)
Mn1—N1	2.075(2)	2.049(2)	2.096(2)
Avg Mn1—N _{eq}	2.052(2)	2.063(2)	2.053(2)
M1—O7	2.342(2)	2.430(2)	2.740(2)
M1···O1	2.332(2)	2.503(2)	2.745(2)
M1···O3	2.369(2)	2.482(2)	2.727(2)
Mn1···M1	3.7478(6)	3.897(2)	4.2394(4)
O7···O5	2.693(6)	2.664(6)	2.712(6)
Avg M1—O _{crown}	2.486(2)	2.640(2)	2.877(2)
d[Mn—N _{eq}]	0.284	0.301	0.327
d[M1—O _{crown}]	1.158	1.308	0.803

The difference in coordination environment of the Ba^{II} ion compared to the Ca^{II} and Sr^{II} ions was initially a source of concern for the comparison of the properties of the three complexes. As a result, the 15-crown-5 analog of the [(OTf)Ba^{II}(OH)Fe^{III}] complex was pursued. However, the isolation of this complex differed significantly from the other three complexes in the series; whereas the original three complexes could be crystallized from DCM/pentane or tetrahydrofuran (THF)/pentane in high yields, these conditions

gave mostly non-crystalline solids for the product of the reaction with Ba(OTf)₂/15-crown-5. However, high dilution conditions in DCM/pentane yielded diffraction-quality crystals, which were determined to contain a multinuclear structure consisting of four [Fe^{III}(OH)MST]⁻ complexes bridged by two 8-coordinate Ba^{II} ions (Figure 2.7A). In contrast, recrystallization from acetonitrile (MeCN)/ether at -30 °C yielded the heterobimetallic complex in low crystalline yield (<5 %, Figure 2.7B, Tables 2.3 and A.1). In this complex, the crown ether remained coordinated to one face of the Ba^{II} center and significant puckering of the crown ether opened a coordination site *cis* to the MST ligand that was occupied by the triflate anion. These results suggested that several species are present in solution, which complicated the overall chemistry of the system and prevented examination of the kinetics of dioxygen activation and the electrochemistry of

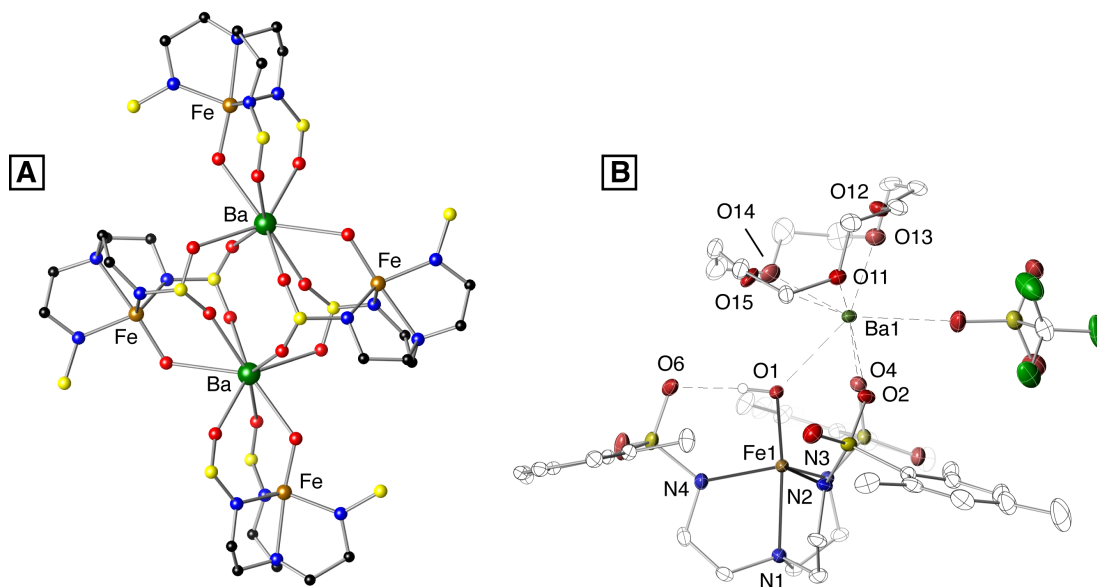


Figure 2.7. Molecular structures of the products from the reaction of NMe₄[Fe^{III}MST], Ba(OTf)₂/15-crown-5, and O₂ that were crystallized from (A) DCM/pentane at room temperature and (B) MeCN/ether at -30 °C. Ellipsoids are drawn at the 50% probability and only H1 is shown for clarity. In (A), only the primary coordination spheres of the four [Fe^{III}MST]⁻ complexes and the oxygen atoms involved in coordination of the Ba^{II} ion are shown. Red atoms correspond to oxygen, yellow to sulfur, blue to nitrogen, and black to carbon.

the heterobimetallic complex. As a result, we concluded that the 18-crown-6 complex of [(OTf)Ba^{II}(OH)Fe^{III}] was a more appropriate comparison to the Ca^{II} and Sr^{II} complexes because the larger crown ether is better matched to the larger Ba^{II} ion and supports the formation of a single species. The following discussion therefore includes only the 18-crown-6 adduct of [(OTf)Ba^{II}(OH)Fe^{III}].

Table 2.3. Select metrical parameters for [(OTf)(15-crown-5)⊃Ba^{II}-(μ-OH)-Fe^{III}MST].

Bond Distances (Å)	
Fe1—O1	1.853(4)
Fe1—N1	2.242(5)
Avg Fe1—N _{eq}	2.028(4)
Ba1—O1	2.619(4)
Ba1···O2	2.690(4)
Ba1···O4	2.712(4)
Fe1···Ba1	4.097(4)
O1···O6	2.66(1)
Avg M1—O _{crown}	2.849(4)
d[Fe—N _{eq}]	0.393
d[M1—O _{crown}]	1.680
Bond Angles (°)	
O1—Fe1—N1	173.1(2)
N2—Fe1—N3	109.4(2)
N2—Fe1—N4	119.7(2)
N3—Fe1—N4	119.8(2)
τ value	0.89

Vibrational Properties. The effects of the redox-inactive metal ion on the properties of the hydroxide unit in the heterobimetallic complexes of Fe^{III} were examined via analysis of the O–H bond vibration by Fourier transform infrared (FTIR) spectroscopy. The position of ν(OH) was comparable for all three complexes, with a maximum difference of only 24 cm⁻¹. Within this range, the strength of the O–H bonds in the Ca^{II} and Ba^{II} complexes were most similar, with vibration frequencies of 3365 cm⁻¹ and 3370 cm⁻¹, respectively (Figure 2.8). The O–H bond in the [Sr^{II}(OH)Fe^{III}]⁺ complex was the strongest, with a ν(OH) of 3389 cm⁻¹. This observed trend does not follow the

one expected based purely on the Lewis acidity of the redox-inactive metal ion, in which Ba^{II} ion would be expected to give the strongest O–H bond as a result of withdrawing the least electron density from the hydroxide unit. In contrast, the strength of the H-bonding interaction, which is determined by the broadness of the O–H peak, does follow the expected trend: $[\text{Ca}^{\text{II}}(\text{OH})\text{Fe}^{\text{III}}]^+$ contains the strongest H-bond with a FWHM value of 104 cm^{-1} , followed by $[\text{Sr}^{\text{II}}(\text{OH})\text{Fe}^{\text{III}}]^+$ (FWHM = 70 cm^{-1}) and $[(\text{OTf})\text{Ba}^{\text{II}}(\text{OH})\text{Fe}^{\text{III}}]$ (FWHM = 59 cm^{-1}). Therefore, the most Lewis acidic Ca^{II} ion gives the largest polarization of the O–H bond and the strongest H-bonding interaction.

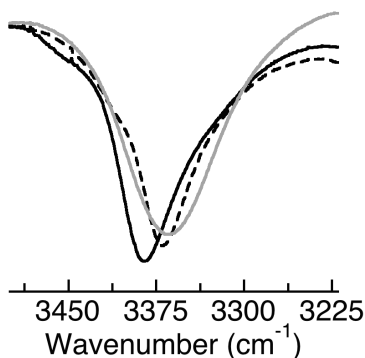


Figure 2.8. FTIR spectra in Nujol of the OH vibration in $[\text{Ca}^{\text{II}}(\text{OH})\text{Fe}^{\text{III}}]^+$ (grey), $[\text{Sr}^{\text{II}}(\text{OH})\text{Fe}^{\text{III}}]^+$ (black), $[(\text{OTf})\text{Ba}^{\text{II}}(\text{OH})\text{Fe}^{\text{III}}]$ (dashed black).

Electron-Transfer Properties. The presence of group 2 metal ions had a strong impact on the rate of dioxygen reduction by $[\text{Fe}^{\text{II}}\text{MST}]^-$, which was analyzed by measurement of the change in absorption at 383 nm upon the addition of dioxygen to a DCM solution of $\text{NMe}_4[\text{Fe}^{\text{II}}\text{MST}]$ (Figure 2.4). In the absence of secondary metal ions, $[\text{Fe}^{\text{II}}\text{MST}]^-$ showed slow reactivity with O_2 (Figure 2.9A). The addition of 3 equivalents of $\text{Ba}(\text{OTf})_2/18\text{-crown-6}$ to the reaction mixture resulted in a 10-fold enhancement of the initial rate from $2.2(1) \times 10^{-4}\text{ s}^{-1}$ to $2.3(6) \times 10^{-3}\text{ s}^{-1}$. An even greater enhancement was observed upon the addition of either $\text{Ca}(\text{OTf})_2/15\text{-crown-5}$ or $\text{Sr}(\text{OTf})_2/15\text{-crown-5}$ to the reaction; both metal ions gave a 30-fold increase in initial rate over $\text{NMe}_4[\text{Fe}^{\text{II}}\text{MST}]$.

Strikingly, their rates of reaction were identical within experimental error ($7.9(4) \times 10^{-3} \text{ s}^{-1}$ for Ca^{II} and $7.4(1.6) \times 10^{-3} \text{ s}^{-1}$ for Sr^{II}).

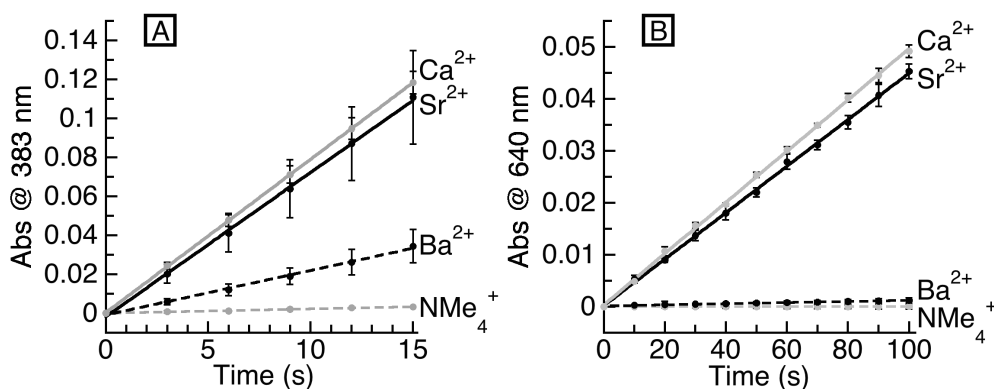


Figure 2.9. Initial rate data for (A) the reaction of $[\text{Fe}^{\text{II}}\text{MST}]^-$ with dioxygen in the presence of NMe_4^+ , 3 equivalents of $\text{Ca}(\text{OTf})_2/15\text{-crown-5}$, 3 equivalents of $\text{Sr}(\text{OTf})_2/15\text{-crown-5}$, and 3 equivalents of $\text{Ba}(\text{OTf})_2/18\text{-crown-6}$. (B) The reaction of $[\text{Mn}^{\text{II}}\text{MST}]^-$ with dioxygen in the presence of NMe_4^+ , 1 equivalent $\text{Ca}(\text{OTf})_2/15\text{-crown-5}$, 1 equivalent $\text{Sr}(\text{OTf})_2/15\text{-crown-5}$, and 1 equivalent $\text{Ba}(\text{OTf})_2/18\text{-crown-6}$.

The effect of Sr^{II} ions on the rate of O_2 reduction by the Mn analog, $[\text{Mn}^{\text{II}}\text{MST}]^-$, was also examined and compared to the results previously published for Ca^{II} , Ba^{II} , and NMe_4^+ ions.¹⁶ Although the enhancement conferred by Sr^{II} ions on the reduction of dioxygen by $[\text{Mn}^{\text{II}}\text{MST}]^-$ was not identical to that imposed by Ca^{II} ions as was observed for the Fe^{II} complex, the initial rates differed by less than 10%, with Ca^{II} ions giving a slightly faster rate than Sr^{II} ions ($4.9(1) \times 10^{-4} \text{ s}^{-1}$ and $4.5(1) \times 10^{-4} \text{ s}^{-1}$, respectively, Figure 2.9B). These enhancements were greater than the initial rate reported for Ba^{II} ($1.8 \times 10^{-5} \text{ s}^{-1}$). The findings that Ca^{II} and Sr^{II} ions give nearly identical rate enhancements with both the Mn and Fe complexes were unexpected based on our hypothesis that the influence of redox-inactive metal ions on the reduction of dioxygen by a transition metal ion is governed by Lewis acidity. This observation also contrasts previous studies that found that the rate of electron transfer processes occurring at transition metal centers is strongly

correlated to the Lewis acidity of the redox-inactive metal ions.^{5,6,8,18} For example, Fukuzumi observed a rate of electron transfer from $\text{Co}^{\text{II}}\text{TPP}$ to dioxygen that was 10 times faster in the presence of Ca^{II} ions than in Sr^{II} ions.⁶ Kurz reports a similar result in the oxidation of water to dioxygen by layered manganese oxides in which a 2-fold greater rate of oxidation was observed for oxides containing Ca^{II} ions compared to those containing Sr^{II} ions.⁸ Both of these results correspond to a trend in Lewis acidity of the two metal ions. Our results clearly do not follow this trend, suggesting that the strength of the Lewis acid is not the only factor of importance in the modulation of electron transfer in our system.

Electrochemical analysis of the isolated heterobimetallic complexes in both the Fe^{III} and Mn^{III} series again revealed similar trends in the influences of Ca^{II} and Sr^{II} ions. The cyclic voltammograms of the complexes exhibited quasi-reversible one-electron redox processes that were assigned to the $\text{M}^{\text{II}}/\text{M}^{\text{III}}$ couple. In the Fe^{III} series, the reduction potentials of this process in the $[\text{Ca}^{\text{II}}(\text{OH})\text{Fe}^{\text{III}}]^+$ and $[\text{Sr}^{\text{II}}(\text{OH})\text{Fe}^{\text{III}}]^+$ complexes differed by only 0.01 V (-1.13 V and -1.12 V) whereas the reduction of the $[(\text{OTf})\text{Ba}^{\text{II}}(\text{OH})\text{Fe}^{\text{III}}]$ complex occurred at a potential 0.1 V more negative (-1.22 V, Figure 2.10A). Similarly, in the Mn^{III} series, the potentials of the Ca^{II} - and Sr^{II} -containing complexes differed by only 0.02 V (-0.72 V and -0.70 V, respectively) while the Ba^{II} -containing complex was positioned at -0.76 V and was much less reversible (Figure 2.10B). These observed trends in redox potential are again contrary to the one predicted based on Lewis acidity. However, similar results were reported by Agapie for tetranuclear clusters containing three Mn ions and a redox-inactive metal ion (Figure 2.2).^{55,58} Examination of the electrochemical properties of these clusters revealed a linear relationships between the

one-electron reduction potential of the cluster and the Lewis acidity of the redox-inactive metal ion, which was quantified by the pK_a of the metal aqua ion ($M(OH_2)_m^{n+}$). Furthermore, the clusters containing a Ca^{2+} or Sr^{2+} ion exhibited nearly identical reduction potentials. The observed linear trend between reduction potential and Lewis acidity indicates that the redox-inactive metal ion plays an important role in tuning the electrochemical properties of the Mn ions even though it cannot directly participate in electron transfer.

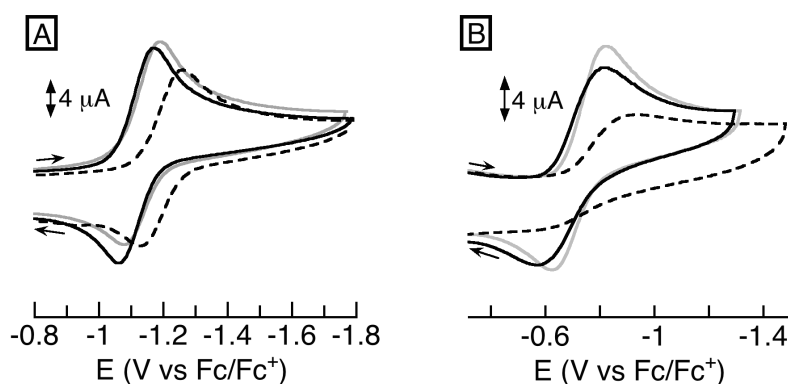


Figure 2.10. Cyclic voltammograms of (A) $[M^{II}(OH)Fe^{III}]^+$ and (B) $[M^{II}(OH)Mn^{III}]^+$ where $M^{II} = Ca$ (grey), Sr (black), and Ba (dashed black) showing a quasi-reversible Fe^{II}/Fe^{III} or Mn^{II}/Mn^{III} redox couple in DCM (0.1 M TBAP, 100 mV/s, with ferrocene as an internal standard).

Summary and Conclusion

The functional dependence of the OEC on the incorporation of a Ca^{II} ion and the limit of substitution to Sr^{II} are key properties of the enzyme whose origins are not yet understood. The study of these properties is made difficult by the complexity of the cluster and of the mechanism leading to dioxygen evolution, and so synthetic constructs that mimic certain aspects of the active site provide a useful method for deconvoluting the individual contributions to function. This chapter has described the preparation and characterization of heterobimetallic complexes that contain a transition metal center and a

group 2 metal ion. These complexes are supported by a multifunctional ligand that contains two distinct metal binding sites, which has allowed us to develop a series of complexes in which the group 2 metal ion was varied while the core structure was unchanged. As a result, we could compare the influences of the secondary metal ion on the electron transfer properties of the transition metal center without complications from structural variations. An unexpected trend was observed in both the initial rate of dioxygen activation and in the one electron reduction potential of the Mn^{II/III} or Fe^{II/III} couple—Ca^{II} and Sr^{II} ions exhibited nearly identical rate enhancements and reduction potentials for both the Mn and Fe complexes, despite their differences in Lewis acidity. These enhancements were greater than that imposed by Ba^{II} ions, which also gave a more negative reduction potential than the Ca^{II} and Sr^{II} analogs.

One proposal put forth by Brudvig to explain the limit of functional substitution of Ca^{II} for Sr^{II} in the OEC implicates a balance between similar coordination properties and Lewis acidities of the two ions; the comparable ionic radii (1.12 Å for Ca^{II}, 1.26 Å for Sr^{II}) allows Sr^{II} to take the place of Ca^{II} without significantly changing the structure of the cluster or altering the surrounding H-bonding network, and similar p*K*_a's of coordinated water molecules maintain the same protonation state for the two ions.^{34,36} The structural studies of the heterobimetallic complexes in this chapter show that Ca^{II} and Sr^{II} ions can adopt identical coordination environments, with the only differences attributed to the slightly larger ionic radius of Sr^{II} giving rise to longer bond lengths. In addition, the close agreement between ν(OH) of the [Ca^{II}(OH)Fe^{III}]⁺ and [Sr^{II}(OH)Fe^{III}]⁺ complexes indicates that the p*K*_a's of the hydroxo units are comparable.

The similar influence of the Ca^{II} and Sr^{II} ions on the reduction potentials of our heterobimetallic complexes and on the tetranuclear clusters of Agapie suggests another explanation for the ability of Sr^{II} to maintain the function of the OEC—the Ca^{2+} ion tunes the redox potential of the cluster into a range in which oxidation becomes feasible, and all other ions besides Sr^{2+} push the potential of out of this range. This tuning of the redox potential could explain the nearly identical rates of O_2 activation by the $[\text{Fe}^{\text{II}}\text{MST}]^-$ complex in the presence of Ca^{II} and Sr^{II} ions—a multi-electron process with relevance to the function of the OEC.

Experimental Details

General Methods

Syntheses of metal complexes were completed under an argon atmosphere in a VAC drybox. Solvents were sparged with argon and dried over columns containing Q-5 and molecular sieves. All reagents were purchased from commercial suppliers and used as received unless otherwise noted. Sodium hydride as a 30% suspension in mineral oil was filtered and washed five times each with Et_2O and pentane and dried under vacuum. H_3MST , $\text{NMe}_4[\text{Mn}^{\text{II}}\text{MST}]$, $\text{Ca}(\text{OTf})_2/15\text{-crown-5}$, and $\text{Ba}(\text{OTf})_2/18\text{-crown-6}$ were prepared according to literature procedures.¹⁶ The heterobimetallic complexes $[15\text{-crown-5}\supset\text{Ca}^{\text{II}}-(\mu\text{-OH})\text{-Fe}^{\text{III}}\text{MST}]$, $\text{OTf}[15\text{-crown-5}\supset\text{Sr}^{\text{II}}-(\mu\text{-OH})\text{-Fe}^{\text{III}}\text{MST}]\text{OTf}$, and $[(\text{OTf})18\text{-crown-6}\supset\text{Ba}^{\text{II}}-(\mu\text{-OH})\text{-Fe}^{\text{III}}\text{MST}]$ were initially prepared and characterized by Dr. Young Jun Park, and the products of the synthetic procedures described below were confirmed by comparison of the physical properties to those of the previously characterized complexes.

Complex Syntheses

NMe₄[Fe^{II}MST]. This complex was prepared according to the literature procedure for NMe₄[Mn^{II}MST] with minor modifications.¹⁶ A solution of H₃MST (0.40 g, 0.58 mmol) in 10 mL anhydrous dimethylacetamide (DMA) was treated with three equivalents of solid NaH (42 mg, 1.7 mmol). After the evolution of H₂ gas ceased, Fe(OAc)₂ (0.10 g, 0.578 mmol) and NMe₄OAc (77 mg, 0.58 mmol) were added to the clear, colorless solution. The mixture was stirred for three hours and then filtered to remove three equivalents of insoluble NaOAc (0.14 g, 1.7 mmol). The yellow filtrate was concentrated under vacuum to ca. 1 mL DMA and treated with 40 mL Et₂O to precipitate the product. The product was collected on a frit, washed with twice with 1 mL of THF and three times with 3 mL of Et₂O, and dried under vacuum to give 360 mg (75%) of a white solid. FTIR (KBr disc, cm⁻¹, selected bands): 3040, 2975, 2935, 2830, 1604, 1564, 1488, 1467, 1446, 1403, 1379, 1277, 1236, 1138, 1127, 1105, 1072, 1055, 1039, 976, 928, 847, 824, 739, 723, 661, 604, 579, 542.

[15-crown-5]Ca^{II}-(μ-OH)-Fe^{III}MST]OTf. A solution of NMe₄[Fe^{II}MST] (0.10 g, 0.12 mmol) and Ca(OTf)₂/15-crown-5 adduct (75 mg, 0.13 mmol) in 10 mL DCM was prepared in a Schleck flask that was sealed with a rubber septum. This flask was brought out of the drybox and 10 mL of dry O₂ was added to the headspace. The reaction was stirred for two hours, after which volatiles were removed under vacuum and the flask brought back into the dry box. The orange residue was redissolved in 10 mL DCM, filtered, and layered under pentane for recrystallization. After 3 days, orange needle-like crystals were collected on a glass frit and dried to yield 60 mg (42%) of product. FTIR (KBr disc, cm⁻¹, selected bands): 3377 (OH), 2968, 2936, 1604, 1468, 1274, 1143, 1090,

1031, 954, 812, 659, 638. EPR (DCM, 10 K): $g = 9.2, 4.7, 4.0$. λ_{max} , nm (DCM, ϵ , $\text{M}^{-1}\text{cm}^{-1}$): 383 (4800).

[15-crown-5 \supset Sr^{II}-(μ -OH)-Fe^{III}MST]OTf. This complex was prepared according to the same procedure used to prepare the [15-crown-5 \supset Ca^{II}-(μ -OH)-Fe^{III}MST]OTf complex with 25 mg (0.031 mmol) $\text{NMe}_4[\text{Fe}^{\text{II}}\text{MST}]$ and 19 mg (0.031 mmol) $\text{Sr}(\text{OTf})_2/15\text{-crown-5}$ in 4 mL of DCM. Recrystallization from DCM/pentane gave orange needle-like crystals in 32% yield. FTIR (KBr disc, cm^{-1} , selected bands): 3398 (OH), 2938, 2866, 1604, 1459, 1283, 1144, 1087, 1031, 955, 809, 658, 638. EPR (DCM, 10K): $g = 9.3, 4.7, 4.1$. λ_{max} , nm (DCM, ϵ , $\text{M}^{-1}\text{cm}^{-1}$): 386 (5300).

[(OTf)18-crown-6 \supset Ba^{II}-(μ -OH)-Fe^{III}MST]. This complex was prepared according to the same procedure used to prepare the [15-crown-5 \supset Ca^{II}-(μ -OH)-Fe^{III}MST]OTf complex with 0.10 g (0.12 mmol) $\text{NMe}_4[\text{Fe}^{\text{II}}\text{MST}]$ and 96 mg (0.13 mmol) $\text{Ba}(\text{OTf})_2/18\text{-crown-6}$ in 10 mL of DCM. Recrystallization from THF/pentane gave orange needle-like crystals in 46% yield. FTIR (KBr disc, cm^{-1} , selected bands): 3378 (OH), 2916, 2864, 1603, 1468, 1352, 1282, 1261, 1143, 1097, 1034, 965, 818, 658, 637. EPR (DCM, 10 K): $g = 9.3, 4.6, 4.1$. λ_{max} , nm (DCM, ϵ , $\text{M}^{-1}\text{cm}^{-1}$): 383 (4900).

[(OTf)15-crown-5 \supset Ba^{II}-(μ -OH)-Fe^{III}MST]. This complex was prepared according to the same procedure used to prepare the [15-crown-5 \supset Ca^{II}-(μ -OH)-Fe^{III}MST]OTf complex with 50 mg (0.061 mmol) $\text{NMe}_4[\text{Fe}^{\text{II}}\text{MST}]$ and 41 mg (0.061 mmol) $\text{Ba}(\text{OTf})_2/15\text{-crown-5}$ in 10 mL of DCM. Single crystals suitable for X-Ray diffraction were obtained in two ways: (1) 25 mg were dissolved in 2 mL MeCN, filtered, and layered under Et_2O at -30°C ; (2) 25 mg were dissolved in 5 mL DCM, filtered, and layered under pentane at 25°C .

Ba(OTf)₂/15-crown-5 adduct. A solution of 15-crown-5 (0.29 g, 1.3 mmol) in 2.5 mL MeCN was added to a suspension of Ba(OTf)₂ (0.57 g, 1.3 mmol) in 5.5 mL MeCN. The mixture was heated at 50°C for 1 hr. Upon cooling, white solid began to form. The reaction mixture was concentrated to ca. 1 mL and 10 mL Et₂O were added to complete precipitation of the product. The resulting fine white solid was collected on a fritted glass funnel, washed with Et₂O, and dried under vacuum to give 0.83 g (95%) of product, which was used without further purification. FTIR (KBr disc, cm⁻¹, selected bands): 2933, 2887, 1301, 1257, 1178, 1094, 1033, 948, 868, 762, 633, 515.

Sr(OTf)₂/15-crown-5 adduct. This complex was made using the same method as the Ba(OTf)₂/15-crown-5 adduct with 0.86g (2.2 mmol) Sr(OTf)₂ and 0.49 g (2.2 mmol) 15-crown-5 in 15 mL MeCN. The product was isolated as white powder in 96% yield and was used without further purification. FTIR (KBr disc, cm⁻¹, selected bands): 2945, 2889, 1458, 1356, 1303, 1243, 1170, 1093, 1037, 952, 871, 634, 516.

Physical Methods

Electronic absorption spectra were recorded in a 1 cm cuvette on a Cary 50 spectrophotometer or an 8453 Agilent UV-Vis spectrometer equipped with an Unisoku Unispeks cryostat. Negative mode electrospray ionization electrospray mass spectra were collected using a Micromass MS Technologies LCT Premier Mass Spectrometer. X-band (9.28 GHz) EPR spectra were collected as frozen solutions using a Bruker EMX spectrometer equipped with an ER041XG microwave bridge. IR spectra were recorded on a Varian 800 Scimitar Series FTIR spectrometer as KBr disks.

Cyclic voltammetric experiments were conducted using a CHI600C electrochemical analyzer under an Ar atmosphere with 0.1 M tetrabutylammonium

hexafluorophosphate as the supporting electrolyte. A glassy carbon electrode was used for the working electrode with a silver wire reference electrode and a platinum wire counter electrode. A cobaltocenium/cobaltocene couple ($[\text{CoCp}_2]^{+/0}$) was used to monitor the reference electrode.

X-Ray Crystallographic Methods

A Bruker SMART APEX II diffractometer was used to collect all the data. The APEX2⁵⁹ program package was used to determine the unit-cell parameters and for data collections. The raw frame data was processed using SAINT⁶⁰ and SADABS⁶¹ to yield the reflection data file. Subsequent calculations were carried out using the SHELXTL⁶² program. The structures were solved by direct methods and refined on F^2 by full-matrix least-squares techniques. The analytical scattering factors⁶³ for neutral atoms were used throughout the analysis.

Hydrogen atom H(1) in $[(\text{OTf})(15\text{-crown-5})\text{D}\text{Ba}^{\text{II}}-(\mu\text{-OH})\text{-Fe}^{\text{III}}\text{MST}]$ was located from a difference-Fourier map and refined (x,y,z and fixed U_{iso}), $d(\text{O-H}) = 0.85\text{\AA}$. The remaining hydrogen atoms were included using a riding model. There were 3.5 molecules of acetonitrile solvent present. One solvent molecule was located on a two-fold rotation axis and was disordered. The absolute structure was assigned by refinement of the Flack parameter⁶⁴. There were several high residuals present in the final difference-Fourier map. It appeared that additional acetonitrile solvent was present, however, the solvent could not be properly refined. The SQUEEZE⁶⁵ routine in the PLATON⁶⁶ program package was used to account for the electrons in the solvent accessible voids.

Kinetic Studies

Kinetic measurements for the activation of dioxygen with $[\text{Fe}^{\text{II}}\text{MST}]^-$ and $[\text{Mn}^{\text{II}}\text{MST}]^-$ complexes were conducted on an Agilent 8453 UV-vis spectrometer equipped with a Unisoku Unispeks cryostat. The studies of $[\text{Fe}^{\text{II}}\text{MST}]^-$ were performed at 20.0 °C on a 0.30 mM CH_2Cl_2 solution that was prepared in an Ar-filled drybox. Two separate 12 mL aliquots (3.6 μmol of $[\text{Fe}^{\text{II}}\text{MST}]^-$) of the solution were premixed with 3 equivalents of $\text{M}^{\text{II}}(\text{OTf})_2/\text{crown}$ ($\text{M}^{\text{II}} = \text{Ca}, \text{Sr}$). A 3 mL portion was transferred to a 1.0 cm quartz cuvette, which was sealed with a rubber septum and removed from the box. Excess O_2 (5 mL, $T = 298 \text{ K}$, $P = 1 \text{ atm}$, 0.20 mmol) was added to the headspace of the cuvette via a gas-tight syringe and the absorbance change was monitored every 3 s at 383 nm. For studies with $[\text{Mn}^{\text{II}}\text{MST}]^-$, a 3.0 mL portion (11 μmol of $[\text{Mn}^{\text{II}}\text{MST}]^-$) of a 3.5 mM solution of complex was transferred to a cuvette and sealed with a rubber septum. Immediately before addition of 5 mL of O_2 into the headspace, 0.50 mL of a 21 mM $\text{M}^{\text{II}}/15\text{-crown-5}(\text{OTf})_2$ solution ($\text{M}^{\text{II}} = \text{Ca}, \text{Sr}$, 11 μmol , 1 equivalent) were injected directly into the solution, giving a final $[\text{Mn}^{\text{II}}\text{MST}]^-$ concentration of 3.0 mM. The absorbance change was monitored at 640 nm every 10 seconds at 25.0 °C. All experiments were repeated 3 times for $[\text{Mn}^{\text{II}}\text{MST}]^-$ and 6 times for $[\text{Fe}^{\text{II}}\text{MST}]^-$. Note that the kinetic experiments with $[\text{Fe}^{\text{II}}\text{MST}]^-$ and $[\text{Mn}^{\text{II}}\text{MST}]^-$ were conducted at different temperatures (20.0 °C and 25.0 °C, respectively); these temperatures were utilized because they gave the best reproducibility.

References

- (1) Kobayashi, S.; Yamashita, Y. *Acc. Chem. Res.* **2011**, *44*, 58–71.
- (2) Harder, S. *Chem. Rev.* **2010**, *110*, 3852–3876.
- (3) Yamashita, Y.; Tsubogo, T.; Kobayashi, S. *Chem. Sci.* **2012**, *3*, 967–975.
- (4) Liu, B.; Roisnel, T.; Carpentier, J.-F.; Sarazin, Y. *Angew. Chem. Int. Ed.* **2012**,

- 51, 4943–4946.
- (5) Miller, C. G.; Gordon-Wylie, S. W.; Horwitz, C. P.; Strazisar, S. A.; Peraino, D. K.; Clark, G. R.; Weintraub, S. T.; Collins, T. J. *J. Am. Chem. Soc.* **1998**, *120*, 11540–11541.
 - (6) Fukuzumi, S.; Ohkubo, K. *Chem. Eur. J.* **2000**, *6*, 4532–4535.
 - (7) Fukuzumi, S.; Morimoto, Y.; Kotani, H.; Naumov, P.; Lee, Y.-M.; Nam, W. *Nat. Chem.* **2010**, *2*, 756–759.
 - (8) Wiechen, M.; Zaharieva, I.; Dau, H.; Kurz, P. *Chem. Sci.* **2012**, *3*, 2330–2339.
 - (9) Darensbourg, M. Y.; Darensbourg, D. J.; Burns, D.; Drew, D. A. *J. Am. Chem. Soc.* **1976**, *98*, 3127–3136.
 - (10) Gambarotta, S.; Arena, F.; Floriani, C.; Zanazzi, P. F. *J. Am. Chem. Soc.* **1982**, *104*, 5082–5092.
 - (11) Betley, T. A.; Peters, J. C. *J. Am. Chem. Soc.* **2003**, *125*, 10782–10783.
 - (12) Ohkubo, K.; Menon, S. C.; Orita, A.; Otera, J.; Fukuzumi, S. *J. Org. Chem.* **2003**, *68*, 4720–4726.
 - (13) Smith, J. M.; Sadique, A. R.; Cundari, T. R.; Rodgers, K. R.; Lukat-Rodgers, G.; Lachicotte, R. J.; Flaschenriem, C. J.; Vela, J.; Holland, P. L. *J. Am. Chem. Soc.* **2006**, *128*, 756–769.
 - (14) Ding, K.; Brennessel, W. W.; Holland, P. L. *J. Am. Chem. Soc.* **2009**, *131*, 10804–10805.
 - (15) Ding, K.; Pierpont, A. W.; Brennessel, W. W.; Lukat-Rodgers, G.; Rodgers, K. R.; Cundari, T. R.; Bill, E.; Holland, P. L. *J. Am. Chem. Soc.* **2009**, *131*, 9471–9472.
 - (16) Park, Y. J.; Ziller, J. W.; Borovik, A. S. *J. Am. Chem. Soc.* **2011**, *133*, 9258–9261.
 - (17) Lee, Y.; Peters, J. C. *J. Am. Chem. Soc.* **2011**, *133*, 4438–4446.
 - (18) Morimoto, Y.; Kotani, H.; Park, J.; Lee, Y.-M.; Nam, W.; Fukuzumi, S. *J. Am. Chem. Soc.* **2011**, *133*, 403–405.
 - (19) Park, J.; Morimoto, Y.; Lee, Y.-M.; Nam, W.; Fukuzumi, S. *J. Am. Chem. Soc.* **2011**, *133*, 5236–5239.
 - (20) Park, J.; Morimoto, Y.; Lee, Y.-M.; You, Y.; Nam, W.; Fukuzumi, S. *Inorg. Chem.* **2011**, *50*, 11612–11622.
 - (21) Rodriguez, M. M.; Bill, E.; Brennessel, W. W.; Holland, P. L. *Science* **2011**, *334*, 780–783.
 - (22) Hazari, A.; Labinger, J. A.; Bercaw, J. E. *Angew. Chem. Int. Ed.* **2012**, *51*, 8268–8271.
 - (23) Leeladee, P.; Baglia, R. A.; Prokop, K. A.; Latifi, R.; de Visser, S. P.; Goldberg, D. P. *J. Am. Chem. Soc.* **2012**, *134*, 10397–10400.
 - (24) Yoon, H.; Lee, Y.-M.; Wu, X.; Cho, K.-B.; Sarangi, R.; Nam, W.; Fukuzumi, S. *J. Am. Chem. Soc.* **2013**, *135*, 9186–9194.
 - (25) Lee, Y.-M.; Bang, S.; Kim, Y. M.; Cho, J.; Hong, S.; Nomura, T.; Ogura, T.; Troeppner, O.; Ivanović-Burmazović, I.; Sarangi, R.; Fukuzumi, S.; Nam, W. *Chem. Sci.* **2013**, *4*, 3917–3923.
 - (26) Valentine, J. S.; Doucette, P. A.; Zittin Potter, S. *Annu. Rev. Biochem.* **2005**, *74*, 563–593.
 - (27) Umena, Y.; Kawakami, K.; Shen, J.-R.; Kamiya, N. *Nature* **2011**, *473*, 55–60.

- (28) Ferreira, K. N.; Iverson, T. M.; Maghlaoui, K.; Barber, J.; Iwata, S. *Science* **2004**, *303*, 1831–1838.
- (29) Yano, J.; Kern, J.; Sauer, K.; Latimer, M. J.; Pushkar, Y.; Biesiadka, J.; Loll, B.; Saenger, W.; Messinger, J.; Zouni, A.; Yachandra, V. K. *Science* **2006**, *314*, 821–825.
- (30) Barber, J. *Inorg Chem* **2008**, *47*, 1700–1710.
- (31) Sauer, K.; Yano, J.; Yachandra, V. K. *Coord. Chem. Rev.* **2008**, *252*, 318–335.
- (32) Pecoraro, V. L.; Baldwin, M. J.; Caudle, M. T.; Hsieh, W. Y.; Law, N. A. *Pure Appl. Chem.* **1998**, *70*, 925–929.
- (33) Cady, C. W.; Crabtree, R. H.; Brudvig, G. W. *Coord. Chem. Rev.* **2008**, *252*, 444–455.
- (34) Vrettos, J. S.; Stone, D. A.; Brudvig, G. W. *Biochemistry* **2001**, *40*, 7937–7945.
- (35) McEvoy, J. P.; Brudvig, G. W. *Chem. Rev.* **2006**, *106*, 4455–4483.
- (36) Brudvig, G. W. *Philos. Trans. R. Soc. Lond., B*, **2008**, *363*, 1211–1219.
- (37) Yocum, C. F. *Coord. Chem. Rev.* **2008**, *252*, 296–305.
- (38) Ghanotakis, D. F.; Babcock, G. T.; Yocum, C. F. *FEBS Lett.* **1984**, *167*, 127–130.
- (39) Boussac, A.; Rutherford, A. W. *Biochemistry* **1988**, *27*, 3476–3483.
- (40) Boussac, A.; Zimmermann, J.-L.; Rutherford, A. W. *FEBS Lett.* **1990**, *277*, 69–74.
- (41) Ono, T.-A.; Inoue, Y. *FEBS Lett.* **1988**, *227*, 147–152.
- (42) Pistorius, E. K. *Eur. J. Biochem.* **1983**, *135*, 217–222.
- (43) Boussac, A. *J. Biol. Chem.* **2004**, *279*, 22809–22819.
- (44) Cox, N.; Rapatskiy, L.; Su, J.-H.; Pantazis, D. A.; Sugiura, M.; Kulik, L.; Dorlet, P.; Rutherford, A. W.; Neese, F.; Boussac, A.; Lubitz, W.; Messinger, J. *J. Am. Chem. Soc.* **2011**, *133*, 3635–3648.
- (45) Waggoner, C. M.; Pecoraro, V.; Yocum, C. F. *FEBS Lett.* **1989**, *244*, 237–240.
- (46) Ono, T.; Rompel, A.; Mino, H.; Chiba, N. *Biophys. J.* **2001**, *81*, 1831–1840.
- (47) Hewitt, I. J.; Tang, J.-K.; Madhu, N. T.; Cl rac, R.; Buth, G.; Anson, C. E.; Powell, A. K. *Chem. Comm.* **2006**, 2650–2652.
- (48) Mishra, A.; Yano, J.; Pushkar, Y.; Yachandra, V. K.; Abboud, K. A.; Christou, G. *Chem. Comm.* **2007**, 1538–1540.
- (49) Nayak, S.; Nayek, H. P.; Dehnen, S.; Powell, A. K.; Reedijk, J. *Dalton Trans.* **2011**, *40*, 2699–2702.
- (50) Mukherjee, S.; Stull, J. A.; Yano, J.; Stamatatos, T. C.; Pringouri, K.; Stich, T. A.; Abboud, K. A.; Britt, R. D.; Yachandra, V. K.; Christou, G. *Proc. Nat. Acad. Sci.* **2012**, *109*, 2257–2262.
- (51) Zhang, C.; Chen, C.; Dong, H.; Shen, J. R.; Dau, H.; Zhao, J. *Science* **2015**, *348*, 690–693.
- (52) Najafpour, M. M.; Ehrenberg, T.; Wiechen, M.; Kurz, P. *Angew. Chem. Int. Ed.* **2010**, *49*, 2233–2237.
- (53) Najafpour, M. M.; Pashaei, B.; Nayeri, S. *Chem. Comm.* **2012**, *41*, 4799–4805.
- (54) Kanady, J. S.; Tsui, E. Y.; Day, M. W.; Agapie, T. *Science* **2011**, *333*, 733–736.
- (55) Tsui, E. Y.; Agapie, T. *Proc. Nat. Acad. Sci.* **2013**, *110*, 10084–10088.
- (56) Blake, M. P.; Kaltsoyannis, N.; Mountford, P. *J. Am. Chem. Soc.* **2011**, *133*, 15358–15361.

- (57) Park, Y. J.; Cook, S. A.; Sickerman, N. S.; Sano, Y.; Ziller, J. W.; Borovik, A. S. *Chem. Sci.* **2013**, *4*, 717–726.
- (58) Tsui, E. Y.; Tran, R.; Yano, J.; Agapie, T. *Nat. Chem.* **2013**, *5*, 293–299.
- (59) APEX2 Version 2010.3-0, Bruker AXS, Inc.; Madison, WI 2010.
- (60) SAINT Version 7.68a, Bruker AXS, Inc.; Madison, WI 2009.
- (61) Sheldrick, G. M. SADABS, Version 2008/1, Bruker AXS, Inc.; Madison, WI 2008.
- (62) Sheldrick, G. M. SHELXTL, Version 2008/4, Bruker AXS, Inc.; Madison, WI 2008.
- (63) International Tables for X-Ray Crystallography 1992, Vol. C., Dordrecht: Kluwer Academic Publishers.
- (64) Parsons, S., Flack, H. D., Wagner, T. *Acta. Cryst.* B69, 249-259, 2013.
- (65) Spek, A. L. SQUEEZE, *Acta. Cryst.* 2015, C71, 9-19.
- (66) Spek, A. L. PLATON, *Acta. Cryst.* 2009, D65, 148-155.

CHAPTER 3

Intramolecular Hydroxylation of Tripodal Sulfonimido Ligands by Putative High-Valent Fe and Mn complexes

Introduction

The foundation of modern coordination chemistry is rooted in the study of simple coordination complexes such as the ammine cobalt(III)chloride complexes used by Werner to establish the fundamental concepts of ligand coordination to a metal ion. In these types of coordination complexes, the properties of the metal center dictate the structure and properties of the complexes that are formed.¹ In particular, the coordination number of the metal ion is governed by its oxidation state, which in turn is determined by the electronic structure of the metal center. As a result, the types of structures that can be formed in these simple coordination complexes are limited by the available oxidation states and coordination number of the metal ion. These apparent limits in coordination can be challenged through the rational design of ligands that enforce unusual coordination numbers or geometries around a metal center. For example, introducing steric bulk into amido ligands via trimethylsilyl groups provided access to three-coordinate complexes of Mn(II), Fe(II), Co(II), and Ni(II), and continued modification of the amido ligands to provide additional steric bulk led to further restriction of the coordination number and the first crystallographic characterization of two-coordinate Fe(II) and Co(II) complexes.²

The rational design of ligands for the purpose of controlling the properties of metal centers continues to drive a major area of research in modern coordination chemistry, including aspects of bioinspired inorganic chemistry and inorganic catalysis. As discussed in Chapter 1, the development of synthetic compounds that mimic the

properties of metalloprotein active sites requires the design of complex ligand scaffolds that incorporate multiple types of bonding interactions. In order to mimic the function of metalloenzymes, these ligands need to also be capable of stabilizing multiple coordination numbers and oxidation states. Similarly, synthetic molecular catalysts must be able to generate reactive intermediates, change coordination number, and cycle through several oxidation states.

A challenge that must be considered in the design of ligand scaffolds for supporting transition metal centers that undergo changes in oxidation state is the possibility of self-decay of the complex through intramolecular reactivity of unstable intermediates with the supporting ligand. This self-decay process is exceptionally prominent in reactions that involve oxidation of the metal center to unusual oxidation states. For example, a number of well-characterized Fe(IV)–oxo³⁻⁸ and Fe(IV)–imido^{9,10} species have been shown to undergo self-decay via reaction with the supporting ligand. These high-valent complexes are popular synthetic targets due to their biological relevance and potential application as oxidation catalysts, and so the development of robust ligand systems that can support these reactive species continues to be a common topic of study.

In this chapter, a limitation of the [MST]³⁻ ligand system in supporting the oxidation of its Mn(II) and Fe(II) complexes with an oxygen-atom (O-atom) transfer reagent is described. This ligand contains mesityl units whose methyl groups are susceptible to oxidation, as evidenced by isolation of an Fe(III)-alkoxide complex in which an *ortho* methyl group has been hydroxylated and is coordinated to the Fe center. In order to address this limitation of [MST]³⁻, the ligand was modified to remove the

groups that are most susceptible to C–H activation via replacement of the mesityl groups with naphthyl and tolyl groups. The oxidation studies of these two additional ligand derivatives are also described in this chapter.

Results and Discussion

Reactivity of the $[Fe^II MST]^-$ Complex with Dioxygen. In Chapter 2, the preparation of bimetallic complexes that are supported by the tripodal ligand N,N',N'' -[2,2',2''-nitriлотris(ethane-2,1-diyl)]tris(2,4,6-trimethylbenzenesulfonamido) ($[MST]^{3-}$ = mesityl sulfonamide tripod) was described (Chart 3.1A).^{11,12} These complexes were produced by treating $NMe_4[Fe^II MST]$ or $NMe_4[Mn^II MST]$ with dioxygen in the presence of a group 2 metal ion. In the absence of this second metal ion, the reaction with dioxygen was sluggish, with the Mn(II) complex reacting so slowly that completion of the reaction could not be observed. Reaction of the Fe(II) complex was faster than the Mn(II) complex, and analysis of the reaction mixture in dichloromethane (DCM) after five hours suggested formation of the analogous monometallic $NMe_4[Fe^III MST(OH)]$ salt (Chart 3.1B and Figure 3.1). The electrospray ionization mass spectrum (ESI-MS) contained a negative ion peak whose mass-to-charge ratio (m/z) of 762 corresponds to the formulation $[FeMST(OH)]^-$ (Figure 3.1A), and based on charge balance, the Fe center

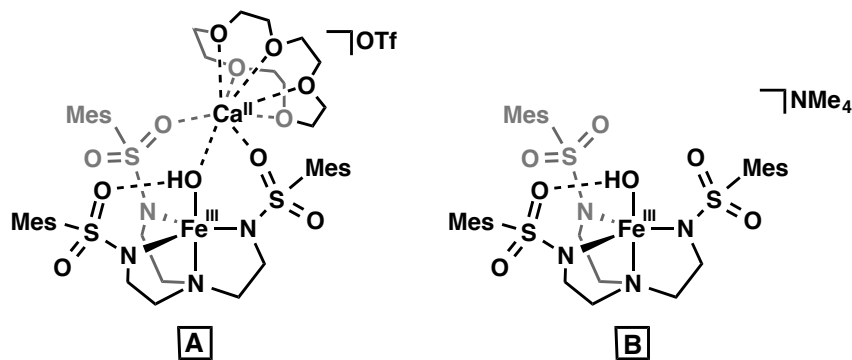


Chart 3.1. A) Bimetallic and B) monometallic Fe(III)–hydroxide complexes.

must be in the 3+ oxidation state. This oxidation state is supported by electron paramagnetic resonance (EPR) spectroscopy, which exhibits a rhombic signal with g values of 4.2 and 8.6 that are consistent with a high spin Fe(III) center (Figure 3.1B). Furthermore, a broad band was observed at a frequency of 3463 cm^{-1} in the Fourier transform infrared (FTIR) spectrum of the reaction mixture, which is consistent with the O–H vibration of a hydroxo ligand (Figure 3.1C). Together, these ESI-MS, EPR, and FTIR data suggest that the monometallic $[\text{Fe}^{\text{III}}\text{MST}(\text{OH})]^-$ complex is formed from the reaction of $\text{NMe}_4[\text{Fe}^{\text{II}}\text{MST}]$ with O_2 .

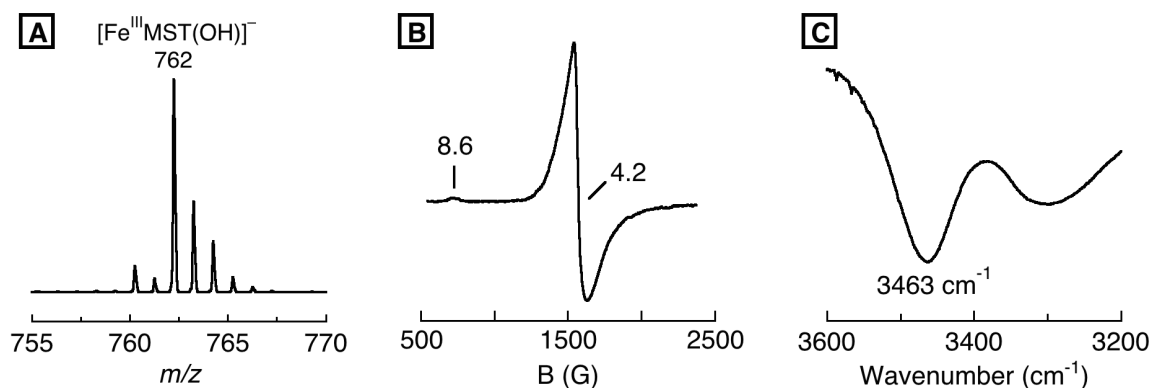


Figure 3.1. Spectra collected of the reaction mixture of $\text{NMe}_4[\text{Fe}^{\text{II}}\text{MST}]$ and O_2 five hours after the addition of O_2 : A) ESI-MS showing the molecular ion peak assigned to $[\text{Fe}^{\text{III}}\text{MST}(\text{OH})]^-$; B) perpendicular mode EPR spectrum collected at 77 K; C) solution IR spectrum of a 24 mM DCM solution.

Attempts to establish dioxygen as the source of the hydroxo ligand in the $[\text{Fe}^{\text{III}}\text{MST}(\text{OH})]^-$ complex via reactivity with $^{18}\text{O}_2$ were inconclusive, presumably due to the fast exchange of the ^{18}O -labeled hydroxo ligand with adventitious ^{16}O water. In order to test this premise, $\text{NMe}_4[\text{Fe}^{\text{III}}\text{MST}(\text{OH})]$ was treated with one equivalent of H_2^{18}O and the mixture was analyzed by ESI-MS, which indicated ^{18}O incorporation (Figure 3.2). Note that definitive incorporation was not observed from the reaction mixture with $^{18}\text{O}_2$ by ESI-MS. Further complicating the analysis of ^{18}O incorporation from reaction with

$^{18}\text{O}_2$ was the broadness of the O–H vibration of the hydroxo ligand ($\text{FWHM} \approx 110 \text{ cm}^{-1}$) in the FTIR spectrum, which prevented determination of the relative energies of the $\nu(^{16}\text{OH})$ and $\nu(^{18}\text{OH})$ bands; a shift of only 10 cm^{-1} was predicted based on a harmonic O–H oscillator model.

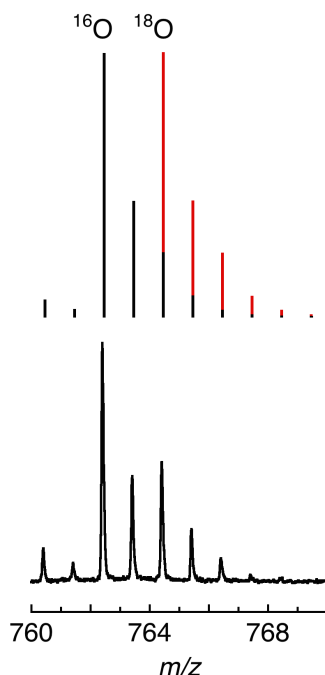


Figure 3.2. ESI mass spectrum of $\text{NMe}_4[\text{Fe}^{\text{III}}\text{MST}(\text{OH})]$ after the addition of 1 equivalent of H_2^{18}O in DCM (bottom) and the calculated isotope distribution patterns for the $[\text{Fe}^{\text{III}}\text{MST}^{16}\text{OH}]^-$ ion (black) and the $[\text{Fe}^{\text{III}}\text{MST}^{18}\text{OH}]^-$ ion (red).

Crystallization attempts of the proposed Fe(III)–hydroxide product, $\text{NMe}_4[\text{Fe}^{\text{III}}\text{MST}(\text{OH})]$, instead resulted in isolation of the Fe(II)–aquo salt, $\text{NMe}_4[\text{Fe}^{\text{II}}\text{MST}(\text{OH}_2)]$, whose molecular structure was determined by X-ray diffraction (XRD) methods (Figure 3.3, Tables A.2 and A.3). This isolated product presumably results from further reaction of the initial Fe(III)–hydroxide species with an H atom in solution, which is supported by an FTIR study of the reaction mixture after removal of the excess dioxygen. Over the course of seven days, the O–H vibration from the putative $[\text{Fe}^{\text{III}}\text{MST}(\text{OH})]^-$ complex (at 3463 cm^{-1}) decreased in intensity with a concomitant

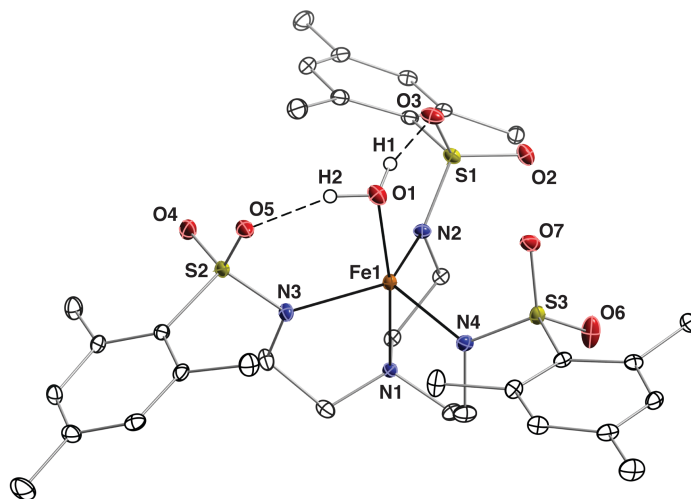


Figure 3.3. Molecular structure of the $\text{NMe}_4[\text{Fe}^{\text{II}}\text{MST}(\text{OH}_2)]$ product that was crystallized from the reaction of $\text{NMe}_4[\text{Fe}^{\text{II}}\text{MST}]$ with excess O_2 . Ellipsoids are drawn at the 50% probability level. The counter cation and all hydrogen atoms except those of the aquo ligand are omitted for clarity.

increase in a new O–H vibration at 3300 cm^{-1} that matches the vibration observed for the aquo ligand of independently-prepared $[\text{Fe}^{\text{II}}\text{MST}(\text{OH}_2)]^-$ (Figure 3.4). When half an equivalent of diphenylhydrazine (DPH) was added to the initial reaction mixture as a source of one equivalent of H-atoms, both the O–H band corresponding to the hydroxo ligand and the N–H vibrations of DPH were replaced by the O–H band of the Fe(II)–aquo complex within two hours, and $\text{NMe}_4[\text{Fe}^{\text{II}}\text{MST}(\text{OH}_2)]$ was crystallized from the reaction in 85% yield. The increase in the rate of $[\text{Fe}^{\text{II}}\text{MST}(\text{OH}_2)]^-$ formation in the presence of DPH suggests that the observed instability of $\text{NMe}_4[\text{Fe}^{\text{III}}\text{MST}(\text{OH})]$ results from H-atom abstraction from the solvent or from an external substrate to give $\text{NMe}_4[\text{Fe}^{\text{II}}\text{MST}(\text{OH}_2)]$. This observed reactivity is a departure from the stability of the analogous heterobimetallic complexes of Fe(III)–hydroxide containing a group 2 metal ion in the secondary coordination sphere; the $[\text{M}^{\text{II}}(\text{OH})\text{Fe}^{\text{III}}]^+$ complexes are indefinitely stable in a solution free from water and O_2 , and they show poor reactivity with the weak N–H bonds of DPH to form $[\text{M}^{\text{II}}(\text{OH}_2)\text{Fe}^{\text{II}}]^{2+}$ species. This stability likely results from a combination

of reduced electron density on the bridging hydroxide ligand compared to the terminal hydroxide ligand of the monometallic complex as well as limited substrate access to the Fe–OH unit as a result of the capping Ca^{II} ion (Chart 3.1).

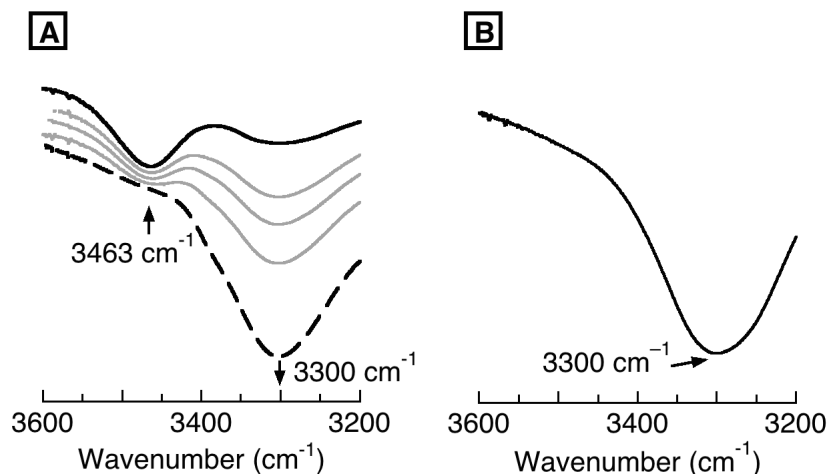
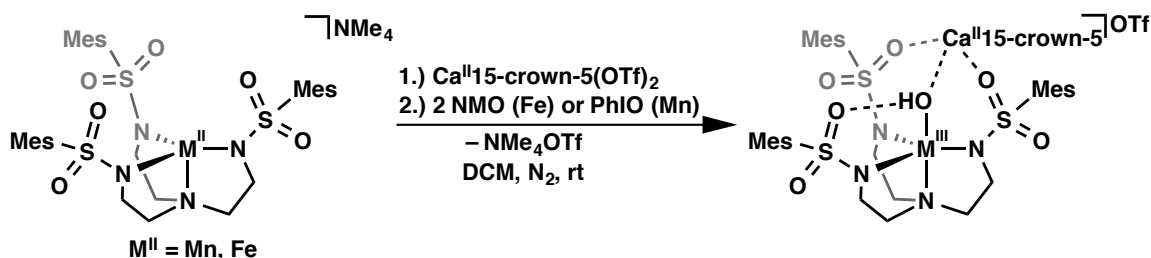


Figure 3.4. A) FTIR spectra showing the conversion of $[\text{Fe}^{\text{III}}\text{MST}(\text{OH})]^-$ to $[\text{Fe}^{\text{II}}\text{MST}(\text{OH}_2)]^-$ after the removal of excess O_2 from the reaction of $\text{NMe}_4[\text{Fe}^{\text{II}}\text{MST}]$ with O_2 . The spectra were collected on a 24 mM DCM solution over the course of 7 days (dashed black), with the first spectrum collected after 5 hours (solid black). B) FTIR spectrum of independently prepared $\text{NMe}_4[\text{Fe}^{\text{II}}\text{MST}(\text{OH}_2)]^-$ in 24 mM DCM solution.

Generation of Bimetallic Complexes from Oxygen-Atom Transfer Reagents.

Oxidation of $\text{NMe}_4[\text{Mn}^{\text{II}}\text{MST}]$ and $\text{NMe}_4[\text{Fe}^{\text{II}}\text{MST}]$ using O-atom transfer reagents was explored as an alternate route to the $[\text{M}^{\text{III}}\text{MST}(\text{OH})]^-$ complexes due to the slow reactivity of the $[\text{M}^{\text{II}}\text{MST}]^-$ complexes with O_2 in the absence of secondary metal ions. Such reagents are understood to react in two-electron processes with M(II) centers to generate M(IV)–oxo intermediates, which can then abstract an H-atom from solvent or a substrate to give a M(III)–hydroxide product. In accordance with this understanding, the O-atom transfer reagents 4-methylmorpholine-*N*-oxide (NMO) and iodosylbenzene (PhIO) produced the same bimetallic M(III)–hydroxide complexes (M(III) = Mn, Fe) as the analogous reaction with O_2 . For instance, reaction of $\text{NMe}_4[\text{Fe}^{\text{II}}\text{MST}]$ and



Scheme 3.1. Preparation of heterobimetallic complexes from O-atom transfer reagents.

Ca(OTf)₂/15-crown-5 with two equivalents of NMO produced [(15-crown-5)₂Ca^{II}-(μ-OH)-Fe^{III}MST]OTf in 85% crystalline yield, which is similar to the yield obtained from reaction with O₂ (60-70%, Scheme 3.1).¹² Note that two equivalents of NMO were used in reactions with NMe₄[Fe^{II}MST] because it gave the highest yield of crystalline products. For [Mn^{II}MST]⁻, generation of the bimetallic complexes required the stronger transfer reagent PhIO due to the higher oxidation potential of [Mn^{II}MST]⁻ vs. [Fe^{II}MST]⁻ (0 V compared to -0.7 V vs. Fc^{0/+}, respectively). Reaction of NMe₄[Mn^{II}MST] and Ca(OTf)₂/15-crown-5 with PhIO gave [(15-crown-5)₂Ca^{II}-(μ-OH)-Mn^{III}MST]OTf in 50% crystalline yield. Based on this match in the products obtained from O₂ and NMO/PhIO in the presence of Ca^{II} ions, the monometallic [M^{III}MST(OH)]⁻ complexes that were formed from dioxygen were also expected to be generated from NMO and PhIO.

Reactivity of [Fe^{II}MST]⁻ with NMO. In the absence of a second metal ion, NMe₄[Fe^{II}MST] also reacts with NMO, as indicated by a rapid change from colorless to orange. Evidence for the predicted [Fe^{III}MST(OH)]⁻ product was again observed by FTIR spectroscopy in which an O-H vibration at 3460 cm⁻¹ that matched the band obtained from the analogous reaction with O₂ was replaced by a second O-H vibration at 3300 cm⁻¹ after 9 days (Figure 3.5A). However, the ESI mass spectrum of the initial reaction

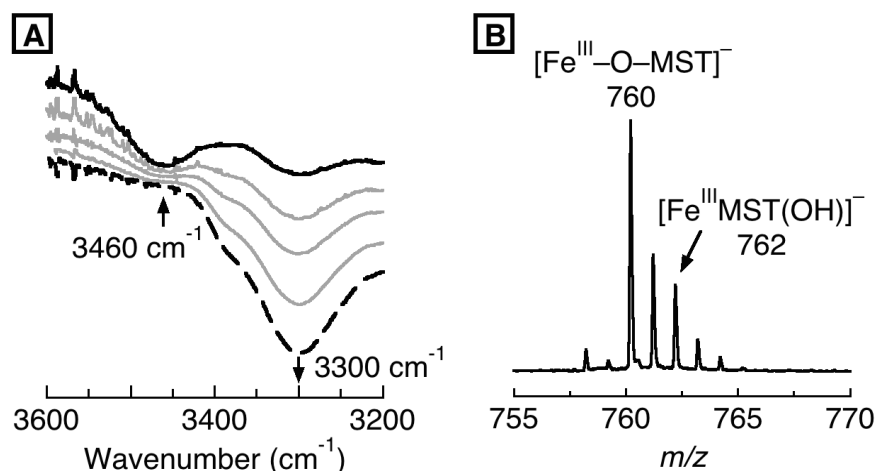


Figure 3.5. Spectra obtained of the reaction mixture of $\text{NMe}_4[\text{Fe}^{\text{II}}\text{MST}]$ and 2 equivalents of NMO: A) FTIR spectra of a 24 mM DCM solution showing the conversion of the initial product to $[\text{Fe}^{\text{II}}\text{MST}(\text{OH}_2)]^-$ over the course of 9 days (dashed black), with the first spectrum collected after 5 hours (solid black); B) ESI-MS showing the molecular ion peak assigned to $[\text{Fe}^{\text{III}}-\text{O}-\text{MST}]^-$.

mixture contained only a minor peak corresponding to the $[\text{Fe}^{\text{III}}\text{MST}(\text{OH})]^-$ ion while a dominant ion peak was observed two mass units lower at a m/z of 760 (Figure 3.5B). Structural determination of the product that crystallized from the reaction via XRD methods revealed the source of the dominant molecular ion: an *ortho* methyl group on one ligand arm had been hydroxylated to form an alkoxide-coordinated Fe(III) product ($[\text{Fe}^{\text{III}}-\text{O}-\text{MST}]^-$, Figure 3.6, Table A.2). This Fe(III)-alkoxide species was the major product formed and was isolated in 50% crystalline yield.

The Fe(III) center in $[\text{Fe}^{\text{III}}-\text{O}-\text{MST}]^-$ has an N_4O primary coordination environment in which all five donors are provided by the $[\text{MST}]^{3-}$ ligand. The anionic nitrogen atoms and neutral apical nitrogen donor provide the base of a distorted trigonal bipyramid ($\tau = 0.82$)¹³ with an average Fe- N_{eq} distance of 2.021(2) Å and an Fe- N_1 distance of 2.358(2) Å (Table 3.1). The deprotonated hydroxyl group that resulted from the functionalization of a mesityl group completes the coordination sphere of the Fe center. In order to accommodate the binding of the hydroxyl group, the functionalized

mesityl group twists above the Fe–N_{eq} plane, whereas those on the two unfunctionalized ligand arms point outward from the metal center. The oxygen atom of the deprotonated hydroxyl group tilts away from the Fe–N1 vector towards N4 with an O1–Fe–N1 bond angle of 171.09(6)° and an Fe–O1 distance of 1.805(1) Å.

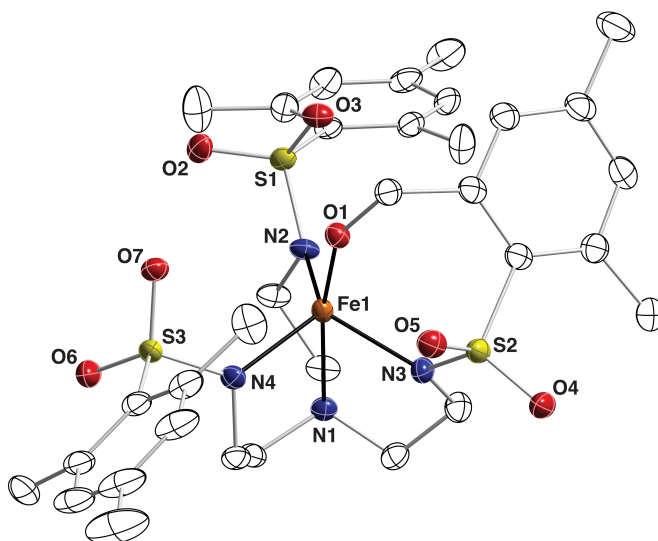


Figure 3.6. Thermal ellipsoid diagram depicting [Fe^{III}–O–MST][–]. Ellipsoids are drawn at the 50% probability level, and all hydrogen atoms and the counter cation are omitted for clarity.

Table 3.1. Select metrical parameters for [Fe^{III}–O–MST][–].

Bond Distances (Å)	
Fe1—O1	1.805(1)
Fe1—N1	2.358(2)
Fe1—N2	2.034(2)
Fe1—N3	2.030(2)
Fe1—N4	1.999(2)
Bond Angles (°)	
O1—Fe1—N1	171.09(6)
N2—Fe1—N3	122.11(7)
N2—Fe1—N4	115.18(7)
N3—Fe1—N4	108.08(7)
τ value	0.82

The reaction of NMe₄[Fe^{II}MST] with NMO was further probed through determination of the extent of ligand oxidation after isolation of the ligand from the complex. The metal ion was removed from the ligand in an aqueous acid workup of the

reaction mixture in DCM to give a mixture of H₃MST and oxidized ligand species, which were recovered in a combined yield of 82%. The identities of the products were determined by ¹H and ¹³C NMR spectroscopy, ESI-MS, and FTIR techniques after partial separation by column chromatography (See Figures A.1 through A.8 for NMR spectra). Five different ligand products were identified, including the hydroxylated ligand **1**, which is isolated from [Fe^{III}-O-MST]⁻, and unfunctionalized H₃MST, which we propose is isolated from [Fe^{III}MST(OH)]⁻ or [Fe^{II}MST(OH₂)]⁻. The remaining three species have been further oxidized beyond hydroxylation of the *ortho* metal group; two of the species are assigned to cyclization of one arm through the sulfonamide nitrogen atom and the hydroxylated *ortho* carbon atom of the activated ligand arm (Chart 3.2). Of these two products, one retained the hydroxyl functionality (**2**) and the other was further oxidized to the carbonyl (**3**). In the final ligand species, two of the ligand arms contained the cyclized carbonyl product (**4**).

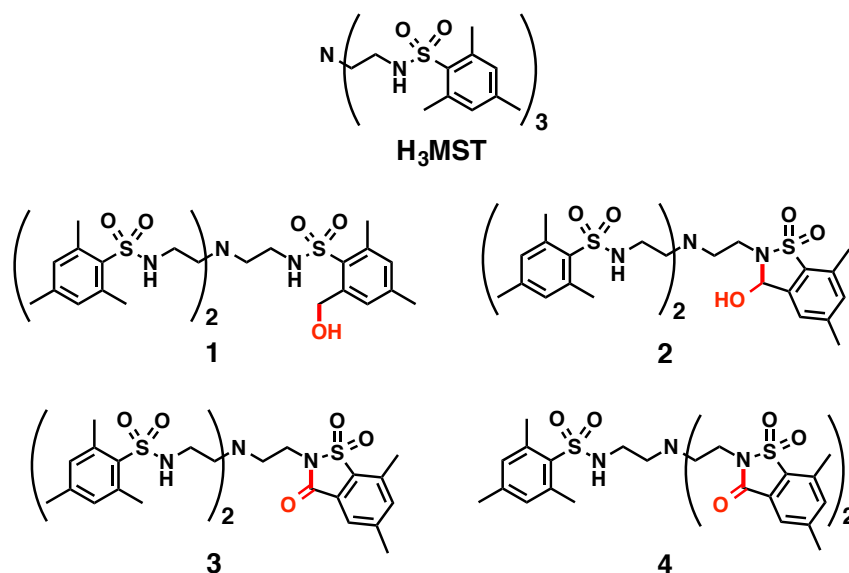


Chart 3.2. Ligand products isolated from oxidation of [Mn^{II}MST]⁻ and [Fe^{II}MST]⁻ with O-atom transfer reagents.

Analysis of the crude mixture of ligand products by NMR spectroscopy after the reaction of $\text{NMe}_4[\text{Fe}^{\text{II}}\text{MST}]$ with NMO provided an estimate of the yields of the Fe(III)–hydroxide and Fe(III)–alkoxide products (Figure A.9). The hydroxylated ligand **1** makes up 56% of the ligand products, while unfunctionalized H_3MST makes up 25%. This corresponds to a 56% yield of $[\text{Fe}^{\text{III}}\text{–O–MST}]^-$ and a 25% yield of $[\text{Fe}^{\text{III}}\text{MST}(\text{OH})]^-$ (or $[\text{Fe}^{\text{II}}\text{MST}(\text{OH}_2)]^-$). The remaining 19% of the products is composed of 12% of the cyclized product **2**, 5% of **3**, and 2% of the multiply-functionalized product **4**. Oxidation of $\text{NMe}_4[\text{Fe}^{\text{II}}\text{MST}]$ with two equivalents of PhIO instead of NMO gave four of the same ligand products, although in different ratios (Table 3.2). Note that no further ligand oxidation is observed from the reaction of pure $[\text{Fe}^{\text{III}}\text{–O–MST}]^-$ with NMO or PhIO; only the singly-hydroxylated ligand product **1** was observed after isolation of the ligand products from these reactions. This indicates that products **2-4** do not result from stepwise oxidation of $[\text{Fe}^{\text{III}}\text{–O–MST}]^-$. Moreover, free H_3MST and **1** show no reactivity with NMO and only unidentifiable products with PhIO, which suggests that the ligand must be coordinated to the metal center in order to form products **2-4**. Finally, none of the oxidized ligand products were observed when O_2 was used as the oxidant instead of an O-atom transfer reagent.

Table 3.2. Distribution of the isolated ligand products.

	FeMST		MnMST
	NMO	PhIO	PhIO
H_3MST	25%	48%	24%
1	56%	38%	64%
2	19%	0%	11%
3	5%	10%	1%
4	2%	17%	0%

Reactivity of $[\text{Mn}^{\text{II}}\text{MST}]^-$ with PhIO. Reaction of $\text{NMe}_4[\text{Mn}^{\text{II}}\text{MST}]$ with an equivalent of PhIO in the absence of a second metal ion generated a dark green, EPR

silent (\perp -mode) product whose ESI mass spectrum also contained a major ion peak that was two mass units below that expected for $\text{NMe}_4[\text{Mn}^{\text{III}}\text{MST}(\text{OH})]$. In addition, the isolated solid contained no observable O–H vibration corresponding to the expected hydroxide ligand in the FTIR spectrum. Analysis of the ligand products after the reaction indicated formation of three of the same oxidized ligand products that were observed from the reaction of $\text{NMe}_4[\text{Fe}^{\text{II}}\text{MST}]$ and NMO or PhIO, and in comparable ratios (Table 3.2, products **1-3**). Note that product **4** was only observed from the oxidation reactions of $\text{NMe}_4[\text{Fe}^{\text{II}}\text{MST}]$. The isolation of 64% of the hydroxylated ligand **1** from the reaction of $\text{NMe}_4[\text{Mn}^{\text{II}}\text{MST}]$ and PhIO indicates that the major Mn-containing product can be formulated as $\text{NMe}_4[\text{Mn}^{\text{III}}\text{–O–MST}]$.

Ligand Oxidation in the Presence of Ca^{II} ions. The ligand products of the reactions with O-atom transfer reagents conducted in the presence of Ca^{II} ions to generate the heterobimetallic complexes were also analyzed after demetalation of the ligand. In the case of Fe, none of the oxidized ligand products **1-4** shown in Chart 3.2 were observed. With the exception of a small amount of an unidentified ligand product (<5% overall, **5**), only unfunctionalized H_3MST was isolated. For Mn, a small amount of the hydroxylated ligand product **1** was observed (5%), and the unidentified ligand product **5** was formed in higher yield (22%). In an attempt to determine the identity of the unknown product, **5** was separated from the unfunctionalized H_3MST via column chromatography as a mixture with product **1** and analyzed via ^1H and ^{13}C NMR spectroscopy and ESI-MS techniques. The molecular ion peak of **5** in negative mode ESI-MS indicated loss of two protons from the parent $[\text{H}_2\text{MST}]^-$ ion, and the pattern of the ^1H NMR resonances suggested functionalization of an *ortho* methyl group of one mesityl ring (Figure A.10).

However, no major changes in the IR spectrum or ^{13}C NMR spectrum relative to H_3MST were observed, as would be expected for modification of the ligand (Figure A.11). As a result of these complications, the identity of **5** could not be determined.

One explanation for the limited formation of product **1** when the reactions are carried out in the presence of Ca^{II} ions could be spatial separation of the *ortho* methyl groups and the reactive M–O unit as a result of pre-association of a Ca^{II} ion within the secondary coordination sphere. Binding of Ca^{II} to a sulfonamido oxygen atom of all three ligand arms would rigidify the structure and position the mesityl groups far enough away from the metal center to prevent hydroxylation of an *ortho* methyl group upon addition of the O-atom transfer reagent. Such an arrangement of the mesityl groups is observed in the molecular structures of the bimetallic $[\text{M}^{\text{II}}(\text{OH})\text{M}^{\text{III}}]^+$ complexes ($\text{M}^{\text{II}} = \text{Ca}, \text{Sr}, \text{Ba}$; $\text{M}^{\text{III}} = \text{Mn}, \text{Fe}$; Figure 2.5 for reference) even though only two of the ligand arms participate in bonding interactions with the group 2 metal ions at a time, which provides support that a similar arrangement would be adopted upon coordination to all three arms.

Examination of New Ligand Derivatives. The observed oxidation of the $[\text{MST}]^{3-}$ ligand upon reaction of its Mn(II) and Fe(II) complexes with O-atom transfer reagents prompted the pursuit of a more robust ligand that could withstand oxidation of the metal center. The one step synthetic route used to make the tripodal sulfonamido ligands from sulfonyl chloride starting materials allows for facile preparation of a variety of ligand derivatives. One such derivative that was explored for the purpose of preventing ligand oxidation incorporates naphthyl groups (NST = naphthyl sulfonamido tripod, Chart 3.3), whose C–H bond dissociation energies (BDEs) are estimated to be 23 kcal mol^{-1} stronger than the methyl groups of mesitylene.¹⁴ Despite this increased bond strength, evidence for

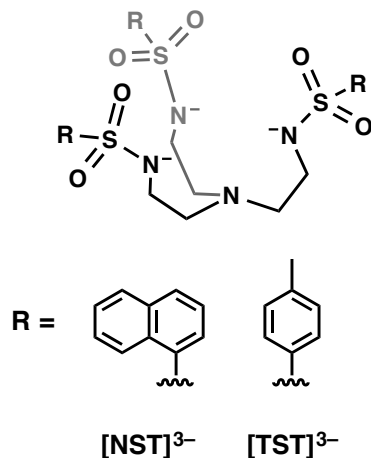


Chart 3.3. Ligand derivatives studied in an attempt to prevent ligand oxidation.

hydroxylation of the ligand was still observed by ESI-MS for the oxidation of the $\text{NMe}_4[\text{Fe}^{\text{II}}\text{NST}]$ complex with two equivalents of NMO (Figure 3.7A and B). In addition to the oxidized ligand product, a mass corresponding to the desired hydroxide product was observed in ratios that depended on the solvent used in the reaction. Solvents with weaker C–H bonds such as tetrahydrofuran (THF, $\text{BDE}_{\text{C-H}} = 92 \text{ kcal mol}^{-1}$) gave predominantly hydroxide product, whereas reaction in acetonitrile (MeCN, $\text{BDE}_{\text{C-H}} = 96 \text{ kcal mol}^{-1}$) gave mostly oxidized ligand (Scheme 3.2).¹⁵ This suggests the possibility that the BDE of the O–H group in the hydroxide product is between 92 and 96 kcal mol^{-1} . The green color of the oxidized ligand product ($\lambda_{\text{max}} = 615 \text{ nm}$) is consistent with a phenolate-to-Fe(III) charge transfer band, which supports hydroxylation of the aryl ring.^{4,16} This 615 nm band is not present in the predominantly hydroxide product, which has a $\lambda_{\text{max}} = 360 \text{ nm}$. Both products exhibit EPR signals at $g = 4.2$ and 8.7 that are consistent with Fe(III) species, and the hydroxide product displays an O–H vibration at 3473 cm^{-1} in the IR spectrum.

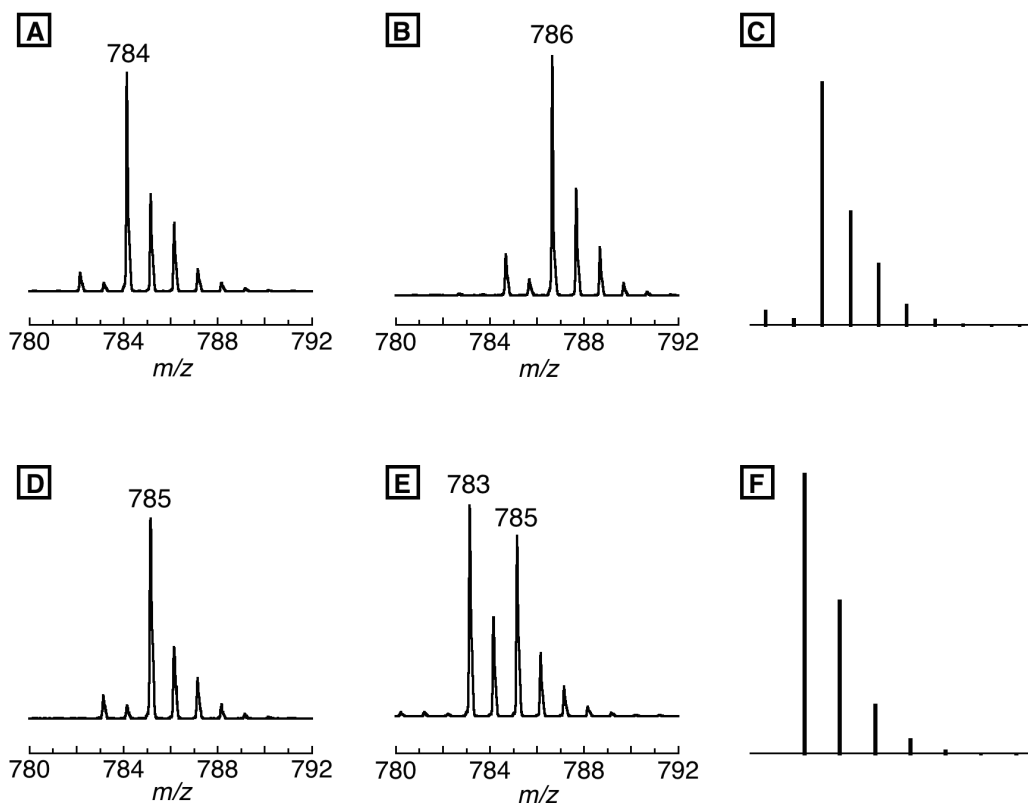
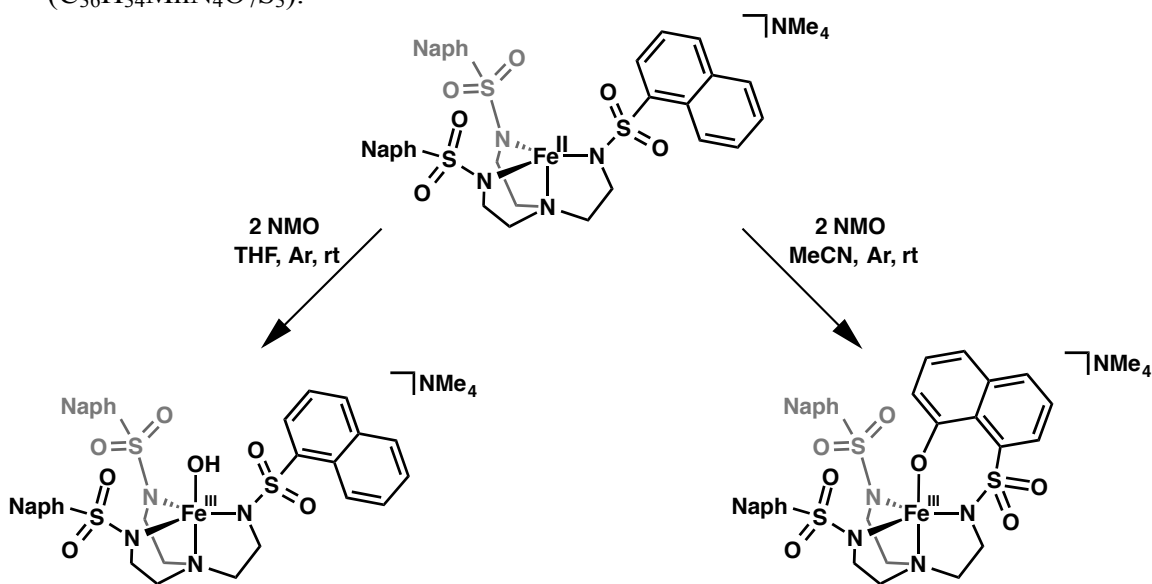


Figure 3.7. ESI mass spectra from reaction of $[\text{Fe}^{\text{II}}\text{NST}]$ with NMO in (A) MeCN and (B) THF where 786 = hydroxide product and 784 = phenoxide product. (C) Calculated isotope pattern of $[\text{Fe}^{\text{III}}\text{NST}(\text{OH})]^-$ ($\text{C}_{36}\text{H}_{34}\text{FeN}_4\text{O}_7\text{S}_3$). (D) Reaction of $[\text{Mn}^{\text{II}}\text{NST}]$ in THF and (E) MeCN where 785 = hydroxide product and 783 = phenoxide product. (F) Calculated isotope pattern of $[\text{Mn}^{\text{III}}\text{NST}(\text{OH})]^-$ ($\text{C}_{36}\text{H}_{34}\text{MnN}_4\text{O}_7\text{S}_3$).



Scheme 3.2. Major products observed in the oxidation of $\text{NMe}_4[\text{Fe}^{\text{II}}\text{NST}]$ with NMO.

In the analogous study of the $\text{NMe}_4[\text{Mn}^{\text{II}}\text{NST}]$ complex, oxidation with two equivalents of PhIO in THF again yielded a high ratio of the hydroxide product relative to the phenoxide product (Figure 3.7D). However, in MeCN, the ESI-MS peak ratio of hydroxide to phenoxide product was closer to one (Figure 3.7E). This lower selectivity for the phenoxide product by Mn in MeCN compared to the Fe products suggests that the Mn intermediate is a weaker oxidant than the Fe intermediate.

The molecular structure of the proposed $\text{NMe}_4[\text{Mn}^{\text{III}}\text{-O-NST}]$ and $\text{NMe}_4[\text{Fe}^{\text{III}}\text{-O-NST}]$ products could not be determined due to difficulties in growing X-ray diffraction-quality crystals, which prevented determination of the location of ligand hydroxylation. However, based on comparison to the molecular structure of $[\text{Fe}^{\text{III}}\text{-O-MST}]^-$ shown in Figure 3.5, we propose that the 9 position of the naphthyl ring is functionalized. The carbon atom in this position occupies the same location relative to the metal center as the carbon that is hydroxylated in the *ortho* methyl group of the mesityl ligand, which should make it similarly susceptible to oxidation based on spatial arguments. A third ligand derivative was therefore prepared in which this *ortho* carbon was removed via substitution with a tolyl group ($[\text{TST}]^{3-}$). The increased strain that would be created within the ligand in order to make this group accessible to the active oxidizing species was predicted to make it less prone to oxidation than $[\text{NST}]^{3-}$. This hypothesis was supported by analysis of the isolated ligand products after oxidation of the Mn^{II} and Fe^{II} complexes with O-atom transfer reagents, which showed no evidence for hydroxylation of the ligand. This greater stability of the $[\text{TST}]^{3-}$ ligand compared to $[\text{MST}]^{3-}$ and $[\text{NST}]^{3-}$ allowed for further study of the reactivity with O-atom transfer reagents, which will be discussed in the next chapter.

Mechanistic Proposals for Ligand Hydroxylation. Similar oxidations of benzylic and aromatic C–H bonds within ligands have been reported by others for oxidation of Fe(II) complexes with O-atom transfer reagents. For example, Chang reported hydroxylation of both the mesityl and phenyl derivatives of their tris(pyrrolylmethyl)amine (tpa^R) ligand platforms upon oxidation of the [tpa^RFe^{II}]⁻ complexes with an O-atom transfer reagent, trimethylamine N-oxide (TMO) (Chart 3.4A).^{5,6} Que has also characterized an Fe(III)–phenoxide product from oxidation of [(6-PhTPA)Fe^{II}(NCCH₃)₂]²⁺ (TPA = tris(2-pyridylmethyl)amine) with PhIO and an Fe(III)–alkoxide product from reaction of [Fe^{II}(TMG₃tren)(CH₃CN)]²⁺ (TMG₃tren = 1,1,1-tris{2-[N²-(1,1,3,3-tetramethyl-guanidino)]ethyl}amine) with a substituted PhIO derivative (Chart 3.4B).^{7,9} As discussed above, O-atom transfer reagents such as the three described in this chapter (TMO, NMO, and PhIO) are understood to react in two-electron processes with Fe(II) centers to generate Fe(IV)–oxo intermediates, which Chang could observe

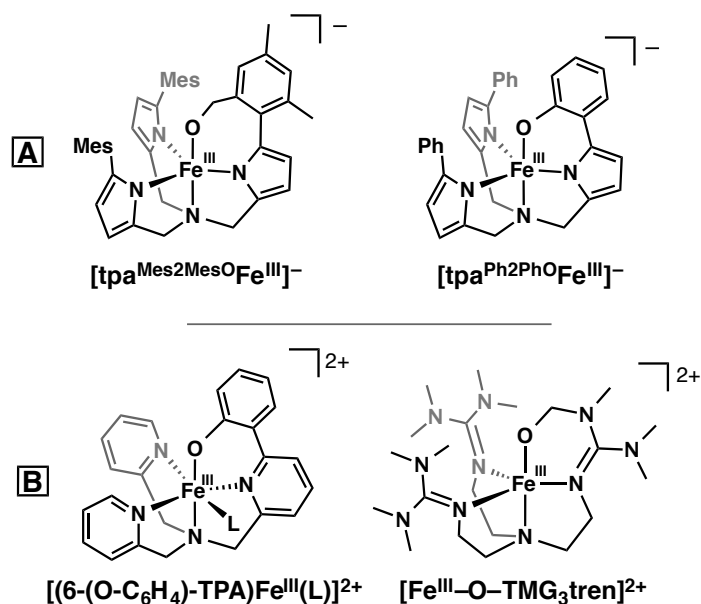
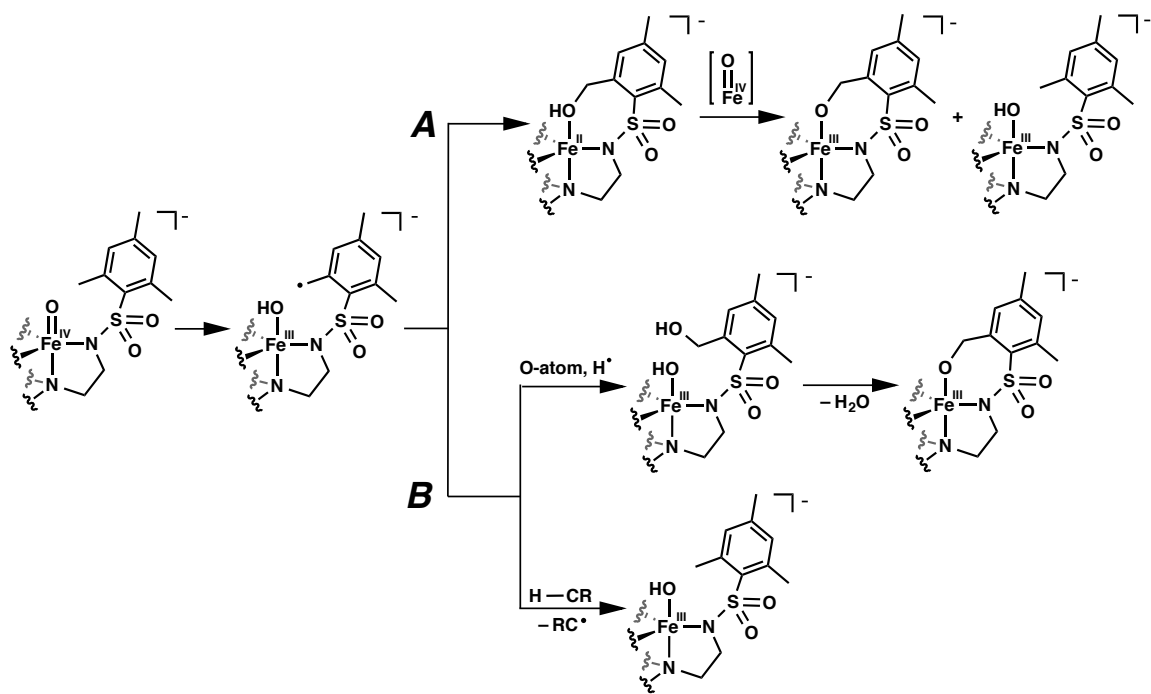


Chart 3.4. Alkoxide and phenoxide products of A) Chang and B) Que that were generated from reaction of the corresponding Fe(II) salts with O-atom transfer reagents.

spectroscopically with the phenyl ligand derivative and which Que crystallographically characterized for the TMG_3tren complex. Based on their observations, possible mechanisms for the hydroxylation of $[\text{MST}]^{3-}$ and $[\text{NST}]^{3-}$ are discussed below for the Fe complexes. Note, however, that no definitive evidence of an Fe(IV)–oxo intermediate was observed for the complexes of either $[\text{MST}]^{3-}$ and $[\text{NST}]^{3-}$. Although the discussion focuses on Fe, a similar mechanism is expected to be operative in the Mn complexes as well.

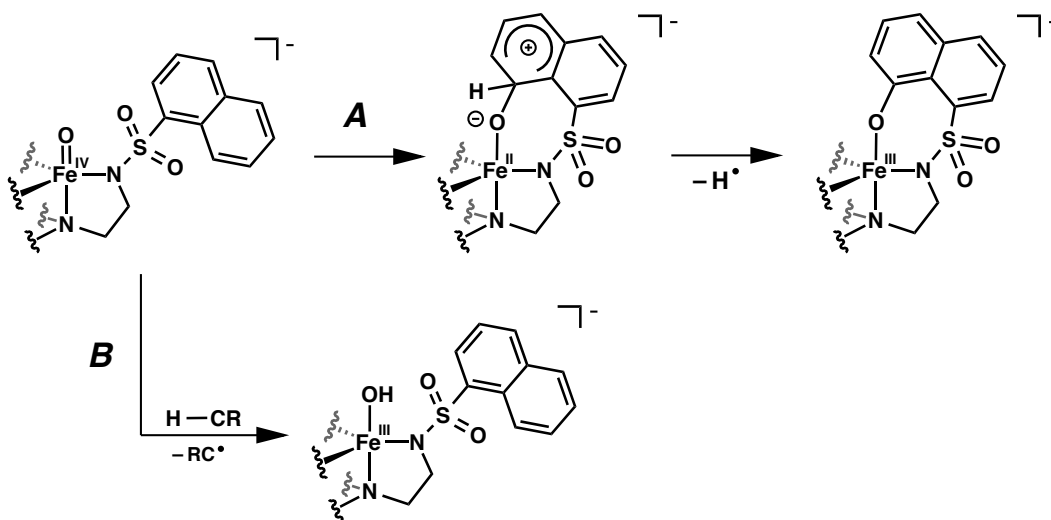
The most obvious step to follow the formation of Fe(IV)–oxo involves intra- or intermolecular C–H bond cleavage of the ligand or a substrate/solvent molecule to generate a carbon radical (Scheme 3.3). This radical can either rebound intramolecularly into the Fe(III)–hydroxide unit or be quenched intermolecularly with an exogenous substrate or solvent molecule. For the intramolecular rebound reaction, the resulting product is an Fe(II) species with a coordinated alcohol that must be deprotonated and oxidized by one electron to give the observed Fe(III)–alkoxide product (Scheme 3.3, pathway *A*). Que proposed that in his TMG_3tren complex, a second Fe(IV)–oxo unit performs this final electron and proton transfer, producing a mixture of Fe(III)–alkoxide and Fe(III)–hydroxide products, which is consistent with the products observed with our $[\text{MST}]^{3-}$ and $[\text{NST}]^{3-}$ systems.⁷ However, Nam has proposed an alternate pathway based on detailed study of C–H bond activation by non-heme Fe(IV)–oxo units, from which he concluded that dissociation of the carbon radical is favored over the intramolecular radical rebound mechanism in non-heme systems.¹⁷ In this case, after C–H bond cleavage from the ligand to give a ligand-based radical and an Fe(III)–hydroxide unit, the radical could react intermolecularly with a C–H bond of a solvent or substrate molecule to return

to the unfunctionalized methyl group and give the final Fe(III)–hydroxide product, or the radical could react with another equivalent of O-atom transfer reagent to hydroxylate the ligand (Scheme 3.3, pathway *B*). Proton transfer to the Fe(III)–OH unit followed by displacement of the resulting aquo ligand upon coordination of the alkoxide could then give the observed Fe(III)–alkoxide product. Although detailed mechanistic studies were not performed for the $[\text{MST}]^{3-}$ system, the observed formation of the oxidized ligand products **2-4** is suggestive of a long-lived radical species, as these types of five-membered rings are typically prepared through radical reactions.^{18,19} This reactivity better correlates with the dissociation and intermolecular reactivity pathway suggested by Nam than the intramolecular radical rebound mechanism of Que.



Scheme 3.3. Two possible mechanistic routes leading to the observed mixture of Fe(III)–hydroxide and Fe(III)–alkoxide products from the oxidation of $[\text{Fe}^{\text{II}}\text{MST}]^-$ with an O-atom transfer reagent: A) intramolecular (or radical rebound) mechanism; B) intermolecular reaction of the ligand-based radical with solvent, substrate, or oxidant.

The high bond strength of the naphthyl rings of $[\text{NST}]^{3-}$ (BDE = 112 kcal mol⁻¹)²⁰ and of the phenyl rings of Chang and Que's tripodal ligands indicate that a different mechanism of hydroxylation must give rise to the Fe(III)–phenoxide products than the Fe(III)–alkoxide products. One possible mechanism that was described by Que invokes electrophilic attack of the Fe(IV)–oxo unit on the aryl ring to give an unstable Fe(II) species that is then oxidized to return aromaticity and produce the observed Fe(III)–phenoxide products (Scheme 3.4, pathway *A*). The Fe(III)–hydroxide product that is also observed in the reaction of $[\text{NST}]^{3-}$ could be generated from abstraction of an H-atom from the solvent by the Fe(IV)–oxo intermediate (Scheme 3.4, pathway *B*), which is consistent with the dependence of the product distribution on the C–H bond strength of the solvent.



Scheme 3.4. Possible mechanism leading to the observed mixture of Fe(III)–hydroxide and Fe(III)–phenoxide products from the oxidation of $[\text{Fe}^{\text{II}}\text{NST}]^-$ with an O-atom transfer reagent. A) Electrophilic attack of the Fe(IV)–oxo unit on the aromatic ring followed by oxidation to give the Fe(III)–phenoxide product. B) Intermolecular H-atom abstraction to give the Fe(III)–hydroxide product.

Summary and Conclusions

In summary, reaction of $\text{NMe}_4[\text{Fe}^{\text{II}}\text{MST}]$ with dioxygen produced an Fe(III)–hydroxide complex that is analogous to the bimetallic complexes formed in the presence of a secondary metal ion. However, unlike the bimetallic Fe(III)–hydroxide products, the $\text{NMe}_4[\text{Fe}^{\text{III}}\text{MST}(\text{OH})]$ species is not stable in solution and converts to $\text{NMe}_4[\text{Fe}^{\text{II}}\text{MST}(\text{OH}_2)]$. The $\text{NMe}_4[\text{Mn}^{\text{II}}\text{MST}]$ salt reacts too sluggishly with O_2 to isolate the monometallic $[\text{Mn}^{\text{III}}\text{MST}(\text{OH})]^-$ product, and so oxidation with O-atom transfer reagents was pursued as an alternate pathway to the mono- and bimetallic M(III)-hydroxides of Mn and Fe. While the same bimetallic Fe(III)–hydroxide complex was isolated from NMO and Ca^{II} as from dioxygen, a new product was isolated when NMO was reacted with $\text{NMe}_4[\text{Fe}^{\text{II}}\text{MST}]$ alone. This product was determined to be an Fe(III)–alkoxide species that resulted from activation of a C–H bond in a mesityl group of the ligand ($\text{BDE}_{\text{C-H}} \sim 88 \text{ kcal mol}^{-1}$). Additional analysis of the ligand products after the reaction revealed further oxidation to ring-closed products that had hydroxyl and carbonyl functionalities as well as a product in which two ligand arms had been activated. A similar distribution of oxidized ligand products was also observed from oxidation of the $[\text{Mn}^{\text{II}}\text{MST}]^-$ complex with PhIO. When Ca^{II} ions were present in the oxidation reactions, only trace amounts of the hydroxylated ligand product **1** were observed—a result that is attributed in part to an inaccessible spatial orientation of the mesityl groups relative to the metal center upon precoordination of the Ca^{II} ion to the three ligand arms.

A naphthyl ligand derivative was prepared in an attempt prevent ligand oxidation based on the higher strength of the aromatic C–H bonds compared to those of the mesityl ligand. However, formation of the hydroxylated ligand product was again observed by

ESI-MS analysis of the reaction mixture. For both $[\text{Mn}^{\text{II}}\text{NST}]^-$ and $[\text{Fe}^{\text{II}}\text{NST}]^-$, a solvent-dependent mixture of the $[\text{M}^{\text{III}}\text{NST}(\text{OH})]^-$ and $[\text{M}^{\text{III}}\text{-O-NST}]^-$ products were observed, which suggests that the BDE of the O–H group in the hydroxide products is between 92 and 96 kcal mol⁻¹. The carbon atom in the 9 position of the naphthyl ring was proposed to be hydroxylated based on comparison to the molecular structure of $[\text{Fe}^{\text{III}}\text{-O-MST}]^-$, which suggests that the carbon atom off of the *ortho* position of the R group is most susceptible to oxidation. A tolyl ligand derivative was therefore prepared, and oxidation of its complexes of Mn^{II} and Fe^{II} with PhIO and NMO showed no evidence of ligand hydroxylation. This is attributed to the greater separation between the tolyl group and the metal center compared to the mesityl and naphthyl derivatives, which makes this group less accessible to the active oxidizing species.

The observed oxidation of the mesityl and naphthyl ligand derivatives highlights the oxidizing power of their Mn and Fe complexes as well as a limitation of these ligand systems in generating high-valent species. Addressing this limitation by removing susceptible C–H bonds from the ligand framework should allow the high reactivity of the oxidized intermediate to be redirected toward intramolecular substrates—a topic that is discussed in Chapter 4.

Experimental Section

General Methods

Syntheses of metal complexes were completed under an argon or nitrogen atmosphere in a VAC drybox. Solvents were sparged with argon and dried over columns containing Q-5 and molecular sieves. All reagents were purchased from commercial suppliers and used as received unless otherwise noted. Sodium hydride as a 30%

suspension in mineral oil was filtered and washed five times each with Et₂O and pentane and dried under vacuum. PhIO,²¹ H₃MST, NMe₄[Mn^{II}MST],¹¹ NMe₄[Fe^{II}MST],¹² and H₃TST²² were prepared according to literature procedures.

Complex Syntheses

NMe₄[Fe^{II}MST(OH₂)]. A suspension of NMe₄[Fe^{II}MST] (0.10 g, 0.12 mmol) in 4 mL THF at room temperature was treated with 3 μ L (0.17 mmol) H₂O via syringe, causing the solution to become homogenous. The reaction was stirred vigorously for five minutes, after which the solvent was removed under vacuum. The resulting residue was redissolved in DCM and filtered through Celite to remove fine particulate solid. The product was crystallized from the DCM filtrate via diffusion of pentane to give 0.10 g (93%) of NMe₄[Fe^{II}MST(OH₂)] as colorless needle crystals. Elemental analysis calcd for NMe₄[Fe^{II}MST(OH₂)], C₃₇H₅₉N₅O₇S₃Fe: C, 53.03; H, 7.10; N, 8.36%, found: C, 53.00; H, 7.03; N, 8.38%. FTIR (KBr disc, cm⁻¹, selected bands): 3255 (m), 2968 (m), 2852 (m), 1604 (w), 1491 (m), 1255 (s), 1127 (s), 974 (s), 812 (s), 654 (s).

NMe₄[Fe^{III}-O-MST]. A solution of NMe₄[Fe^{II}MST] (0.25 g, 0.30 mmol) in 15 mL DCM at room temperature was treated with a solution of NMO (72 mg, 6.1 mmol) in 5 mL DCM, resulting in immediate color change to red. The reaction was stirred for three hours and then filtered through Celite. The product was recrystallized twice from DCM via pentane diffusion to give 0.13 g (50%) of orange crystals. Elemental analysis calcd for NMe₄[Fe^{III}-O-MST]·0.5 CH₂Cl₂, C_{37.5}H₅₇N₅O₇S₃Cl₂Fe: C, 51.34; H, 6.55; N, 7.98%, found: C, 51.69; H, 6.51; N, 7.77%. FTIR (KBr disc, cm⁻¹, selected bands): 3029 (w), 2932 (m), 2855 (m), 1604 (m), 1488 (m), 1292 (s), 1136 (s), 958 (s), 797 (s), 654 (s). λ_{max} , nm (DCM, ϵ , M⁻¹cm⁻¹): 351 (7500). EPR (1:1 DCM:THF, 77K): g = 9.0, 4.2.

[(15-crown-5)⊃Ca-(μ-OH)-Fe^{III}MST]OTf. A solution of NMe₄[Fe^{II}MST] (50 mg, 0.061 mmol) and Ca(OTf)₂/15-crown-5 (37 mg, 0.067 mmol) in 3 mL DCM at room temperature was treated with a solution of NMO (14 mg, 0.12 mmol) in 2 mL DCM, resulting in immediate color change to orange. After 5 hours, the reaction mixture was filtered through Celite and the product was recrystallized twice via pentane diffusion to give 60 mg (85%) of yellow-orange crystals. Elemental analysis calcd for [(15-crown-5)⊃Ca^{II}-(μ-OH)-Fe^{III}MST]OTf·0.5CH₂Cl₂, C_{44.5}H₆₇CaClF₃N₄O₁₅S₄Fe: C, 44.00; H, 5.56; N, 4.61%, found: C, 44.13; H, 5.31; N, 4.50%. FTIR (KBr disc, cm⁻¹, selected bands, strong (s), medium (m), weak (w)): 3379 (m), 2937 (m), 2868 (m), 1604 (w), 1266 (s), 1144 (s), 1090 (s), 1031 (s), 955 (s), 811 (s), 659 (s), 638 (s). λ_{max}, nm (DCM, ε, M⁻¹cm⁻¹): 383 (6000). EPR (1:1 DCM:THF, 77K): g = 9.4, 4.7, 4.2.

[(15-crown-5)⊃Ca^{II}-(μ-OH)-Mn^{III}MST]OTf. A solution of NMe₄[MnMST] (240 mg, 0.293 mmol) and Ca(OTf)₂/15-crown-5 (164 mg, 0.294 mmol) in 10 mL DCM was treated with iodosylbenzene (77 mg, 0.41 mmol). The reaction mixture was stirred overnight and filtered to remove an insoluble brown material. The solvent was removed under vacuum and the blue-green solid redissolved in DCM. An initial recrystallization from diffusion of pentane gave the desired blue-green crystals as well as colorless crystals on the upper walls of the flask. The colorless crystals were scraped from the sides of the vial and suspended in solution. Most of these crystals were removed by decanting of the solvent. The product was recrystallized two more times using this method, after which the blue-green crystals were collected on a glass frit and washed with Et₂O and pentane. Drying of the crystals under vacuum gave 0.17 g (50%) of the desired product. FTIR (KBr disc, cm⁻¹, selected bands): 3329 (w), 2935 (m), 1604 (m), 1457 (m), 1277

(s), 1147 (s), 1089 (s), 1030 (s), 954 (m), 837 (m), 638 (s). λ_{max} , nm (DCM, ϵ , $\text{M}^{-1}\text{cm}^{-1}$): 449 (250), 642 (410), 770 (sh, 340).

$\text{NMe}_4[\text{Fe}^{\text{II}}\text{NST}]$. A solution of H_3NST (400 mg, 0.56 mmol) in 10 mL anhydrous DMA at room temperature was treated with three equivalents of solid NaH (40 mg, 1.7 mmol). After the evolution of H_2 gas had ceased, $\text{Fe}(\text{OAc})_2$ (97 mg, 0.56 mmol), and NMe_4OAc (74 mg, 0.56 mmol) were added. The reaction was stirred for three hours and then filtered through a medium porosity frit to remove nearly three equivalents of NaOAc (131 mg, 1.6 mmol). The filtrate was concentrated under vacuum to 2 mL of DMA, and Et_2O (40 mL) was added to precipitate the complex. The resulting solid was collected on a frit, redissolved in MeCN, and filtered through Celite to remove a small amount of fine insolubles. The complex was precipitated with Et_2O after concentrating the filtrate to 1 mL of MeCN, collected on frit, washed with Et_2O , and dried under vacuum to give 0.40 g (84%) of a light yellow powder. FTIR (KBr disc, cm^{-1} , selected bands): 3049 (w), 2856 (w), 1488 (w), 1256 (m), 1119 (s), 991 (m), 958 (w) 804 (m), 773 (s), 677 (m), 590 (m).

$\text{NMe}_4[\text{Mn}^{\text{II}}\text{NST}]\cdot\text{DMA}$. A solution of H_3NST (0.20 g, 0.28 mmol) in 4 mL anhydrous DMA was treated with three equivalents of solid NaH (20 mg, 0.84 mmol). After the evolution of H_2 gas ceased, $\text{Mn}(\text{OAc})_2$ (48 mg, 0.28 mmol) and NMe_4OAc (37 mg, 0.28 mmol) were added to the light yellow solution. The mixture was stirred overnight and then 4 mL Et_2O was added to precipitate the NaOAc byproduct. After 15 minutes of stirring, the solution was filtered to remove three equivalents of NaOAc (66 mg, 0.80 mmol). The orange filtrate was concentrated under vacuum to ca. 1 mL and treated with 20 mL Et_2O to precipitate the product, which was collected on a glass frit and dried under vacuum to give 0.26 g (95%) of light yellow powder. FTIR (KBr disc,

cm⁻¹, selected bands): 3047 (w), 2851 (w), 1626 (m), 1250 (m), 1150 (m), 1133 (s), 992 (m), 830 (m), 800 (m), 676 (m), 607 (m).

NMe₄[Fe^{II}TST(OH₂)]. A solution of the ligand H₃TST (0.20 g, 0.33 mmol) in 4 mL anhydrous dimethylacetamide (DMA) at room temperature was treated with three equivalents of solid NaH (24 mg, 1.0 mmol), causing H₂ evolution and precipitation of the deprotonated ligand. After the evolution of H₂ gas ceased, Fe(OAc)₂ (57 mg, 0.33 mmol) and NMe₄OAc (44 mg, 0.33 mmol) were added to the heterogeneous mixture, which was then stirred for three hours. One equivalent (6 μL) of H₂O was then added via syringe and the reaction mixture filtered through a medium porosity frit to remove three equivalents of insoluble NaOAc (79 mg, 0.96 mmol). Vapor diffusion of Et₂O into the pale yellow filtrate gave the product as pale blue crystals in 90% yield. Elemental analysis calcd for NMe₄[Fe^{II}TST(OH₂)], C₃₁H₄₇N₅O₇S₃Fe: C, 49.40; H, 6.28; N, 9.29%, found: C, 49.13; H, 6.23; N, 9.14%. FTIR (KBr disc, cm⁻¹, selected bands): 3257 (m), 3037 (w), 2896 (w), 2845 (m), 1599 (w), 1494 (m), 1246 (s), 1129 (s), 973 (s), 815 (s), 663 (s), 597 (m), 555 (s).

NMe₄[Mn^{II}TST]. A solution of the ligand H₃TST (0.40 g, 0.66 mmol) in 10 mL anhydrous dimethylacetamide (DMA) at room temperature was treated with three equivalents of solid NaH (47 mg, 1.7 mmol), causing H₂ evolution and precipitation of the deprotonated ligand. After the evolution of H₂ gas ceased, Mn(OAc)₂ (114 mg, 0.66 mmol) and NMe₄OAc (87 mg, 0.66 mmol) were added to the heterogeneous mixture, which was then stirred overnight. The solution was filtered to remove three equivalents of NaOAc (0.14 g, 1.7 mmol). The light yellow filtrate was concentrated under vacuum to ca. 1 mL and treated with 50 mL Et₂O to precipitate the product, which was collected on

a glass frit and then redissolved in THF. The solution was filtered through Celite to remove a small amount of fine insolubles and then concentrated under vacuum to ca. 3 mL. Et₂O (40 mL) was added to precipitate the complex, which was collected on a frit, washed with Et₂O, and dried under vacuum to give 0.43 g (89%) of white powder. FTIR (KBr disc, cm⁻¹, selected bands): 3035 (w), 2962 (w), 2853 (w), 1577 (w), 1491 (w), 1247 (s), 1193 (s), 976 (m), 816 (m), 662 (m), 555 (m).

Ligand isolation studies

In a typical experiment, a DCM solution of the reaction mixture was brought out of the dry box and the metal ion extracted with 1 M HCl. The organic layer was washed with brine, dried over MgSO₄, and filtered. The DCM solution was then passed through a plug of silica, which was flushed with additional DCM. The ligand was eluted from the silica with 5% MeOH in DCM and the solvent removed under vacuum. To verify that this procedure did not cause any changes to the ligand, control experiments were performed in which the ligand was isolated from [Zn^{II}MST]⁻ and [Fe^{III}-O-MST]⁻; clean H₃MST and **1** were isolated in these experiments.

Physical Methods.

Electronic absorption spectra were recorded in a 1.0 or 0.1 cm quartz cuvette on a Cary 50 spectrophotometer or an 8453 Agilent UV-vis spectrometer equipped with a Unisoku Unispeks cryostat. Negative mode electrospray ionization electrospray mass spectra were collected using a Micromass MS Technologies LCT Premier Mass Spectrometer. X-band (9.28 GHz) EPR spectra were collected as frozen solutions using a Bruker EMX spectrometer equipped with an ER041XG microwave bridge. IR spectra

were recorded on a Varian 800 Scimitar Series FTIR spectrometer as KBr disks or as a solution using a Beckman liquid IR cell.

X-Ray Crystallographic Methods

A Bruker SMART APEX II diffractometer was used to collect all the data. The APEX²³ program package was used to determine the unit-cell parameters and for data collections. The raw frame data was processed using SAINT²⁴ and SADABS²⁵ to yield the reflection data file. Subsequent calculations were carried out using the SHELXTL²⁶ program. The structures were solved by direct methods and refined on F² by full-matrix least-squares techniques. The analytical scattering factors²⁷ for neutral atoms were used throughout the analysis. Hydrogen atoms were included using a riding model. The data set of NMe₄[Fe^{III}-O-MST] contained several high residuals in the final difference-Fourier map. It was not possible to determine the nature of the residuals although it is probable that a pentane or DCM solvent molecule was present. The SQUEEZE routine in the PLATON²⁸ program package was used to account for the electrons in the solvent accessible voids.

In NMe₄[Fe^{II}MST(OH₂)], Hydrogen atoms H(1) and H(2) were located from a difference-Fourier map and refined (x,y,z and U_{iso}). The remaining hydrogen atoms were included using a riding model. The tetramethylammonium ion was disordered. Carbon atoms C(35)-C(40) were included using multiple components with partial site-occupancy-factors.

References

- (1) Constable, E. C.; Housecroft, C. E. *Chem. Soc. Rev.* **2013**, *42*, 1429–1439.
- (2) Bartlett, R. A.; Power, P. P. *J. Am. Chem. Soc.* **1987**, *109*, 7563–7564.
- (3) Lange, S. J.; Miyake, H.; Que, L. *J. Am. Chem. Soc.* **1999**, *121*, 6330–6331.
- (4) Jensen, M. P.; Lange, S. J.; Mehn, M. P.; Que, E. L.; Que, L. *J. Am. Chem. Soc.*

- 2003**, *125*, 2113–2128.
- (5) Harman, W. H.; Chang, C. J. *J. Am. Chem. Soc.* **2007**, *129*, 15128–15129.
 - (6) Bigi, J. P.; Harman, W. H.; Lassalle-Kaiser, B.; Robles, D. M.; Stich, T. A.; Yano, J.; Britt, R. D.; Chang, C. J. *J. Am. Chem. Soc.* **2012**, *134*, 1536–1542.
 - (7) England, J.; Guo, Y.; Farquhar, E. R.; Young, V. G., Jr; Münck, E.; Que, L., Jr. *J. Am. Chem. Soc.* **2010**, *132*, 8635–8644.
 - (8) Sahu, S.; Quesne, M. G.; Davies, C. G.; Dürr, M.; Ivanović-Burmazović, I.; Siegler, M. A.; Jameson, G. N. L.; de Visser, S. P.; Goldberg, D. P. *J. Am. Chem. Soc.* **2014**, *136*, 13542–13545.
 - (9) Jensen, M. P.; Mehn, M. P.; Que, L., Jr. *Angew. Chem. Int. Ed.* **2003**, *42*, 4357–4360.
 - (10) King, E. R.; Betley, T. A. *Inorg. Chem.* **2009**, *48*, 2361–2363.
 - (11) Park, Y. J.; Ziller, J. W.; Borovik, A. S. *J. Am. Chem. Soc.* **2011**, *133*, 9258–9261.
 - (12) Park, Y. J.; Cook, S. A.; Sickerman, N. S.; Sano, Y.; Ziller, J. W.; Borovik, A. S. *Chem. Sci.* **2013**, *4*, 717–726.
 - (13) Addison, A. W.; Rao, T. N.; Reedijk, J.; van Rijn, J.; Verschoor, G. C. *J. Chem. Soc., Dalton Trans.* **1984**, 1349–1356.
 - (14) Reed, D. R.; Kass, S. R. *J. Mass Spectrom.* **2000**, *35*, 534–539.
 - (15) Rayne, S.; Forest, K. *Nature Proceedings* **2010**.
 - (16) Sahu, S.; Widger, L. R.; Quesne, M. G.; de Visser, S. P.; Matsumura, H.; Moëne-Loccoz, P.; Siegler, M. A.; Goldberg, D. P. *J. Am. Chem. Soc.* **2013**, *135*, 10590–10593.
 - (17) Cho, K.-B.; Wu, X.; Lee, Y.-M.; Kwon, Y. H.; Shaik, S.; Nam, W. *J. Am. Chem. Soc.* **2012**, *134*, 20222–20225.
 - (18) Togo, H.; Katohgi, M.; Yokoyama, M. *Synlett* **1998**, *1998*, 131–132.
 - (19) Xu, L.; Shu, H.; Liu, Y.; Zhang, S.; Trudell, M. L. *Tetrahedron* **2006**, *62*, 7902–7910.
 - (20) Wu, Y.-D.; Wong, C.-L.; Chan, K. W. K.; Ji, G. Z.; Jiang, X.-K. *J. Org. Chem.* **1996**, *61*, 746–750.
 - (21) Dauban, P.; Sanière, L.; Tarrade, A.; Dodd, R. H. *J. Am. Chem. Soc.* **2001**, *123*, 7707–7708.
 - (22) Motekaitis, R. J.; Martell, A. E.; Murase, I. *Inorg. Chem.* **1986**, *25*, 938–944.
 - (23) APEX2 Version 2011.4-1, Bruker AXS, Inc.; Madison, WI 2011.
 - (24) SAINT Version 7.68a, Bruker AXS, Inc.; Madison, WI 2009.
 - (25) Sheldrick, G. M. SADABS, Version 2012/1, Bruker AXS, Inc.; Madison, WI 2012.
 - (26) Sheldrick, G. M. SHELXTL, Version 2014/2, Bruker AXS, Inc.; Madison, WI 2014.
 - (27) International Tables for X-Ray Crystallography 1992, Vol. C., Dordrecht: Kluwer Academic Publishers.
 - (28) Spek, A. L. PLATON, Acta. Cryst. 2009, D65, 148-155.

CHAPTER 4

Evidence for Formation of an Fe(IV)–oxo Intermediate in a Tripodal Sulfonamido Fe Complex

Introduction

High-valent iron species are often reactive intermediates and are understood to be involved in the C–H bond functionalization of a variety of substrates. For example, non-heme iron-containing monooxygenases utilize a mononuclear iron(IV)–oxo unit as the active species to perform a diverse set of reactions, including hydroxylation, halogenation, desaturation, and epoxidation.^{1–6} These diverse and important reactions have made non-heme high-valent iron complexes a target for synthetic chemists, both for understanding the functional aspects of active sites in enzymes and for developing new synthetic oxidants for chemical transformations such as C–H activation.

Within the last 13 years, over 50 unique synthetic Fe(IV)–oxo complexes have been reported in the literature.^{2,7–12} While the study of these complexes has led to a greater understanding of the electronic and structural properties of M–oxo units in synthetic complexes and in biology, their reactivities with C–H bonds have generally been limited.^{13–24} One common explanation for this limited relative reactivity is that most synthetic Fe(IV)–oxo complexes are low spin while biological non-heme Fe(IV)–oxo units are high spin.²⁵ In support of this hypothesis, Que compared the reactivities of his numerous synthetic complexes and found that those with S=2 spin states were overall more reactive than those with S=1 spin states.²⁴ Despite this correlation, there is still significant uncertainty as to whether unpaired spin is important at all in determining reactivity, as several closed-shell systems such as permanganate ion (MnO_4^-) are capable of reacting with C–H bonds.²⁶ Further complicating the understanding of spin state's

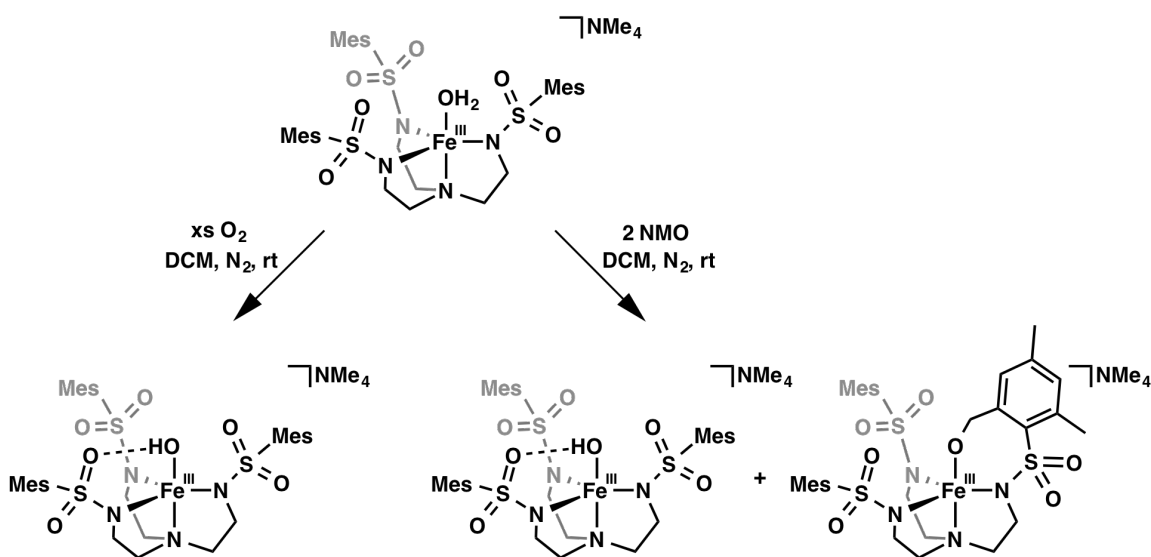
contribution to reactivity is the limited availability of synthetic high spin Fe(IV)–oxo complexes, with only five well-characterized examples reported.^{16,24,27-29} Continued exploration of synthetic Fe(IV)–oxo complexes with $S = 2$ spin states is therefore needed to better understand the fundamental origins of C–H activation reactivity. Utilization of ligand frameworks that establish trigonal bipyramidal geometry around the Fe center—such as the tripodal sulfonamido ligands described throughout this dissertation—provide a means of enforcing the desired high spin electronic configuration; of the five previously characterized high spin Fe(IV)–oxo complexes, four are supported by tripodal ligand frameworks.^{16,24,28,29}

Numerous routes to synthetic Fe(IV)–oxo complexes have been reported, but a common preparative method includes reaction of an oxygen-atom (O-atom) transfer reagent with an Fe(II) starting complex. For example, the first structurally characterized Fe(IV)–oxo complex, $[\text{Fe}^{\text{IV}}(\text{O})(\text{TMC})(\text{NCCH}_3)]^{2+}$ (TMC = 1,4,8,11-tetramethyl-1,4,8,11-tetraaza-cyclotetradecane) was generated from oxidation of $[\text{Fe}^{\text{II}}(\text{TMC})(\text{OTf})_2]$ with iodobenzene (PhIO) in CH_3CN at $-40\text{ }^\circ\text{C}$.³⁰ Similarly, the first high spin Fe(IV)–oxo complex, $[\text{Fe}^{\text{IV}}(\text{O})(\text{TMG}_3\text{tren})]^{2+}$, was prepared via reaction of the Fe(II) precursor with a substituted PhIO derivative.¹⁶ Although O-atom transfer reagents often provide a straightforward method for generating Fe(IV)–oxo intermediates, weak points in the ligand that are susceptible to oxidation can prevent the observation of an Fe(IV) species. An example of this was discussed in Chapter 3 for the reactions between our $\text{NMe}_4[\text{Fe}^{\text{II}}\text{MST}]$ and $\text{NMe}_4[\text{Fe}^{\text{II}}\text{NST}]$ salts and O-atom transfer reagents, which resulted in hydroxylation of the ligand. This undesirable intramolecular reactivity was eliminated in the tolyl ligand derivative, $[\text{TST}]^{3-}$, which allowed us to further explore the oxidation

of its Fe(II) complex. Particular interest was given to probing the intermediate that could not be observed in the complexes of $[\text{MST}]^{3-}$ and $[\text{NST}]^{3-}$ but whose high reactivity was apparent in the observed oxidized ligand products. Described here is preliminary evidence for the formation of an Fe(IV)–oxo intermediate from oxidation of the Fe(II) complex with an O-atom transfer reagent as well as the reactivity of this intermediate with C–H bonds.

Results and Discussion

Unlike $[\text{Fe}^{\text{II}}\text{MST}]^-$, the four-coordinate $[\text{Fe}^{\text{II}}\text{TST}]^-$ complex could not be cleanly isolated due to partial coordination of adventitious water to form the aquo complex, $[\text{Fe}^{\text{II}}\text{TST}(\text{OH}_2)]^-$, that could not be separated from $[\text{Fe}^{\text{II}}\text{TST}]^-$ during purification. Therefore, $[\text{Fe}^{\text{II}}\text{TST}(\text{OH}_2)]^-$ was purposely prepared via addition of an equivalent of water and used as the starting complex for all oxidation reactions. In order to verify that the presence of an aquo ligand would not influence the reactivity of the Fe center, the analogous $[\text{Fe}^{\text{II}}\text{MST}(\text{OH}_2)]^-$ complex was also prepared and its oxidation with O_2 and 4-



Scheme 4.1. Reactivity of $\text{NMe}_4[\text{Fe}^{\text{II}}\text{MST}(\text{OH}_2)]^-$ with O_2 and NMO.

methylmorpholine-*N*-oxide (NMO) were compared to the reactivity of the $[\text{Fe}^{\text{II}}\text{MST}]^-$ complex that was described in the previous chapter (Scheme 4.1). For both complexes, the same $[\text{Fe}^{\text{III}}\text{MST}(\text{OH})]^-$ and $[\text{Fe}^{\text{III}}-\text{O}-\text{MST}]^-$ products were generated from the aquo precursor as from the four-coordinate, empty cavity complex. In addition, a similar distribution of ligand oxidation products was observed from reaction with excess NMO. These results suggest that the presence of an aquo ligand does not significantly influence the oxidative reactivity of the Fe center, and so all experiments described in this chapter were carried out using the $[\text{Fe}^{\text{II}}\text{TST}(\text{OH}_2)]^-$ complex.

Reactivity of the $[\text{Fe}^{\text{II}}\text{TST}(\text{OH}_2)]^-$ Complex. Oxidation of the $[\text{Fe}^{\text{II}}\text{TST}(\text{OH}_2)]^-$ complex with O_2 or NMO in dichloromethane (DCM) resulted in the isolation of identical products that were assigned to the Fe(III)–hydroxide product, $[\text{Fe}^{\text{III}}\text{TST}(\text{OH})]^-$. The identity of this product was confirmed by X-ray diffraction (XRD) of a single crystal that was grown from the NMO reaction. The $[\text{Fe}^{\text{III}}\text{TST}(\text{OH})]^-$ ion consists of a five-coordinate Fe(III) center in trigonal bipyramidal geometry ($\tau = 0.82$)³¹ that is established by the four nitrogen donors of $[\text{TST}]^{3-}$ and a terminal hydroxo ligand (Figure 4.1, Table

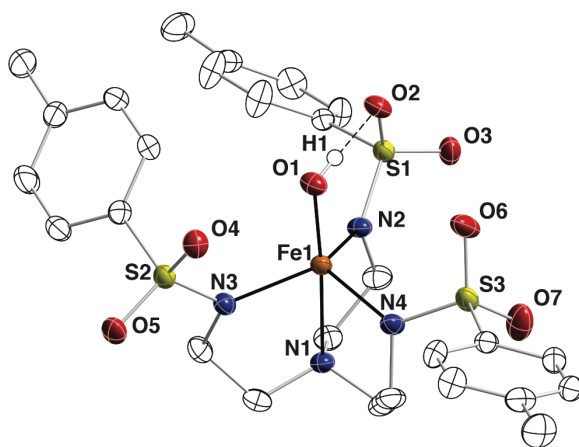


Figure 4.1. Thermal ellipsoid diagram depicting $[\text{Fe}^{\text{III}}\text{TST}(\text{OH})]^-$. Ellipsoids are drawn at the 50% probability level, and only the hydroxo hydrogen atom is shown. The NMe_4^+ counter ion is omitted for clarity.

A.4). The average Fe–N_{eq} distance of 2.035(2) Å and the Fe–N1 distance of 2.329(2) Å are similar to the distances in [Fe^{III}–O–MST][–] (2.021 and 2.358 Å, Figure 3.6), which is the only other structurally characterized Fe(III) complex of a tripodal sulfonamido ligand. The Fe–O1 distance in [Fe^{III}TST(OH)][–] is slightly longer at 1.831(1) Å compared to 1.803 Å in [Fe^{III}–O–MST][–], and the oxygen atom of the hydroxo ligand is also tilted out of the Fe–N1 vector with an O1–Fe–N1 angle of 173.56(6) (Table 4.1). One sulfonamido oxygen atom on each of the three ligand arms of [Fe^{III}TST(OH)][–] points nearly parallel to the Fe1–O1 vector, forming a negatively-polarized fence around the hydroxo ligand. A short distance (2.743 Å) between the oxygen atom of the hydroxo ligand and one of these sulfonamide oxygen atoms (O2) is suggestive of an intramolecular hydrogen bonding interaction between these two groups.

Table 4.1. Select metrical parameters for [Fe^{III}TST(OH)][–].

Bond Distances (Å)	
Fe1—O1	1.831(1)
Fe1—N1	2.329(2)
Fe1—N2	2.053(2)
Fe1—N3	2.031(2)
Fe1—N4	2.022(2)
O1···O2	2.743
Bond Angles (°)	
O1—Fe1—N1	173.56(6)
N2—Fe1—N3	124.46(7)
N2—Fe1—N4	110.42(6)
N3—Fe1—N4	111.26(6)
τ value	0.82

The NMe₄[Fe^{III}TST(OH)] product exhibited a number of similarities to the analogous complex with the [MST]^{3–} ligand that was described in the previous chapter; characterization by electrospray ionization mass spectrometry (ESI-MS) revealed a negative ion peak with a mass-to-charge ratio (*m/z*) of 687 that corresponds to the formulation [FeTST(OH)][–], and the electron paramagnetic resonance (EPR) spectrum

exhibited a signal at $g = 9.7$ and 4.3 that is consistent with a high spin Fe(III) center (Figures 4.2A and B). The Fourier transform infrared (FTIR) spectrum of $[\text{Fe}^{\text{III}}\text{TST}(\text{OH})]^-$ contained a well defined band at 3450 cm^{-1} that is nearly identical to that of $[\text{Fe}^{\text{III}}\text{MST}(\text{OH})]^-$ (3463 cm^{-1} , Figure 4.2C). Furthermore, like $\text{NMe}_4[\text{Fe}^{\text{III}}\text{MST}(\text{OH})]$, the $\text{NMe}_4[\text{Fe}^{\text{III}}\text{TST}(\text{OH})]$ product is unstable in DCM solution, and the $\nu(\text{OH})$ band decreased over time with the concomitant increase of a new band at 3279 cm^{-1} that belongs to the Fe(II)–aquo complex, $[\text{Fe}^{\text{II}}\text{TST}(\text{OH}_2)]^-$. However, the rate of this conversion was significantly slower in the $[\text{TST}]^{3-}$ complex than the $[\text{MST}]^{3-}$ analog, with incomplete conversion observed even after 14 days, while full conversion of the $[\text{MST}]^{3-}$ complex was accomplished within 7 days. The cause for this difference in stability between the Fe(III)–hydroxide complexes of $[\text{TST}]^{3-}$ and $[\text{MST}]^{3-}$ is still under investigation, but this increased stability is likely the reason that $\text{NMe}_4[\text{Fe}^{\text{III}}\text{TST}(\text{OH})]$ could be crystallized in high yield (60%) while crystallization attempts of $\text{NMe}_4[\text{Fe}^{\text{III}}\text{MST}(\text{OH})]$ gave only the aquo salt, $\text{NMe}_4[\text{Fe}^{\text{II}}\text{MST}(\text{OH}_2)]$.

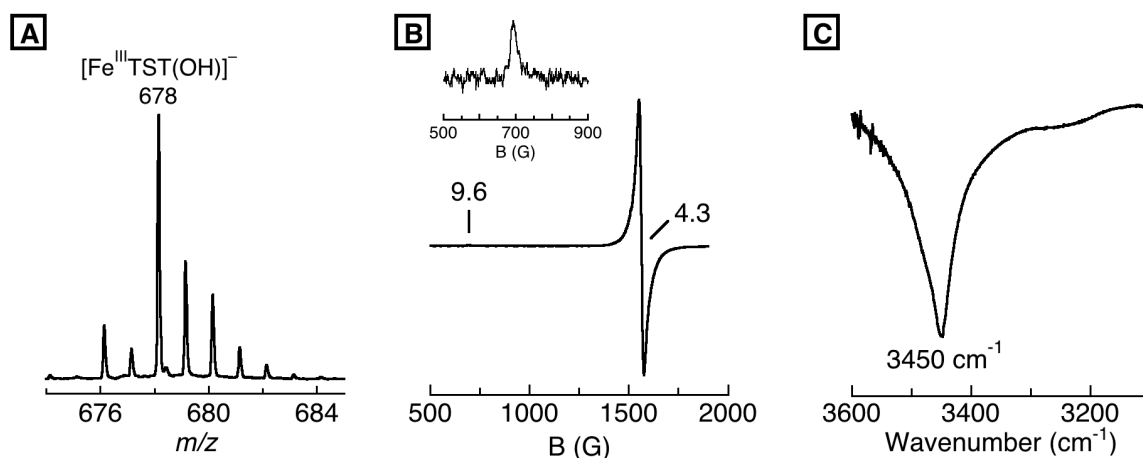


Figure 4.2. Spectra collected of isolated $\text{NMe}_4[\text{Fe}^{\text{III}}\text{TST}(\text{OH})]$: A) ESI-MS showing the molecular ion peak assigned to $[\text{Fe}^{\text{III}}\text{TST}(\text{OH})]^-$; B) perpendicular mode EPR spectrum collected at 77 K on a 5 mM 1:1 DCM:THF solution, inset showing an expansion of the $g = 9.6$ signal; C) IR spectrum of the crystalline solid as a KBr disk.

Despite the isolation of identical products from the reactions of $[\text{Fe}^{\text{II}}\text{TST}(\text{OH}_2)]^-$ with NMO and O_2 , these two reactions produced visibly different color changes; while the O_2 reaction gave a slow change from colorless to the increasingly intense orange color of the $[\text{Fe}^{\text{III}}\text{TST}(\text{OH})]^-$ product, addition of NMO resulted in the immediate formation of a red species that faded to orange over the course of several minutes. When this reaction was monitored optically, an intermediate with peaks at 380 and 895 nm appeared and then converted to a new species containing a single optical feature at 352 nm that matched the isolated $[\text{Fe}^{\text{III}}\text{TST}(\text{OH})]^-$ product (Figure 4.3). Although the mechanism for the oxidation of $[\text{Fe}^{\text{II}}\text{TST}(\text{OH}_2)]^-$ with NMO is unknown, the observation of a low intensity absorbance band at $\lambda_{\text{max}} = 895 \text{ nm}$ ($\epsilon_{\text{M}} = 100$) indicates that the reaction may have involved an Fe(IV)–oxo intermediate. There is a growing body of data to suggest that synthetic non-heme Fe(IV)–oxo complexes have optical features between 800-900 nm that arise from d-d transitions, and these features appear to be independent of

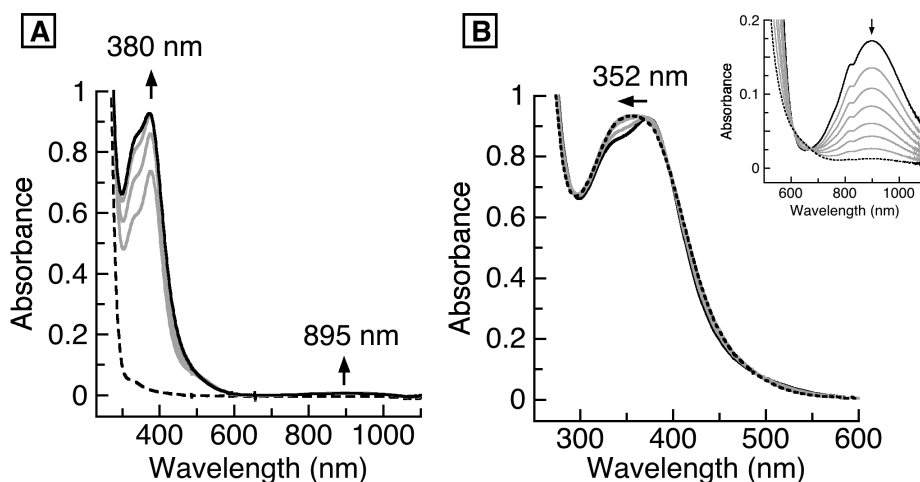


Figure 4.3. Electronic absorption spectra for the oxidation of a 0.2 mM DCM solution of $\text{NMe}_4[\text{Fe}^{\text{II}}\text{TST}(\text{H}_2\text{O})]$ with NMO at 25°C showing (A) conversion of the Fe(II) complex (dashed black) to the intermediate species (solid black) and (B) further reaction of the intermediate to the final $\text{NMe}_4[\text{Fe}^{\text{III}}\text{TST}(\text{OH})]$ product (dotted black). The inset of (B) shows the decay of the low energy band in a 5 mM DCM solution.

spin state and molecular structure.^{2,9,11} For example, we have previously characterized the related trigonal bipyramidal Fe(IV)–oxo complex $[\text{Fe}^{\text{IV}}\text{H}_3\text{buea}(\text{O})]^-$ ($[\text{H}_3\text{buea}$, tris[*N*-*tert*-butylureaylato)-*N*-ethylene]aminato), which exhibits a band at 808 nm ($\epsilon_{\text{M}} = 280$).²⁸ Similarly, the $[\text{Fe}^{\text{IV}}(\text{O})(\text{TMC})(\text{NCCH}_3)]^{2+}$ complex exhibits a band at 820 nm ($\epsilon_{\text{M}} = 400$) in the optical spectrum despite having a different coordination geometry (tetragonal) and spin state ($S = 1$).³² Reactivity of this putative Fe(IV)–oxo intermediate with a C–H bond in the solvent could possibly be the source of the isolated $[\text{Fe}^{\text{III}}\text{TST}(\text{OH})]^-$ product.

When $\text{Ca}(\text{OTf})_2/15\text{-crown-5}$ was introduced into the reaction between $[\text{Fe}^{\text{II}}\text{TST}(\text{OH}_2)]^-$ and NMO, no intermediate species containing the diagnostic low energy band of an Fe(IV)–oxo species was observed by UV-vis spectroscopy (Figure 4.4A). Instead, the complex converted directly to a single species that was determined to be the heterobimetallic Fe(III)–hydroxide product, $[15\text{-crown-5} \supset \text{Ca}^{\text{II}}-(\mu\text{-OH})\text{-Fe}^{\text{III}}\text{TST}]\text{OTf}$, via XRD methods (Figure A.12, Tables A.4 and A.5). Furthermore, when $\text{Ca}(\text{OTf})_2/15\text{-crown-5}$ was added to the proposed Fe(IV)–oxo intermediate that was stabilized at low temperature, the spectrum immediately converted to one that matches the heterobimetallic Fe(III)–hydroxide product (Figure 4.4B). This result is important because in the last 5-6 years, there have been a number of reports in the literature of redox-inactive metal ions binding to the oxido³³⁻³⁶ or nitrido³⁷ ligand of high valent transition metal complexes. For example, Nam reported the coordination of a Sc^{3+} ion to the oxido unit of $[\text{Fe}^{\text{IV}}(\text{O})(\text{TMC})(\text{NCMe})]^{2+}$ to form a neutral $[(\text{TMC})(\text{Fe}^{\text{IV}}\text{-O-Sc}^{\text{III}})(\text{OTf})_4(\text{OH})]$ complex.³³ However, in the last two years, this formulation has been called into question by two independent researchers, both of whom cited the metrical parameters of the molecular structure that was used to assign the

complex as a source of concern. Swart first used DFT calculations to argue that the bond lengths of the proposed $\text{Fe}^{\text{IV}}\text{-O-Sc}^{\text{III}}$ adduct actually fit better to $[(\text{TMC})\text{Fe}^{\text{III}}\text{-O-Sc}^{\text{III}}(\text{OTf})_4(\text{OH}_2)]$,³⁸ and Que synthetically reproduced the adduct and performed further spectroscopic analysis that also pointed to an Fe oxidation state of 3+ instead of 4+.³⁹ Our preliminary results with the formation of an Fe(III) species upon addition of Ca^{2+} ions to the proposed $[\text{Fe}^{\text{IV}}\text{TST}(\text{O})]^-$ complex provides additional support that coordination of a Lewis acid to a high valent M-oxo unit effects an oxidation state change.

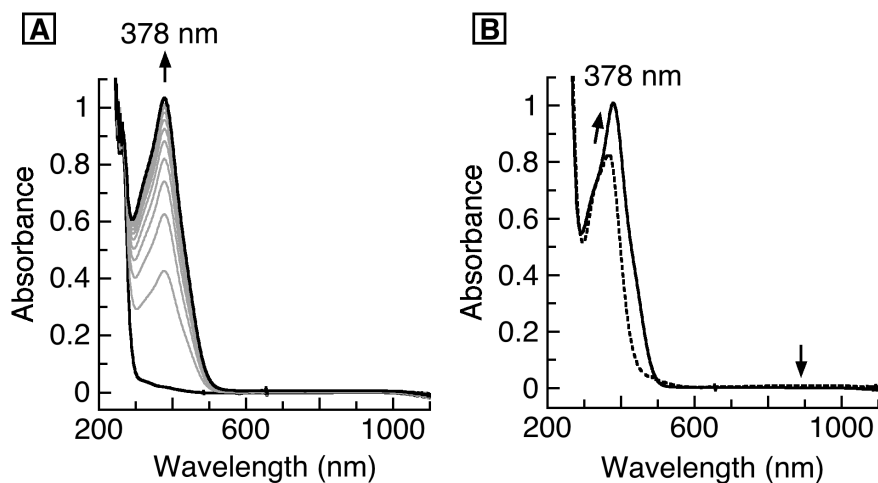


Figure 4.4. Electronic absorption spectra of 0.2 mM MeCN solutions for (A) oxidation of $[\text{Fe}^{\text{II}}\text{TST}(\text{OH}_2)]^-$ with NMO in the presence of $\text{Ca}(\text{OTf})_2/15\text{-crown-5}$ at 20 °C showing the direct conversion to a single species that was assigned to $[15\text{-crown-5}\supset\text{Ca}^{\text{II}}\text{-(}\mu\text{-OH)-Fe}^{\text{III}}\text{TST}]\text{OTf}$ and (B) addition of $\text{Ca}(\text{OTf})_2/15\text{-crown-5}$ to the proposed $[\text{Fe}^{\text{IV}}\text{TST}(\text{O})]^-$ intermediate stabilized at -40 °C (dotted black) showing immediate conversion to $[15\text{-crown-5}\supset\text{Ca}^{\text{II}}\text{-(}\mu\text{-OH)-Fe}^{\text{III}}\text{TST}]\text{OTf}$.

Reactivity of Fe(IV)-oxo Intermediate with External Substrates. The observation of a putative Fe(IV)-oxo species that did not react with the ancillary tripodal ligand suggested that we might be able to intercept this reactive intermediate to activate an X-H bond of an external substrate. Indeed, addition of half an equivalent of diphenylhydrazine (DPH) to the stabilized Fe(IV)-oxo intermediate at low temperature resulted in the rapid

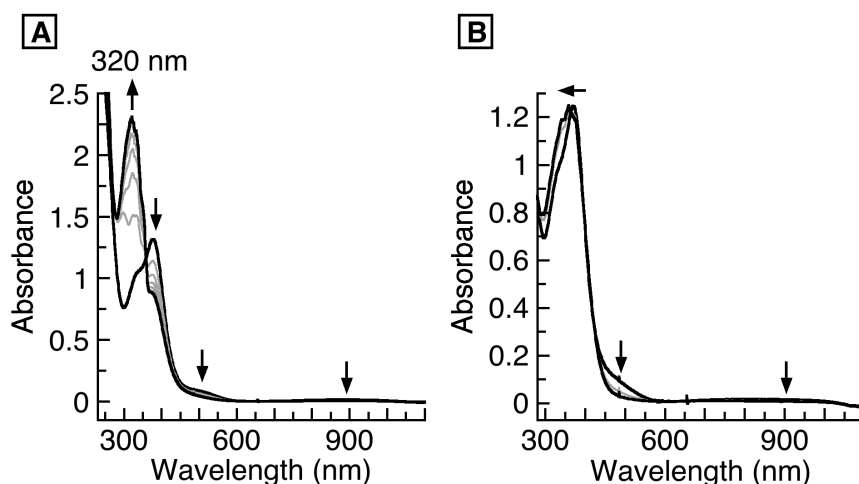
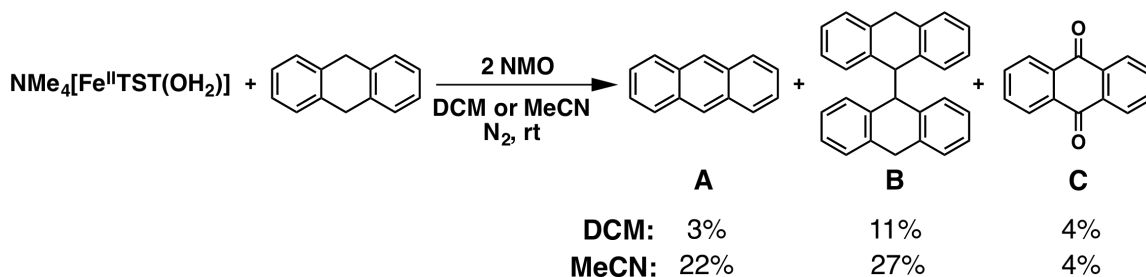


Figure 4.5. Electronic absorption spectra for the reaction of 0.2 mM $[\text{Fe}^{\text{IV}}\text{TST}(\text{O})]^-$ intermediate stabilized at $-40\text{ }^\circ\text{C}$ with (A) 0.5 DPH in THF and (B) 20 DHA in MeCN.

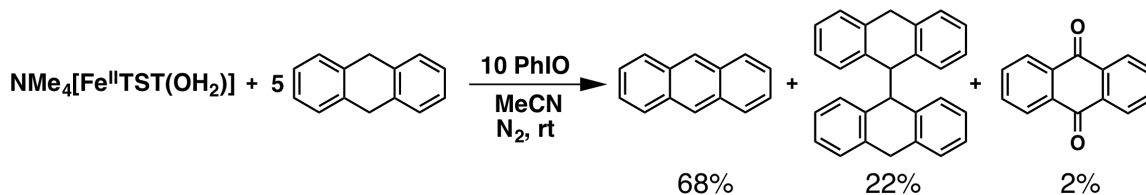
loss of the 895 nm band and concomitant growth of the high energy band of azobenzene at 320 nm (Figure 4.5A).⁴⁰ Similarly, addition of excess dihydroanthracene (DHA) resulted in the appearance of the sharp, high energy features of anthracene⁴¹ and loss of the 895 nm band (Figure 4.5B). Furthermore, when the reaction of $[\text{Fe}^{\text{II}}\text{TST}(\text{OH}_2)]^-$ with NMO was carried out in the presence of 1 equivalent of DHA on a larger scale, 20% conversion of DHA to the oxidized products anthracene (A), 9,9',10,10'-tetrahydro-9,9'-bianthracene (B), and anthraquinone (C, Scheme 4.2 and Figure A.13) was observed. For comparison, no conversion of DHA was observed for the identical reactions with



Scheme 4.2. Oxidation products of dihydroanthracene: (A) anthracene, (B) 9,9',10,10'-tetrahydro-9,9'-bianthracene, and (C) anthraquinone and percent conversion obtained from reaction in DCM and MeCN.

$\text{NMe}_4[\text{Fe}^{\text{II}}\text{MST}]$ or $\text{NMe}_4[\text{Fe}^{\text{II}}\text{MST}(\text{OH}_2)]$, and the isolated product, $\text{NMe}_4[\text{Fe}^{\text{III}}\text{TST}(\text{OH})]$, showed no reactivity with DHA. When the reaction of the $[\text{Fe}^{\text{II}}\text{TST}(\text{OH}_2)]^-$ complex with NMO was conducted in MeCN instead of DCM, 50% of the DHA was converted to oxidized products, and the $\text{NMe}_4[\text{Fe}^{\text{III}}\text{TST}(\text{OH})]$ product was crystallized from the reaction in 90% yield. Based on the proposed mechanism of H-atom abstraction by the Fe(IV)-oxo intermediate from either substrate or solvent molecules, this increase in DHA conversion is thought to result from the stronger C-H bonds of MeCN relative to DCM ($\text{BDE}_{\text{C-H}} = 96$ and 92 kcal mol^{-1} , respectively)⁴², which allows the reactivity with the substrate to be more favored.

The conversion of DHA was further improved by using PhIO as the oxidant instead of NMO. In fact, this switch in oxidant led to catalytic conversion, with 90% yield of oxidized products obtained from 10% catalyst loading and stoichiometric oxidant (relative to H-atoms, Scheme 4.3). This significant improvement in yield was initially proposed to be a consequence of the low solubility of PhIO in DCM and MeCN, which serves to introduce the oxidant into the reaction slowly. Because the $[\text{Fe}^{\text{III}}\text{TST}(\text{OH})]^-$ product is known to convert back to the $[\text{Fe}^{\text{II}}\text{TST}(\text{OH}_2)]^-$ starting complex over time, it was thought that the slow introduction of oxidant allowed this Fe(II) complex to be produced and then react again with PhIO. To test this hypothesis, NMO was added to a 5:1 mixture of DHA and $\text{NMe}_4[\text{Fe}^{\text{II}}\text{MST}(\text{OH}_2)]$ in MeCN over the course of five hours



Scheme 4.3. Reaction conditions that give catalytic conversion of DHA.

via syringe pump, and the conversion of DHA was compared to the analogous reaction in which NMO was added in one portion. No enhancement in conversion was observed from the slow addition of NMO, which suggests that another factor is responsible for the catalytic reactivity. However, no further studies were conducted to understand this difference in reactivity between PhIO and NMO.

Summary and Conclusions

In summary, rational modification of the mesityl-containing sulfonamido tripodal ligand, $[\text{MST}]^{3-}$, to incorporate tolyl groups successfully prevented undesirable intramolecular reactivity and allowed for further examination of the oxidative reactivity of the corresponding Fe complex. The Fe(II)–aquo complex of this tolyl ligand, $[\text{Fe}^{\text{II}}\text{TST}(\text{OH}_2)]^-$, reacted with O_2 and NMO to generate identical Fe(III)–hydroxide products, $[\text{Fe}^{\text{III}}\text{TST}(\text{OH})]^-$, that could be crystallographically characterized due to its improved stability over the analogous complex of the $[\text{MST}]^{3-}$ ligand, $[\text{Fe}^{\text{III}}\text{MST}(\text{OH})]^-$. Despite the isolation of identical products from O_2 and NMO, these two reactions appeared to proceed through different mechanisms, with NMO producing a red intermediate whose low energy band is characteristic of an Fe(IV)–oxo species. Importantly, this intermediate was not observed in the same reaction with the Fe(II) complex of $[\text{MST}]^{3-}$, which converted directly to a single spectrum; the ability to observe the low energy band of the proposed Fe(IV)–oxo therefore depended on the removal of the ortho methyl groups in the tolyl derivative.

The proposed Fe(IV)–oxo intermediate that was produced from NMO could be stabilized at low temperature so that its further reactivity could be studied. Addition of Ca^{II} ions to this stabilized intermediate resulted in immediate generation of a bimetallic

Fe(III)–hydroxide product, which supports recent claims in the literature that the binding of a Lewis acid to the oxido ligand of a high valent metal center effects an oxidation state change. The Fe(IV)–oxo intermediate also reacted with the X–H bonds of DPH and DHA by UV-vis spectroscopy, and isolation of the DHA products of the large scale reaction revealed conversion to a mixture of three oxidized products. The extent of conversion was improved with the choice of solvent, and the reaction became catalytic when PhIO was used as the oxidant instead of NMO. Although the cause of the improved conversion by PhIO is not understood, the catalytic conversion observed for DHA highlights how rational molecular design can lead to functional small molecules.

Experimental Section

General Methods

Syntheses of metal complexes were completed under an argon or nitrogen atmosphere in a VAC drybox. Solvents were sparged with argon and dried over columns containing Q-5 and molecular sieves. All reagents were purchased from commercial suppliers and used as received unless otherwise noted. Sodium hydride as a 30% suspension in mineral oil was filtered and washed five times each with Et₂O and pentane and dried under vacuum. PhIO⁴³ and H₃TST⁴⁴ were prepared according to literature procedures.

Complex Syntheses

NMe₄[Fe^{II}TST(OH₂)]. A solution of the ligand H₃TST (0.20 g, 0.33 mmol) in 4 mL anhydrous dimethylacetamide (DMA) at room temperature was treated with three equivalents of solid NaH (24 mg, 1.0 mmol), causing H₂ evolution and precipitation of the deprotonated ligand. After the evolution of H₂ gas ceased, Fe(OAc)₂ (57 mg, 0.33

mmol) and NMe₄OAc (44 mg, 0.33 mmol) were added to the heterogeneous mixture, which was then stirred for three hours. One equivalent (6 μL) of H₂O was then added via syringe and the reaction mixture filtered through a medium porosity frit to remove three equivalents of insoluble NaOAc (79 mg, 0.96 mmol). Vapor diffusion of Et₂O into the pale yellow filtrate gave the product as pale blue crystals in 90% yield. Elemental analysis calcd for NMe₄[Fe^{II}TST(OH₂)], C₃₁H₄₇N₅O₇S₃Fe: C, 49.40; H, 6.28; N, 9.29%, found: C, 49.13; H, 6.23; N, 9.14%. FTIR (KBr disc, cm⁻¹, selected bands): 3257 (m), 3037 (w), 2896 (w), 2845 (m), 1599 (w), 1494 (m), 1246 (s), 1129 (s), 973 (s), 815 (s), 663 (s), 597 (m), 555 (s).

NMe₄[Fe^{III}TST(OH)]. A solution of NMe₄[Fe^{II}TST(H₂O)] (0.10 mg, 0.13 mmol) in 6 mL of DCM at room temperature was treated with a solution of NMO (15 mg, 0.13 mmol) in 2 mL of DCM, causing an immediate color change to red. The reaction was stirred for four hours, during which time the color faded to orange. After filtering through Celite, the product was recrystallized twice by layering the DCM solution under Et₂O to give 60 mg (60%), of yellow-orange crystals. Elemental analysis calcd for NMe₄[Fe^{III}TST(OH)], C₃₁H₄₆N₅O₇S₃Fe: C, 49.46; H, 6.16; N, 9.30%, found: C, 49.55; H, 6.00; N, 8.98%. FTIR (KBr disc, cm⁻¹, selected bands): 3450 (m), 3036 (w), 2962 (w), 2859 (m), 1599 (w), 1490 (m), 1270 (s), 1138 (s), 1091 (s), 962 (s), 816 (s), 666 (s), 553 (s). λ_{max}, nm (DCM, ε, M⁻¹cm⁻¹): 355 (5500). EPR (1:1 DCM:THF, 77K): g = 9.7, 4.3.

Electronic absorption studies

In a typical experiment, a 0.2 mM stock solution of the metal complex was prepared in the glove box, and 3 mL of the solution was transferred to a quartz cuvette, which was sealed with a rubber septum. The cuvette was brought out of the glovebox and

allowed to equilibrate in the sample holder at 25°C for ten minutes before NMO was added as a 30 mM solution via syringe.

Substrate oxidation studies

In a typical experiment, a solution of NMO was added in one portion to a solution containing the Fe complex and DHA. After 3 hours, the solvent was evaporated to dryness and the resulting yellow residue stirred in Et₂O. The Et₂O was then filtered through Celite, passed through a silica plug, and evaporated to give the DHA products as an off white residue. The residue was redissolved in CDCl₃ and the ratio of products was determined by integration of their signals in the ¹H NMR spectrum. The Fe-containing products were redissolved in DCM and recrystallized by Et₂O layering.

Physical Methods

Electronic absorption spectra were recorded in a 1.0 or 0.1 cm quartz cuvette on a Cary 50 spectrophotometer or an 8453 Agilent UV-Vis spectrometer equipped with an Unisoku Unispeks cryostat. Negative mode electrospray ionization electrospray mass spectra were collected using a Micromass MS Technologies LCT Premier Mass Spectrometer. X-band (9.28 GHz) EPR spectra were collected as frozen solutions using a Bruker EMX spectrometer equipped with an ER041XG microwave bridge. IR spectra were recorded on a Varian 800 Scimitar Series FTIR spectrometer as KBr disks or as a solution using a Beckman liquid IR cell.

X-Ray Crystallographic Methods

A Bruker SMART APEX II diffractometer was used to collect all the data. The APEX2⁴⁵ program package was used to determine the unit-cell parameters and for data collections. The raw frame data was processed using SAINT⁴⁶ and SADABS⁴⁷ to yield

the reflection data file. Subsequent calculations were carried out using the SHELXTL⁴⁸ program. The structures were solved by direct methods and refined on F^2 by full-matrix least-squares techniques. The analytical scattering factors⁴⁹ for neutral atoms were used throughout the analysis. Hydrogen atoms were included using a riding model. Hydrogen atoms H(1) of $\text{NMe}_4[\text{Fe}^{\text{III}}\text{TST}(\text{OH})]$ and H(7) of $[\text{15-crown-5}\supset\text{Ca}^{\text{II}}-(\mu\text{-OH})\text{-Fe}^{\text{III}}\text{TST}]\text{OTf}$ were located from a difference-Fourier map and refined (x, y, z and U_{iso}) with $d(\text{O-H}) = 0.85\text{\AA}$ for the latter.

The data set for $\text{NMe}_4[\text{Fe}^{\text{III}}\text{TST}(\text{OH})]$ contained several high residuals in the final difference-Fourier map. It was not possible to determine the nature of the residuals although it is probable that a pentane solvent molecule was present. The SQUEEZE routine in the PLATON⁵⁰ program package was used to account for the electrons in the solvent accessible voids.

There was one molecule of tetrahydrofuran solvent present in the unit cell of $[\text{15-crown-5}\supset\text{Ca}^{\text{II}}-(\mu\text{-OH})\text{-Fe}^{\text{III}}\text{TST}]\text{OTf}$. Several atoms were disordered and included using multiple components with partial site-occupancy-factors.

References

- (1) Costas, M.; Mehn, M. P.; Jensen, M. P.; Que, L. *Chem. Rev.* **2004**, *104*, 939–986.
- (2) Nam, W. *Acc. Chem. Res.* **2007**, *40*, 522–531.
- (3) Krebs, C.; Galonić Fujimori, D.; Walsh, C. T.; Bollinger, J. M. *Acc. Chem. Res.* **2007**, *40*, 484–492.
- (4) Eser, B. E.; Barr, E. W.; Frantom, P. A.; Saleh, L.; Bollinger, J. M.; Krebs, C.; Fitzpatrick, P. F. *J. Am. Chem. Soc.* **2007**, *129*, 11334–11335.
- (5) Tinberg, C. E.; Lippard, S. J. *Acc. Chem. Res.* **2011**, *44*, 280–288.
- (6) Panay, A. J.; Lee, M.; Krebs, C.; Bollinger, J. M.; Fitzpatrick, P. F. *Biochemistry* **2011**, *50*, 1928–1933.
- (7) Shan, X.; Que, L., Jr. *J. Inorg. Biochem.* **2006**, *100*, 421–433.
- (8) Groves, J. T. *J. Inorg. Biochem.* **2006**, *100*, 434–447.
- (9) Que, L. *Acc. Chem. Res.* **2007**, *40*, 493–500.
- (10) Hohenberger, J.; Ray, K.; Meyer, K. *Nat. Comm.* **2012**, *3*, 720–13.
- (11) McDonald, A. R.; Que, L., Jr. *Coord. Chem. Rev.* **2013**, *257*, 414–428.

- (12) Nam, W.; Lee, Y.-M.; Fukuzumi, S. *Acc. Chem. Res.* **2014**, *47*, 1146–1154.
- (13) Kaizer, J.; Klinker, E. J.; Oh, N. Y.; Rohde, J.-U.; Song, W. J.; Stubna, A.; Kim, J.; Münck, E.; Nam, W.; Que, L. *J. Am. Chem. Soc.* **2004**, *126*, 472–473.
- (14) Martinho, M.; Banse, F.; Bartoli, J.-F.; Mattioli, T. A.; Battioni, P.; Horner, O.; Bourcier, S.; Girerd, J.-J. *Inorg. Chem.* **2005**, *44*, 9592–9596.
- (15) Sastri, C. V.; Lee, J.; Oh, K.; Lee, Y. J.; Lee, J.; Jackson, T. A.; Ray, K.; Hirao, H.; Shin, W.; Halfen, J. A.; Kim, J.; Que, L.; Shaik, S.; Nam, W. *Proc. Nat. Acad. Sci.* **2007**, *104*, 19181–19186.
- (16) England, J.; Martinho, M.; Farquhar, E. R.; Frisch, J. R.; Bominaar, E. L.; Münck, E.; Que, L., Jr. *Angew. Chem. Int. Ed.* **2009**, *48*, 3622–3626.
- (17) Yoon, J.; Wilson, S. A.; Jang, Y. K.; Seo, M. S.; Nehru, K.; Hedman, B.; Hodgson, K. O.; Bill, E.; Solomon, E. I.; Nam, W. *Angew. Chem. Int. Ed.* **2009**, *48*, 1257–1260.
- (18) Thibon, A.; Bartoli, J.-F.; Bourcier, S.; Banse, F. *Dalton Trans.* **2009**, 9587–9594.
- (19) Wang, D.; Farquhar, E. R.; Stubna, A.; Münck, E.; Que, L. *Nature Chem.* **2009**, *1*, 145–150.
- (20) Comba, P.; Maurer, M.; Vadivelu, P. *Inorg. Chem.* **2009**, *48*, 10389–10396.
- (21) Xue, G.; De Hont, R.; Münck, E.; Que, L. *Nature Chem.* **2010**, *2*, 400–405.
- (22) Seo, M. S.; Kim, N. H.; Cho, K.-B.; So, J. E.; Park, S. K.; Clémancey, M.; Garcia-Serres, R.; Latour, J.-M.; Shaik, S.; Nam, W. *Chem. Sci.* **2011**, *2*, 1039–1045.
- (23) Company, A.; Prat, I.; Frisch, J. R.; Mas-Ballesté, D. R.; Güell, M.; Juhász, G.; Ribas, X.; Münck, D. E.; Luis, J. M.; Que, L., Jr.; Costas, M. *Chem. Eur. J.* **2011**, *17*, 1622–1634.
- (24) England, J.; Guo, Y.; Van Heuvelen, K. M.; Cranswick, M. A.; Rohde, G. T.; Bominaar, E. L.; Münck, E.; Que, L., Jr. *J. Am. Chem. Soc.* **2011**, *133*, 11880–11883.
- (25) Usharani, D.; Janardanan, D.; Li, C.; Shaik, S. *Acc. Chem. Res.* **2013**, *46*, 471–482.
- (26) Gardner, K. A.; Kuehnert, L. L.; Mayer, J. M. *Inorg. Chem.* **1997**, *36*, 2069–2078.
- (27) Pestovsky, O.; Stoian, S.; Bominaar, E. L.; Shan, X.; Münck, E.; Que, L.; Bakac, A. *Angew. Chem. Int. Ed.* **2005**, *44*, 6871–6874.
- (28) Lacy, D. C.; Gupta, R.; Stone, K. L.; Greaves, J.; Ziller, J. W.; Hendrich, M. P.; Borovik, A. S. *J. Am. Chem. Soc.* **2010**, *132*, 12188–12190.
- (29) Bigi, J. P.; Harman, W. H.; Lassalle-Kaiser, B.; Robles, D. M.; Stich, T. A.; Yano, J.; Britt, R. D.; Chang, C. J. *J. Am. Chem. Soc.* **2012**, *134*, 1536–1542.
- (30) Rohde, J.-U.; In, J.-H.; Lim, M. H.; Brennessel, W. W.; Bukowski, M. R.; Stubna, A.; Münck, E.; Nam, W.; Que, L. *Science* **2003**, *299*, 1037–1039.
- (31) Addison, A. W.; Rao, T. N.; Reedijk, J.; van Rijn, J.; Verschoor, G. C. *J. Chem. Soc., Dalton Trans.* **1984**, 1349–1356.
- (32) Lim, M. H. *Proc. Nat. Acad. Sci.* **2003**, *100*, 3665–3670.
- (33) Fukuzumi, S.; Morimoto, Y.; Kotani, H.; Naumov, P.; Lee, Y.-M.; Nam, W. *Nature Chem.* **2010**, *2*, 756–759.
- (34) Pfaff, F. F.; Kundu, S.; Risch, M.; Pandian, S.; Heims, F.; Pryjomska-Ray, I.;

- Haack, P.; Metzinger, R.; Bill, E.; Dau, H.; Comba, P.; Ray, K. *Angew. Chem. Int. Ed.* **2010**, *50*, 1711–1715.
- (35) Chen, J.; Lee, Y.-M.; Davis, K. M.; Wu, X.; Seo, M. S.; Cho, K.-B.; Yoon, H.; Park, Y. J.; Fukuzumi, S.; Pushkar, Y. N.; Nam, W. *J. Am. Chem. Soc.* **2013**, *135*, 6388–6391.
- (36) Hong, S.; Pfaff, F. F.; Kwon, E.; Wang, Y.; Seo, M. S.; Bill, E.; Ray, K.; Nam, W. *Angew. Chem. Int. Ed.* **2014**, *53*, 10403–10407.
- (37) Kundu, S.; Miceli, E.; Farquhar, E.; Pfaff, F. F.; Kuhlmann, U.; Hildebrandt, P.; Braun, B.; Greco, C.; Ray, K. *J. Am. Chem. Soc.* **2012**, *134*, 14710–14713.
- (38) Swart, M. *Chem. Commun.* **2013**, *49*, 6650–6652.
- (39) Prakash, J.; Rohde, G. T.; Meier, K. K.; Jasniewski, A. J.; Van Heuvelen, K. M.; Münck, E.; Que, L., Jr. *J. Am. Chem. Soc.* **2015**, *137*, 3478–3481.
- (40) Birnbaum, P. P.; Linfood, J. H.; Style, D. W. G. *Trans. Faraday Soc.* **1953**, *49*, 735.
- (41) Jones, R. N. *Chem. Rev.* **1947**, *41*, 353–371.
- (42) Rayne, S.; Forestb, K. *Nature Proceedings* **2010**.
- (43) Dauban, P.; Sanière, L.; Tarrade, A.; Dodd, R. H. *J. Am. Chem. Soc.* **2001**, *123*, 7707–7708.
- (44) Motekaitis, R. J.; Martell, A. E.; Murase, I. *Inorg. Chem.* **1986**, *25*, 938–944.
- (45) APEX2 Version 2010.3-0, Bruker AXS, Inc.; Madison, WI 2010.
- (46) SAINT Version 7.68a, Bruker AXS, Inc.; Madison, WI 2009.
- (47) Sheldrick, G. M. SADABS, Version 2012/1, Bruker AXS, Inc.; Madison, WI 2008.
- (48) Sheldrick, G. M. SHELXTL, Version 2012/4, Bruker AXS, Inc.; Madison, WI 2008.
- (49) International Tables for X-Ray Crystallography 1992, Vol. C., Dordrecht: Kluwer Academic Publishers.
- (50) Spek, A. L. PLATON, *Acta. Cryst.* 2009, D65, 148-155.

CHAPTER 5

Coordination Properties of a Tridentate, Redox Active, Sulfonamido Ligand

Introduction

A constant area of interest in synthetic inorganic chemistry is the preparation of highly active molecular catalysts for the functionalization of simple commodity chemicals into complex fine chemicals. While many types of reactions are needed for building complex molecules, one approach that has gained particular interest in recent years is the activation of unfunctionalized C–H bonds. This reaction is exceptionally important both in the early stages of molecular synthesis where hydrocarbon feedstocks are converted into synthetically useful building blocks and in the late stage introduction of functional groups in complicated target syntheses. Tremendous progress has been made in the field of homogeneous catalysis, with numerous examples of highly active and selective catalysts reported in the literature.¹ However, the great majority of these successful catalysts employ expensive second and third row transition metals such as palladium and iridium. The rising cost of these metals has limited the practicality of their application in long term and large scale synthetic applications, and so a recent drive is to replace these precious metals with earth-abundant, first row transition metal catalysts.²

The reactivity requirement that makes second and third row transition metal catalysts so good at C–H bond functionalization and that complicates the development of first row transition metal catalysts is the need to perform multielectron processes; while the lower transition metals are capable of easily undergoing 2 electron oxidation state changes, first row metals typically favor single electron transfer processes. Although two consecutive single electron transfer processes can lead to productive C–H bond

activation,³ the likely occurrence of unwanted side reactions in these radical pathways is a constant threat to the yield and selectivity of the reaction as well as to the lifetime of the catalyst.

One approach that has gained recent attention for improving the function of first row transition metal catalysts in multielectron transformations is the development of redox active ligand frameworks that can supply or store electrons during the reaction.⁴⁻⁸ These ligands contain frontier orbitals that have similar energies as those of the metal center that it is coordinated to, which allows the redox events to be localized on the ligand instead of the metal center. The utility of this approach is clearly demonstrated by the reactivity of d^0 metals that are supported by redox active ligands in multielectron transformations. For example, a Zr(IV) complex supported by two iminophenolate ligands was shown to readily react with chlorine gas via oxidative addition at the metal center to form a dichloride complex in which the necessary electrons were supplied by the two iminophenolate ligands (Chart 5.1A).⁹ A related complex containing two aryl ligands was shown to undergo C–C bond coupling to form biphenyl upon two-electron oxidation of the complex.¹⁰ In another example, a trianionic N_3 ligand, bis(aminophenyl)amine ligand ($[NNN^{cat}]^{3-}$) was shown to facilitate oxidative reactivity at the d^0 metal centers Zr(IV) and Ta(V).^{11,12} Both of these complexes reacted with aryl azides to form M–imido complexes in which the necessary electrons for the two-electron reduction of the azide were provided by the ligand (Chart 5.1B). Furthermore, the Zr(IV)–imido complex was shown to catalytically transfer the nitrene unit to isonitrile.

The ability of redox active ligands to support multielectron transformations at late first row transition metal centers has also been previously demonstrated. For example, C–

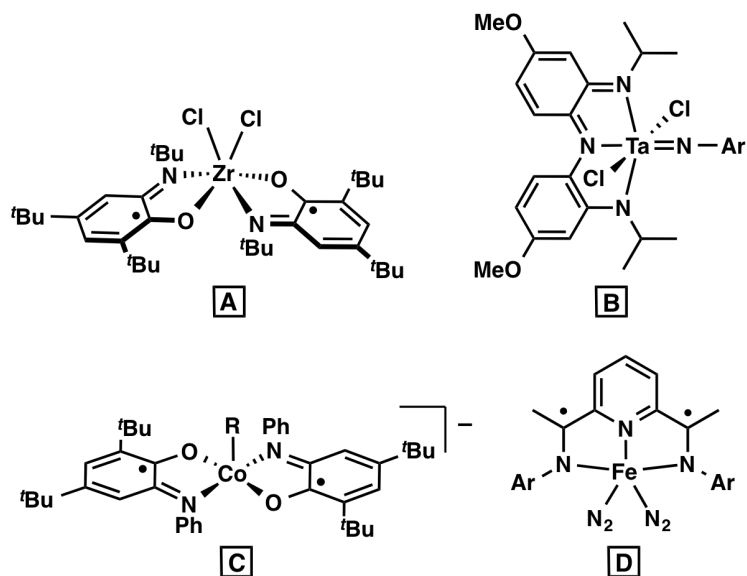


Chart 5.1. Complexes whose redox active ligand frameworks have facilitated A) oxidative addition of Cl_2 gas at a d^0 Zr(IV) center, B) activation of aryl azide at a d^0 Ta(V) center, C) C–C bond formation with organo zinc reagents, and D) cycloaddition of dienes, enynes, and diyne.

C bond forming reactions by a square planar Co(III) center were shown to result from one-electron oxidation of the two bidentate iminophenolate ligands upon oxidative addition of an alkyl halide; the resulting square pyramidal complex (Chart 5.1C) reacts with organozinc reagents to form the coupled products via reductive C–C bond formation, which regenerates the fully reduced complex.^{6,13,14} C–C bond forming reactions were also shown to be catalyzed by the redox activity of a pyridinediimine (Chart 5.1D) ligand in the reaction of its Fe complex with dienes, enynes, and diyne.^{15,16} These examples illustrate the utility of developing new transition metal complexes that are supported by redox active ligand frameworks for the purpose of organic catalysis.

The work that will be described in the final two chapters of this dissertation was begun in 2014 in collaboration with Professor Cora MacBeth at Emory University through the NSF Center for Selective C–H Functionalization. MacBeth and coworkers have developed a derivative of the $[\text{NNN}]^{3-}$ ligand scaffold with amide functional groups

that was shown to facilitate catalytic oxidation of triphenylphosphine to triphenylphosphine oxide with two Co(II) complexes (Chart 5.2A) and dioxygen.¹⁷ Electrochemical studies of the mononuclear complex revealed three reversible events—two one-electron processes and one two-electron process—that illustrated the contribution of the ligand to the redox properties of the complex. In addition to the catalytic reactivity with dioxygen, the dinuclear Co(II) complex was also shown to perform catalytic intramolecular benzylic C–H amination of aryl azides with appended phenyl groups.¹⁸

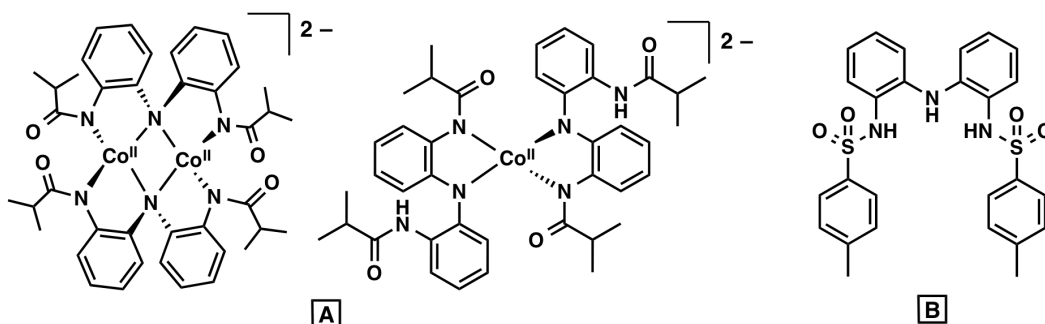


Chart 5.2. The Co(II) complexes of MacBeth that are supported by the amidate derivate of the $[\text{NNN}]^{3-}$ ligand framework (A), and the sulfonamido ligand derivative examined in this chapter (B).

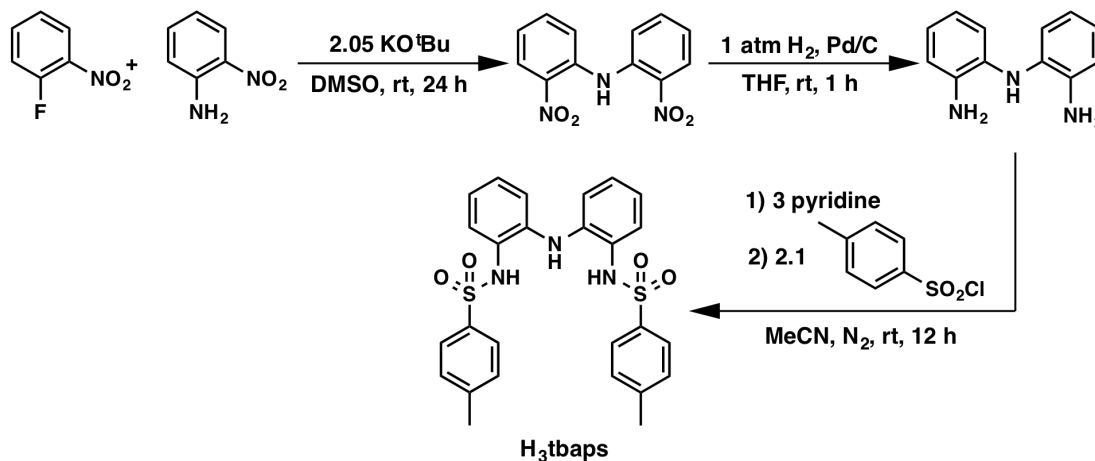
The collaboration with the MacBeth lab was born out of the hypothesis that the reactivity observed with the Co(II) complexes could be further modulated by incorporating non-covalent interactions within the secondary coordination sphere. Our group has conclusively shown that secondary sphere interactions could be used to influence reactivity by stabilizing reactive intermediates such as highly basic Fe(III)–oxo unit using intramolecular H-bond donors,¹⁹ and also to enhance the rate of dioxygen reduction via electrostatic interactions with a redox inactive metal ion, as discussed in Chapter 2.^{20,21} We therefore sought to similarly incorporate both types of interactions within the $[\text{NNN}]^{3-}$ ligand framework used previously in the MacBeth lab and to examine

their influences on the reactivity of the resulting complexes. In this collaborative project, the MacBeth lab pursued the incorporation of H-bond donating groups within the secondary coordination sphere while I pursued functionalization with sulfonamido groups. This chapter describes the development of a tolyl sulfonamido ligand derivative (Chart 5.2B) and the characterization of its complexes with Fe, Co, and Cu. Structures with dinuclear cores similar to those of the amidate ligand derivative of MacBeth (Chart 5.2A, left) were determined for all three metal ions, and spectroscopic characterization revealed a number of anomalies for the Cu complex that suggested a complicated electronic structure. However, the coordination properties of this tolyl ligand derivative did not align with our motivation of preparing discrete complexes whose reactivity could be influenced by controlled interactions with secondary metal ions, which lead us to prepare a second ligand derivative that will be described in Chapter 6.

Results and Discussion

Synthetic Methods. A sulfonamido ligand derivative containing tolyl groups was selected for these initial studies based on the results described in Chapters 3 and 4 in which both the mesityl and naphthyl derivatives of a tripodal ligand were shown to be susceptible to oxidation while the tolyl derivative was not. The synthesis of this tridentate tolyl ligand derivative, denoted H₃tbaps, was accomplished in three steps from commercially available starting materials (Scheme 5.1). The first two steps have been previously published and involve nucleophilic aromatic substitution of 1-fluoro-2-nitrobenzene with 2-nitroaniline to give the dinitro compound HN(*o*-PhNO₂)₂ that is then reduced under H₂ gas with catalytic palladium on carbon (Pd/C, 10 wt%) to give the bis(2-aminophenyl)amine (HN(*o*-PhNH₂)₂) precursor.¹⁷ Functionalization of this

compound is then performed using a similar procedure as the tripodal sulfonamido ligands described in the previous three chapters: nucleophilic attack of the 2-aminophenyl groups on *p*-tolyl sulfonyl chloride liberates HCl and produces the ligand precursor, *N,N'*-(azanediylbis(2,1-phenylene))bis(4-methylbenzenesulfonamide) (H_3tbaps) in 79% crystalline yield. This ligand is air-stable as a solid but turns pink over time in solution.

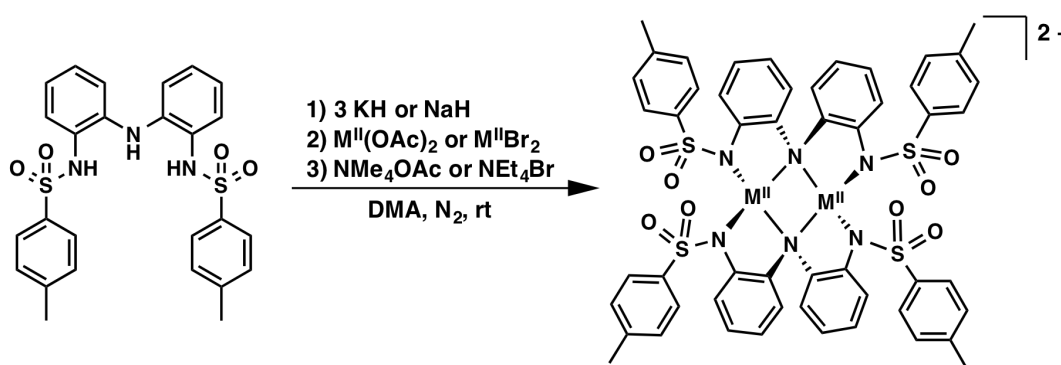


Scheme 5.1. Synthetic route to H_3tbaps .

Characterization of H_3tbaps by 1H NMR and ^{13}C NMR spectroscopies is consistent with the expected C_2 symmetry; only 6 resonances are observed for the 16 total aromatic protons, and two distinct N–H resonances are observed that integrate to three total protons and which disappear upon addition of D_2O to the sample. The ligand precursor is detected as the monodeprotonated anion, $[H_2tbaps]^-$, by electrospray ionization mass spectrometry (ESI-MS) with a mass of 506. The FTIR spectrum of the H_3tbaps contains two sharp bands at 3409 and 3270 cm^{-1} that are assigned to the N–H groups of the sulfonamides and the central amine.

Metalation of H_3tbaps was modeled after the procedure previously reported by MacBeth and coworkers for the amidate redox active ligand with cobalt ions.¹⁷ The modified procedure described here utilizes three equivalents of potassium hydride (KH)

or sodium hydride (NaH) to triply deprotonate the ligand precursor in dimethylacetamide (DMA), followed by transmetalation with either a $M^{II}(\text{OAc})_2$ or a $M^{II}\text{Br}_2$ salt ($M^{II} = \text{Fe}, \text{Co}, \text{Cu}$) (Scheme 5.2). The resulting complexes were either isolated as the potassium salts or treated *in situ* with NMe_4OAc or NEt_4Br to generate the corresponding tetraalkylammonium salts. Complexes of both counter ions were isolated for all three metal ions. Recrystallization from either DMA or MeCN via vapor diffusion of Et_2O into a concentrated solution gave crystalline products in high yields (55 – 90%).



Scheme 5.2. Synthetic route to $[\text{M}^{II}_2(\text{tbaps})_2]^{2-}$ complexes. The third step is omitted in the isolation of the dipotassium salts.

Structural Properties. The molecular structures of all of the Fe(II), Co(II), and Cu(II) complexes with both K^+ and NR_4^+ counter ions, except for the $(\text{NEt}_4)_2[\text{Fe}_2(\text{tbaps})_2]$ salt, were determined by X-ray diffraction (XRD) methods, which revealed nearly identical coordination properties as the analogous complexes of the amidate ligand derivative that were described by MacBeth (Figure 5.1, Tables A.6 and A.7). These complexes consist of a dinuclear structure containing two four-coordinate metal centers and two ligands per molecule. One arm of each ligand coordinates to each metal ion, and the central deprotonated amido donor bridges between the two ions to form a M_2N_2 diamond core. The metrical parameters of the ligand backbone indicate that the ligand remains in its fully reduced form (Table A.8) The geometry around each metal center can

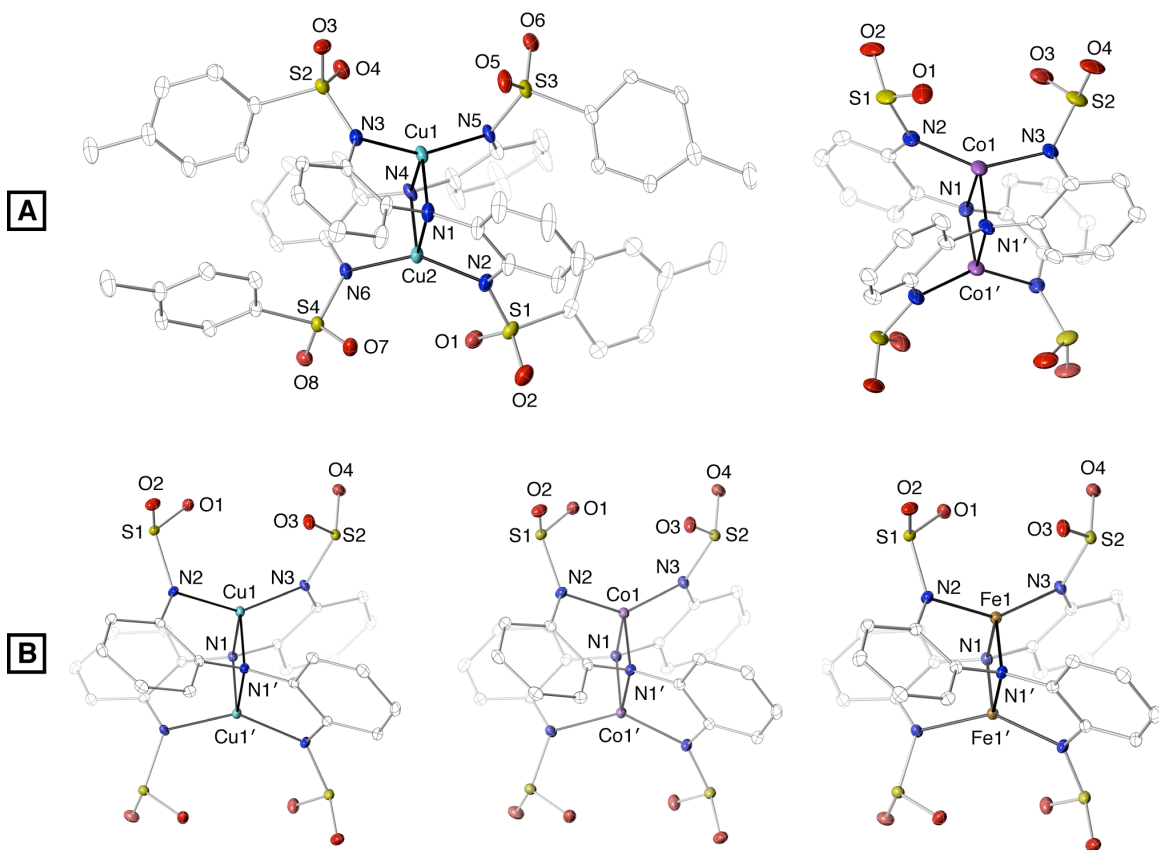


Figure 5.1. Depictions of the molecular structures of the $[M^{II}_2(\text{tbaps})_2]^{2-}$ complexes determined by XRD methods: A) complexes with NR_4^+ counter ions; B) complexes with K^+ counter ions. The tolyl groups adopt the same arrangement in all five complexes but are shown only for the $[\text{Cu}_2(\text{tbaps})_2]^-$ complex in A. The three complexes in A and the Co complex in B contain a two-fold rotation axis that is orthogonal to the plane of the diamond core. Thermal ellipsoids are drawn at the 50% probability level.

be described as distorted seesaw based on calculation of its τ_4 value. This parameter, initially described by Houser, provides a straightforward method of evaluating the geometry around four coordinate metal centers.²² The value is calculated by subtracting the sum of the two largest bond angles within the primary coordination sphere of the metal center from 360 and dividing by 141 (Equation 5.1, where α and β are the two largest angles). The extreme values of 0 and 1 correspond to perfectly square planar and

$$\tau_4 = \frac{360 - (\alpha + \beta)}{141} \quad (5.1)$$

perfectly tetrahedral geometries, respectively. Intermediate values can be assigned to intermediate geometries, such as trigonal pyramidal (0.85) and different classes of seesaw (0.07 - 0.64). The calculated values for the dinuclear $[\text{tbaps}]^{3-}$ complexes fall in the range 0.66 - 0.68 (Tables 5.1 and 5.2), indicating a geometry that is closer to tetrahedral than square pyramidal. These values are similar to those reported for the amidate ligand derivative (0.62 - 0.69), which indicates that the functionalization of the redox active ligand backbone with sulfonamide groups does not significantly influence the primary coordination sphere.²³

Table 5.1. Metrical parameters for the primary coordination spheres of the $[\text{M}^{\text{II}}_2(\text{tbaps})_2]^{2-}$ complexes.

	K ⁺ salts			NEt ₄ ⁺ salt
	$[\text{Fe}_2(\text{tbaps})_2]^-$	$[\text{Co}_2(\text{tbaps})_2]^-$	$[\text{Cu}_2(\text{tbaps})_2]^-$	$[\text{Co}_2(\text{tbaps})_2]^-$
Bond Distances (Å)				
M1–N1	2.093 (2)	2.050(1)	2.102(1)	2.067(3)
M1–N1'	2.110(2)	2.053(1)	2.095(1)	2.087(3)
M1–N2	1.997(2)	1.954(1)	1.926(1)	1.943(3)
M1–N3	1.988(2)	1.944(1)	1.020(1)	1.955(3)
M···M	2.3759(6)	2.5734(4)	2.5332(6)	2.6083(9)
Bond Angles (°)				
N3–M1–N2	143.67(7)	140.40(5)	145.41(6)	143.8(1)
N3–M1–N1	122.75(6)	123.07(5)	120.17(5)	119.0(1)
N2–M1–N1	82.12(6)	84.64(5)	83.51(5)	84.2(1)
N3–M1–N1'	81.35(6)	84.78(5)	83.41(5)	84.2(1)
N2–M1–N1'	116.39(6)	119.10(5)	116.12(5)	119.8(1)
N1–M1–N1'	111.14(5)	102.31(4)	105.75(4)	102.2(1)
M1–N1–M1'	68.86(5)	77.68(5)	74.16(4)	77.8(8)
τ_4 value	0.66	0.68	0.67	0.68

The tolyl groups of the sulfonamido moiety are oriented outward from the complex such that they are nearly orthogonal to the plane formed by the M_2N_2 diamond core (Figure 5.1A). This positions the sulfonamido oxygen atoms from one arm of each ligand on the same face and within close proximity ($< 5 \text{ \AA}$ separation) to form a

Table 5.2. Metrical parameters for the primary coordination spheres of the two distinct Cu(II) centers in (NMe₄)₂[Cu₂(tbaps)₂].

Cu1		Cu2	
Bond Distances (Å)			
Cu1–N1	2.058(4)	Cu2–N2	1.919(3)
Cu1–N3	1.936(3)	Cu2–N4	2.122(4)
Cu1–N5	1.935(3)	Cu2–N6	1.930(3)
Cu1–N4	2.078(3)	Cu2–N1	2.161(3)
M···M	2.5715(7)		
Bond Angles (°)			
N5–Cu1–N3	151.6(1)	N2–Cu2–N6	146.2(1)
N5–Cu1–N4	83.6(1)	N2–Cu2–N4	119.8(1)
N3–Cu1–N4	113.3(1)	N6–Cu2–N4	82.9(1)
N5–Cu1–N1	114.0(1)	N2–Cu2–N1	82.3(1)
N3–Cu1–N1	83.8(1)	N6–Cu2–N1	119.4(1)
N1–Cu1–N4	107.3(1)	N4–Cu2–N1	102.1(1)
Cu1–N1–Cu2	75.1(1)	Cu1–N4–Cu2	75.5(1)
τ_4 value	0.67	τ_4 value	0.67

negatively polarized pocket. Two such pockets of sulfonamido oxygen atoms are formed in each complex. In the dipotassium salts, two potassium ions bridge between pockets on adjacent molecules, thereby creating a linear chain within the unit cell (Figure 5.2). DMA molecules complete the coordination spheres of the potassium ions. In the structures of the NR₄⁺ salts that were obtained for Co(II) and Cu(II), the same negatively polarized pockets of sulfonamido oxygen atoms are formed even though there is no metal ion to coordinate to. This pre-organized secondary binding site is therefore promising for controlled coordination of secondary metal ions such as Ca(II).

Analysis of the bond lengths in the series of dinuclear complexes revealed relatively short M···M separations for all three metal ions (Tables 5.1 and 5.2). An exceptionally short separation of 2.3759(6) Å in the K₂[Fe₂(tbaps)₂] salt suggests the presence of an Fe–Fe bond, as this distance is shorter than the Fe–Fe distance of 2.48 Å in metallic iron and falls within the range of 2.29 Å and 2.46 Å that has been reported for

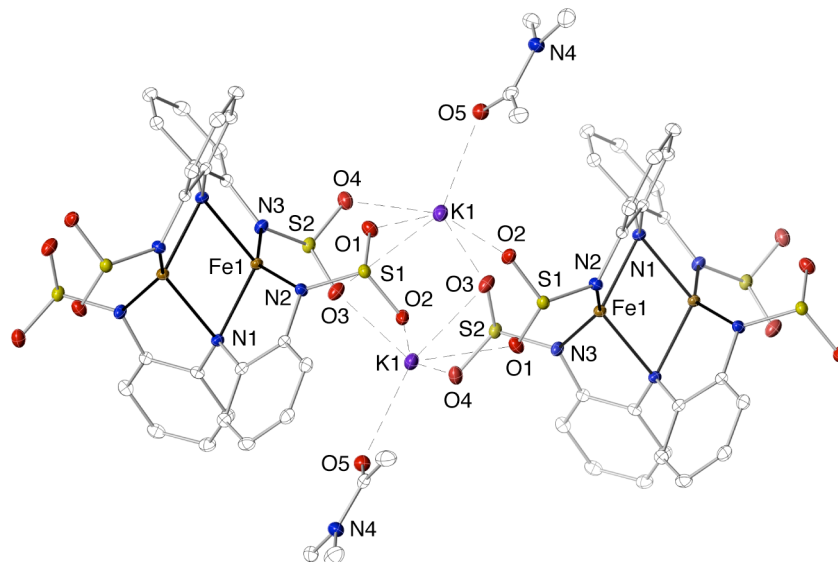


Figure 5.2. Depiction of the interactions of the K^+ ions with the pockets of sulfonamido oxygen atoms that give rise to a polymeric structure. The tolyl groups are excluded for clarity. Thermal ellipsoids are drawn at the 50% probability level.

other dinuclear Fe(II)Fe(II) complexes with metal–metal bonds.^{24–26} A short separation is also observed in the $K_2[Co_2(tbaps)_2]$ salt, with a distance of 2.5734(4) Å. However, this value falls outside of the range that is associated with metal–metal bonds, which typically have distances below 2.4 Å.²⁷ Finally, the separation of 2.5332(6) Å observed in the $K_2[Cu_2(tbaps)_2]$ salt is slightly shorter than the distance observed in a related Cu_2P_2 diamond core reported by Peters (2.596 Å)²⁸ and in the analogous complex with the amidate ligand derivative (2.562 Å).²³ Note that the $M\cdots M$ separations for the $(NEt_4)^+$ salts of the Co and Cu complexes are slightly longer than in the K^+ salts, at 2.6083(9) Å and 2.5715(7) Å, respectively.

Spectroscopic Characterization. Characterization of the dinuclear complexes by UV-vis spectroscopy highlighted a major difference in the electronic properties of the Cu(II) species compared to the Co(II) and Fe(II) analogs; while the latter two metal ions exhibited weak absorption bands that are consistent with d–d transitions, the Cu(II)

spectra contained significantly more intense bands that are suggestive of charge transfer transitions (Figure 5.3). In particular, an intense band was observed at $\lambda_{\text{max}} = 1000 \text{ nm}$ ($\epsilon = 3000 \text{ M}^{-1}\text{cm}^{-1}$) that was not present in the Co(II) or Fe(II) spectra. This type of band in dinuclear compounds is typically assigned to an intervalence charge-transfer between mixed-valent metals centers.²⁹⁻³² Furthermore, all of the features within the Cu(II) spectra resemble those of a dinuclear Cu_2P_2 complex and a Cu_2N_2 complex that have both been assigned to an oxidation state of $\text{Cu}^{1.5}\text{Cu}^{1.5}$.^{28,33} This result suggests that the $[\text{Cu}^{\text{II}}_2(\text{tbaps})_2]^{2-}$ complexes have been reduced by one electron and actually contain the mixed-valent dimer, $\text{Cu}^{\text{I}}\text{Cu}^{\text{II}}$. However, this formulation is not consistent with the overall charge of the complex, as two counter cations are observed per molecule in the solid state structure

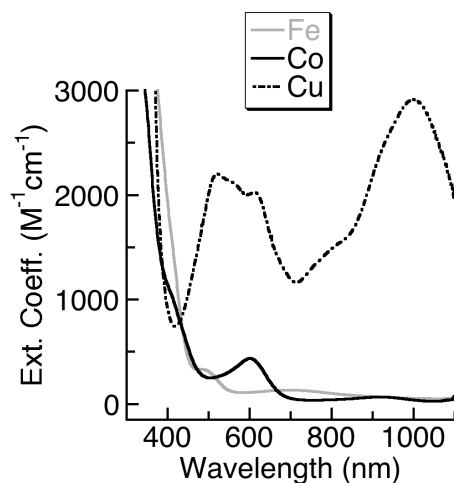


Figure 5.3. Electronic absorbance spectra for the $[\text{M}^{\text{II}}_2(\text{tbaps})_2]^{2-}$ complexes in MeCN at room temperature.

Further complicating the analysis of the Cu dinuclear complexes is the observation of an EPR spectrum that is more consistent with a mononuclear Cu(II) center than either a $\text{Cu}^{\text{II}}_2\text{N}_2$ core or a $\text{Cu}^{\text{I}}\text{Cu}^{\text{II}}$ mixed-valent dimer. For the latter two formulations, a silent spectrum or a $g = 2$ spectrum with a complex Cu hyperfine pattern

would be predicted, respectively.³⁴⁻³⁷ However, the observed spectrum contains a hyperfine pattern with a splitting of $A_{\text{Cu}} = 160$ G that suggests two electronically independent Cu(II) centers (Figure 5.4A). An additional 13-line hyperfine pattern with $A = 13$ G is observed on the g_{\perp} signal, which can be attributed to interaction with the four nitrogen nuclei that are coordinated to the metal ions. The similarity of the observed signal to that of other mononuclear Cu(II) centers suggests that the dinuclear structure characterized in the solid state could exist as mononuclear complexes in solution.³³ However, the EPR spectrum of a solid crystalline sample also contained an intense $g = 2.05$ signal (Figure 5.4B). In addition, the extensive ^{14}N hyperfine splitting observed in the frozen solution suggests that the complex remains assembled in solution. Altogether, the spectroscopic features of the Cu(II) complex give disparate results that require further investigation to correctly assign its electronic structure.

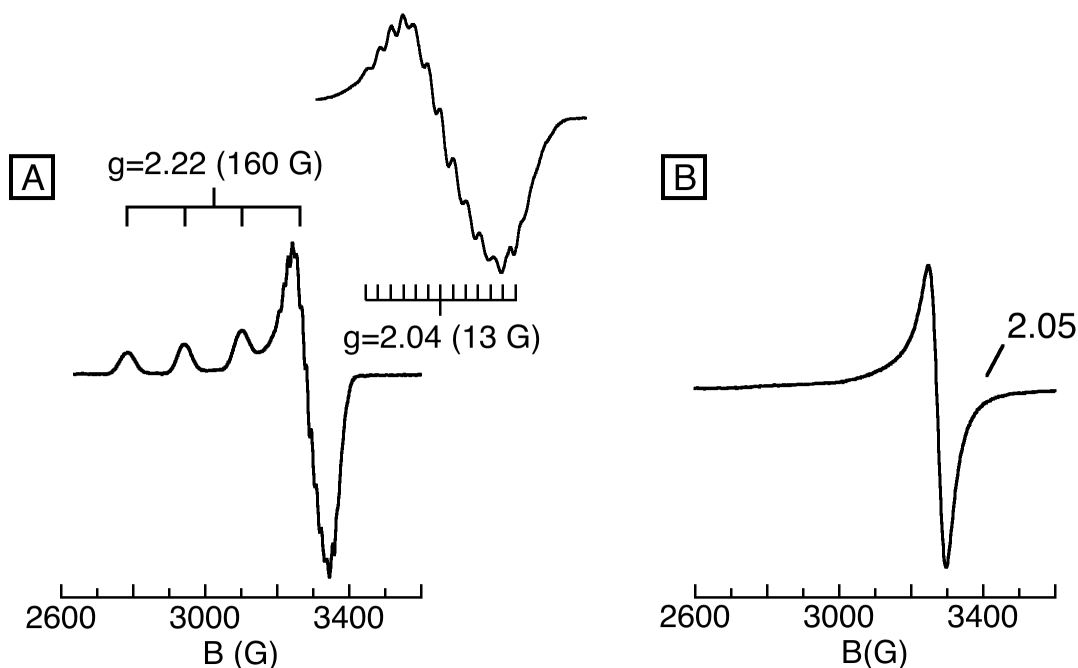


Figure 5.4. EPR spectra of the $\text{K}_2[\text{Cu}_2(\text{tbaps})_2]$ complex at 77K A) as a 5 mM solution (relative to Cu) in 1:1 DMF:THF with an inset showing the 13-line hyperfine pattern on the $g = 2.04$ signal, and B) as a solid sample.

Unlike the Cu(II) complex, the EPR spectra of the Fe(II) and Co(II) analogs are consistent with electronic coupling between two divalent metal centers; for the $[\text{Fe}_2(\text{tbaps})_2]^{2-}$ complexes, a sharp feature at $g = 16$ was observed in the parallel mode spectrum at 10 K (Figure 5.5). This high g -value is consistent with the ferromagnetic coupling between two $S = 2$ Fe(II) centers to give an $S = 4$ spin state.³⁸ A silent spectrum was observed for the $[\text{Co}_2(\text{tbaps})_2]^{2-}$ complexes in both parallel and perpendicular modes, which suggests that the Co(II) centers are antiferromagnetically coupled through the bridging nitrogen donors. These results are summarized in an unexpected trend: the Fe centers couple ferromagnetically, the Co centers couple antiferromagnetically, and the Cu centers do not couple at all.

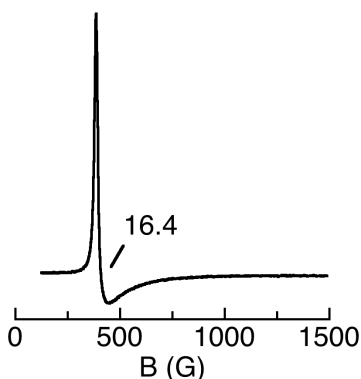


Figure 5.5. Parallel mode EPR spectrum of a 5 mM (based on Fe) solution of $\text{K}_2[\text{Fe}_2(\text{tbaps})_2]$ in 1:1 DMF:THF at 10 K.

The UV-vis spectra for the Fe(II), Co(II), and Cu(II) complexes of $[\text{tbaps}]^{3-}$ closely match those recorded by MacBeth and coworkers for the analogous complexes with the amidate ligand derivative,²³ which suggests that similar anomalies in the electronic structure should be observed for the Cu(II) complex of the amidate ligand. However, this complex was found to be diamagnetic via NMR spectroscopy, which

contrasts the obvious paramagnetic nature of the [tbaps]³⁻ derivative. Additional studies are needed to elucidate the electronic structure of this complex.

Electrochemical Properties. Characterization of the three dinuclear complexes by cyclic voltammetry revealed rich but complicated electrochemical properties (Figure 5.6). Due to the complexity of the signals, no attempts were made to assign each electrochemical process. However, the interaction of the K⁺ counterions clearly influences the electrochemical properties of the dinuclear complexes relative to the (NR₄)⁺ salts. The origin of the irreversible electrochemical behavior is not understood. Although similarly complicated voltammograms were also reported for the Fe(II), Co(II),

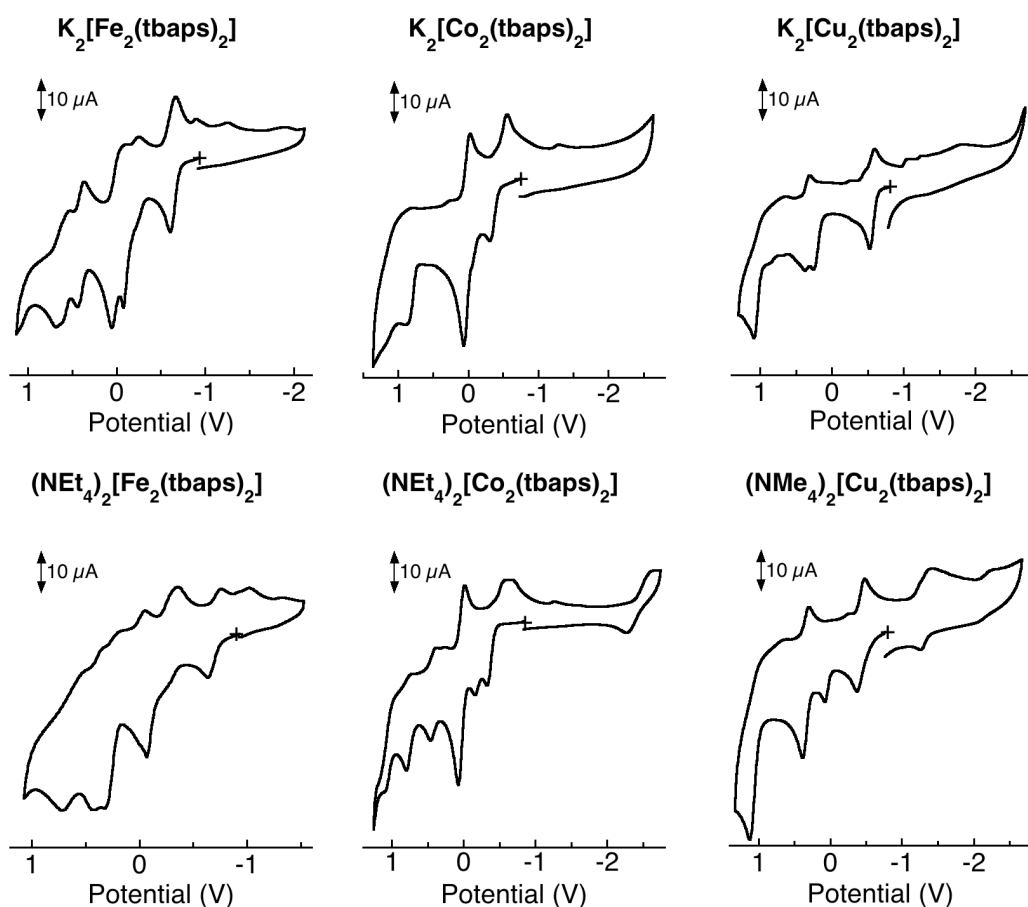


Figure 5.6. Cyclic voltammograms of the six $[M_2(tbaps)_2]^{2-}$ salts in MeCN referenced to $Fc^{0/+}$ (1mM, 0.1 M TBAP, 100 mV/s, with cobaltocenium hexafluorophosphate as an internal standard).

and Cu(II) complexes of the amidate ligand,²³ the related Cu₂P₂ complex of Peters exhibited fully reversible redox events.²⁸

Examination of Secondary Metal Ion Binding. As discussed in the introduction, part of the motivation for incorporating sulfonamido groups within a redox active ligand scaffold was to explore the coordination of additional metal ions within the secondary coordination spheres of transition metal complexes. The molecular structures of the five complexes described above confirmed the formation of a secondary binding site, but the oligomeric structure formed in the crystal lattice from coordination of potassium ions to adjacent molecules indicated that aggregation could complicate the reactivity studies. The formation of discrete heterometallic complexes was therefore explored via the addition of group 2 and group 3 metal ions as crown ether adducts. The ability of these crown ether adducts to support the formation of discrete heterobimetallic complexes was illustrated in Chapter 2.

Binding of the Mⁿ(OTf)_n/(crown ether) adducts to the [Cu₂(tbaps)₂]²⁻ complex was examined by UV-vis spectroscopy, and addition of Ca(OTf)₂/15-crown-5 to either the (NMe₄⁺)₂ or the (K⁺)₂ salt resulted in an immediate color change from pink to blue and the appearance of new features at 454, 535, 644, and 873 nm (Figure 5.7A). A similar change in the absorption spectrum was also observed upon addition of Sr(OTf)₂/15-crown-5 and Ba(OTf)₂/18-crown-6 (Figure 5.7B). These spectral changes suggest that the group 2 metal ion/crown ether adducts have a different mode of interaction with the [Cu₂(tbaps)₂]²⁻ complex than the potassium ions within the isolated salts. Addition of a trivalent metal ion, Sc(OTf)₃/15-crown-5, also caused a dramatic change in the absorption spectrum, but this new spectrum was not stable and began to decrease within

several seconds. A possible explanation for this continued change is that initial coordination of Sc(III) is followed by structural rearrangement of the complex. Finally, no spectral changes were observed upon addition of the monocation adduct, Na(OTf)₂/15-crown-5.

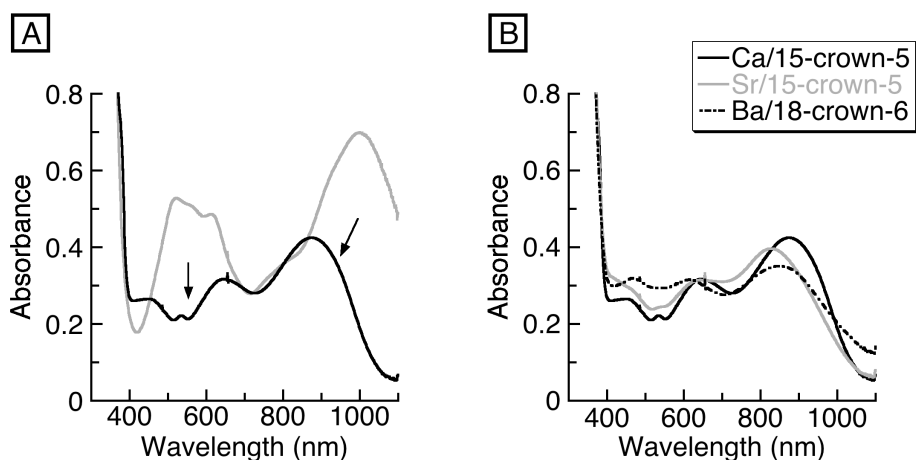


Figure 5.7. A) UV-vis spectral changes for the addition of Ca(OTf)₂/15-crown-5 to a 0.24 mM (with respect to Cu) solution of (NMe₄)₂[Cu₂(tbaps)₂] in acetonitrile, and B) Comparison of the spectra obtained from the addition of group 2 metal ions as crown ether adducts.

In order to determine the mode of interaction between [Cu₂(tbaps)₂]²⁻ and the group 2 metal ions, crystallization of the proposed [(15-crown-5)Ca]Cu₂(tbaps)₂ complex was pursued. Diffusion of Et₂O into a concentrated solution of (NEt₄)₂[Cu^{II}₂(tbaps)₂] and Ca(OTf)₂/15-crown-5 gave a purple crystal whose molecular structure indicated that the crown ether ligand did not prevent oligomerization of the complex (Figure 5.8, Tables 5.3 and A.7). Two Ca(II) ions were observed per molecule: one seven-coordinate ion remained bound to the 15-crown-5 macrocycle and also coordinated to one sulfonamido oxygen atom from each ligand within the pocket. A second Ca(II) ion that was no longer bound by a crown ether molecule coordinated to the other two sulfonamido oxygen atoms of the same pocket and bridged to the second

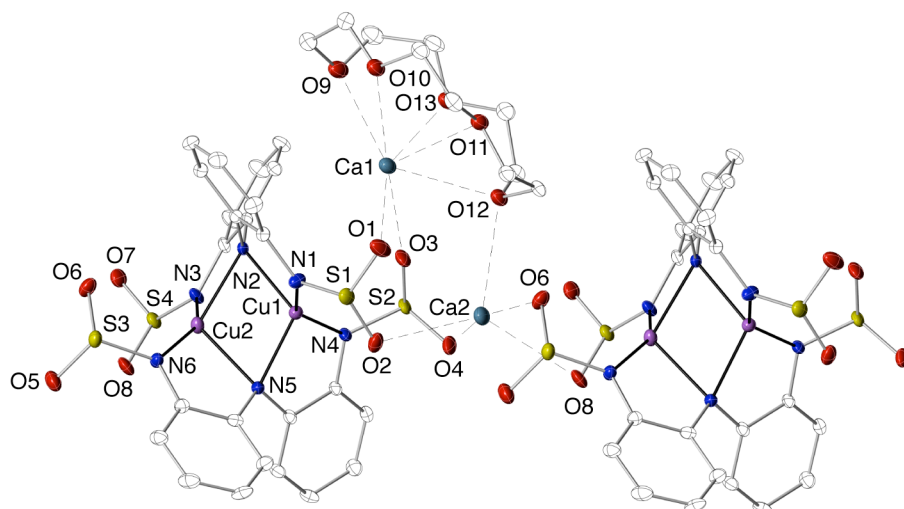


Figure 5.8. Molecular structure of the complex obtained from crystallization of $[\text{Cu}_2(\text{tbaps})_2]^{2-}$ in the presence of $\text{Ca}(\text{OTf})_2/15\text{-crown-5}$.

pocket of a neighboring molecule. This molecular structure highlighted a fundamental problem created by the binding of two $[\text{tbaps}]^{3-}$ ligands per molecule: the resulting formation of two binding pockets prohibits the formation of the desired discrete heterometallic complexes.

Table 5.3. Metrical parameters for the primary coordination spheres of the two distinct Cu(II) centers in the $[\text{Cu}_2(\text{tbaps})_2]^{2-}$ containing Ca(II) ions.

Cu1		Cu2	
Bond Distances (Å)			
Cu1–N4	1.916(3)	Cu2–N3	1.912(3)
Cu1–N1	1.919(3)	Cu2–N6	1.916(4)
Cu1–N2	2.042(3)	Cu2–N5	2.145(3)
Cu1–N5	2.058(3)	Cu2–N2	2.175(3)
M···M	2.5194(6)		
Bond Angles (°)			
N4–Cu1–N1	140.9(1)	N3–Cu2–N6	147.5(1)
N4–Cu1–N2	115.7(1)	N3–Cu2–N5	118.3(1)
N1–Cu1–N2	84.8(1)	N6–Cu2–N5	82.5(1)
N4–Cu1–N5	84.3(1)	N3–Cu2–N2	82.2(1)
N1–Cu1–N5	121.0(1)	N6–Cu2–N2	119.6(1)
N2–Cu1–N5	110.5(1)	N5–Cu2–N2	102.5(1)
Cu1–N1–Cu2	73.3(1)	Cu1–N4–Cu2	73.7(1)
τ_4 value	0.70	τ value	0.66

Summary and Conclusions

In summary, the structural and spectroscopic properties of six dinuclear complexes supported by a tridentate sulfonamido ligand derivative were described. This ligand was found to enforce nearly identical coordination properties as the amidate ligand derivative reported by MacBeth; all of the sulfonamido and amidate complexes have distorted tetrahedral geometries around the metal centers with τ_4 values within the range 0.62 – 0.69, and similar M...M separations were observed between the two series of complexes with a bonding interaction observed between the metal centers in the Fe complexes.

Both the Fe and Co complexes exhibited low intensity absorption bands in their UV-vis spectra that are consistent with d–d transitions within the Fe(II) and Co(II) centers. Furthermore, magnetic coupling between metal centers was observed for both complexes; a $g=16$ signal for $[\text{Fe}_2(\text{tbaps})_2]^{2-}$ is consistent with ferromagnetic coupling while the silent spectrum observed for $[\text{Co}_2(\text{tbaps})_2]^{2-}$ suggests antiferromagnetic coupling. In contrast, $[\text{Cu}_2(\text{tbaps})_2]^{2-}$ complexes displayed electronic properties that are not consistent with the expected strong electronic coupling between the two metal centers; while the UV-vis spectrum contained an intense low energy band that is suggestive of intervalence charge transfer between mixed-valent metal centers, the structural parameters are consistent with two Cu(II) centers in distorted tetrahedral geometry, and the EPR spectrum does not match either formulation. Instead, the observed signal is suggestive of a mononuclear Cu(II) species, which could result from the dinuclear structure breaking apart in solution. However, the observation of an EPR signal

for a solid state sample is not consistent with this explanation. These spectral anomalies require more in depth study to understand their origins.

Addition of di- and trivalent redox inactive metal ions as crown ether adducts to the $(\text{NMe}_4)_2[\text{Cu}_2(\text{tbaps})_2]$ and $\text{K}_2[\text{Cu}_2(\text{tbaps})_2]$ salts caused a significant change in the optical spectrum that suggested a unique mode of interaction compared to that observed for the K^+ ions in the isolated salt. However, the molecular structure of the $[\text{Cu}_2(\text{tbaps})_2]^{2-}$ complex crystallized in the presence of $\text{Ca}(\text{OTf})_2/15\text{-crown-5}$ indicated that an oligomeric structure was still formed due to interactions of $\text{Ca}(\text{II})$ ions with sulfonamido binding pockets of adjacent molecules. This inability to form discreet heterometallic complexes as well as the close similarities of our dinuclear complexes to those of the amidate ligand system lead us to pursue a new ligand derivative that could enforce different coordination properties. The studies of this new ligand derivative are described in the next chapter.

Experimental Details

General Methods

Syntheses of metal complexes were completed under a nitrogen atmosphere in a VAC drybox. Solvents were sparged with argon and dried over columns containing Q-5 and molecular sieves. All reagents were purchased from commercial suppliers and used as received unless otherwise noted. Potassium hydride and sodium hydride as 30% suspensions in mineral oil were filtered and washed five times each with Et_2O and pentane and dried under vacuum. The ligand precursor $\text{HN}(o\text{-PhNH}_2)_2$ was prepared according to literature procedures.¹⁷ Multiple attempts at elemental analyses for

$\text{K}_2[\text{Cu}_2(\text{tbaps})_2]\cdot 2\text{DMA}$ and $(\text{NEt}_4)_2[\text{Fe}_2(\text{tbaps})_2]\cdot 2\text{DMA}$ failed to match the calculated values.

Ligand Synthesis

N,N'-(azanediylbis(2,1-phenylene))bis(4-methylbenzenesulfonamide) (H_3tbaps). The triamine (1.2 g, 6.0 mmol) and pyridine (1.19 g, 15.0 mmol) were dissolved in 30 mL of MeCN in the glove box. *p*-tolyl sulfonyl chloride (2.29 g, 12.1 mmol) was dissolved in 6 mL of MeCN and added dropwise to the acetonitrile solution over the course of ten minutes, causing a change from clear orange to heterogeneous pink-orange. The reaction was stirred overnight in the glovebox at room temp to give a dark orange solution. After checking the reaction for completion by ESI-MS, the mixture was concentrated to dryness under vacuum, redissolved in DCM, and washed with 1M HCl until the aqueous layer was no longer colored. The organic layer was further washed with H_2O and brine, dried over MgSO_4 , filtered, and concentrated under vacuum to a foam. The ligand precursor was recrystallized from hot MeOH as light yellow crystals in 79% yield (2.4 g). ^1H NMR (500 MHz, CDCl_3 , ppm): 9.32, (s, 2H, NH), 7.52 (d, 4H), 7.17 (d, 4H), 7.03 (s, 1H, NH) 6.93 (t, 2H), 6.86 (d, 2H), 6.73 (t, 2H), 6.53 (d, 2H), 2.26 (s, 6H). ^{13}C NMR (125 MHz, CDCl_3 , ppm): 142.9, 139.0, 136.7, 129.3, 127.1, 128.9, 126.2, 120.8, 118.7, 21.0. FTIR (Nujol, cm^{-1} , selected bands): 3409 (NH), 3270 (NH), 1591 (s), 1525 (s), 1333 (s), 1153 (s), 812 (s). HRMS (ES+): Exact mass calcd (found) for $[\text{M} + \text{Na}]$: 530.1184 (530.1179).

Complex Syntheses

$\text{K}_2[\text{Cu}_2(\text{tbaps})_2]\cdot 2\text{DMA}$ A solution of H_3tbaps (0.10 g, 0.20 mmol) in 3 mL of DMA was treated with three equivalents of solid KH (24 mg, 0.6 mmol). The reaction

was stirred until gas evolution ceased, and then $\text{Cu}(\text{OAc})_2$ (36 mg, 0.20 mmol) was added. After 2 h, the reaction was filtered through a medium porosity fritted funnel to remove approximately one equivalent (15 mg, 0.15 mmol) of insoluble KOAc. The reaction mixture was diluted to 5 mL of DMA, and the product was crystallized by vapor diffusion of Et_2O into the concentrated solution to give 123 mg (90%) of purple crystals. Elemental analysis calcd (found) for $\text{K}_2[\text{Cu}_2(\text{tbaps})_2]\cdot 2\text{DMA}$ ($\text{C}_{60}\text{H}_{62}\text{N}_8\text{O}_{10}\text{S}_4\text{Cu}_2\text{K}_2$): C, 51.89 (49.37); H, 4.50 (5.42); N, 8.07 (8.45)% FTIR (Nujol, cm^{-1} , selected bands): 1630 (m), 1461 (s), 1257 (m), 1330 (m), 1086 (m), 960 (m), 816 (w), 661 (m). λ_{max} , nm (MeCN, ϵ , $\text{M}^{-1}\text{cm}^{-1}$): 520 (2600), 610 (2400), 1000 (3600). EPR (1:1 DMF:THF, 77 K): $g_{\text{par}} = 2.22$ (160 G), $g_{\text{perp}} = 2.04$ (13 G).

(NMe₄)₂[Cu₂(tbaps)₂]·3DMA** A solution of H_3tbaps (0.10 g, 0.20 mmol) in 3 mL of DMA was treated with three equivalents of solid NaH (14 mg, 0.6 mmol). The reaction was stirred until gas evolution ceased, and then $\text{Cu}(\text{OAc})_2$ (36 mg, 0.20 mmol) and NMe₄OAc (26 mg, 0.2 mmol) were added. After 3 h, the reaction was filtered through a medium porosity fritted funnel to remove approximately two equivalents (35 mg, 0.43 mmol) of insoluble NaOAc. The reaction mixture was diluted to 5 mL of DMA, and the product was crystallized by vapor diffusion of Et_2O into the concentrated solution to give 140 mg (46%) of red-purple crystals. Elemental analysis calcd (found) for $(\text{NMe}_4)_2[\text{Cu}_2(\text{tbaps})_2]\cdot 3\text{DMA}$ ($\text{C}_{72}\text{H}_{95}\text{N}_{11}\text{O}_{11}\text{S}_4\text{Cu}_2$): C, 55.94 (55.83); H, 6.19 (6.06); N, 9.97 (9.76)%. FTIR (Nujol, cm^{-1} , selected bands) 1584 (m), 1460 (s), 1261 (s), 1136 (s), 1094 (m), 975 (m), 820 (w), 725 (s). λ_{max} , nm (MeCN, ϵ , $\text{M}^{-1}\text{cm}^{-1}$): 520 (2300), 614 (2100), 1000 (3000). EPR (1:1 DMF:THF, 77 K): $g_{\text{par}} = 2.22$ (162 G), $g_{\text{perp}} = 2.04$ (14 G).**

K₂[Co₂(tbaps)₂]·2DMA** This dipotassium salt of Co was prepared using the same**

procedure as $\text{K}_2[\text{Cu}_2(\text{tbaps})_2]\cdot 2\text{DMA}$, with H_3tbaps (0.10 g, 0.20 mmol), KH (24 mg, 0.60 mmol), and CoBr_2 (43 mg, 0.20 mmol) in 3 mL of DMA. The product was isolated as dark green crystals (75 mg, 55%) from diffusion of Et_2O into a concentrated DMA solution. Elemental analysis calcd (found) for $\text{K}_2[\text{Co}_2(\text{tbaps})_2]\cdot 2\text{DMA}$ ($\text{C}_{60}\text{H}_{62}\text{N}_8\text{O}_{10}\text{S}_4\text{Co}_2\text{K}_2$): C, 52.24 (52.31); H, 4.53 (4.94); N, 8.12 (8.78)%. FTIR (Nujol, cm^{-1} , selected bands): 1637 (s), 1464 (s), 1294 (m), 1255 (s), 1087 (m), 968 (m), 831 (m), 751 (m), 671 (m). λ_{max} , nm (MeCN, ϵ , $\text{M}^{-1}\text{cm}^{-1}$): 602 (390), 925 (50).

$(\text{NEt}_4)_2[\text{Co}_2(\text{tbaps})_2]$ This ammonium salt of Co was prepared using a similar procedure as $(\text{NMe}_4)_2[\text{Cu}_2(\text{tbaps})_2]\cdot 2\text{DMA}$, with H_3tbaps (0.10 g, 0.20 mmol), NaH (14 mg, 0.6 mmol), CoBr_2 (43 mg, 0.20 mmol), and NEt_4Br (41 mg, 0.20 mmol) in 3 mL of DMA. After 3 hours, the reaction was concentrated to dryness and redissolved in MeCN. The dark green solution was filtered to remove approximately 2.5 equivalents of NaBr (52 mg, 0.5 mmol) and then the solvent was removed under vacuum. The product was isolated as dark green crystals (100 mg, 74%) from diffusion of Et_2O into a concentrated DMA solution. Elemental analysis calcd (found) for $(\text{NEt}_4)_2[\text{Co}_2(\text{tbaps})_2]$ ($\text{C}_{68}\text{H}_{84}\text{N}_8\text{O}_8\text{S}_4\text{Co}_2$): C, 58.86 (58.37); H, 6.10 (6.16); N, 8.08 (8.07)%. FTIR (Nujol, cm^{-1} , selected bands) 1661 (m), 1578 (m), 1479 (s), 1252 (s), 1134 (s), 1085 (s), 962 (s), 833 (m), 739 (s). λ_{max} , nm (MeCN, ϵ , $\text{M}^{-1}\text{cm}^{-1}$): 602 (430), 925 (50).

$\text{K}_2[\text{Fe}_2(\text{tbaps})_2]\cdot 2\text{DMA}$ This dipotassium salt of Fe was prepared using the same procedure as $\text{K}_2[\text{Cu}_2(\text{tbaps})_2]\cdot 2\text{DMA}$, with H_3tbaps (0.10 g, 0.20 mmol), KH (24 mg, 0.60 mmol), and FeBr_2 (42 mg, 0.20 mmol) in 3 mL of DMA. The product was isolated as dark green crystals (119 mg, 88%) from diffusion of Et_2O into a concentrated DMA solution. Elemental analysis calcd (found) for $\text{K}_2[\text{Fe}_2(\text{tbaps})_2]\cdot 2\text{DMA}$

(C₆₀H₆₂N₈O₁₀S₄Co₂K₂): C, 52.48 (52.12); H, 4.55 (4.46); N, 8.16 (7.60)%. FTIR (Nujol, cm⁻¹, selected bands): 1657 (w), 1574 (s), 1254 (s), 1132 (m), 1085 (m), 966 (m), 740 (m). λ_{max}, nm (MeCN, ε, M⁻¹cm⁻¹): 485 (320), 700 (130). EPR (1:1 DMF:THF, 77 K, parallel mode): g = 16.4.

(NEt₄)₂[Fe₂(tbaps)₂] This ammonium salt of Fe was prepared using a similar procedure as (NMe₄)₂[Cu₂(tbaps)₂] \cdot 2DMA, with H₃tbaps (0.10 g, 0.20 mmol), KH (24 mg, 0.6 mmol), FeBr₂ (43 mg, 0.20 mmol), and NEt₄Br (41 mg, 0.20 mmol) in 3 mL of DMA. After 3 h, the reaction was concentrated to dryness and redissolved in MeCN. The dark green solution was filtered to remove almost three equivalents of KBr (64 mg, 0.54 mmol) and then the solvent was removed under vacuum. The product was isolated as dark green crystals (150 mg, 64%) from diffusion of Et₂O into a concentrated DMA solution. Elemental analysis calcd (found) for (NEt₄)₂[Fe₂(tbaps)₂] (C₆₈H₈₄N₈O₈S₄Fe₂): C, 59.12 (56.61); H, 6.13 (6.03); N, 8.11 (7.78)%. FTIR (Nujol, cm⁻¹, selected bands): 3029 (w), 2932 (m), 2855 (m), 1604 (m), 1488 (m), 1292 (s), 1136 (s), 958 (s), 797 (s), 654 (s). λ_{max}, nm (MeCN, ε, M⁻¹cm⁻¹): 700 (120), 485 (300). EPR (1:1 DMF:THF, 77 K, parallel mode): g = 16.4.

Physical Methods

Electronic absorption spectra were recorded in a 1 cm cuvette on a Cary 50 spectrophotometer or an 8453 Agilent UV-Vis spectrometer equipped with an Unisoku Unispeks cryostat. Negative mode electrospray ionization electrospray mass spectra were collected using a Micromass MS Technologies LCT Premier Mass Spectrometer. X-band (9.28 GHz) EPR spectra were collected as frozen solutions using a Bruker EMX

spectrometer equipped with an ER041XG microwave bridge. IR spectra were recorded on a Varian 800 Scimitar Series FTIR spectrometer as suspensions in Nujol.

Cyclic voltammetric experiments were conducted using a CHI600C electrochemical analyzer under an N₂ atmosphere with 0.1 M tetrabutylammonium hexafluorophosphate as the supporting electrolyte. A glassy carbon electrode was used for the working electrode with a silver wire reference electrode and a platinum wire counter electrode. A cobaltocenium/cobaltocene couple ([CoCp₂]^{+ / 0}) was used to monitor the reference electrode.

X-Ray Crystallographic Methods. A Bruker SMART APEX II diffractometer was used to collect all the data. The APEX2³⁵ program package was used to determine the unit-cell parameters and for data collections. The raw frame data was processed using SAINT³⁶ and SADABS³⁷ to yield the reflection data file. Subsequent calculations were carried out using the SHELXTL³⁸ program. The structures were solved by direct methods and refined on F² by full-matrix least-squares techniques. The analytical scattering factors³⁹ for neutral atoms were used throughout the analysis. Hydrogen atoms were included using a riding model.

In the three potassium salts, the molecule was located about a two-fold rotation axis and was polymeric. One molecule of dimethylacetamide was disordered and included using multiple components with partial site-occupancy-factors.

In (NMe₄)₂[Cu₂(tbaps)₂], there were three molecules of dimethylacetamide solvent present, and several atoms were disordered and included using multiple components with partial site-occupancy-factors.

In (NEt₄)₂[Co₂(tbaps)₂], the molecule was located about a two-fold rotation axis.

There were several high residuals present in the final difference-Fourier map. It was not possible to determine the nature of the residuals although it was probable that diethylether solvent was present. The SQUEEZE⁴⁰ routine in the PLATON⁴¹ program package was used to account for the electrons in the solvent accessible voids.

In the Ca salt, carbon atom C(38) was disordered and included using multiple components with partial site-occupancy-factors. There was one-half molecule of dimethylacetamide (DMA) solvent present per formula-unit. The DMA was located on an inversion center and was disordered. The solvent atoms were included with site-occupancy-factors = 0.50. There were three high residuals present in the final difference-Fourier map. It was not possible to determine the nature of the residuals although it was probable that diethylether solvent was present. The SQUEEZE routine in the PLATON⁴⁰ program package was used to account for the electrons in the solvent accessible voids

References

- (1) Yamaguchi, J.; Yamaguchi, A. D.; Itami, K. *Angew. Chem. Int. Ed.* **2012**, *51*, 8960–9009.
- (2) Su, B.; Cao, Z.-C.; Shi, Z.-J. *Acc. Chem. Res.* **2015**, *48*, 886–896.
- (3) Li, Y.-Z.; Li, B.-J.; Lu, X.-Y.; Lin, S.; Shi, Z.-J. *Angew. Chem. Int. Ed.* **2009**, *48*, 3817–3820.
- (4) Chirik, P. J.; Wieghardt, K. *Science* **2010**, *327*, 794–795.
- (5) Crabtree, R. H. *New J. Chem.* **2011**, *35*, 18–23.
- (6) Dzik, W. I.; van der Vlugt, J. I.; Reek, J. N. H.; de Bruin, B. *Angew. Chem. Int. Ed.* **2011**, *50*, 3356–3358.
- (7) van der Vlugt, J. I. *Eur. J. Inorg. Chem.* **2011**, *2012*, 363–375.
- (8) Luca, O. R.; Crabtree, R. H. *Chem. Soc. Rev.* **2013**, *42*, 1440–1459.
- (9) Karen J Blackmore; Joseph W Ziller, A.; Heyduk, A. F. *Inorg. Chem.* **2005**, *44*, 5559–5561.
- (10) Haneline, M. R.; Heyduk, A. F. *J. Am. Chem. Soc.* **2006**, *128*, 8410–8411.
- (11) Nguyen, A. I.; Blackmore, K. J.; Carter, S. M.; Zarkesh, R. A.; Heyduk, A. F. *J. Am. Chem. Soc.* **2009**, *131*, 3307–3316.
- (12) Nguyen, A. I.; Zarkesh, R. A.; Lacy, D. C.; Thorson, M. K.; Heyduk, A. F. *Chem. Sci.* **2011**, *2*, 166–169.
- (13) Smith, A. L.; Clapp, L. A.; Hardcastle, K. I.; Soper, J. D. *Polyhedron* **2010**, *29*, 164–169.

- (14) Smith, A. L.; Hardcastle, K. I.; Soper, J. D. *J. Am. Chem. Soc.* **2010**, *132*, 14358–14360.
- (15) Bouwkamp, M. W.; Bowman, A. C.; Lobkovsky, E.; Chirik, P. J. *J. Am. Chem. Soc.* **2006**, *128*, 13340–13341.
- (16) Sylvester, K. T.; Chirik, P. J. *J. Am. Chem. Soc.* **2009**, *131*, 8772–8774.
- (17) Sharma, S. K.; May, P. S.; Jones, M. B.; Lense, S.; Hardcastle, K. I.; MacBeth, C. E. *Chem. Commun.* **2011**, *47*, 1827–1829.
- (18) Villanueva, O.; Weldy, N. M.; Blakey, S. B.; MacBeth, C. E. *Chem. Sci.* **2015**, –.
- (19) MacBeth, C. E.; Golombek, A. P.; Young, V. G.; Yang, C.; Kuczera, K.; Hendrich, M. P.; Borovik, A. S. *Science* **2000**, *289*, 938–941.
- (20) Park, Y. J.; Ziller, J. W.; Borovik, A. S. *J. Am. Chem. Soc.* **2011**, *133*, 9258–9261.
- (21) Park, Y. J.; Cook, S. A.; Sickerman, N. S.; Sano, Y.; Ziller, J. W.; Borovik, A. S. *Chem. Sci.* **2013**, *4*, 717–726.
- (22) Yang, L.; Powell, D. R.; Houser, R. P. *Dalton Trans.* **2007**, 955.
- (23) Villanueva, O. Design and Development of Novel Bis(amidophenyl)amine Redox-active Ligands to Promote Novel Reactivity at First-row Transition Metal Centers. Ph.D. Dissertation, Emory University.
- (24) Klose, A.; Solari, E.; Floriani, C.; Chiesi-Villa, A.; Rizzoli, C.; Re, N. *J. Am. Chem. Soc.* **1994**, *116*, 9123–9135.
- (25) Cotton, F. A.; Daniels, L. M.; Matonic, J. H.; Murillo, C. A. *Inorg. Chim. Acta* **256**, 277–282.
- (26) Tereniak, S. J.; Carlson, R. K.; Clouston, L. J.; Young, V. G.; Bill, E.; Maurice, R.; Chen, Y.-S.; Kim, H. J.; Gagliardi, L.; Lu, C. C. *J. Am. Chem. Soc.* **2014**, *136*, 1842–1855.
- (27) Murillo, C. A. Iron, Cobalt, and Iridium Compounds. In *Multiple Bonds Between Metal Atoms*. Cotton, A. F., Murillo, C. A., Walton, R. A., Eds. Springer Science + Business Media, Inc.: New York, **2005**; 447–464.
- (28) Mankad, N. P.; Rivard, E.; Harkins, S. B.; Peters, J. C. *J. Am. Chem. Soc.* **2005**, *127*, 16032–16033.
- (29) Borovik, A. S.; Murch, B. P.; Que, L.; Papaefthymiou, V.; Munck, E. *J. Am. Chem. Soc.* **1987**, *109*, 7190–7191.
- (30) Gamelin, D. R.; Randall, D. W.; Hay, M. T.; Houser, R. P.; Mulder, T. C.; Canters, G. W.; de Vries, S.; Tolman, W. B.; Lu, Y.; Solomon, E. I. *J. Am. Chem. Soc.* **1998**, *120*, 5246–5263.
- (31) Day, P.; Hush, N. S.; Clark, R. J. H. *Phil. Trans. R. Soc. A* **2008**, *366*, 5–14.
- (32) Canzi, G.; Goeltz, J. C.; Henderson, J. S.; Park, R. E.; Maruggi, C.; Kubiak, C. P. *J. Am. Chem. Soc.* **2014**, *136*, 1710–1713.
- (33) Harkins, S. B.; Peters, J. C. *J. Am. Chem. Soc.* **2004**, *126*, 2885–2893.
- (34) Gupta, R.; Zhang, Z. H.; Powell, D.; Hendrich, M. P.; Borovik, A. S. *Inorg. Chem.* **2002**, *41*, 5100–5106.
- (35) Hagadorn, J. R.; Zahn, T. I.; Que, L., Jr.; Tolman, W. B. *Dalton Trans.* **2003**, 1790–1794.
- (36) Yang, L.; Powell, D. R.; Klein, E. L.; Grohmann, A.; Houser, R. P. *Inorg. Chem.* **2007**, *46*, 6831–6833.

- (37) Mankad, N. P.; Harkins, S. B.; Antholine, W. E.; Peters, J. C. *Inorg. Chem.* **2009**, *48*, 7026–7032.
- (38) Borovik, A. S.; Hendrich, M. P.; Holman, T. R.; Munck, E.; Papaefthymiou, V.; Que, L. *J. Am. Chem. Soc.* **1990**, *112*, 6031–6038.
- (39) APEX2 Version 2010.3-0, Bruker AXS, Inc.; Madison, WI 2010.
- (40) SAINT Version 7.68a, Bruker AXS, Inc.; Madison, WI 2009.
- (41) Sheldrick, G. M. SADABS, Version 2008/1, Bruker AXS, Inc.; Madison, WI 2008.
- (42) Sheldrick, G. M. SHELXTL, Version 2008/4, Bruker AXS, Inc.; Madison, WI 2008.
- (43) International Tables for X-Ray Crystallography 1992, Vol. C., Dordrecht: Kluwer Academic Publishers.
- (44) Spek, A.L. SQUEEZE, *Acta Cryst.* 2015, C71, 9-19.
- (45) Spek, A. L. PLATON, *Acta. Cryst.* 2009, D65, 148-155.

CHAPTER 6

Mononuclear Fe(II) and Co(II) Complexes of a Tridentate, Redox Active Ligand Derivative Containing Sulfonamido Groups

Introduction

As discussed in the previous chapter, one approach to accessing multi-electron transformations with first row transition metal catalysts is the development of redox-active ligands that can contribute electrons to the reaction. I became involved in this effort through a collaboration with Professor Cora MacBeth at Emory University, who observed catalytic C–H bond amination with a cobalt complex of her amidate ligand derivative (refer to Chart 5.1D). My contribution to the collaboration was to incorporate sulfonamido groups within the $[\text{NNN}]^{3-}$ ligand framework in order to modulate the catalytic reactivity of the resulting complexes via secondary coordination sphere interactions. Using a ligand derivative that contained tolyl groups off of the sulfonamido units, I developed a series of dinuclear complexes that were structurally and spectroscopically similar to those that were supported by MacBeth's amidate ligand derivative. In addition, the sulfonamido groups were shown to favor the coordination of bridging secondary metal ions to form oligomeric structures in the solid state, even when the secondary metal ion was added as a crown ether adduct. Together, these results indicated that the ligand derivative containing tolyl groups would likely not support discreet complexes whose reactivity could be influenced by controlled interactions with secondary metal ions, and so a modified derivative was pursued.

Two different avenues are typically used to modulate the properties of metal complexes through modification of the supporting ligand(s): 1) altering the steric bulk to enforce higher or lower coordination numbers or to change the geometry around the

metal center; or 2) adjusting the electronic properties through introduction of electron donating or withdrawing groups to influence the redox properties of the metal center. While the latter method is useful for fine-tuning the properties of a system, the first approach of changing the steric bulk has the ability to significantly alter the structure and reactivity of the resulting complexes. For example, initial coordination studies of the bidentate β -diketiminate ligand system utilized derivatives with alkyl substituents off of the nitrogen atoms, which lead to the characterization of four coordinate, homoleptic complexes of Co(II), Ni(II), and Cu(II) (Figure 6.1A).¹⁻⁵ Modification of the steric properties of this ligand system via introduction of sterically-encumbering 2,6-diisopropylbenzene groups as the N,N' substituents⁶ prevented the coordination of two β -diketiminate ligands to a single metal center and supported the formation of the first

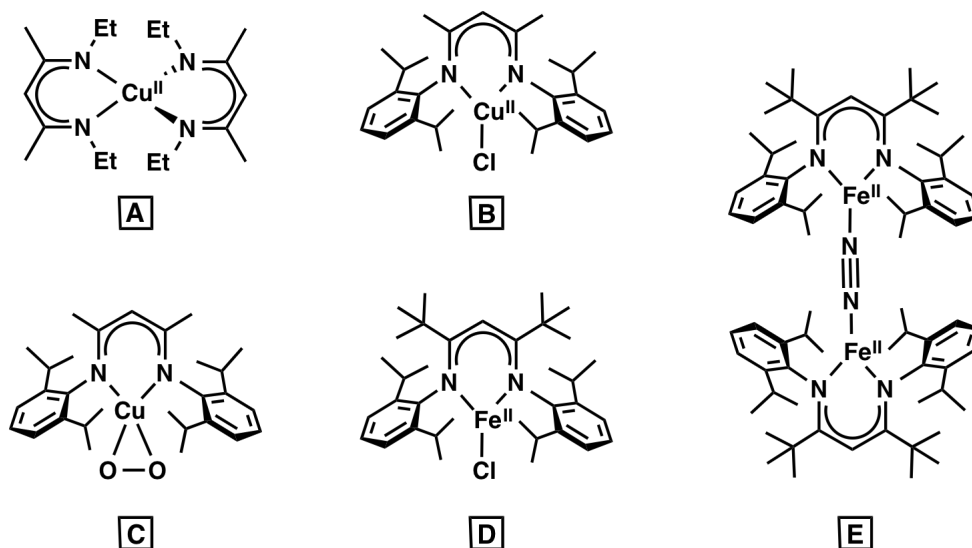


Chart 6.1. Complexes of the β -diketiminate ligand system that illustrate the influence of steric bulk on the coordination properties: A) An example of an early homoleptic complex prepared with a non-bulky derivative; B) The first example of a three coordinate Cu(II) complex made possible by the introduction of 2,6-diisopropylbenzene; C) Cu-superoxide complex isolated from the reaction of the starting Cu(I) complex with O_2 ; D) A three coordinate Fe(II) complex whose isolation required additional steric bulk in the ligand backbone; E) Unusual dinitrogen compound isolated from a three coordinate Fe(I) complex.

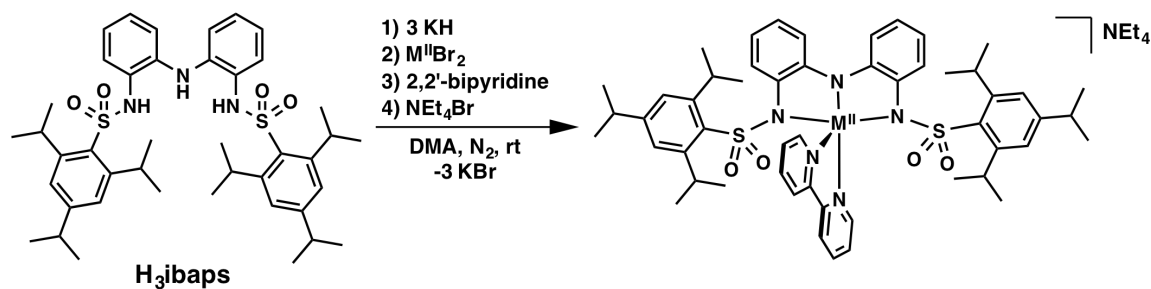
example of a three coordinate Cu(II) complex with trigonal planar geometry (Chart 6.1B).⁷ This bulky ligand derivative was also shown to support a low-coordinate Cu(I) center that reacted with dioxygen to give an unprecedented, low coordinate Cu(II)–superoxo complex while less bulky ligand derivatives gave bis(μ -oxo) bridged dimers (Chart 6.1C).⁸⁻¹⁰ Further modification of the steric properties at the R,R' positions in the backbone via replacement of the methyl groups with tert-butyl substituents provided access to a related three coordinate Fe(II) complex,¹¹ and reduction of the metal center to Fe(I) lead to the isolation of an unusual three coordinate dinitrogen adduct (Chart 6.1D and E).^{12,13} The stabilization of these unusual low coordinate Fe and Cu complexes illustrates the efficacy of this approach for altering the properties of metal complexes.

Based on the successful modification of the coordination properties described above for the β -diketiminato ligand system, the introduction of steric bulk into the sulfonamido [NNN]³⁻ ligand derivative was chosen as the next approach to modifying the coordination properties of the tridentate ligand system. This approach is easily accommodated by the versatility of the reaction to functionalize amines with sulfonamide groups, which allows the R group off of the sulfur atom to be easily substituted for more sterically bulky substituents. Although these groups are not directly connected to the same atom that coordinates to the metal center as they are in the β -diketiminato ligand, the molecular structures of the [tbaps]³⁻ complexes indicate that the tolyl groups lie in close enough proximity to the metal center to influence the coordination properties. The tolyl groups of the [tbaps]³⁻ ligand were therefore replaced with more sterically encumbering triisopropylbenzene groups in an attempt to prevent the formation of the dinuclear structures that were described in Chapter 5. As predicted, this modification of

the ligand significantly influenced the coordination properties of the ligand and resulted in the isolation of monomeric complexes of Fe and Co. The preparation, characterization, and preliminary reactivity studies of these complexes are described in this chapter.

Results and Discussion

Synthetic Methods. The sterically encumbered triisopropylbenzene ligand precursor H₃ibaps was prepared from the sulfonyl chloride and 2-(*o*-aminophenyl)amine in an analogous reaction as the tolyl derivative (H₃tbaps) that was described in Chapter 5. The precursor was isolated in 64% yield as a light pink crystalline solid that contained three distinct N–H vibrations in the Fourier transform infrared (FTIR) spectrum between 3370 and 3213 cm⁻¹. Coordination of the ligand to a metal center was initiated by deprotonation of the ligand precursor with potassium hydride (KH) followed by metalation with a M^{II}Br₂ salt (M^{II} = Fe, Co). In order to complete the coordination sphere of the metal center, an additional mono- or bidentate pyridine ligand derivative (dimethylaminopyridine (DMAP) or 2,2'-bipyridine (bpy)) was added following the metalation step. Finally, *in situ* salt metathesis of the K⁺ ions with NEt₄Br was performed in an attempt to prevent the oligomerization that was caused by coordination of bridging potassium ions in the [tbaps]³⁻ complexes (Scheme 6.1).



Scheme 6.1. Synthetic route to monomeric complexes containing bipyridine. DMAP was also added in the place of 2,2'-bipyridine to give a [Co(II)DMAP]⁻ complex.

Structural Properties. Determination of the molecular structures of the isolated complexes by X-ray diffraction (XRD) methods revealed that the increased steric bulk of the triisopropylbenzene derivative was sufficient to enforce mononuclear species. Three different complexes were structurally characterized that contained one metal ion, one [ibaps]³⁻ ligand, and one DMAP or bpy ligand: NEt₄[Co^{II}(ibaps)DMAP], NEt₄[Co^{II}(ibaps)bpy], and NEt₄[Fe^{II}(ibaps)bpy]. In the NEt₄[Co^{II}(ibaps)DMAP] salt, the Co(II) ion is four coordinate with a distorted seesaw geometry ($\tau_4 = 0.62$) (Figure 6.1, Tables 6.1 and A.9). The primary coordination sphere is made up of the neutral nitrogen donor of the DMAP ligand and the three anionic nitrogen atoms of [ibaps]³⁻. Within the [ibaps]³⁻ ligand, the phenyl rings of the backbone are nearly planar, which causes the three anionic donors to coordinate in a meridional fashion at distances of 1.985(6) and 1.985(7) Å. The bond distances within the backbone indicate that the [ibaps]³⁻ ligand remains in the fully reduced form (Table A.10) The central deprotonated amine has a nearly trigonal planar geometry and coordinates at distances of 1.970(5) Å. The four sulfonamido oxygen atoms are positioned on one face of the complex, forming a

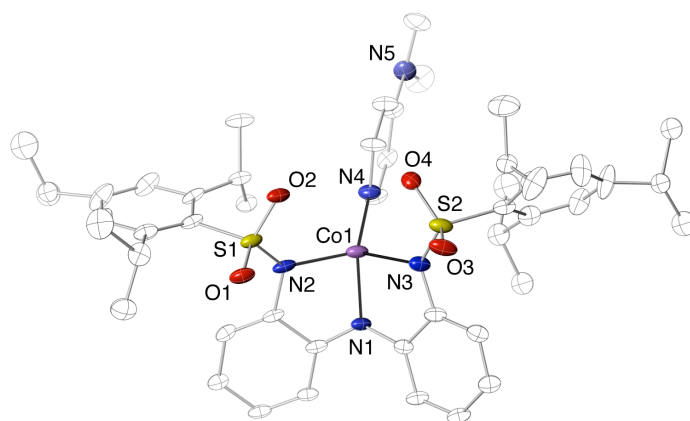


Figure 6.1. Molecular structure of [Co^{II}(ibaps)DMAP]⁻ determined by XRD methods. The NEt₄⁺ counter ion is omitted for clarity. Thermal ellipsoids are drawn at the 50% probability level.

negatively polarized pocket similar to what is observed in [tbaps]³⁻. Note that in the tolyl derivative, this pocket was formed by one sulfonamido group from each ligand in the dinuclear complex, whereas both sulfonamido groups from the single [ibaps]³⁻ ligand form the pocket in the [Co(ibaps)DMAP]⁻ complex. The DMAP ligand coordinates on the face opposite of the sulfonamido groups with a bond distance of 2.037(6) Å.

Table 6.1. Key metrical parameters for NEt₄[Co^{II}(ibaps)DMAP].

Bond Distances (Å)	
Co1–N1	1.970(5)
Co1–N2	1.985(7)
Co1–N3	1.985(6)
Co1–N4	2.037(6)
Bond Angles (°)	
N1–Co1–N2	82.0(2)
N1–Co1–N3	82.9(2)
N2–Co1–N3	141.8(2)
N1–Co1–N4	131.1(2)
N2–Co1–N4	107.4(3)
N3–Co1–N4	107.4(3)
τ ₄ value	0.62

Numerous attempts to crystallize the analogous four coordinate Fe complex with a DMAP ligand were unsuccessful, and so formation of a five coordinate complex using the bidentate ligand bpy was explored as an alternate route to a mononuclear complex. A low resolution molecular structure of the resulting complex was determined by XRD methods and can be only used to discuss connectivity (Figure 6.2A, Table A.9). The complex contains an Fe(II) center whose geometry is best described as midway between square pyramidal ($\tau = 0$) and trigonal bipyramidal ($\tau = 1$) based on an estimated τ value of 0.56. The three anionic donors of the [ibaps]³⁻ ligand coordinate in a similar meridional fashion as was observed in the [Co^{II}(ibaps)DMAP]⁻ complex, and one of the neutral donors of the bpy ligand coordinates almost exactly opposite of the central amine. The sulfonamido oxygen atoms adopt a slightly staggered orientation on one face of the

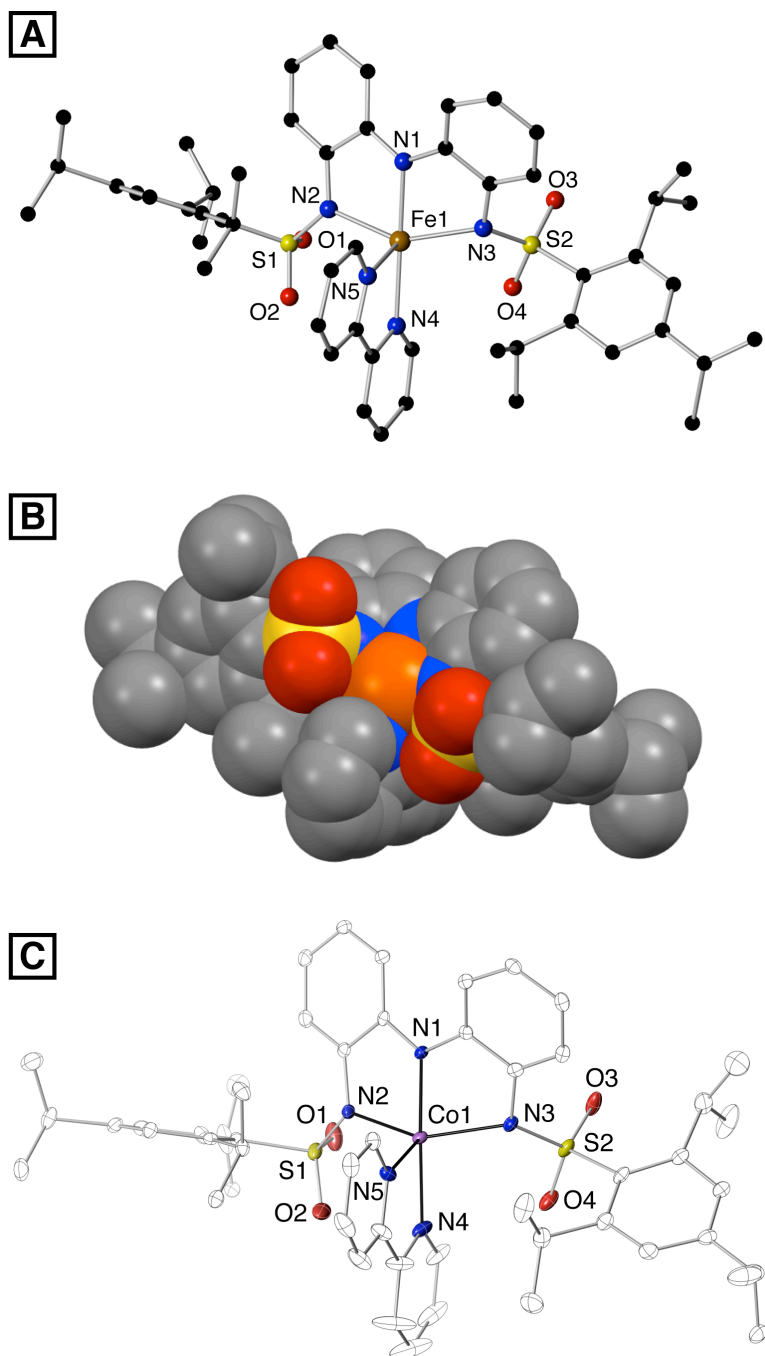


Figure 6.2. Molecular structures of the $[M^{II}(\text{ibaps})\text{bpy}]^-$ complexes determined by XRD methods; A) $[\text{Fe}^{II}(\text{ibaps})\text{bpy}]^-$, B) Space filling model of $[\text{Fe}^{II}(\text{ibaps})\text{bpy}]^-$ illustrating the open coordination site that is framed by the sulfonamido oxygen atoms; C) $[\text{Co}^{II}(\text{ibaps})\text{bpy}]^-$. All of the NEt_4^+ counter ions are excluded for clarity. Thermal ellipsoids of C are drawn at the 50% probability level.

complex and frame an open coordination site on the iron center that is clearly exposed, as illustrated in a space filling representation of the structure (Figure 6.2B). This orientation suggests that an additional metal ion should be able to coordinate to the sulfonamido oxygen atoms and possibly influence the binding and activation of small molecules at the open coordination site.

Table 6.2. Key metrical parameters for $\text{NEt}_4[\text{Co}^{\text{II}}(\text{ibaps})\text{bpy}]$.

Bond Distances (Å)	
Co1–N1	1.970(3)
Co1–N2	2.113(3)
Co1–N3	2.159(3)
Co1–N4	2.132(3)
Co1–N5	2.077(3)
Bond Angles (°)	
N1–Co1–N5	106.1(1)
N1–Co1–N2	79.2(1)
N5–Co1–N2	108.2(1)
N1–Co1–N4	177.2(1)
N5–Co1–N4	76.5(1)
N2–Co1–N4	101.2(1)
N1–Co1–N3	78.9(1)
N5–Co1–N3	102.0(1)
N2–Co1–N3	146.5(1)
N4–Co1–N3	99.4(1)
τ value	0.51

The molecular structure of the $\text{NEt}_4[\text{Co}^{\text{II}}(\text{ibaps})\text{bpy}]$ salt is isomorphous to that of the Fe analog but co-crystallizes with an Et_2O molecule that changes that space group (Table A.9). The geometry around the Co(II) center again is midway between square pyramidal and trigonal bipyramidal, with a calculated τ value of 0.52 (Figure 6.2C, Tables 6.2 and A.10). One neutral pyridine donor is again opposite of the central deprotonated amine with an angle of $177.2(1)^\circ$, which lengthens the $\text{N}_{\text{pyr}}\text{--Co}$ distance by $0.055(3)$ Å relative to the other pyridine donor ($2.132(3)$ vs. $2.077(3)$ Å, respectively). The bond distances to the sulfonamido nitrogen donors of the $[\text{ibaps}]^{3-}$ ligand are

elongated by approximately 0.15 Å relative to the four-coordinate DMAP complex, which is consistent with the increase in the coordination number. An open coordination site on the Co(II) center is again framed by the sulfonamido oxygen atoms.

Spectroscopic Characterization. The EPR spectra of the three characterized [ibaps]³⁻ complexes support their formulations as mononuclear species in solution. The spectrum of $\text{NEt}_4[\text{Co}^{\text{II}}(\text{ibaps})\text{DMAP}]$ contains features at $g = 4.4$ and 2.02 that are indicative of an $S = 3/2$ spin state for a Co(II) center with approximately axial symmetry (Figure 6.3A). A hyperfine pattern of 8 lines (one unresolved) with $A = 74$ G on the $g = 2$ signal further supports the formulation as a mononuclear Co(II) complex. The parallel mode spectrum obtained of the $\text{NEt}_4[\text{Fe}^{\text{II}}(\text{ibaps})\text{bpy}]$ salt at 10 K is also indicative of a high spin Fe(II) center, with a sharp feature at $g = 9.0$ that is consistent with an $S = 2$ spin state (Figure 6.3B).^{14,15} Finally, a complicated spectrum is observed for the $\text{NEt}_4[\text{Co}^{\text{II}}(\text{ibaps})\text{bpy}]$ salt with features at $g = 5.94$, 2.35, and 2.23 (Figure 6.3C). The position of these features is not immediately explainable by either an $S = 1/2$ or an $S = 3/2$ electronic configuration; although the signal in the $g = 2$ region is similar to the

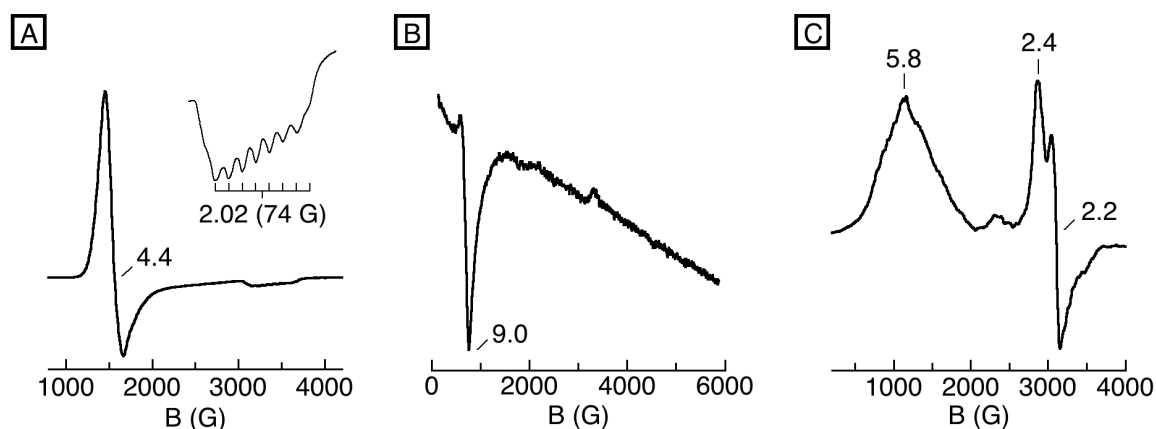


Figure 6.3. EPR spectra of the monomeric M(II) complexes at 10 K: A) 10 mM $\text{NEt}_4[\text{Co}^{\text{II}}(\text{ibaps})\text{DMAP}]$ in THF; B) parallel mode spectrum of 1 mM $\text{NEt}_4[\text{Fe}^{\text{II}}(\text{ibaps})\text{bpy}]$ in 1:1 THF:Et₂O; C) 10 mM $\text{NEt}_4[\text{Co}^{\text{II}}(\text{ibaps})\text{bpy}]$ in THF.

spectrum observed for a five-coordinate, low spin, square pyramidal Co(II) complex, the $g = 5.8$ signal for $[\text{Co}^{\text{II}}(\text{ibaps})\text{bpy}]^-$ does not fit with this spin state.¹⁶ The location of the features could be assigned to a highly rhombic $S = 3/2$ system, but their shapes do not match this description.¹⁵ Further studies are therefore needed to understand the spin state and EPR spectrum of this complex.

Redox Chemistry. The electrochemical properties of the three structurally characterized mononuclear complexes were examined by cyclic voltammetry and chemically probed by reaction with FcBF_4 . The $\text{NEt}_4[\text{Co}^{\text{II}}(\text{ibaps})\text{DMAP}]$ salt exhibits the fewest accessible redox processes of the three complexes, with three total events observed in the cyclic voltammogram (Figure 6.4). Two quasireversible oxidations are observed, one of which occurs at a potential negative of $\text{Fc}^{0/+}$ (-0.68 V). The third event is an irreversible oxidation that occurs at 0.9 V.

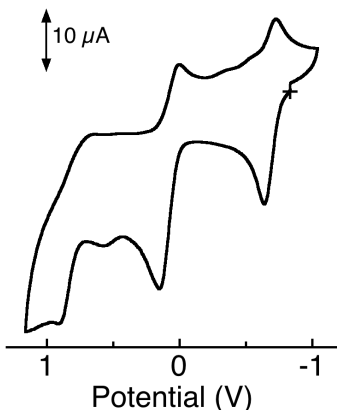


Figure 6.4. Cyclic voltammogram of $\text{NEt}_4[\text{Co}^{\text{II}}(\text{ibaps})\text{DMAP}]$ in MeCN referenced to $\text{Fc}^{0/+}$ (1mM, 0.1 M TBAP, 100 mV/s, with cobaltocenium hexafluorophosphate as an internal standard).

As predicted based on the cyclic voltammogram, the $[\text{Co}^{\text{II}}(\text{ibaps})\text{DMAP}]^-$ complex reacts with one equivalent of FcBF_4 at -80 °C to generate an absorption spectrum with an intense band at 878 nm ($\epsilon_M = 8300$) and additional features at higher

energy (Figure 6.5). Furthermore, in the corresponding EPR experiment, the $S = 3/2$ signal of the Co(II) center nearly disappears with the addition of one equivalent of FcBF₄. This almost silent perpendicular mode spectrum could result from either metal-based or ligand-based oxidation; oxidation of the Co(II) center to Co(III) would give a silent spectrum in perpendicular mode, and the $S = 1$ signal that would be expected if the complex remains high spin after oxidation would be difficult to detect in parallel mode. Oxidation of the ligand backbone would generate a ligand-based radical that would couple with the unpaired electrons on the Co(II) center to give a species with integer spin, which would again be difficult to detect with EPR spectroscopy.

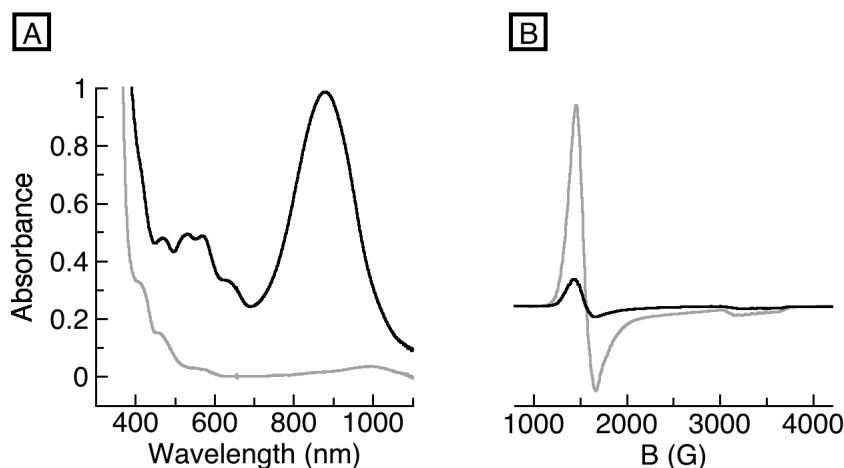


Figure 6.5. Spectral changes upon addition of 1 equivalent of FcBF₄ (black) to NEt₄[Co^{II}(ibaps)DMAP] (grey) in THF at -80 °C: A) UV-vis spectra of a 0.12 mM solution, and B) EPR spectra of 10 mM solutions collected at 10 K. The $g = 4.4$ signal in the oxidized sample is thought to arise from an error in stoichiometry.

Both the [Fe^{II}(ibaps)bpy]⁻ and [Co^{II}(ibaps)bpy]⁻ complexes exhibit rich and reversible electrochemical properties by cyclic voltammetry, with three reversible oxidation events observed for both complexes (Figure 6.6A and B). The first of these oxidations occur at the same potential for both metal complexes in tetrahydrofuran

(THF), which suggests that this event is ligand-based (Table 6.3). The second oxidation occurs at a slightly more negative potential for the Fe complex and is therefore assigned as the $M^{II/III}$ couple based on the lower 3rd ionization potential of Fe(II) compared to Co(II).¹⁷ Finally, a third reversible oxidation is observed only in acetonitrile (MeCN) for the Fe complex; in THF, this oxidation is irreversible, and introduces additional irreversible reduction features that are not observed when the scan is stopped at 0.4 V (Figure 6.6C). The assignment of this final oxidation has not been determined.

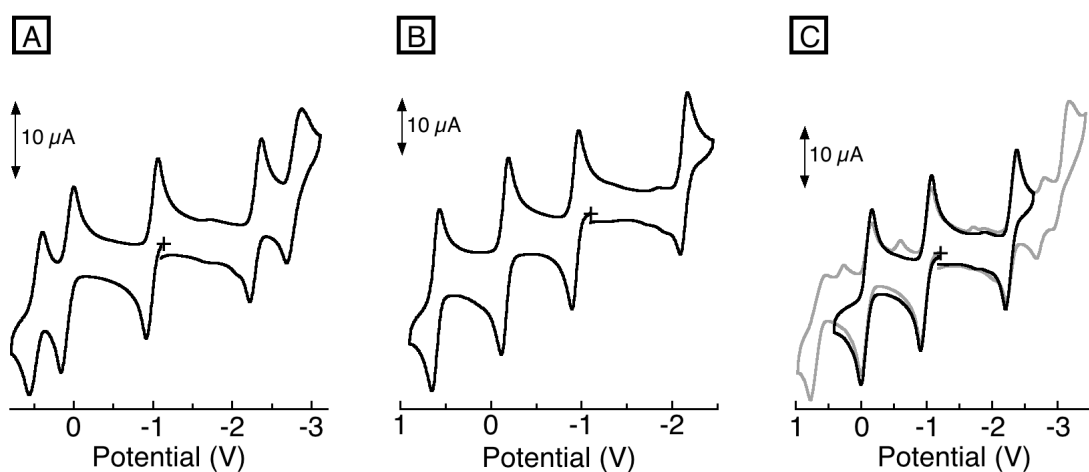


Figure 6.6. Cyclic voltammograms of A) $NEt_4[Co^{II}(ibaps)bpy]$ in THF, B) $NEt_4[Fe^{II}(ibaps)bpy]$ in MeCN, and C) $NEt_4[Fe^{II}(ibaps)bpy]$ in THF showing the irreversible behavior observed when the potential is scanned to the edges of the solvent window (grey). Conditions for all experiments are 1 mM complex, 0.1 M TBAP, 100 mV/s, with cobaltocenium hexafluorophosphate as an internal standard. Potentials are referenced to $Fc^{0/+}$.

Table 6.3. Electrochemical potentials (V vs. $Fc^{0/+}$) of the $[M^{II}(ibaps)bpy]^-$ complexes in THF and MeCN.

		$[Fe^{II}(ibaps)bpy]^-$		$[Co^{II}(ibaps)bpy]^-$	
		THF	MeCN	THF	MeCN
Oxidations	$E_{1/2}(1)$	-0.99	-0.94	-0.99	-0.81
	$E_{1/2}(2)$	-0.53	-0.15	0.08	-0.09
	$E_{1/2}(3)$	–	0.60	0.47	0.45
Reductions	$E_{1/2}(1)$	-2.29	-2.09	-2.29	-2.17
	$E_{1/2}(2)$	–	–	-2.78	–

In addition to the three oxidative events observed for $[\text{Fe}^{\text{II}}(\text{ibaps})\text{bpy}]^-$ and $[\text{Co}^{\text{II}}(\text{ibaps})\text{bpy}]^-$, both complexes exhibit reversible reduction chemistry, with one reduction event observed for $[\text{Fe}^{\text{II}}(\text{ibaps})\text{bpy}]^-$ and two events observed for $[\text{Co}^{\text{II}}(\text{ibaps})\text{bpy}]^-$ (Figure 6.6A and B). Additional reduction events are observed for $[\text{Fe}^{\text{II}}(\text{ibaps})\text{bpy}]^-$ when the potential is scanned to the edge of the solvent window, but this again introduced irreversible features that were not observed when the window was limited to -2.6 V (Figure 6.6C). The only reversible reduction in the Fe complex and the first reduction event of the Co analog both occur at -2.29 V in THF, which again suggests that this reduction is ligand-based. However, the $[\text{ibaps}]^{3-}$ ligand is already in its most reduced form and so this reduction must be localized on the bpy ligand. Similar potentials have been observed for the reduction of bpy in other transition metal complexes.¹⁸⁻²⁰ The second reduction at -2.78 V in the Co complex is assigned to the $\text{Co}^{\text{II/I}}$ couple. The four total redox events that occur at or below the potential of $\text{Fc}^{0/+}$ suggest the exciting possibility that a four-electron chemical transformation should be accessible from the doubly-reduced $[\text{Co}(\text{ibaps})\text{bpy}]^{3-}$ complex.

The observation of two reversible oxidative features that are at or below the reduction potential of $\text{Fc}^{0/+}$ in the $[\text{Fe}^{\text{II}}(\text{ibaps})\text{bpy}]^-$ and $[\text{Co}^{\text{II}}(\text{ibaps})\text{bpy}]^-$ complexes indicates that both of these complexes should react with two equivalents of FcBF_4 . Indeed, titration of one and two equivalents of FcBF_4 into UV-vis samples of these complexes at -80 °C generates two new spectra for each (Figure 6.7A and B). The singly-oxidized $[\text{Fe}(\text{ibaps})\text{bpy}]$ and $[\text{Co}(\text{ibaps})\text{bpy}]$ complexes share several spectral similarities including broad absorption bands at around 650 nm and 1000 nm that support the assignment of the first oxidation as ligand-based event (Figure 6.7C). In contrast, no clear

similarities are observed between the doubly-oxidized species, which is consistent with metal-based oxidation by the second equivalent of FcBF₄.

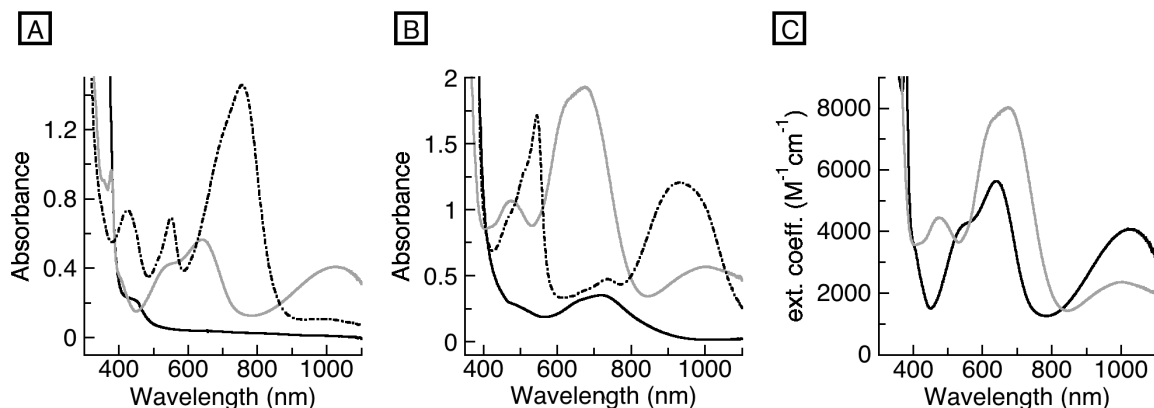


Figure 6.7. Spectral changes upon addition of 1 equivalent (grey) and 2 equivalents (dashed black) of FcBF₄ to THF solutions of the NEt₄[M^{II}(ibaps)bpy] salts (black) at -80 °C: A) 0.1 mM Fe and B) 0.24 mM Co. C) Overlay of the singly oxidized spectra of Fe (black) and Co (grey).

The assignments of the oxidation events in the [Fe^{II}(ibaps)bpy]⁻ and [Co^{II}(ibaps)bpy]⁻ complexes are less clear in the corresponding EPR experiments. In NEt₄[Fe^{II}(ibaps)bpy], the first oxidation generates an $S = 5/2$ spectrum with features at $g = 8.9$ and 4.3 that are typically associated with a rhombic Fe(III) signal (Figure 6.8A). This suggests that the Fe center and not the ligand becomes oxidized with the first equivalent of FcBF₄. However, the possibility that the ligand is first oxidized to generate a radical that couples ferromagnetically with the four unpaired electrons of the Fe(II) center cannot be ruled out. Addition of a second equivalent of FcBF₄ results in a nearly silent perpendicular mode spectrum, which would be expected regardless of the location of oxidation. In NEt₄[Co^{II}(ibaps)bpy], reaction with one equivalent of FcBF₄ generates a silent spectrum in perpendicular mode that could result from oxidation of the Co center to give an $S = 1$ species, or oxidation of the ligand to generate a radical that couples with the Co(II) center. After the second oxidation, a broad $g = 2$ signal is observed with a poorly

resolved hyperfine pattern that has yet to be fit (Figure 6.8B). However, the complexity of the pattern suggests a ligand radical coupled with the Co(III) center.

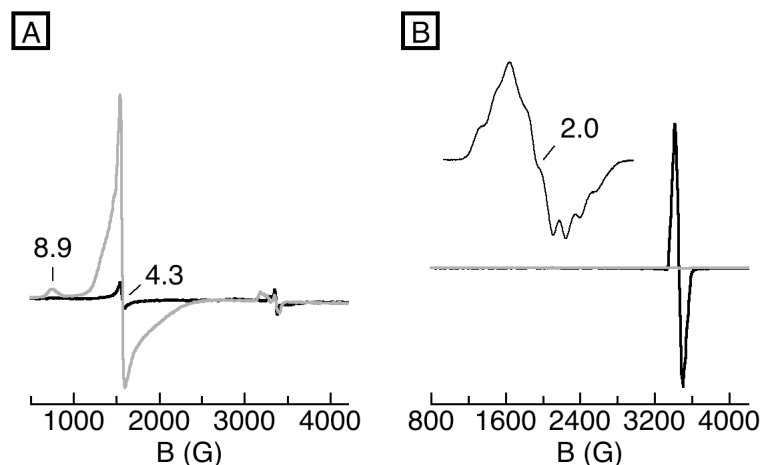


Figure 6.8. Spectral changes upon addition of 1 equivalent (grey) and 2 equivalents (black) of FcBF_4 to THF solutions of the $\text{NEt}_4[\text{M}^{\text{II}}(\text{ibaps})\text{bpy}]$ complexes at $-80\text{ }^\circ\text{C}$: A) 5 mM Fe collected at 77K and B) 10 mM Co collected at 10K.

Preliminary Reactivity Studies. As predicted by the low oxidation potentials of the $[\text{ibaps}]^{3-}$ complexes, all three species react rapidly with dioxygen both in the solid state and in solution. However, the products of the reactions with O_2 are not stable at room temperature, so the reactions were examined at $-100\text{ }^\circ\text{C}$ in THF by UV-vis and EPR spectroscopy. Under these conditions, the $\text{NEt}_4[\text{Co}(\text{ibaps})\text{DMAP}]$ salt reacts with excess O_2 to generate a moderately stable species with optical features at 500, 630, 770, and 994 nm (Figure 6.9A). The corresponding EPR experiment resulted in a decrease in the $g = 4.4$ signal of the Co(II) complex and the appearance of a new signal at $g = 2.2$ that contains a complicated hyperfine pattern (Figure 6.9B). These combined optical and EPR spectral changes indicate that the Co center reacts readily with dioxygen, but the identity

of the product has not yet been determined. One possibility is a Co(III)–superoxide species, which is known to give similarly complicated signals at around $g = 2$.²¹⁻²³

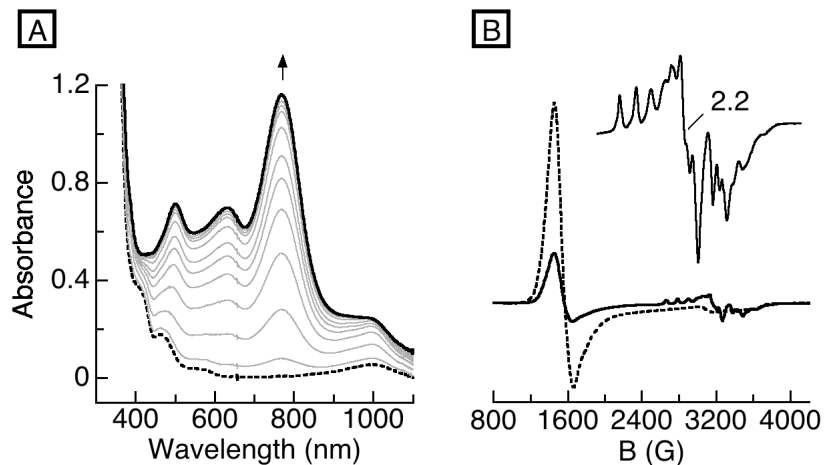


Figure 6.9. Spectral changes (solid black) upon addition of excess O_2 to $NEt_4[Co^{II}(ibaps)DMAP]$ (dashed black) in THF at $-100\text{ }^\circ\text{C}$: A) UV-vis spectra of a 0.12 mM solution and B) EPR spectra of 10 mM solutions at 10 K with an expansion of the $g=2$ signal. The spectrum of the Co(II) starting complex is shown for reference.

Signals at $g = 2$ were also observed from the reactions of the $[M^{II}(ibaps)bpy]^-$ complexes with excess O_2 at $-100\text{ }^\circ\text{C}$. In the Co complex, this $g = 2$ signal is broad and contains an unresolved hyperfine pattern (Figure 6.10A). The corresponding UV-vis experiment shows nearly isosbestic conversion between the 719 nm band of the Co(II) starting complex and a sharp band at 520 nm of the product. An additional broad low energy band at approximately 900 nm also grows in (Figure 6.10B). In the Fe complex, the $g = 2$ signal appeared to contain multiple species based on a hyperfine pattern that partially fits to coupling with ^{14}N ($A_N = 24\text{ G}$) (Figure 6.10C). The optical spectrum that corresponds to this EPR signal contains features at 542, 628, and 1030 nm (Figure 6.10D) and is quite similar to the spectrum obtained from one-electron oxidation with $FcBF_4$;

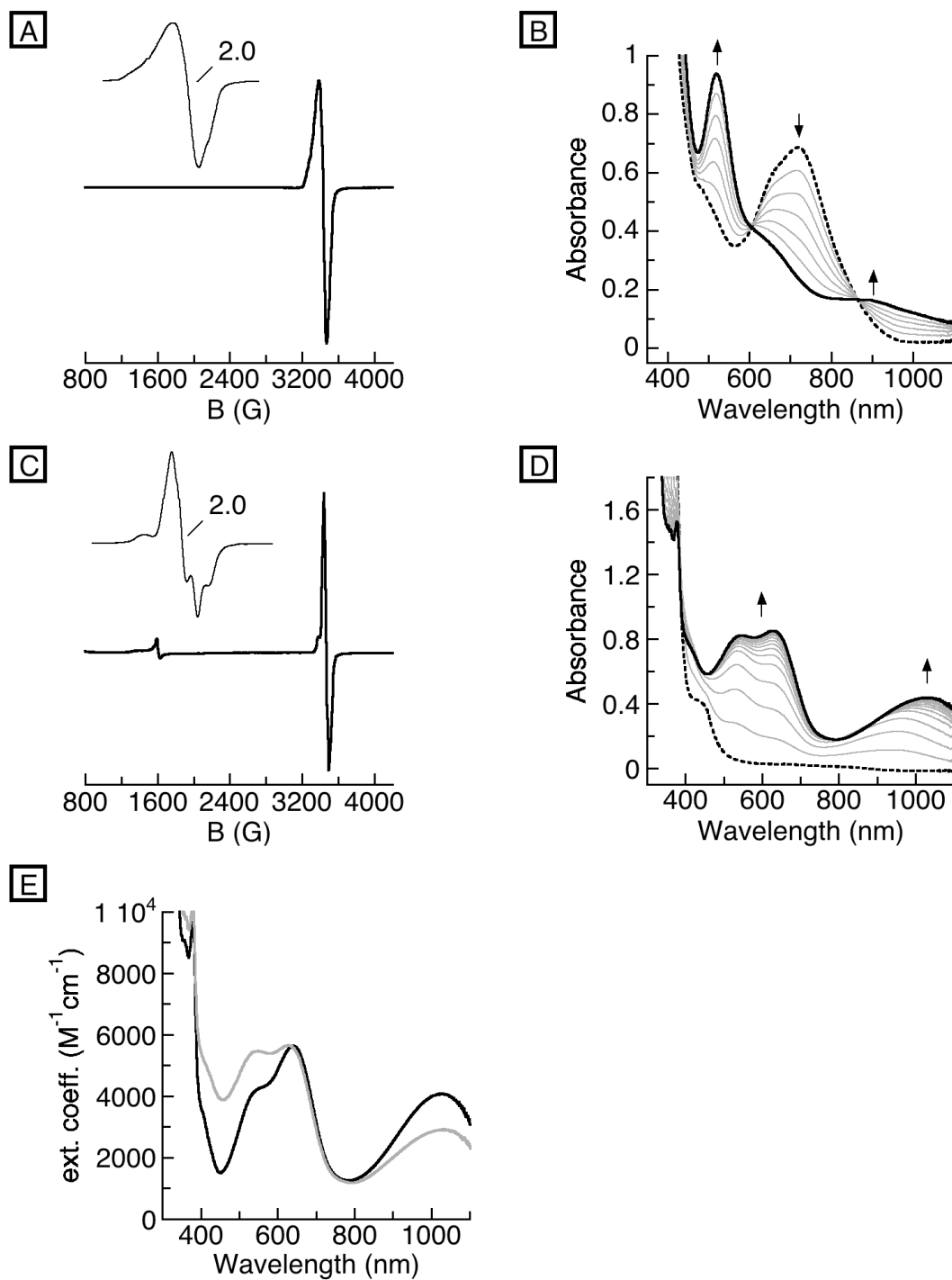


Figure 6.10. Spectral changes (solid black) upon addition of excess O₂ to the NEt₄[M^{II}(ibaps)bpy] complexes (dashed black) in THF at -100 °C: A) EPR spectrum of 10 mM Co at 10 K with an expansion of the g=2 signal; B) UV-vis spectra of a 0.12 mM Co solution; C) EPR spectrum of 6 mM Fe at 10 K with an expansion of the g=2 signal; D) UV-vis spectra of a 0.15 mM Fe solution; E) Comparison of the optical spectra from the reactions of NEt₄[Fe^{II}(ibaps)bpy] with 1 equivalent of FcBF₄ at -80 °C (black) and excess O₂ at -100 °C (grey).

although the intensities of the features are slightly different, the spectrum from one equivalent of FcBF₄ also contains bands at 540, 630, and 1030 nm (Figure 6.10E). These similarities in the spectra suggest that the reaction with O₂ might proceed through an outer sphere electron transfer process to give a singly-oxidized species. However, the EPR spectra of the two reactions are significantly different—while the FcBF₄ reaction generates a spectrum with an S = 5/2 signal (Figure 6.8A), the low temperature reaction with O₂ gives rise to multiples species with g = 2 signals (Figure 6.10C). Therefore, this reaction must be more complicated than outer sphere electron transfer, and further study is needed to determine the identities of the products.

Addition of a Secondary Metal Ion. In the molecular structures of the [Co^{II}(ibaps)bpy][−] and [M^{II}(ibaps)bpy][−] complexes, the sulfonamido oxygen atoms are located spatially near to one another and are not sterically encumbered by the [ibaps]^{3−} and auxiliary pyridine ligands. This positioning suggests that a secondary metal ion that is capped by a crown ether molecule should be able to bind within the negatively polarized pocket created by these oxygen atoms and form discrete heterobimetallic complexes similar to those discussed in Chapter 2. In order to test this premise, Ca(OTf)₂/15-crown-5 was added to the [Co^{II}(ibaps)bpy][−] complex, and single crystals were grown from diethyl ether (Et₂O) via vapor diffusion into a concentrated MeCN solution. However, the molecular structure determined by XRD methods did not contain a Ca(II) ion within the secondary sphere (Figure 6.11, Table A.9). Instead, the central nitrogen of the [ibaps]^{3−} backbone was protonated to give a neutral complex, [Co^{II}(Hibaps)bpy]. This caused an elongation of the Co–N₁ bond by 0.326 Å relative to the anionic complex and a distortion in the backbone such that the two phenyl rings are

nearly orthogonal to one another (Table 6.4). A weak hydrogen bonding interaction is observed between the protonated amine and a sulfonamido oxygen atom, which has rotated around such that the two sulfonamido groups are no longer on the same face. The source of the proton to give this neutral complex is not known, but the elucidation of this structure reveals an unexpected flexibility in the coordination properties of the [ibaps]³⁻ ligand framework and suggests an additional variable that may be used to further tune to properties of the monomeric complexes.

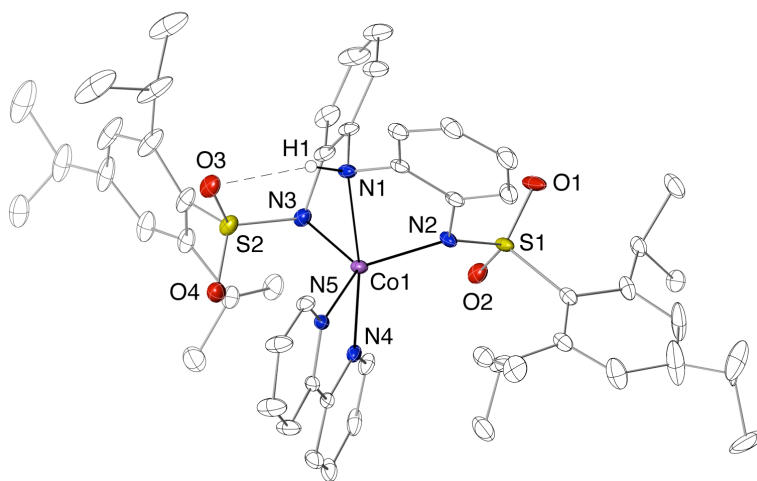


Figure 6.11. Molecular structure of [Co^{II}(Hibaps)bpy] determined by XRD methods. Thermal ellipsoids are drawn at the 50% probability level.

Summary and Conclusions

Introduction of steric bulk into a sulfonamido derivative of the [NNN]³⁻ ligand framework provided access to a set of mononuclear complexes via coordination of an additional mono- or bidentate pyridine donor. A four coordinate Co(II) complex was prepared with DMAP as the additional ligand, and five coordinate complexes of Co(II) and Fe(II) were prepared with 2,2'-bipyridine. The five coordinate complexes exhibit rich and reversible electrochemistry, with three oxidation events and at least one reduction event observed for each complex. The first oxidation and the first reduction were both

Table 6.4. Key metrical parameters for the [Co^{II}(Hibaps)bpy] complex.

Bond Distances (Å)	
Co1–N1	2.296(2)
Co1–N2	2.018(2)
Co1–N3	2.039(2)
Co1–N4	2.070(2)
Co1–N5	2.070(2)
O3–N1	3.043
Bond Angles (°)	
N2–Co1–N3	122.77(9)
N2–Co1–N4	114.04(9)
N3–Co1–N4	97.11(9)
N2–Co1–N5	110.69(9)
N3–Co1–N5	121.58(9)
N4–Co1–N5	80.01(9)
N2–Co1–N1	75.26(9)
N3–Co1–N1	77.52(9)
N4–Co1–N1	170.67(9)
N5–Co1–N1	96.20(8)
τ value	0.82

assigned to ligand-based redox processes based on the match in potentials between the Co and Fe complexes. Similar optical features for the oxidation of each complex with one equivalent of FcBF₄ support this assignment, although the corresponding EPR experiments are not as clear.

All three mononuclear complexes react rapidly with dioxygen to form intermediates that could be stabilized at -100 °C. The optical features of the intermediate that was observed for the five coordinate Fe complex resemble those of the product from one-electron oxidation with FcBF₄, although differences in the corresponding EPR spectra rule out the possibility that the reaction with dioxygen is simply an outer sphere electron transfer process. Identification of this and other intermediates will require continued in depth study with a variety of spectroscopic techniques.

The isolation of both four and five coordinate metals centers and a neutral complex in which the central amine was protonated illustrates the coordinative versatility of the [ibaps]³⁻ ligand. This flexibility adds variables that can be utilized to optimize the reactivity of the corresponding complexes in addition to the ability to modulate the reactivity via secondary sphere interactions with the sulfonamido oxygen atoms. Furthermore, the synthetic versatility of the reaction to prepare sulfonamido ligand derivatives allows for continued modification of the steric and electronic properties of the ligand framework. These combined properties make this ligand system an ideal candidate for implementing the principles of rational molecular design in order to impart desired properties and function.

Experimental Details

General Methods

Syntheses of metal complexes were completed under a nitrogen atmosphere in a VAC drybox. Solvents were sparged with argon and dried over columns containing Q-5 and molecular sieves. All reagents were purchased from commercial suppliers and used as received unless otherwise noted. Potassium hydride as 30% suspensions in mineral oil were filtered and washed five times each with Et₂O and pentane and dried under vacuum. The ligand precursor HN(*o*-PhNH₂)₂ was prepared according to literature procedures.²⁴

Ligand Synthesis

N,N'-(azanediylbis(2,1-phenylene))bis(2,4,6-triisopropylbenzenesulfonamide) (H₃ibaps). The triamine (1.28 g, 6.43 mmol) and pyridine (1.52 g, 19.2 mmol) were dissolved in 50 mL of MeCN in the glove box. Tri-isopropylbenzene sulfonyl chloride (4.08 g, 13.5 mmol) was dissolved in 20 mL of Et₂O and added dropwise to the

acetonitrile solution over the course of ten minutes, causing a change from clear orange to heterogeneous dark orange to green. The reaction flask was sealed with a rubber septum, brought out of the glovebox, and fitted with a reflux condenser under a flow of N₂. The reaction was refluxed overnight under N₂ to give a dark red solution. After checking the reaction for completion by ESI-MS, the mixture was concentrated to dryness under vacuum, redissolved in DCM, and washed with 1M HCl until the aqueous layer was no longer colored. The organic layer was further washed with H₂O and brine, dried over MgSO₄, filtered, and concentrated under vacuum to a foam. The ligand precursor was recrystallized from hot iso-octane as light pink crystals in 64% yield (3.0 g). ¹H NMR (500 MHz, CDCl₃, ppm): 9.24, (s, 2H, NH), 7.19 (s, 1H, NH), 7.09 (s, 4H), 6.94 (t, 2H), 6.84 (d, 2H), 6.74 (t, 2H), 6.59 (d, 2H), 3.86 (m, 4H), 2.85 (m, 2H), 1.15 (d, 12H), 1.00 (d, 24H). ¹³C NMR (125 MHz, CDCl₃, ppm): 152.0, 150.0, 140.6, 133.4, 128.2, 127.3, 126.0, 123.4, 121.0, 118.9, 33.2, 29.5, 24.6, 23.4. FTIR (Nujol, cm⁻¹, selected bands): 3370 (NH), 3276 (NH), 3213 (NH), 1597 (m), 1314 (s), 1168 (s), 1040 (m), 881 (m), 759 (m). HRMS (ES⁺): Exact mass calcd (found) for [M + Na]: 754.3688 (754.3680).

Complex Syntheses

NEt₄[Co(ibaps)DMAP]·Et₂O. A solution of H₃ibaps (0.10 g, 0.14 mmol) in 3 mL of DMA was treated with three equivalents of solid KH (16 mg, 0.41 mmol). The reaction was stirred until gas evolution ceased, and then CoBr₂ (30 mg, 0.14 mmol) was added. After 1 h, DMAP and NEt₄Br were added to the reaction, which was stirred for an additional two hours before removing the solvent under vacuum. The resulting tacky residue was further dried by triturating with Et₂O followed by removal of the solvent

under vacuum. The solid was then redissolved in 4 mL of MeCN and filtered through a medium porosity frit to remove three equivalents (48 mg, 0.40 mmol) of insoluble KBr. The product was recrystallized by Et₂O vapor diffusion into the MeCN filtrate to give 0.12 g (86%) of the product as red needle crystals. Elemental analysis calcd (found) for NEt₄[Co(ibaps)DMAP]·Et₂O (C₆₁H₉₄N₆O₅S₂Co): C, 65.74 (65.61); H, 8.50 (8.69); N, 7.54 (7.67)%. FTIR (Nujol, cm⁻¹, selected bands): 1613 (s), 1535 (s), 1346 (s), 1230 (s), 1125 (s), 1018 (s), 960 (s), 807 (s), 734 (s), 652 (s). λ_{max}, nm (THF, ε, M⁻¹cm⁻¹): 406 (sh, 2300), 462 (sh, 1100), 570 (sh, 310), 856 (250). EPR (THF, 10K): g = 4.4, 2.02 (A = 74 G).

NEt₄[Fe(ibaps)bpy]. This complex was prepared according to the same procedure as NEt₄[Co(ibaps)DMAP]·Et₂O, with H₃ibaps (0.10 g, 0.14 mmol), KH (16 mg, 0.41 mmol), FeBr₂ (30 mg, 0.14 mmol), bipyridine (21 mg, 0.14 mmol), and NEt₄Br (29 mg, 0.14 mmol) in 3 mL of DMA. The crude product was redissolved in 8 mL of THF and filtered through a medium porosity frit to remove three equivalents (49 mg, 0.40 mmol) of insoluble KBr. The product was crystallized from Et₂O vapor diffusion into the THF filtrate to give 0.110 g (73%) of the product as dark green needle crystals.

Elemental calcd (found) for NEt₄[Fe(ibaps)bpy] (C₆₀H₈₂N₆O₄S₂Fe): C, 67.27 (67.29); H, 7.72 (8.10); N, 7.84 (7.85) %. FTIR (Nujol, cm⁻¹, selected bands): 1564 (w), 1360 (m), 1231 (s), 1119 (s), 947 (m), 725 (m). λ_{max}, nm (THF, ε, M⁻¹cm⁻¹): 438 (sh, 1800). EPR (1:1 THF:Et₂O, 10 K, parallel mode): g = 9.00.

NEt₄[Co(ibaps)bpy]·Et₂O. This complex was prepared according to the same procedure as NEt₄[Co(ibaps)DMAP]·Et₂O, with H₃ibaps (0.10 g, 0.14 mmol), KH (16 mg, 0.41 mmol), CoBr₂ (30 mg, 0.14 mmol), bipyridine (21 mg, 0.14 mmol), and NEt₄Br

(29 mg, 0.14 mmol) in 3 mL of DMA. The crude product was redissolved in 6 mL of MeCN and filtered through a medium porosity frit to remove three equivalents (49 mg, 0.40 mmol) of insoluble KBr. The product was crystallized from Et₂O vapor diffusion into the MeCN filtrate to give 0.130 g (86%) of the product as green needle crystals.

Elemental analysis calcd (found) for NEt₄[Co(ibaps)bpy] (C₆₄H₉₂N₆O₅S₂Co): C, 66.93 (66.53); H, 8.07 (7.97); N, 7.32 (7.72) %. FTIR (Nujol, cm⁻¹, selected bands): 1597 (m), 1562 (m), 1228 (s), 1118 (s), 1060 (m), 1037 (m), 944 (s), 791 (m), 726 (s). λ_{max}, nm (THF, ε, M⁻¹cm⁻¹): 717 (1300). EPR (THF, 10 K): g = 5.94, 2.35, 2.23.

Electronic Absorption Studies

In a typical experiment, a concentrated stock solution of the metal complex was prepared in the glove box and a portion transferred via syringe to 2.0 mL of THF in a quartz cuvette, which was sealed with a rubber septum. The cuvette was brought out of the glovebox and allowed to equilibrate in the sample holder for ten minutes before the reagent was added via syringe. FcBF₄ was added in volumes of 20 μL per equivalent as a solution in 2:1 THF:MeCN. Dioxygen (1 mL) was injected into to the headspace of the sealed, precooled cuvette via a 10 mL gas tight syringe.

EPR Studies

In a typical experiment, 250 uL of a solution containing the metal complex was transferred via syringe to an EPR tube in the glovebox, which was sealed with a rubber septum. The sample was brought out of the glovebox and cooled in a methanol/liquid nitrogen cold bath at -100 °C for ten minutes before the reagent was added via syringe. FcBF₄ was added in volumes of 20 μL per equivalent as a solution in 2:1 THF:MeCN. Dioxygen (1 mL) was injected into to the headspace via a 10 mL gas tight syringe. After

addition of the reagent, the EPR tube was quickly removed from the cold bath, inverted while tapping the end to cause the solution and reagent to mix, and shaken to return the sample to the end of the tube before returning the tube to the cold bath in as little time as possible. This process was repeated five times to insure complete mixing. A total of 15 minutes after the first mix, the sample tubes were wiped clean of methanol and quickly frozen in liquid nitrogen.

Physical Methods

Electronic absorption spectra were recorded in a 1 cm cuvette on a Cary 50 spectrophotometer or an 8453 Agilent UV-Vis spectrometer equipped with an Unisoku Unispeks cryostat. Negative mode electrospray ionization electrospray mass spectra were collected using a Micromass MS Technologies LCT Premier Mass Spectrometer. X-band (9.28 GHz) EPR spectra were collected as frozen solutions using a Bruker EMX spectrometer equipped with an ER041XG microwave bridge. IR spectra were recorded on a Varian 800 Scimitar Series FTIR spectrometer as suspensions in Nujol.

Cyclic voltammetric experiments were conducted using a CHI600C electrochemical analyzer under an N₂ atmosphere with 0.1 M tetrabutylammonium hexafluorophosphate as the supporting electrolyte. A glassy carbon electrode was used for the working electrode with a silver wire reference electrode and a platinum wire counter electrode. A cobaltocenium/cobaltocene couple ($[\text{CoCp}_2]^{+/0}$) was used to monitor the reference electrode.

X-Ray Crystallographic Methods

A Bruker SMART APEX II diffractometer was used to collect all the data. The APEX2²⁵ program package was used to determine the unit-cell parameters and for data

collections. The raw frame data was processed using SAINT²⁶ and SADABS²⁷ to yield the reflection data file. Subsequent calculations were carried out using the SHELXTL²⁸ program. The structures were solved by direct methods and refined on F² by full-matrix least-squares techniques. The analytical scattering factors²⁹ for neutral atoms were used throughout the analysis.

Hydrogen atoms of NEt₄[Co(ibaps)DMAP] were included using a riding model. There was one molecule of diethylether solvent present. Several carbon atoms were disordered and included using multiple components with partial site-occupancy-factors.

Hydrogen atoms of NEt₄[Co(ibaps)bpy] were included using a riding model. Several atoms were disordered and included using multiple components with partial site-occupancy-factors. It was necessary to restrain the distances within the tetraethylammonium ion. There was one-half molecule of diethylether solvent present. The solvent was located about an inversion center and was disordered.

Hydrogen atoms of [Co(Hibaps)bpy] were either located from a difference-Fourier map and refined (x,y,z and U_{iso}) or were included using a riding model. There was one molecule of diethylether solvent present. Several carbon atoms were disordered and included using multiple components with partial site-occupancy-factors.

The data for NEt₄[Fe(ibaps)bpy] was weak and the structure could not be fully refined. The wR2 value is 0.40.

References

- (1) McGeachin, S. G. *Can. J. Chem.* **1968**, *46*, 1903–1912.
- (2) Bonnett, R.; Bradley, D. C.; Fisher, K. J.; Rendall, I. F. *J. Chem. Soc.* **1971**, 1622–1627.
- (3) Bonnett, R.; Bradley, D. C.; Fisher, K. J. *Chem. Commun.* **1968**, 886.
- (4) Parks, J. E.; Holm, R. H. *Inorg. Chem.* **1968**, *7*, 1408–1416.
- (5) Bourget-Merle, L.; Lappert, M. F.; Severn, J. R. *Chem. Rev.* **2002**, *102*, 3031–

3066.

- (6) Feldman, J.; McLain, S. J.; Parthasarathy, A.; Marshall, W. J.; Calabrese, J. C.; Arthur, S. D. *Organometallics* **1997**, *16*, 1514–1516.
- (7) Holland, P. L.; Tolman, W. B. *J. Am. Chem. Soc.* **1999**, *121*, 7270–7271.
- (8) Spencer, D.; Reynolds, A. M.; Holland, P. L. *Inorg. Chem.* **2002**, *41*, 6307–6321.
- (9) Douglas J E Spencer; Nermeen W Aboeella; Anne M Reynolds; Patrick L Holland, A.; Tolman, W. B. *J. Am. Chem. Soc.* **2002**, *124*, 2108–2109.
- (10) Tolman, W. B. *J. Biol. Inorg. Chem.* **2006**, *11*, 261–271.
- (11) Smith, J. M.; Lachicotte, R. J.; Holland, P. L. *Chem. Commun.* **2001**, 1542–1543.
- (12) Smith, J. M.; Lachicotte, R. J.; Pittard, K. A.; Cundari, T. R.; Lukat-Rodgers, G.; Rodgers, K. R.; Holland, P. L. *J. Am. Chem. Soc.* **2001**, *123*, 9222–9223.
- (13) Holland, P. L. *Acc. Chem. Res.* **2008**, *41*, 905–914.
- (14) Popescu, C. V.; Mock, M. T.; Stoian, S. A.; Dougherty, W. G.; Yap, G. P. A.; Riordan, C. G. *Inorg. Chem.* **2009**, *48*, 8317–8324.
- (15) Que, L. *Physical Methods in Bioinorganic Chemistry: Spectroscopy and Magnetism*; University Science Books: Sausalito, CA, 2000.
- (16) Sharma, A. C.; Borovik, A. S. *J. Am. Chem. Soc.* **2000**, *122*, 8946–8955.
- (17) *Handbook of Chemistry and Physics*; Haynes, W. M., Ed.; 96 ed.; CRC Press/Taylor and Francis: Boca Raton, FL; pp. 10.197–10.199.
- (18) Juris, A.; Balzani, V.; Barigelletti, F.; Campagna, S.; Belser, P.; Zelewsky, von, A. *Coord. Chem. Rev.* **1988**, *84*, 85–277.
- (19) Lowry, M. S.; Goldsmith, J. I.; Slinker, J. D.; Rohl, R.; Pascal, R. A.; Malliaras, G. G.; Bernhard, S. *Chem. Mater.* **2005**, *17*, 5712–5719.
- (20) Braterman, P. S.; Song, J. I.; Peacock, R. D. *Inorg. Chem.* **1992**, *31*, 555–559.
- (21) Walker, F. A. *J. Am. Chem. Soc.* **1970**, *92*, 4235–4244.
- (22) Lancashire, R. L.; Smith, T. D.; Pilbrow, J. R. *J. Chem. Soc., Dalton Trans.* **1979**, 66–70.
- (23) Fielding, A. J.; Lipscomb, J. D.; Que, L. *J. Am. Chem. Soc.* **2012**, *134*, 796–799.
- (24) Sharma, S. K.; May, P. S.; Jones, M. B.; Lense, S.; Hardcastle, K. I.; MacBeth, C. E. *Chem. Commun.* **2011**, *47*, 1827–1829.
- (25) APEX2 Version 2010.3-0, Bruker AXS, Inc.; Madison, WI 2010.
- (26) APEX2 Version 2010.3-0, Bruker AXS, Inc.; Madison, WI 2010.
- (27) Sheldrick, G. M. SADABS, Version 2008/1, Bruker AXS, Inc.; Madison, WI 2008.
- (28) Sheldrick, G. M. SHELXTL, Version 2008/4, Bruker AXS, Inc.; Madison, WI 2008.
- (29) International Tables for X-Ray Crystallography 1992, Vol. C, Dordrecht: Kluwer Academic Publishers.

APPENDIX A

Supplementary Information

Table A.1. Crystallographic data and structure refinement parameters for the molecular structures presented in Chapter 2.

Complex	[(OTf)(15-crown-5)⊃Ba ^{II} -(μ-OH)-Fe ^{III} MST]
Formula	C ₄₄ H ₆₆ BaF ₃ N ₄ O ₁₅ S ₄ •3.5(C ₂ H ₃ N)
Formula weight	1413.12
Crystal system	Orthorhombic
Space group	<i>P</i> 2 ₁ 2 ₁ 2
a (Å)	18.066(2)
b (Å)	24.397(2)
c (Å)	15.011(1)
α (°)	90
β (°)	90
γ (°)	90
Volume (Å ³)	6615.9(9)
Z	4
δ _{calc} (Mg/m ³)	1.419
Goodness-of-fit	1.053
R1	0.0374
wR2	0.0983

Table A.2. Crystallographic data and structure refinement parameters for the molecular structures presented in Chapter 3.

Complex	NMe ₄ [Fe ^{II} MST(OH ₂)]	NMe ₄ [Fe ^{III} -O-MST]
Formula	C ₃₇ H ₅₉ Fe N ₅ O ₇ S ₃	C ₃₇ H ₅₆ Fe N ₅ O ₇ S ₃
Formula weight	837.92	834.89
Crystal system	Monoclinic	Triclinic
Space group	<i>C</i> 2/ <i>c</i>	<i>P</i> $\bar{1}$
a (Å)	26.649(1)	12.5853(5)
b (Å)	9.6756(5)	13.3269(6)
c (Å)	31.478(1)	14.4577(6)
α (°)	90	86.7120(5)
β (°)	90.5615(6)	75.4994(5)
γ (°)	90	84.8241(5)
Volume (Å ³)	8116.3(7)	2336.55(17)
Z	8	2
δ _{calc} (Mg/m ³)	1.371	1.187
Goodness-of-fit	1.036	1.050
R1	0.0309	0.0397
wR2	0.0796	0.1108

Table A.3. Select metrical parameters for $\text{NMe}_4[\text{Fe}^{\text{II}}\text{MST}(\text{OH}_2)]$.

Bond Distances (Å)	
Fe1—O1	2.128(1)
Fe1—N1	2.259(1)
Fe1—N2	2.065(1)
Fe1—N3	1.094(1)
Fe1—N4	2.054(1)
O1···O3	2.696(1)
O1···O5	2.693(1)
O1···O7	3.130(1)
Bond Angles (°)	
O1—Fe1—N1	172.17(5)
N2—Fe1—N3	116.90(5)
N2—Fe1—N4	113.44(5)
N3—Fe1—N4	120.47(5)
τ value	0.86

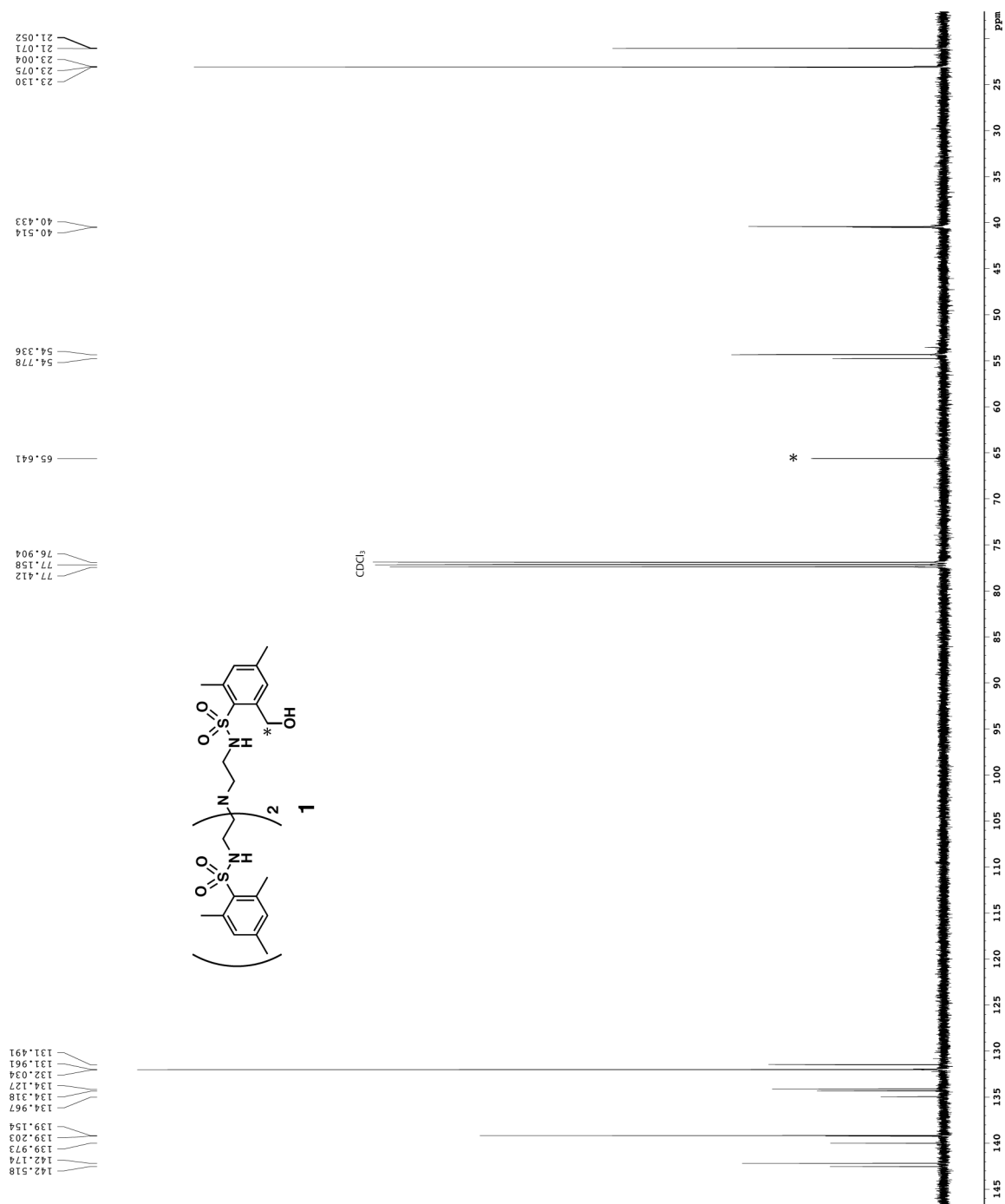


Figure A.2. ^{13}C NMR spectrum of ligand product **1** that was isolated from crystalline $\text{NMe}_4[\text{Fe}^{\text{II}}\text{-O-MST}]$.

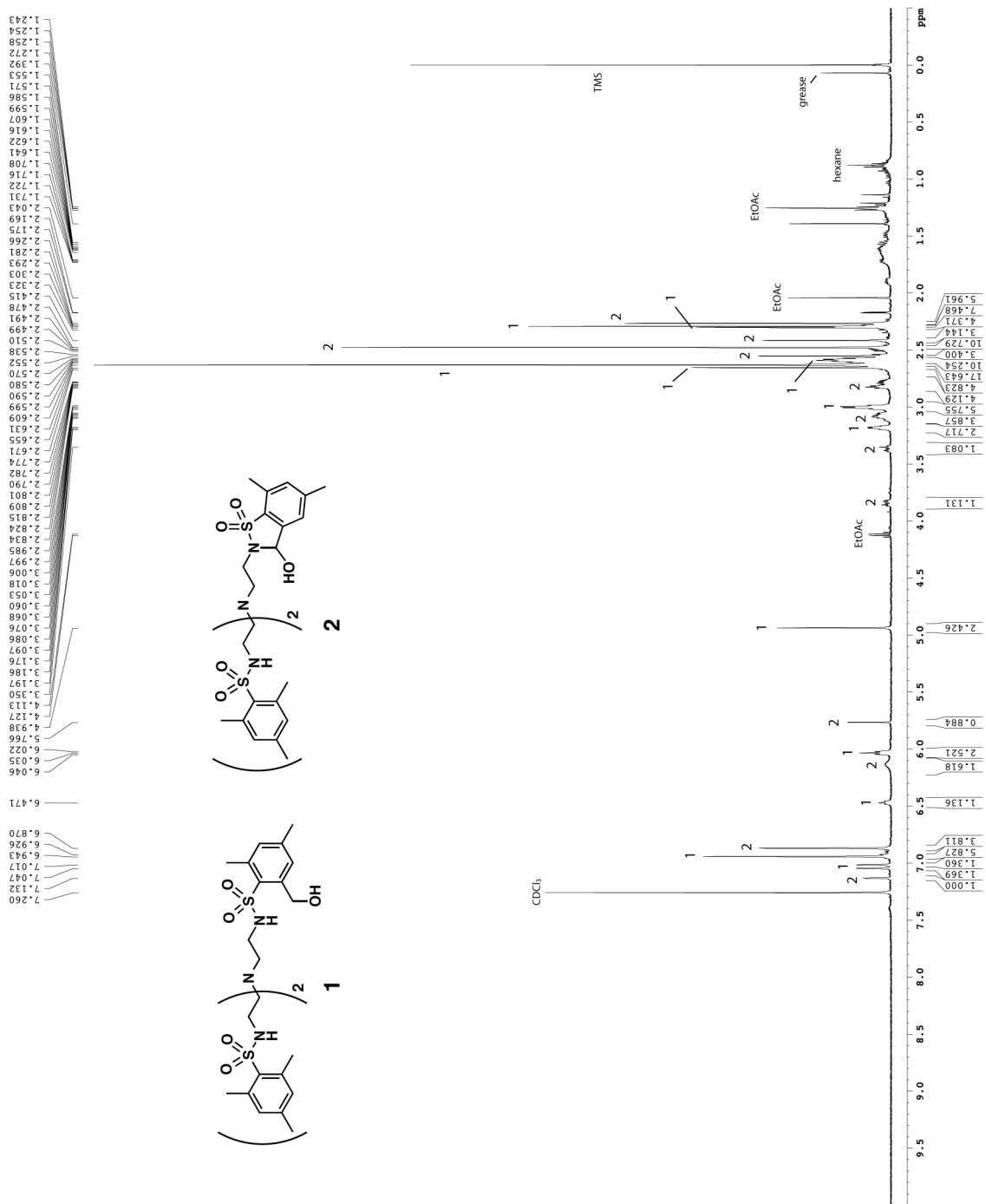


Figure A.3. ^1H NMR spectrum of a mixture of ligand products **1** and **2** that was separated from the remainder of the products via column chromatography.

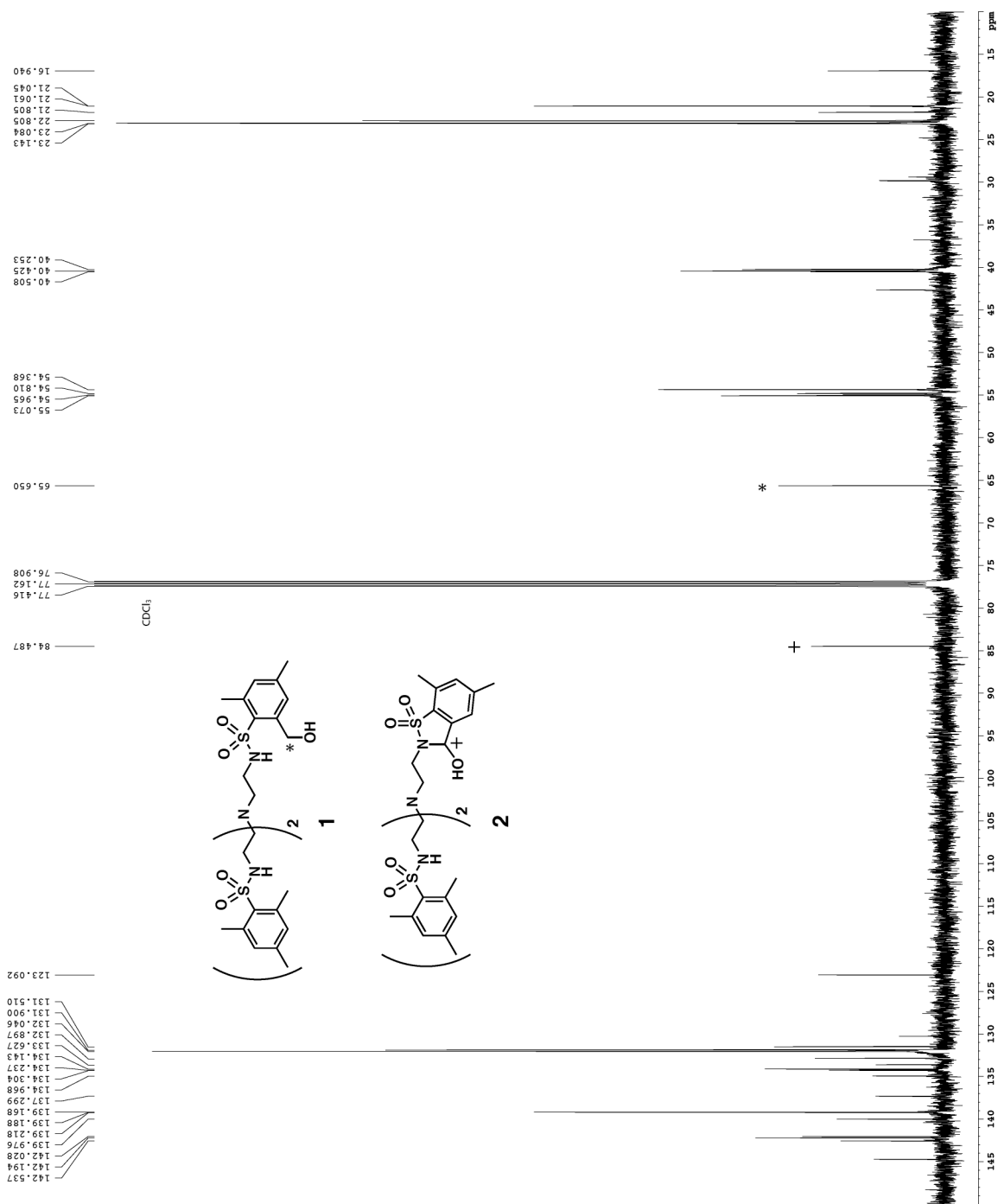


Figure A.4. ^{13}C NMR spectrum of a mixture of ligand products **1** and **2** that was separated from the remainder of the products via column chromatography.

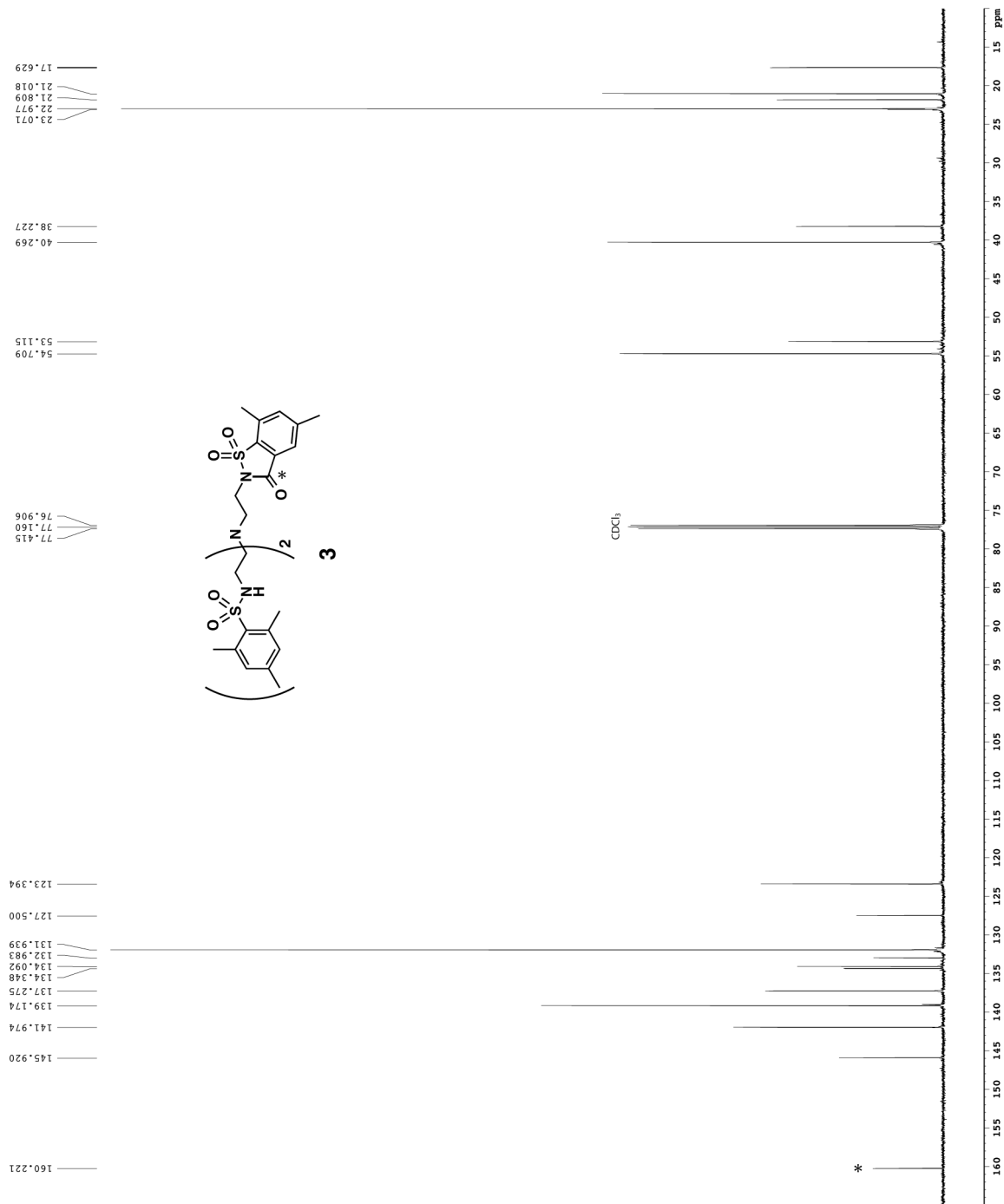


Figure A.6. ^{13}C NMR spectrum of a ligand product **3** with a small impurity of H_3MST that was separated from the remainder of the products via column chromatography.

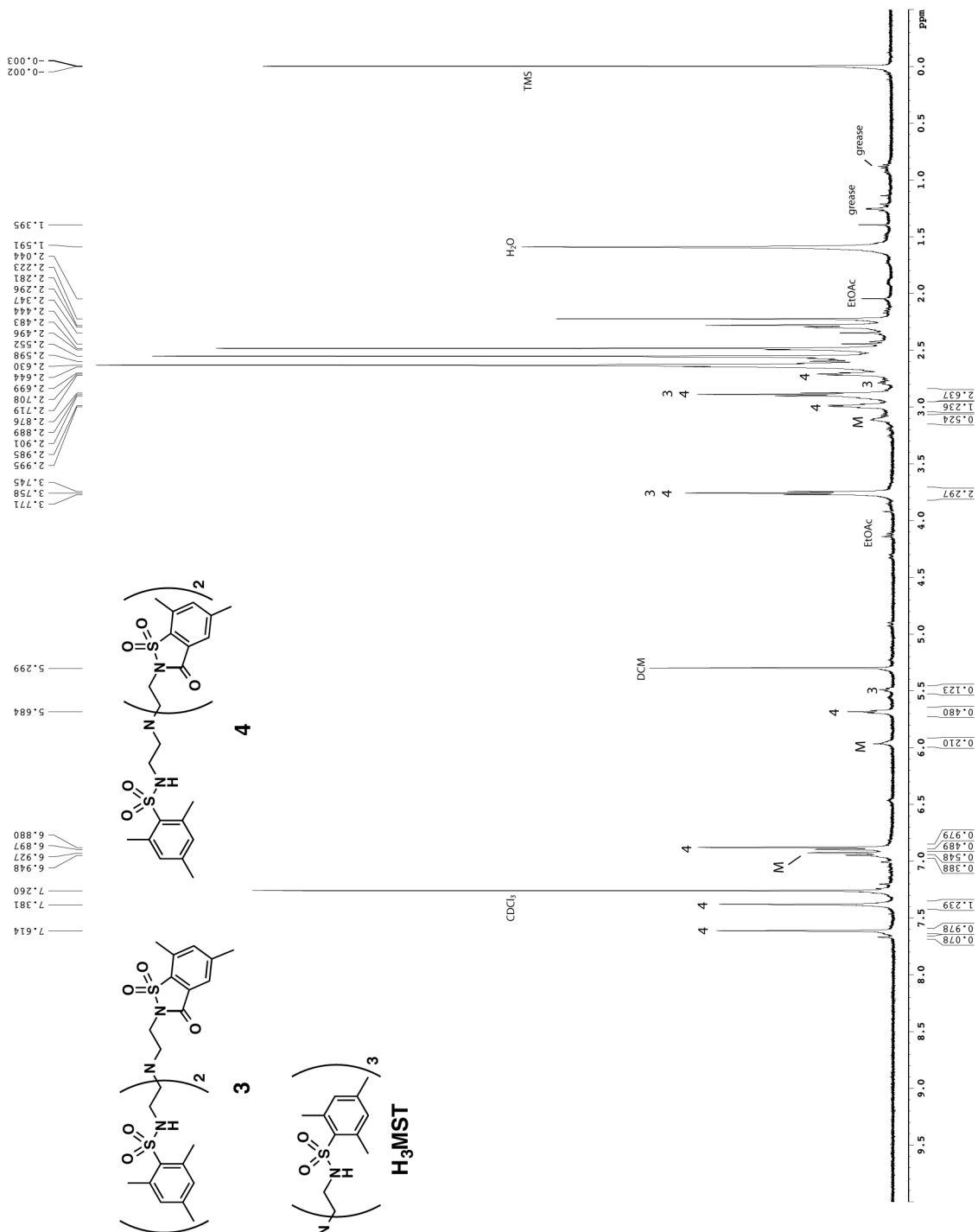


Figure A.7. ^1H NMR spectrum of a mixture of H_3MST and ligand products **3** and **4** that was separated from the remainder of the products via column chromatography.

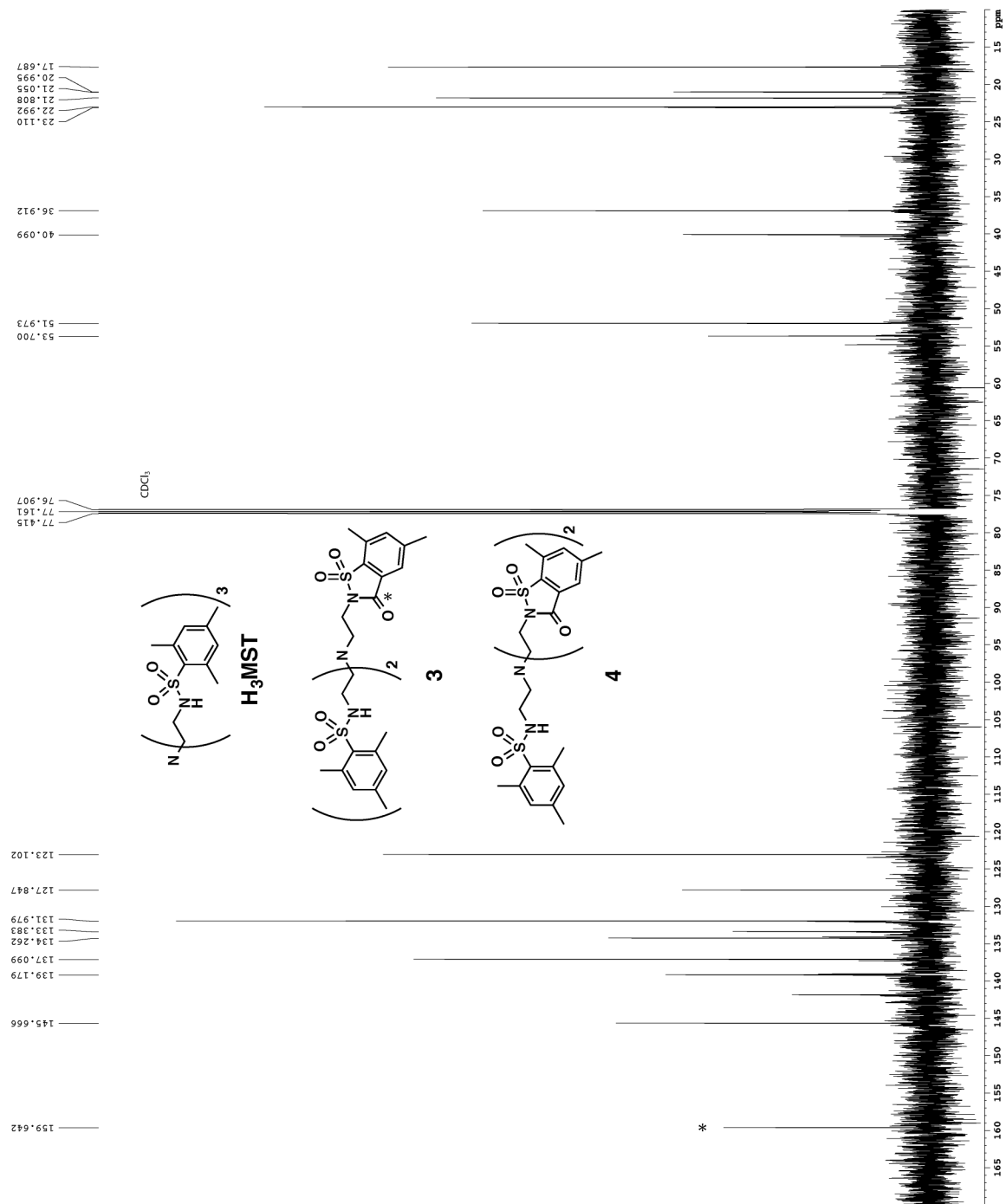


Figure A.8. ^{13}C NMR spectrum of a mixture of H_3MST and ligand products **3** and **4** that was separated from the remainder of the products via column chromatography.

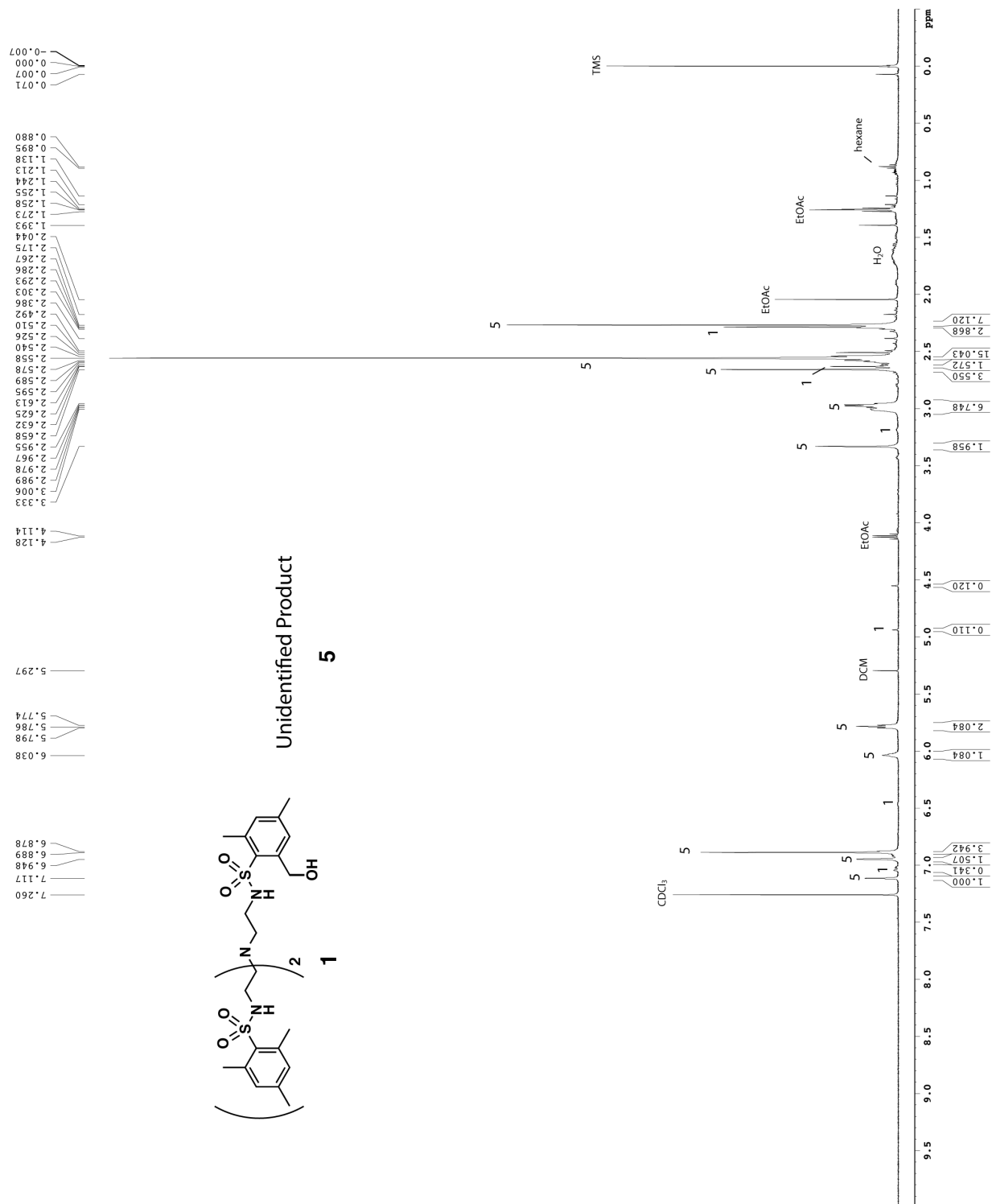


Figure A.10. ^1H NMR spectrum of a mixture of ligand products **1** and the unidentified ligand product **5** that was produced from the reaction of $\text{NMe}_4[\text{Mn}^{\text{II}}\text{MST}]$ and PhIO in the presence of $\text{Ca}(\text{OTf})_2/15\text{-crown-5}$. Products **1** and **5** were separated from H_3MST via column chromatography.

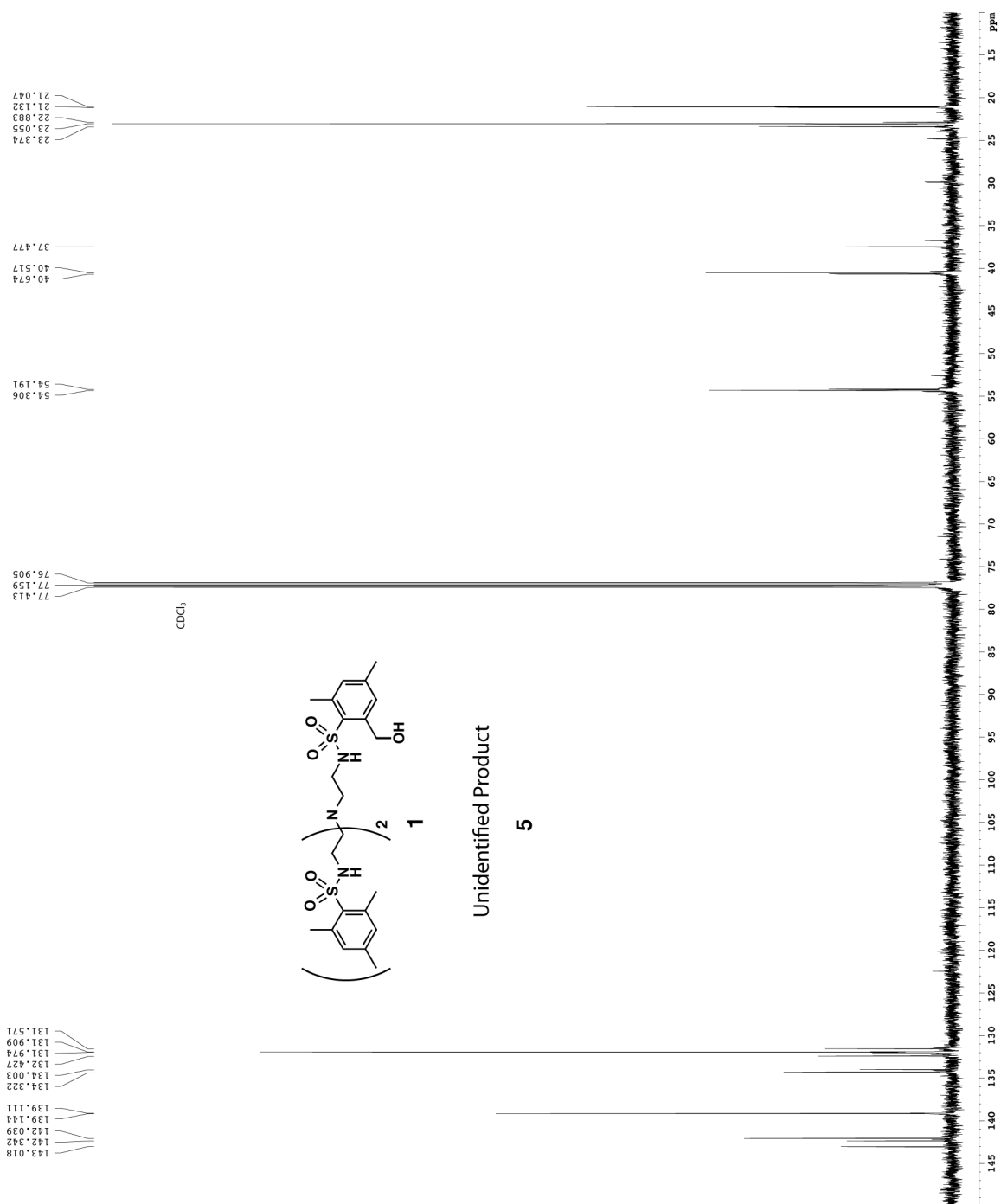


Figure A.11. ^{13}C NMR spectrum of a mixture of ligand products **1** and the unidentified ligand product **5** that was produced from the reaction of $\text{NMe}_4[\text{Mn}^{\text{II}}\text{MST}]$ and PhIO in the presence of $\text{Ca}(\text{OTf})_2/15\text{-crown-5}$. Products **1** and **5** were separated from H_3MST via column chromatography.

Table A.4. Crystallographic data and structure refinement parameters for the molecular structures presented in Chapter 4.

Complex	NMe ₄ [Fe ^{III} TST(OH)]	[15-crown-5⊃Ca ^{II} -(μ-OH)-Fe ^{III} TST]OTf
Formula	C ₃₁ H ₄₆ Fe N ₅ O ₇ S ₃	C ₃₈ H ₅₄ CaF ₃ FeN ₄ O ₁₆ S ₄ •C ₄ H ₈ O
Formula weight	752.76	1160.12
Crystal system	Triclinic	Triclinic
Space group	<i>P</i> $\bar{1}$	<i>P</i> $\bar{1}$
a (Å)	9.2518(5)	9.0916(3)
b (Å)	13.5464(8)	14.2771(5)
c (Å)	15.1289(8)	20.7655(7)
α (°)	85.2057(7)	73.1596(4)
β (°)	75.4487(6)	85.8504(5)
γ (°)	86.5673(7)	77.3919(5)
Volume (Å ³)	1827.36(18)	2517.5(2)
Z	2	2
δ _{calc} (Mg/m ³)	1.368	1.530
Goodness-of-fit	1.041	1.032
R1	0.0333	0.0379
wR2	0.0894	0.0897

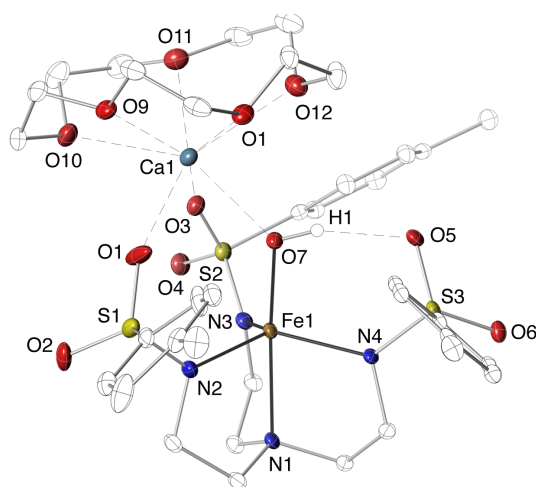


Figure A.12. Molecular structure of [15-crown-5⊃Ca^{II}-(μ-OH)-Fe^{III}TST]OTf determined by XRD methods. Thermal ellipsoids are drawn at the 50% probability level.

Table A.5. Select metrical parameters for [15-crown-5]Ca^{II}-(μ-OH)-Fe^{III}TST]OTf.

Bond Distances (Å)	
Fe1—O1	1.881(1)
Fe1—N1	2.234(2)
Avg Fe1—N _{eq}	2.025(2)
Ca1—O7	2.333(1)
Ca1···O1	2.349(2)
Ca1···O3	2.393(1)
Fe1···Ca1	3.764(6)
O5···O7	2.730(2)
Avg M1—O _{crown}	2.523(2)
d[Fe—N _{eq}]	0.394
d[M1—O _{crown}]	1.137
Bond Angles (°)	
O7—Fe1—N1	174.42(6)
N2—Fe1—N3	108.97(7)
N2—Fe1—N4	124.81(7)
N3—Fe1—N4	115.01(7)
τ value	0.83

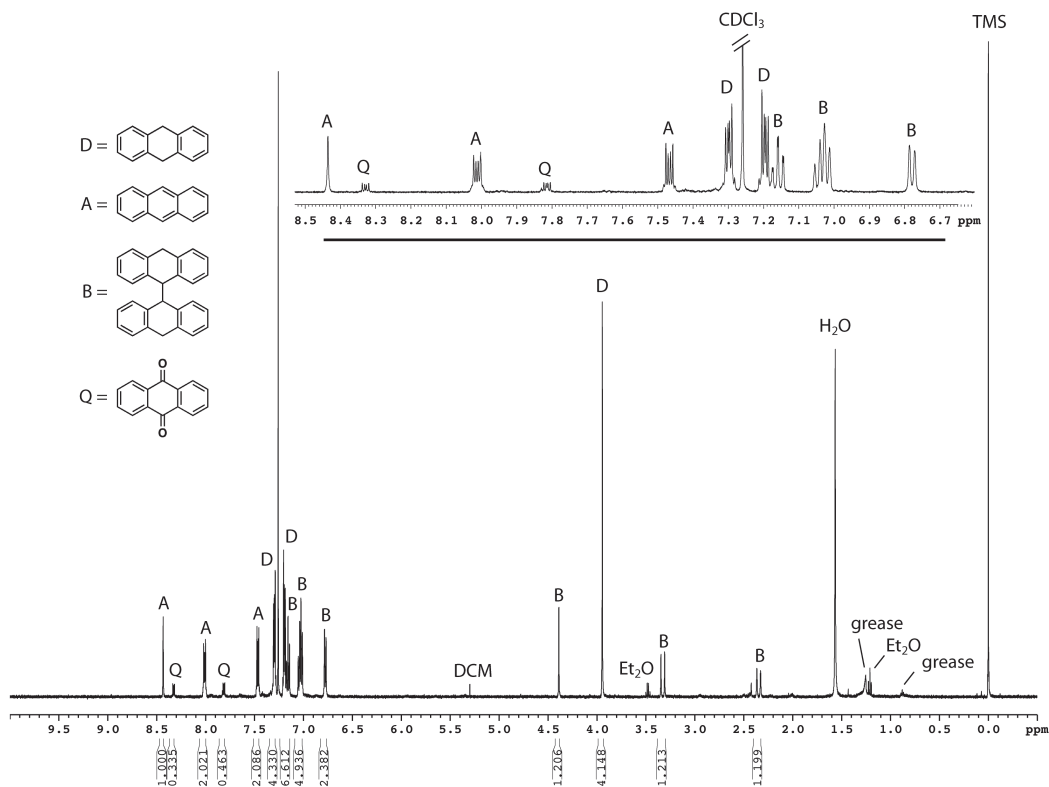


Figure A.13. ¹H NMR spectrum of the DHA products isolated from the reaction of NMe₄[Fe^{III}TST(OH₂)] with 2 equivalents of NMO in MeCN.

Table A.6. Crystallographic data and structure refinement parameters for the molecular structures presented in Chapter 5.

Complex	$K_2[Fe_2(tbaps)_2]$	$K_2[Co_2(tbaps)_2]$	$K_2[Cu_2(tbaps)_2]$
Formula	$C_{60}H_{62}Fe_2K_2N_8O_{10}S_4 \cdot 2(C_4H_9NO)_\infty$	$C_{60}H_{62}Co_2K_2N_8O_{10}S_4 \cdot 2(C_4H_9NO)_\infty$	$C_{60}H_{62}Cu_2K_2N_8O_{10}S_4 \cdot 2(C_4H_9NO)_\infty$
Formula weight	1547.56	1553.72	1562.94
Crystal system	Orthorhombic	Orthorhombic	Orthorhombic
Space group	<i>Pbcn</i>	<i>Pbcn</i>	<i>Pbcn</i>
a (Å)	11.026(1)	11.2306(6)	11.078(2)
b (Å)	29.193(3)	28.973(2)	29.177(6)
c (Å)	22.110(2)	21.836(1)	21.975(4)
α (°)	90	90	90
β (°)	90	90	90
γ (°)	90	90	90
Volume (Å ³)	7117(1)	7105.0(7)	7103(2)
Z	4	4	4
δ_{calc} (Mg/m ³)	1.444	1.453	1.462
Goodness-of-fit	1.019	1.026	1.028
R1	0.0355	0.0303	0.0307
wR2	0.0829	0.0734	0.0735

Table A.7. Crystallographic data and structure refinement parameters for molecular structures presented in Chapter 5.

Complex	$(NEt_4)_2[Co_2(tbaps)_2]$	$(NMe_4)_2[Cu_2(tbaps)_2]$	$[(15\text{-crown-}5)\text{-}2Ca][Ca[Cu_2(tbaps)_2]]$
Formula	$C_{52}H_{44}Co_2N_6O_8S_4 \cdot 2(C_8H_{20}N)$	$C_{72}H_{95}Cu_2N_{11}O_{11}S_4$	$[C_{62}H_{64}Ca_2Cu_2N_6O_{13}S_4 \cdot \frac{1}{2}(C_4H_9NO)]_\infty$
Formula weight	1387.53	1545.90	1480.23
Crystal system	Monoclinic	Monoclinic	Triclinic
Space group	<i>C2/c</i>	<i>P2₁/c</i>	<i>P$\bar{1}$</i>
a (Å)	20.193(3)	26.175(2)	11.367(1)
b (Å)	30.377(4)	12.7910(9)	11.500(1)
c (Å)	13.452(2)	22.539(2)	26.923(3)
α (°)	90	90	82.245(1)
β (°)	98.596(2)	96.0072(7)	83.724(1)
γ (°)	90	90	75.000(1)
Volume (Å ³)	8159(2)	7504.7(9)	3358.3(6)
Z	4	4	2
δ_{calc} (Mg/m ³)	1.130	1.368	1.464
Goodness-of-fit	1.017	1.177	1.025
R1	0.0531	0.0725	0.0562
wR2	0.1238	0.1510	0.1261

Table A.8. Bond distances (Å) within the backbone of one [tbaps]³⁻ ligand for each of the [M₂(tbaps)₂]²⁻ structures. The numbering scheme of the backbone is shown in Figure A.14.

	K ⁺ salts			NR ₄ ⁺ salts		Ca ²⁺ salt
	Fe	Co	Cu	Co	Cu	Cu
N1–C1	1.423(2)	1.428(2)	1.414(1)	1.423(4)	1.413(5)	1.405(4)
N1–C7	1.428(2)	1.434(2)	1.415(1)	1.431(4)	1.416(5)	1.409(4)
N2–C2	1.419(2)	1.415(2)	1.405(1)	1.411(5)	1.397(5)	1.397(4)
N3–C12	1.413(2)	1.414(2)	1.405(1)	1.407(5)	1.401(5)	1.406(4)
C1–C6	1.396(3)	1.396(2)	1.404(2)	1.396(5)	1.404(6)	1.396(5)
C1–C2	1.412(3)	1.408(2)	1.402(2)	1.415(5)	1.412(6)	1.418(4)
C2–C3	1.395(3)	1.394(2)	1.417(2)	1.392(5)	1.407(6)	1.399(5)
C3–C4	1.390(3)	1.390(2)	1.399(2)	1.389(5)	1.378(7)	1.380(5)
C4–C5	1.383(3)	1.384(2)	1.394(2)	1.383(5)	1.376(8)	1.390(5)
C5–C6	1.392(3)	1.393(2)	1.390(2)	1.377(5)	1.377(7)	1.380(5)
C7–C8	1.393(3)	1.396(2)	1.403(2)	1.388(5)	1.392(6)	1.397(4)
C7–C12	1.415(3)	1.413(2)	1.422(2)	1.410(5)	1.415(6)	1.425(5)
C8–C9	1.387(3)	1.384(2)	1.386(2)	1.387(5)	1.383(6)	1.372(5)
C9–C10	1.391(3)	1.387(2)	1.396(2)	1.393(5)	1.381(6)	1.383(5)
C10–C11	1.389(3)	1.392(2)	1.385(2)	1.366(5)	1.375(6)	1.383(5)
C11–C12	1.393(3)	1.397(2)	1.405(2)	1.390(5)	1.407(5)	1.393(5)

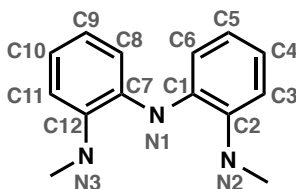


Figure A.14. Numbering scheme that corresponds to the metrical parameters shown in Table A.7.

Table A.9. Crystallographic data and structure refinement parameters for molecular structures presented in Chapter 6.

Complex	[Co(ibaps)DMAP] ⁻	[Fe(ibaps)bpy] ⁻	[Co(ibaps)bpy] ⁻	[Co(Hibaps)bpy]
Formula	C ₅₇ H ₈₄ CoN ₆ O ₅ S ₂ •C ₄ H ₁₀ N	C ₆₀ H ₈₂ FeN ₆ O ₄ S ₂	C ₆₀ H ₈₂ CoN ₆ O ₄ S ₂ •1/2(C ₄ H ₁₀ O)	C ₅₂ H ₆₃ CoN ₅ O ₄ S ₂ •(C ₄ H ₁₀ O)
Formula weight	1114.47	1071.28	1111.42	1019.24
Crystal system	Monoclinic	Triclinic	Monoclinic	Triclinic
Space group	<i>C2/c</i>	<i>P</i> $\bar{1}$	<i>P2</i> ₁ / <i>n</i>	<i>P</i> $\bar{1}$
a (Å)	48.014(9)	10.6445(6)	17.406(1)	9.9691(7)
b (Å)	11.040(2)	17.455(1)	10.7648(8)	16.736(1)
c (Å)	30.020(5)	17.864(1)	31.052(2)	18.086(1)
α (°)	90	113.9121(8)	90	113.0556(8)
β (°)	128.546(2)	98.7901(8)	91.3044(9)	103.2517(9)
γ (°)	90	91.4862(8)	90	95.9372(9)
Volume (Å ³)	12445(4)	2984.3(3)	5816.7(7)	2638.9(3)
Z	8	2	4	2
δ _{calc} (Mg/m ³)	1.190	1.192	1.269	1.283
Goodness-of-fit	1.126	–	1.046	1.029
R1	0.1203	–	0.0718	0.0521
wR2	0.2681	–	0.1912	0.1281

Table A.10. Bond distances (Å) within the [ibaps]³⁻ ligand backbone of the monomeric Co(ibaps)L complexes and within the bpy ligand of the five-coordinate complexes. The numbering scheme used to describe the bond lengths is shown in Figure A.15.

	[Co(ibaps)DMAP] ⁻	[Co(ibaps)bpy] ⁻	[Co(Hibaps)bpy]
N1–C1	1.372(9)	1.389(4)	1.457(3)
N1–C7	1.399(8)	1.372(4)	1.433(4)
N2–C2	1.428(8)	1.426(4)	1.435(4)
N3–C12	1.423(8)	1.421(4)	1.425(3)
C1–C6	1.403(9)	1.404(4)	1.391(4)
C1–C2	1.435(9)	1.429(4)	1.390(4)
C2–C3	1.38(1)	1.394(5)	1.387(4)
C3–C4	1.406(9)	1.395(5)	1.389(5)
C4–C5	1.39(1)	1.383(5)	1.372(6)
C5–C6	1.39(1)	1.394(5)	1.396(5)
C7–C8	1.423(9)	1.409(4)	1.389(4)
C7–C12	1.427(9)	1.439(4)	1.403(4)
C8–C9	1.38(1)	1.395(5)	1.385(5)
C9–C10	1.38(1)	1.382(5)	1.388(5)
C10–C11	1.40(1)	1.393(5)	1.391(4)
C11–C12	1.39(1)	1.398(5)	1.386(4)
bipyridine			
N5–C22	–	1.340(4)	1.335(3)
N5–C18	–	1.344(5)	1.357(3)
N4–C17	–	1.343(6)	1.352(4)
N4–C13	–	1.341(5)	1.338(4)
C13–C14	–	1.393(6)	1.388(4)
C14–C15	–	1.36(1)	1.368(5)
C15–C16	–	1.381(9)	1.378(5)
C16–C17	–	1.393(6)	1.386(4)
C17–C18	–	1.484(6)	1.485(4)
C18–C19	–	1.391(6)	1.389(4)
C19–C20	–	1.386(7)	1.376(5)
C20–C21	–	1.383(6)	1.382(5)
C21–C22	–	1.386(5)	1.378(5)

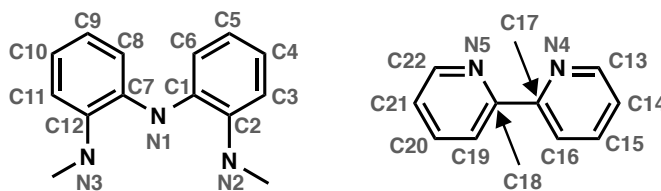


Figure A.15. Numbering scheme that corresponds to the metrical parameters shown in Table A.8.